University of Cyprus

DEPARTMENT OF CHEMISTRY

CONFORMATIONAL EFFECTS ON THE PHOTOPHYSICS OF THIOPHENE-BASED MATERIALS

DOCTOR OF PHILOSOPHY DISSERTATION

ELIANA NICOLAIDOU

2023

University of Cyprus

DEPARTMENT OF CHEMISTRY

CONFORMATIONAL EFFECTS ON THE PHOTOPHYSICS OF THIOPHENE-BASED MATERIALS

ELIANA NICOLAIDOU

A Dissertation Submitted to the University of Cyprus in Partial Fulfillment of the Requirements for the Degree of Doctor of Philosophy

MAY 2023

VALIDATION PAGE

Doctoral Candidate: Eliana Nicolaidou

Doctoral Thesis Tittle: Conformational effects on the photophysics of thiophene-based materials

The present doctoral dissertation was submitted in partial fulfillment of the requirements for the Degree of Doctor of Philosophy at the Department of Chemistry and was approved on the 09/05/2023 by the members of the ***Examination Committee.***

Examination Committee:

Research Supervisor:
Sophia Charalambous-Hayes, Associate Professor
Department of Chemistry, University of Cyprus

Committee Coordinator:
Epameinondas Leontidis, Professor
Department of Chemistry, University of Cyprus

Committee Member:
Eftychia Pinakoulaki, Associate Professor
Department of Chemistry, University of Cyprus

Committee Member:
Tracey Clarke, Associate Professor
Department of Chemistry, University College London

Committee Member:
Jenny Clark, Senior Lecturer
Department of Physics and Astronomy, University of Sheffield

DECLARATION OF DOCTORAL CANDIDATE

The present doctoral dissertation was submitted in partial fulfilment of the requirements for the degree of Doctor of Philosophy of the University of Cyprus. It is a product of original work of my own, unless otherwise mentioned through references, notes, or any other statements.

Eliana Nicolaidou

……………………………………..

Στην οικογένειά μου

Acknowledgements

First and foremost, I would like to express my heartfelt and sincere gratitude to my research supervisor, Associate Prof. Sophia Charalambous-Hayes, for giving me the opportunity to do research and providing invaluable guidance throughout this research. Her constant and invaluable support, caring, patience and feedback were blessings providing me the strength to carry out the research. It was a great privilege and honor to work and study under her guidance.

I would like to warmly thank my committee members: Prof. Epameinondas Leontidis, Associate Prof. Eftychia Pinakoulaki, for their participation to all of my scientific exams and their constructive comments throughout my research journey. Dr. Jenny Clark from the University of Sheffield for the fruitful collaboration and Associate Prof. Tracey Clarke from the University College London for kindly accepting the invitation and honour me with her presence. I thank you all for having accepted to read this thesis dissertation and being part of my jury committee.

I would also like to thank the other collaborators with which I had the honour to work with and who contribute significantly in the work performed in this thesis: Prof. Natalie Banerji and Dr. Lisa Peterhans from the University of Bern, Prof. Ursula Roëthlisberger and Dr. Polydefkis Diamantis from the Ecole Polytechnique Fédérale de Lausanne (EPFL), Dr. Mathieu Surin for the fruitful conversations, Assistant Prof. Theodossis Trypiniotis and PhD candidate Constantinos Nicolaides from University of Cyprus and Dr. Jenny Clark from the University of Sheffield.

I would also like to thank the staff members of Central Laser Facility (CLF) of the Rutherford Lab in the United Kingdom Dr. Mike Towrie, Dr. Greg Greetham, Dr. Igor Sazanovich and Dr. Ian Clark for their assistance during our visit at their facilities for time-resolved IR measurements as well as their guidance through skype meetings. Special thanks to Prof. Tony Parker for his warm hospitality during our time there and his invaluable contribution for the implementation of TRIR data.

I am deeply grateful to Prof. Tullio Scopigno from the Sapienza University of Rome and the Research Fellows, Dr. Giovanni Batignani and Dr. Miles Martinati. I thank Tullio for hosting me in his lab, conducting the Femtosecond Resonance Raman measurements and data and helping me with the analysis during skype meetings.

Additionally, I would like to thank Associate Prof. Eftychia Pinakoulaki for providing me access to her lab for ATR-FTIR measurements.

A special thanks to my present and former lab mates of the Molecular Spectroscopy group Eirini, Elisa, Alexandros, Koulla and Nicolas for support, assistance and the quality time spent together.

Last but not least, I would like to thank my parents Nicos and Eleni and my brothers Constantinos and Andreas for their constant support in all possible ways, their limitless patience and endless love. They are true blessings. My deepest thanks to my loving and supporting boyfriend Panayiotis, who enthusiastically motivates me and all my friends for the moral support that provided me all along this journey.

ABSTRACT

Thiophene-based organic semiconductors are materials widely studied, thanks to their excellent combination of optical and electronic properties that can be exploited for optoelectronic applications. Understanding the strong correlation of their photophysical properties to their backbone structure and the exploitation of this relation can be extremely beneficial, in order to induce desired properties to the materials. Thus, it is essential to establish a strategy of monitoring the structural variations in order to effectively elucidate the structure-property relation. In the present thesis, we employed different spectroscopic techniques which, in combination with other experimental and theoretical methods, provided a better understanding of aspects that trigger the structural variations, in order to determine the key parameters that can be exploited for conformational control, as well as study the effect of the modifications of the structure on the properties that these materials exhibit. Particularly the structural variations in conjugated polymers and small conjugated molecules stem from the ability to change the electron distribution along the conjugated backbone. Effective delocalization across a conjugated core is enabled by the extended π-conjugation.

Therefore, we studied the templating effect of single-stranded DNA oligomers with different sequence, in order to evaluate the ability to induce an extended conformation of cationic polythiophene (CPT). We observed that the optimal templating is achieved with consecutive cytosines through numerous π-stacking interactions with the thiophene rings, leading to rigid assembly with highly ordered chains. The templating effect is also transmitted to the excited state dynamics. Transient absorption measurements detected only excitons while polarons or triplet states were absent. Using a time-resolved IR spectroscopy, we observed that intrachain polarons are produced in larger extent when templating induces extended CPT conformation. This was supported by the femtosecond stimulated Raman measurements.

The effect of the existence of charge carriers on the structure of thiophene-based polymer chains was also studied by using Resonance Raman as the main structural probe. In particular, we detected conformational changes of PEDOT:PSS during chemical or electrochemical doping revealing that upon dedoping, quinoid structure is adopted to a larger extent exhibiting increased planarity, which is linked to weaker spin-orbit coupling.

Finally, we inspected how structural manipulation through alkylation or decrease of conjugation length, by the existence of a freely rotating single band in the core of benzothiophene derivatives (planar small conjugated molecules), affects the change in the molecular geometry in the excited state. We find that alkylation causes a decrease of the conjugation length and that the structural evolution upon transition to the excited state involves in-plane vibrations.

ΠΕΡΙΛΗΨΗ

Οι οργανικοί ημιαγωγοί με δομή βασισμένη στο θειοφαίνειο είναι υλικά που μελετώνται ευρέως, χάρη στο μοναδικό συνδυασμό οπτικών και ηλεκτρονικών ιδιοτήτων, οι οποίες μπορούν να αξιοποιηθούν σε οπτοηλεκτρονικές εφαρμογές. Η κατανόηση της ισχυρής σχέσης των φωτοφυσικών τους ιδιοτήτων με τη δομή της κύριας αλυσίδας και η αξιοποίηση αυτής της σχέσης μπορεί να είναι ιδιαίτερα επωφελής για την επαγωγή επιθυμητών ιδιοτήτων στα υλικά. Επομένως, είναι απαραίτητο να καθοριστεί στρατηγική παρακολούθησης των δομικών μεταβολών, με στόχο την εξακρίβωση της σχέσης δομής-ιδιοτήτων. Στην παρούσα διδακτορική διατριβή, αξιοποιήσαμε διάφορες φασματοσκοπικές τεχνικές οι οποίες, σε συνδυασμό με άλλες πειραματικές και θεωρητικές μεθόδους, συνέβαλαν στην καλύτερη κατανόηση των στοιχείων που προκαλούν τις δομικές αλλαγές, με στόχο να προσδιοριστούν οι κύριες παράμετροι οι οποίες μπορούν να αξιοποιηθούν για τη στοχευμένη ρύθμιση της διαμόρφωσης, καθώς και τη μελέτη της επίδρασης των μεταβολών της δομής στις ιδιότητες που παρουσιάζουν τα υλικά. Συγκεκριμένα, οι δομικές αλλαγές σε συζυγιακά πολυμερή και μικρά συζυγιακά μόρια προκύπτουν από την ικανότητα να αλλάζει η ηλεκτρονιακή κατανομή κατά μήκος της συζυγιακής αλυσίδας. Ο αποδοτικός απεντοπισμός κατά μήκος της συζυγιακής αλυσίδας επιτυγχάνεται μέσω της εκτεταμένης π-συζυγίας.

Επομένως, μελετήσαμε την επίδραση του εκμαγείου (templating effect) των ολιγομερών απλής αλυσίδας DNA με διαφορετική αλληλουχία, έτσι ώστε να αξιολογήσουμε την ικανότητα επαγωγής εκτεταμένης διαμόρφωσης του κατιονικού πολυθειοφαινείου CPT. Παρατηρήσαμε ότι η βέλτιστη επίδραση επιτυγχάνεται με συνεχόμενες κυτοσίνες μέσω π-stacking αλληλεπιδράσεων με τους δακτυλίους θειοφαινείου, που οδηγεί σε άκαμπτη πρόσδεση με επίπεδες αλυσίδες. Η επίδραση του template μεταφέρεται και στη δυναμική της διεγερμένης κατάστασης. Μέσω των μετρήσεων χρονοεξαρτώμενης απορρόφησης ανιχνεύθηκαν μόνο εξιτόνια, ενώ πολαρόνια και καταστάσεις triplet δεν εντοπίστηκαν. Χρησιμοποιώντας φασματοσκοπία χρονοεξαρτώμενης απορρόφησης υπέρυθρου, παρατηρήσαμε την παραγωγή πολαρονίων κατά μήκος της αλυσίδας σε μεγαλύτερο βαθμό όταν η πρόσδεση επάγει εκτεταμένες αλυσίδες CPT. Αυτό επιβεβαιώνεται από τις μετρήσεις χρονοεξαρτώμενης επαγόμενης σκέδασης Raman.

Επιπρόσθετα, μελετήθηκε η επίδραση της παρουσίας φορέων φορτίου στη διαμόρφωση πολυμερούς βασισμένου σε θειοφαίνειο χρησιμοποιώντας φσματοσκοπία Raman

συντονισμού ως το βασικό μέσο παρατήρησης της δομής. Συγκεκριμένα, εντοπίστηκαν αλλαγές στη διαμόρφωση του PEDOT:PSS κατά τη διάρκεια χημικού ή ηλεκτροχημικού doping, υποδεικνύοντας ότι όταν λαμβάνει χώρα dedoping, το πολυμερές λαμβάνει κινοειδή διαμόρφωση σε μεγάλο βαθμό παρουσιάζοντας βελτιωμένη επιπεδότητα, από την οποία προκύπτει ασθενέστερο spin-orbit coupling.

Τέλος, διερευνήσαμε τον τρόπο με τον οποίο η επίδραση στη δομή μέσω αλκυλίωσης ή η μείωση του μήκους συζυγίας, με την ύπαρξη απλού δεσμού στον σκελετό παραγώγου βενζοθειοφαινείου (επίπεδα μικρά συζυγιακά μόρια), επηρεάζει την αλλαγή στη μοριακή γεωμετρία στη διεγερμένη κατάσταση. Παρατηρήσαμε ότι η αλκυλίωση προκαλεί μείωση του μήκους συζυγίας και ότι για την αλλαγή στη δομή στη διεγερμένη κατάσταση συνεισφέρουν οι δονήσεις εντός επιπέδου.

Contents

LIST OF FIGURES

possible coupling or charge transfer to the ssDNA cannot be completely excluded). Concentration: $7.3\cdot10^{-5}$ M (monomeric basis of cytosine bases for dCs alone and of CPT for CPT/dCs).

Figure 4.15. Normalized CD signal as a function of the dC equivalents titrated in CPT solution for the various dC lengths. The x axis has been shifted relative to the position of 50% CD signal.

Figure 4.16. Absorption and CD spectra of (a) dC$_5$ and (b) dC$_{10}$ with different relative amounts of CPT (in PBS buffer with a dC concentration of $7.3\cdot10^{-5}$ M, monomeric basis, 20 °C). The scaled absorption spectrum of CPT alone is added as reference (dashed grey line).

Figure 4.17. Absorption spectra of CPT complexed to various 20-base ssDNA strands (sequences shown in the legend) at 55 °C.

Figure 4.18. (a) RR spectra normalized with respect to the intensity of the band at ~1460 cm^{-1} with excitation at 473 nm for (left) P3HT-PMe$_3$ or (right) P3HT-Im (blue) and its complexes with dA$_{20}$ (black), dT$_{20}$ (green) and dC$_{20}$ (red) in PBS buffer with a concentration of $1.5\text{x}10^{-4}$ M (monomeric basis) at room temperature. (b) Graphical comparison of the wavenumbers of C=C symmetric band of P3HT-PMe$_3$ (blue) or P3HT-Im (magenta) and its complexes with dA$_{20}$, dC$_{20}$ and dT$_{20}$ extracted from the corresponding RR spectra. (c) Absorption spectra of (left) P3HT-PMe$_3$ or (right) P3HT-Im (blue) and its complexes with dA$_{20}$ (black), dT$_{20}$ (green) and dC$_{20}$ (red) in PBS buffer with a concentration of $1.5\cdot10^{-4}$ M (monomeric basis) at room temperature.

Figure 4.19. UVRR spectra of dC$_{20}$ alone and assembled with (a) P3HT-PMe$_3$ and (b) P3HT-Im.

Figure 4.20. Absorption spectra of dC$_{20}$ complexed to CPT, P3HT-PMe$_3$, and P3HT-Im in PBS buffer with a concentration of $1.5\text{x}10^{-4}$ M (monomeric basis) at room temperature.

Figure 5.1. TA data for CPT in solution following excitation at 400 nm (1.5×10^{-4} M on a monomeric unit basis in PBS). TA spectra recorded at selected time delays for CPT at 5 ˚C (top) and 55 ˚C (bottom) with the corresponding stationary absorption (black curves). The two insets show the TA dynamics probed at selected wavelengths.

Figure 5.2. (a) TA spectra recorded following excitation at 400 nm at selected time delays with the corresponding stationary absorption (black curves) for two complexes (top: CPT/dA$_{20}$, bottom: CPT/dC$_{20}$) in solution at 20 °C ($1.5\text{x}10^{-4}$ M on a monomeric unit basis in PBS). The features at around 740 and 860 nm are artefacts due to the white light generation near the fundamental 800 nm laser output. (b) TA dynamics at selected probe wavelengths for the three complexes (dA$_{20}$, T406, and dC$_{20}$). Solid lines correspond to the biexponential global fit.

Figure 5.3. Extracted stimulated emission spectra at different time delays after photoexcitation for CPT/dC$_{20}$.

Figure 5.4. Experimental and calculated stimulated emission spectra for CPT/dC$_{20}$ at selected time delays.

Figure 5.5. Dependence of the displacement (Δ) along the C_{β}-$C_{\beta'}$ and $C_{\alpha}=C_{\beta}$ normal coordinates and E_{0-0} on the delay time, as obtained from modeling the stimulated emission spectra.

Figure 5.6. (a) TRIR spectra of CPT following excitation at 532 nm. The spectral region 1370-1400 cm^{-1}, is dominated by an experimentally-induced artifact feature and has been omitted. No extra vibrational features are expected in this region as seen in Fig. 5.8a and S5.1a. (b) Ground state Raman spectrum of CPT with excitation at 532 nm with inverted y axis.

Figure 5.7. Linear correlation of the intensity of each vibrational band in the TRIR spectra of CPT alone and the intensity of a point (1350 cm^{-1}) considered as background as a function of delay time (between 1.7-200 ps).

Figure 5.8. (a) TRIR spectra of CPT/dC$_{20}$ with excitation at 532 nm (b) Ground state Raman spectrum of CPT/dC$_{20}$ with excitation at 532 nm with reversed y axis.

Figure 5.9. TRIR spectra at 1 ps of CPT (black), CPT/dA$_{20}$ (red) and CPT/dC$_{20}$ (blue). The latter spectrum was divided by 1.25 to adjust for concentration differences.

Figure 5.10. TRIR spectra of CPT/dC$_{20}$ (a) before and (b) after background subtraction with excitation at 266 nm.

Figure 5.11. TRIR spectra after the subtraction of the background of CPT/dC$_{20}$ (red) and dC$_{20}$ at pH 7 (black) and dC$_{30}$ at pH 8.5 (yellow), 5.5 (blue) and 7 (green) (TRIR spectra of dC$_{30}$ were reproduced from the literature) at 2 ps.

Figure 5.12. (a) TRIR spectra after the subtraction of the background of CPT/dA$_{20}$ (red) and dA$_{20}$ at pH 7 (black) at 2 ps (b) TRIR spectra of CPT/dA$_{20}$ without background subtraction with excitation at 266 nm.

Figure 5.13. (a) 2D broadband ISRS spectrum of CPT/dC$_{20}$ as a function of the probe wavelength and the Raman frequency. (b) Stimulated emission spectrum (c) Comparison of ISRS spectra integrated over different probe wavelength regions (see legends) from 610 to 689 nm (stimulated emission), after Fourier transform of the coherent oscillations. The different probe wavelength regions and all the prominent bands are displayed by red and black dashed lines, respectively, in the 2D broadband ISRS spectrum (left inset) in panel c. The inset on the right side of panel c corresponds to TA spectra, recorded following excitation at 400 nm at selected time delays (adopted by Figure 5.2), where the yellow box marks the region of pump excitation wavelengths (on resonance with absorption: 500-600 nm) and the grey box marks the region of probe wavelengths (on resonance with SE: 600-700 nm).

Figure 5.14. Ground state Resonance Raman (RR) spectra with visible excitation at 435.69 nm for CPT/dT$_{20}$, at 473 nm for CPT, CPT/dA$_{20}$, CPT/T406 and CPT/dC$_{20}$ and at 532 nm for CPT/dC$_{20}$ in PBS buffer with a concentration of 1.5x10^{-4} M (monomeric basis) at 20 °C.

Figure 5.15. Comparison of ISRS spectra of CPT /dC_{20} integrated over different probe wavelength regions (see legends) from 500 to 599 nm (absorption), after Fourier transform of the coherent oscillations. The different probe wavelength regions and all the prominent bands are displayed by red and black dashed lines respectively in the 2D broadband ISRS spectrum (left inset). The inset on the right side corresponds to TA spectra, recorded following excitation at 400 nm at selected time delays (adopted by Figure 5.2), where the yellow box marks the region of pump excitation wavelengths (on resonance with SE: 600-700 nm) and the grey box marks the region of probe wavelengths (on resonance with absorption: 500-600 nm).

Figure 5.16. Comparison of ISRS spectra of CPT /dC_{20} integrated over different probe wavelength regions (specified on the left of each spectrum) from 860 to 939 nm (excited-state absorption (ESA)), after Fourier transform of the coherent oscillations. The inset at the right side corresponds to TA spectra, recorded following excitation at 400 nm at selected time delays (adopted by Figure 5.2), where the yellow box marks the region of pump excitation wavelengths (on resonance with absorption: 500-600 nm) and the grey box marks the region of probe wavelengths (on resonance with excited-state absorption: IR 800-970 nm).

Figure 5.17. Comparison SRS spectra of CPT /dC_{20} when probing at blue and red side of Raman pump wavelength (indicated by the colour of each spectrum) using (a) 599 nm, (b) 614 nm and (c) 644 nm as Raman pump wavelengths.

Figure 5.18. (a) Time evolution of actinic pump on and pump off spectra (green and blue spectra respectively) of CPT /dC_{20} using 599 nm as Raman pump wavelength, when probing at red side of Raman pump wavelength (center of spectral region: 643 nm). (b) Difference of actinic pump on – pump off spectra in panel a at different time delays. (c) Kinetics of integrated difference signal of the actinic pump on – pump off spectra obtained by panel b.

Figure 5.19. (a) Temporal evolution of actinic pump on and pump off spectra (green and blue spectra respectively) of CPT /dC_{20} using 614 nm as Raman pump wavelength, when probing at red side of Raman pump wavelength (center of spectral region: 666 nm). (b) Non-normalized and (c) normalized difference of actinic pump on – pump off spectra in panel a at different time delays.

Figure 5.20. (a) Time evolution of actinic pump on and pump off spectra (green and blue spectra respectively) of CPT /dC_{20} using 644 nm as Raman pump wavelength, when probing at red side of Raman pump wavelength (center of spectral region: 704 nm). (b) Difference of actinic pump on – pump off spectra in panel a at different time delays. (c) Kinetics of integrated difference signal of the actinic pump on – pump off spectra obtained by panel b.

Figure 6.1. UV-vis-NIR absorption spectra for all samples of spin-coated films.

Figure 6.2. Estimation of the spin admixture parameter γ^2 for P1–P6. For comparison, we plot the theoretical value of sexithiophene (T6) (blue dashed line) a material with linear conformation and very similar structure with PEDOT.

Figure 6.3 Normalized resonance Raman spectra of the PEDOT:PSS samples at different doping levels with excitation at 532 nm.

LIST OF TABLES

NOMENCLATURE

OSC	Organic Semiconductor
OLED	light-emitting diodes
OFET	field-effect transistors
OPV	organic photovoltaic cells
TT	thienothiophenes
DTT	dithienothiophenes
TA	thioacenes
OTFT	organic thin film transistors
DSSC	dye-sensitized solar cells
rr	regioregularity
k_B	Boltzmann factor
ssDNA	single-stranded DNA
NA	Nucleic Acid
CPE	Conjugated Polyelectrolyte
CPT	Cationic poly(1H-imidazolium,1-methyl(-3-[2-[(4-methyl-3-thienyl)oxy}-ethyl]-chloride
dC	Homonucleotide oligocytosine
CD	Circular Dichroism
RR	Resonance Raman spectroscopy
RRIA	Resonance Raman Intensity Analysis
MD	Molecular Dynamics
PBS	Phosphate Buffered Saline
UVRR	Ultraviolet Resonance Raman spectroscopy
B3LYP	Becke, three parameter, Lee-Yang-Parr
θ	SCCS dihedral angles
REP	Raman Excitation Profile
ω_g	ground state vibrational frequency
ω_e	excited state vibrational frequency
Δ	displacement between the ground and excited state potential energy surface minima in each mode
M	electronic transition dipole moment

Γ	homogeneous broadening
Θ	inhomogeneous broadening
E_{00}	difference between the v = 0 in the ground and excited electronic states
λ_{tot}	total reorganization energy
χ	glycosidic torsional angle
δ	bending vibrations
Mn	number-averaged molecular weight
P3HT-PMe$_3$	poly[3-(6’-(trimethylphosphonium)hexyl)thiophene-2,5-diyl]
P3HT-Im	poly[3-(6′-(imidazolium)hexyl)thiophene-2,5-diyl]
Fwhm	full-width-half-maximum
PDA	polydiacetylene
M_w	molecular weight
PDI	polydispersity index
Vis-NIR	Visible-Near Infrared
TRIR	Ultrafast Time-Resolved Infrared Spectroscopy
TA	Femtosecond Transient Absorption
IRAV	Infrared active vibrational mode
FA	Fano antiresonances
ISRS	impulsive stimulated Raman scattering
SRS	Stimulated Raman Spectroscopy
FSRS	Femtosecond Stimulated Raman Spectroscopy
PIA	Photoinduced Absorption
HOMO	Highest Occupied Molecular Orbital
DP$_1$	delocalized polaron band
CT	charge transfer
PPV	Poly(p-phenylene vinylene)
ESA	excited state absorption
GSB	ground state bleaching
SE	stimulated emission
rr-P3HT	regioregular poly(3-hexylthiophene-2,5-diyl)
CMS	charge modulation spectroscopy

SOC	Spin-orbit coupling
SDL	spin diffusion length
θ_H	spin Hall angle
PEDOT:PSS	poly(3,4-ethylenedioxythiophene):poly(4-styrenesulfonate)
γ	spin-admixture parameter
FMR	Ferromagnetic Resonance
ISHE	Inverse Spin Hall Effect
HFI	hyperfine interaction
T_1	spin-lattice relaxation time
τ	dwell time
α	average hopping distance
ISC	Intersystem crossing
BTBT	[1]benzothieno[3,2- b]-[1]benzothiophene
ΔE_{S-T}	energy gap between lowest singlet and adjacent triplet excited state
IC	Internal Conversion
PBI	Perylene Bisimide
BT	Benzothiophene
Cn-BTBT	monoalkyl-[1]benzothieno[3,2- b]-[1]benzothiophene
Cn-BTBT-Cn	2,7-dialkyl-[1]benzothieno[3,2- b]-[1]benzothiophene
diBT	dibenzothiophene
FC	Frank-Condon
S_n	singlet state
T_n	triplet state
k_{isc}	Intersystem Crossing rate
SOCME	Spin Orbit Coupling Matrix Element
ρ	density of final states
MLJ	Marcus-Levich-Jortner
$\rho_{FCWD}^{MLJ}(\Delta E)$	Franck-Condon Weighted Density of States
S	Huang-Rhys parameter
DPP	diketopyrrolopyrrol

CHAPTER 1

INTRODUCTION

Organic materials are considered electrical insulators due to their low conductivity, caused by absence of free charge carrier into their structure. The discovery of electrical conduction in organic materials can be traced back in 1970s, when Heeger, MacDiarmid and Shirakawa discovered that the polymer poly acetylene after certain modification can be made conductive.[1] The discovery of electrically conductive polymers drastically changed our views on organic materials and formed a basis of the future organic electronics. Even though organic compounds are intrinsic insulators, the presence of conjugation along the backbone can unlock the possibilities to induce electrical conductivity. However, conjugation alone results in low electrical conductivity. Therefore, the key element to convey desired properties onto organic materials is the backbone conjugation and the need to understand the structure – property relation is of utmost importance, in order to determine the structural characteristics that induce functionality in the field of optoelectronics. Subsequently, it is equally important to develop strategies to control the structure of both conjugated polymers and small molecules towards the adoption of the most efficient structures for optoelectronic applications. The unique electrical, optical and mechanical properties, which in combination with their ease of processing, low cost and the ability to adopt a wide range of different structures, makes the conjugated materials particularly attractive for a wide variety of applications.

The originality of the present doctoral dissertation stems from the ability to monitor the structural variations, in order to determine the parameters that affect the structure of the backbone of the conjugated molecules, as well as to correlate the modifications of structure with the properties of these materials. In this work, we were able to obtain atomistic-level information about the ground state and excited state conformation of the cationic polythiophene (CPT), which was assembled to different single-stranded DNAs to assess their templating effect. The selective examination of each component of the complex, enabled by Resonance Raman, time-resolved IR and femtosecond stimulated Raman spectroscopy, revealed by the former the specific interactions that promote the strong assembly and by the two latter the structural implications of each component about the produced excited state species. Moreover, the torsional order of the backbone of another thiophene-based conjugated polymer PEDOT under different doping/dedoping conditions was studied though *resonance Raman by selectively probing the different conformations adopted by the existence of polarons and bipolarons on the polymer backbone. The structural aspects that were derived from the RR spectra were linked for the first time with the spin orbit coupling strength of the polymer. Lastly, we investigated the effect of alkyl substitution on the structural variations between the ground and excited state of planar benzothiophene derivatives (BTBT) by exploring RR spectroscopy. Resonance Raman Intensity Analysis was performed for the study of BTBT molecules and of CPT/ssDNA complexes and provided a detailed insight of the changes of the molecular geometry at the excited state by denoting the specific modes that mostly contribute to the structural evolution.*

This doctoral dissertation consists of 9 chapters and is organized as follows:

In Chapter 2, we firstly determine the important features of thiophene-based small molecules and polymers. We then report how the structure is strongly correlated with the properties of the conjugated materials, especially polymers. Then, we refer to the effect of excitons and polarons on backbone conformation. We continue by highlighting the significant contribution of vibrational spectroscopies to structural characterization. Information about a special class of conjugated polymers, in which the most studied polymer in this thesis, CPT, belongs to, are presented as well as followed by a brief review of how templates can affect structure of polymer chain inducing extended conformations.

In Chapter 3, the main spectroscopic techniques are reviewed, which are Resonance Raman, transient absorption, time-resolved IR, impulsive stimulated Raman and femtosecond stimulated Raman spectroscopies, in order to give to the reader the basic tools to understand what kind of information can be obtained from each technique. The setups and experimental details are also briefly described only for the techniques that were performed by us and not by our collaborators. The experimental details for all the techniques can be found in the chapter referred to the project in which they were used.

The results obtained for cationic polythiophene, CPT/ssDNA complexes are presented and discussed in Chapters 4 and 5. In Chapter 4, we report the templating effect of oligonucleotides on the conformation of CPT at the ground state. We tested different sequences but focused more on the effect of oligocytosine and oligoadenine which correspond to the two extreme cases of templating effect. These assemblies were optically and structurally studied using a combination of spectroscopic techniques combined with Molecular Dynamics. In Chapter 5, the work on CPT in solution is continued by examining again the two complexes CPT/dA_{20} and CPT/dC_{20}, focusing now on their excited state behaviour, which was compared with CPT alone. For this work, we employed different spectroscopic techniques, mostly vibrational, in order to monitor the structural changes at the excited state and relate them with processes that may occur.

In Chapter 6, we elucidate the relation of the conformation changes of the backbone on spin-orbit coupling (SOC) strength.

In Chapter 7, we studied the change in the molecular geometry of planar small BTBT molecules in the excited state.

The conclusions derived from this dissertation are discussed in Chapter 8, while the future perspectives of the work performed are reported in Chapter 9.

References

(1) Heeger, A. J.; MacDiarmid, A. G.; Shirakawa, H. Advanced Information - The Nobel Prize in Chemistry, 2000 : Conductive Polymers. *Nobel Prize Outreach AB 2023* **2000**, 1–16.

CHAPTER 2

Background

Organic semiconductors (OSCs) are organic materials with the ability to conduct electrons, and their electronic conductivity lies between that of metals and insulators.[1] Development of new high performance OSCs, with great potential in plastic electronics applications, including organic light-emitting diodes (OLEDs), organic field-effect transistors (OFETs), sensors or organic photovoltaic cells (OPVs), has been one of the most active research fields over the last few decades.[2–6] They have unique electrical, optical, and mechanical properties, which in combination with their ease of processing through attached solubilizing side chains and the possibility of an exact tailoring of the electronic and mechanical properties to achieve the desired functions, low production cost, and the wide range of different choices of structures makes them a particularly attractive category of materials for a wide variety of applications. Design of high performance organic semiconducting materials requires a thorough understanding of inter- and intra-molecular interactions, solid-state packing, and the influence of both factors on the charge carrier transport. Specifically, thiophene-based organic semiconductors, which are classified in terms of their chemical structures and their structure–property relationships, are materials of great interest thanks to their excellent combination of optical and electronic properties.[7–12]

2.1 Thiophene-based π-Conjugated polymers and small molecules

Thiophene-based π-conjugated organic small molecules and polymers exhibit extensive interest over the strong correlation of the photophysical properties to their structure owing to their potential use as organic semiconductors in material chemistry.[13–16] These materials are beneficial showing fascinating properties such as high conductivity, mobility, chemosensitivity, liquid crystallinity, or chirality.[17] Oligomers and polymers based on thiophenes have attracted considerable attention both experimentally and theoretically. Their design can be readily performed on the molecular level providing outstanding synthetic control of their molecular electronic structures through control of the thiophene chain length, and a variety of substituents that can be used to tune the molecular orbital energies, charge carrier mobilities, and spectral properties of the individual molecular species.[18–22] In addition, a number of thiophene-based fused systems can be constructed and utilized in the field of semiconducting materials.

2.1.1 Fused thiophene-based small molecules as organic semiconductors

Recently, conjugated small molecules have drawn much interest due to well-characterized structures. Unlike conjugated polymers, fused thiophenes provide a better conjugation in the ground state and are utilized for tuning the band gap of organic materials owing to their rigid structures with an elongated π-conjugation. Structural ring planarity, extended π-conjugation and chemical stability provide improved electrical properties and enhance the intermolecular interactions in thin films, which predominantly influence the molecular arrangement.[23]

Acenes are polycyclic aromatic hydrocarbons containing fused aromatic rings (such as pentacene, hexacene, heptacene). Although, they consist of linearly fused benzene rings, they also exhibit instabilities against light and air hindering their use in material chemistry.[24–26] On the contrary, thienoacenes that consist of fused thiophene rings possess higher charge mobilities and improved stabilities under ambient conditions, owing to their favorable electronic properties.[27,28] The advantages of thiophene-based heteroacenes stem from the fact that the thiophene-based building blocks are electron-rich, which make them efficient electron donating units (D) and are fused with electron deficient (acceptor, A) units in D–A–D and A–D–A types. Introduction of planar fused aromatic rings as donors into the small molecules can lower the band gaps and enhance the hole mobilities.[29] The performance of fused thiophenes is related to the role of d-orbitals of sulfur atom, which mix well with aromatic p-orbitals, so that electron-transfer over the π-system to the acceptor unit is made easier, which results in extended injection efficiency.[30] Fused thiophenes (Figure 2.1) are

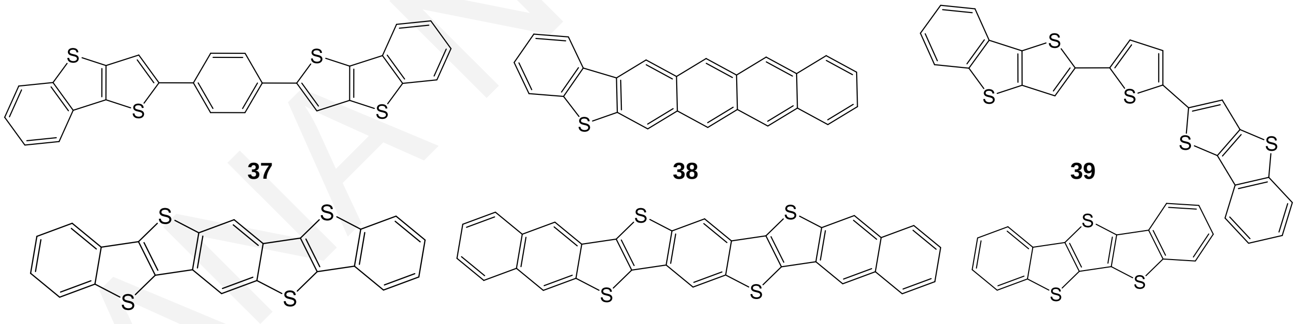
37 **38** **39** **40** **41** **42**

Figure 2.1. Examples of thiophene-based fused heteroacenes (2,5 di[thieno[3,2-b][1]benzothiophenic-2-]benzene (DTBTB, **37**), tetraceno[2,3- b]benzo[d]thiophene (TBT, **38**), 2,5 di[thieno[3,2-b][1]benzothiophenic-2-]thiophene (DTBTT, **39**), bis[1]benzothieno[2,3-d;2',3'-d']benzo[1,2-b;4,5-b']dithiophene (BBTBDT, **40**), bis(naphtho[2,3-b]thieno)[2,3-d;2',3'-d']benzo[1,2-b;4,5-b']dithiophene (BNTBDT, **41**) and dibenzo[d,d′]thieno[3,2-b;4,5-b′]dithiophene (DBTDT, **42**)).[23]

categorized into the three classes; (1) thienothiophenes (TTs), consisting of two fused thiophene units, (2) dithienothiophenes (DTTs) with three thiophene units fused to each other and (3) thioacenes (TAcs) containing more than three fused thiophene units.[30] Among the π-conjugated organic building blocks, fused-thiophenes are one of the most promising moieties for organic thin film transistors (OTFTs), OPVs and dye-sensitized solar cells (DSSCs).[31]

2.1.2 Thiophene-Based conjugated polymers as organic semiconductors

Polymers containing thiophene moieties present intriguing electronic, optical, and redox properties as well as unique self-assembling abilities on solid surfaces or in the bulk. The high polarizability of the sulfur atom in thiophene leads to a stabilization of the conjugated chains and superb charge carrier properties, which are crucial assets for optoelectronic applications.[32] Among homopolymers, poly(3-alkylthiophene)s (P3ATs) are the most representative and well-studied.[33,34] The backbone can be easily subjected to twisting because the inter-ring twisting barrier is quite low (about 2.6-5.5 kcal/mol depending on the different side-chain properties).[35]

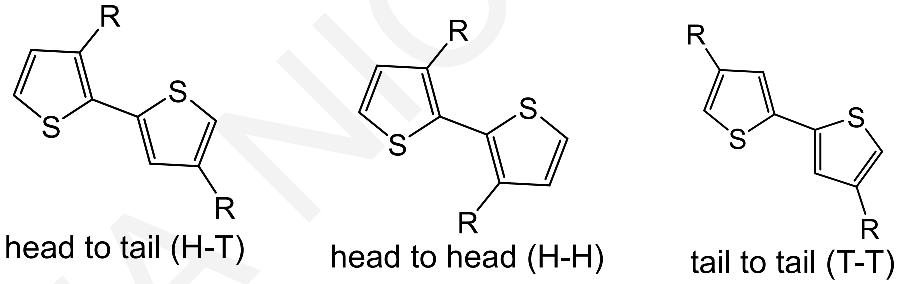

Figure 2.2. Illustration of the three possible connections, head-to-tail (H–T), head-to-head (H–H) or tail-to-tail (T–T), between two 3-alkylthiophene repeat units.[34]

The regioregularity (rr) of P3HT plays an important role in the molecular arrangement and subsequent device performances.[34] rr-P3AT follow the orientation of head to tail (Figure 2.2) repeating units throughout the polymer backbone, while regiorandom P3AT contain a mixture of three connections. In this case, the regioregularity of P3ATs is denoted as the percentage of the arranged H–T units in the backbone. This molecular design provides a simple method to tune the degree of backbone twisting in polymer backbones for the optimization of organic electronic devices.[36]

Important features of thiophene-based polymers are: (1) the optical properties of polythiophenes that can easily be tuned altering the band gaps significantly, (2) polythiophene derivatives can be processed from solution enabling low-cost construction of thin films, (3) higher stabilities for better photovoltaic properties.[37] The focus has been on achieving lower band gaps. There are several factors influencing the band gaps of the conjugated polymers, such as intra-chain charge transfer, aromaticity, π-conjugation length and intermolecular interactions.[38]

For the most part, thiophene containing polymers demonstrate hole transport properties, and have been applied as p-type semiconductors for OFETs and OPV.[39] Because of the strong electron-donating nature, thiophene units have been widely utilized as donor units to construct low band gap D–A polymers with other electron-poor units for applications in organic electronics.[38] The resulting conjugated polymers possess tunable optical and electronic properties owing to the enlargement of the π-conjugation systems, improving the delocalization of electrons. These copolymers have proper electron donating and accepting abilities, and they can be modified using side chains and functional groups. Moreover, their molecular structure exhibits linearity.[41] Some examples of conjugated polymers containing thiophene building blocks are depicted in Figure 2.3.[40]

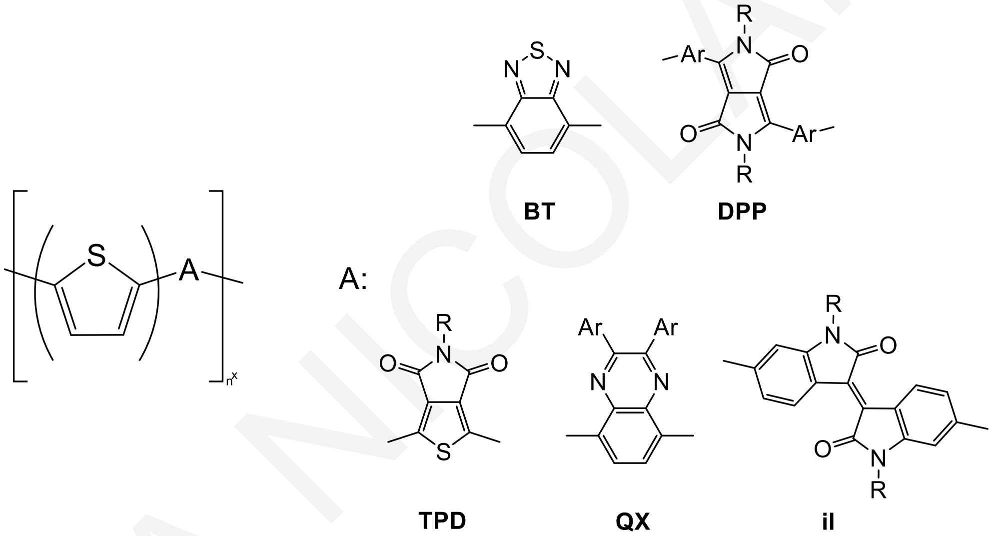

Figure 2.3. Examples of thiophene-based copolymers.[40]

2.2 Structure-property correlation of conjugated polymers

Understanding the structure-property relationship in conjugated polymers and addressing appropriate molecular design strategies are pivotal to improve their optoelectronic performance. Π-conjugated polymers display highly tunable optoelectronic properties that can be manipulated through conformational control. The π-conjugated polymer backbone structure is comprised of a series of overlapping σ orbitals formed via sp^2 hybridization where the π-electron system is left unbonded, thereby creating a conjugated chain of delocalized π-electrons, producing highly anisotropic quasi-one-dimensional (1D) electronic structure. The extent of π-electron delocalization across molecular units can be influenced by the planarity of the polymer backbone.[42]

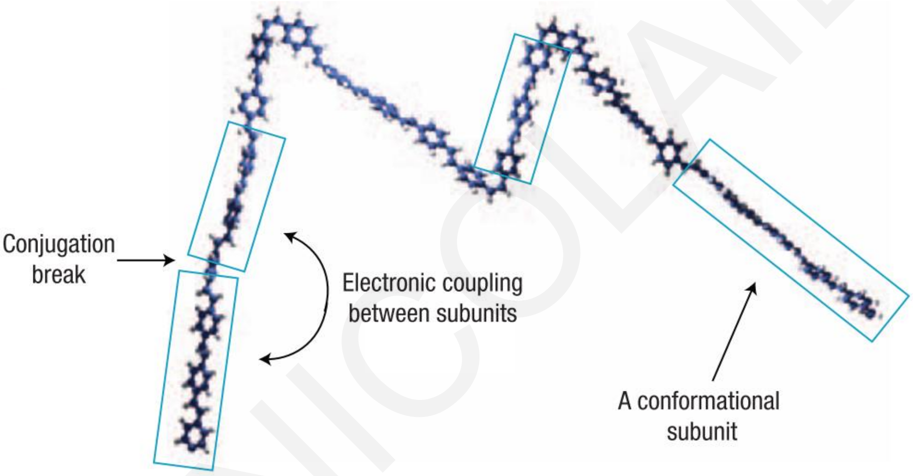

Figure 2.4. Example of single-chain conformation (poly(phenylene vinylene)).[43]

Planar (or torsionaly ordered) conjugated backbone is a structural characteristic that describes the increased extent of electronic coupling between adjacent chromophores stemming from their minimal inter-ring dihedral angle (Figure 2.4). The length of inter-ring planarity of a polymer backbone is optically distinct affecting the optoelectronic properties. This implies a strong coupling between the electronic and structural dynamics that gives rise to unique and fascinating phenomena.[44] When a conjugated polymer adopts an extended conformation with dominant intrachain coupling due to ordering (planarization) of the backbone, exciton delocalization and coherence in exciton migration can be achieved, leading to directional energy and charge transport, desirable for designing highly efficient devices.[13,45] A polymer with ordered conformation can exhibit J-like behaviour, which leads to spectroscopic characteristics such as increased radiative rate, red-shifted absorption spectra with increased ratio of first (A_{0-0}) to second vibronic peak (A_{0-1}) intensity and a mirror image relation between absorption and emission.[15,16] In contrast, decrease of the coplanarity of adjacent thiophene heterocycles, decreases intrachain electronic coupling.[46]

The primary photoexcitations of conjugated polymers generate bound electron-hole pairs (excitons) with large binding energy, rather than free charge carriers or easily dissociated excitons. The binding energy of singlet intrachain excitons has been experimentally shown to be of the order of 0.5 eV,[47,48] which is much higher than the room temperature energy, k_BT (where k_B is the Boltzmann factor and T is the temperature).[49,50] Therefore, achieving efficient charge photogeneration by exciton dissociation is an extremely crucial process in polymer-based optoelectronics. The low aromaticity of thiophene rings and high quinoid character (Figure 2.5) of polythiophene after excitation, contribute to greater delocalized character of the backbone in the excited state relative to its ground state. Therefore, conformational control of thiophene-based polymers can enable effective nonlocal electron exchange with greater conjugation.

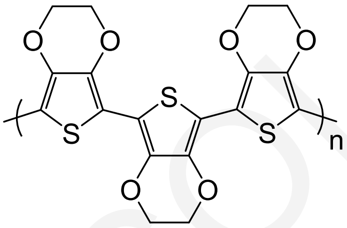

Benzoid structure

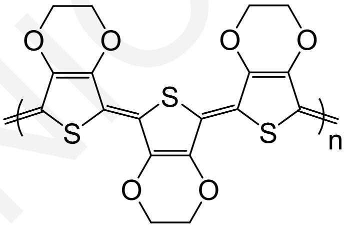

Quinoid structure

Figure 2.5. Comparison of benzoid and quinoid structure of PEDOT.

2.3 Generation of excitons and polarons by photoexcitation

In principle, optical excitation into higher excited states of the polymer photogenerates intrachain excitons, followed by sub-picosecond nonradiative hot exciton relaxation to the lowest excited state.[51] The hot energy relaxation process is due to either vibrational cooling within vibronic sidebands of the same electronic state, or phonon-assisted transitions between two different electronic states, which is known as “internal conversion”.[52] Internal conversion is the fastest relaxation process, in which efficient nonradiative transfer occurs from a higher excited state into the lowest excited state of the same spin multiplicity, from where radiative (fluorescence) or non-radiative deactivation can occur.[52,53]

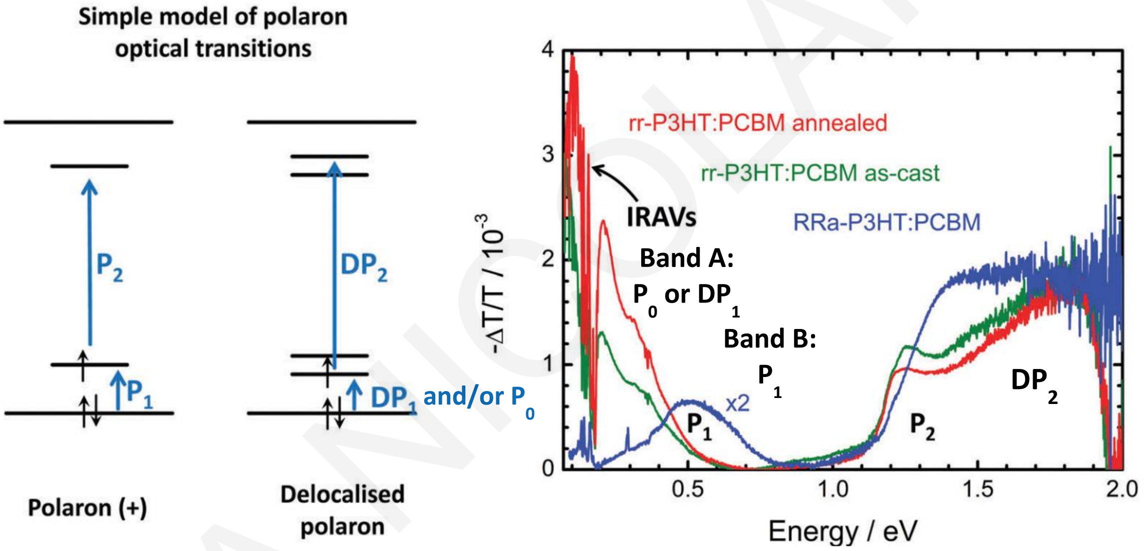

Figure 2.6. PIA spectra consisting of bands attributed to the optical transitions of positive polaron, illustrated on the left side.[54]

Before the exciton relaxes to the lowest excited state, there are two other ultrafast relaxation processes that may interfere with the internal conversion process, known as singlet exciton fission and exciton dissociation.[52] The former process leads to the fast generation of two triplet excitons with opposite spins from one singlet exciton,[55,56] whereas the latter process directly generates charge carriers.[57] However, in conjugated polymers these two processes occur with much smaller probability than the internal conversion process. Finally, excitons may be also trapped or undergo an intersystem crossing into the triplet manifold, creating long-lived triplet (T) states. Thiophene-based molecules were reported to undergo rapid intersystem crossing (ISC)[58–60] leading to extremely high triplet quantum yields. This property deviates strongly from the common behavior found in most organic molecules where the ratio of ISC to internal conversion (IC) and fluorescence is rather small.[61]

Usually, in polymer films spin-1/2 polarons can be produced onto the polymer chain, which results in the formation of two new states in the gap. Figure 2.6[54] shows the associated optical transitions for a positively charged polaron. Two optical transitions are possible named as, band B (or P_1) and P_2.[62–64] Therefore, the existence of these optical transitions upon doping or photogeneration indicates that polarons are created.[63] As reported in the literature, photoinduced absorption (PIA) spectra illustrate these transitions in the near and mid-IR range. Besides the polaron bands band B and P_2 observed at ~4000 and 10000 cm^{-1} respectively, two delocalized polaron bands, named as band A (which has contributions from both interchain and intrachain transitions named as DP_1 and P_0 respectively) and DP_2 at ~1000 and 15000 cm^{-1} respectively may be also present.[54,65,66] According to the literature,[67] highly ordered conjugated polymers such as RR-P3HT film, can self-organize into a lamellae structure. The 2D lamellae sheets have strong interchain interaction resulting in the splitting of polaron levels, forming the delocalized polaron levels DP_1 and DP_2, as depicted in Figure 2.6. Polarons can also form in single polymer chains and can be detected by a band attributed to a transition with energy of ~1000 cm^{-1}.[65,68]

In a similar spectral region strong vibrational IR bands are observed as spectral peaks or dips. These are originally Raman-active (Ag) modes coupled to the π-electron system (combination of carbon-carbon single and double bond) that become strongly absorbing infrared active vibrations due to the local breaking of the symmetry around the charge carrier. These are known as IR-active vibrational modes (IRAVs) and stem from localized charge carriers on the π-conjugated chain (Figure 2.7) creating large changes in bonding dipole moments.[70–73] Therefore, the high intensity of the IRAV bands is motivated by the large variation of the electric dipole moment associated with the oscillation of the charged defect. The corresponding IRAV bands are therefore related to the extension of the electron delocalization along the quasi-one-dimensional pattern of alternating C-C single and double bonds in π-conjugated systems.[72] Consequently, IRAVs can serve as indicators of the existence of polarons onto the backbone. When IRAVs are overlapped with band A, as both are detected in the same spectral region, a series of sharp Fano antiresonances appear.[66,74] The Fano-antiresonances emerge as spectral dips, as this overlap causes a cancellation of oscillator strengths due to destructive quantum interference between the electronic continuum and discrete vibrational transitions.[75]

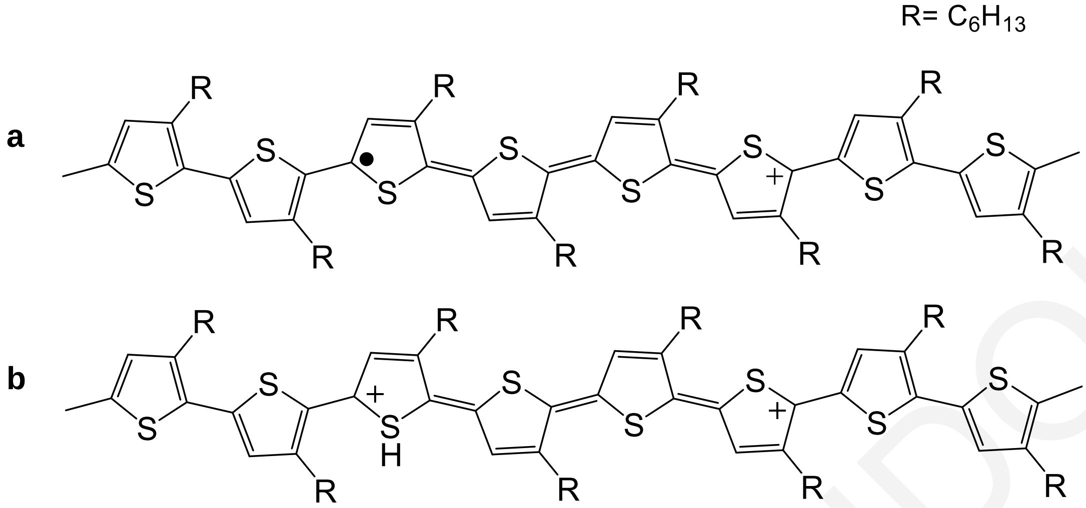

Figure 2.7. Schematic structures of (a) a positive polaron, (b) a positive bipolaron in polythiophene.[69]

2.4 Structural characterization of π-conjugated polymers

According to the above, it is crucial to capture the interplay between electronic structure properties and the backbone structure of organic semiconducting polymers by assessing the local order of polymers. Investigating the relationship between structure and electronic properties of materials requires to detect the key structural characteristics, such as molecular order, bond pattern, and spatial extent of charged and excited states, which are intimately related to the free carrier mobility and exciton lifetime.[74] Addressing this experimentally requires methods that can differentiate amongst structural variations within an ensemble of localized excited states and track excited-state structural relaxation directly in time.[76] Thus, vibrational (IR and Raman) spectroscopy, which is sensitive to variations of local dipole moments and polarizability within the backbone, can be exploited to determine the structural variations that are linked with the photoexcited processes occurring in these systems.[74]

In π-electron conjugated polymers, collective symmetric oscillations that coincide with the change in molecular geometry that accompanies polymer excitation are Raman-active normal modes but IR-silent.[74] These oscillations (most notably the in-phase C=C stretching frequency) are directly sensitive to the extent of delocalization along an oligomer or polymer backbone: the higher the electron delocalization, the lower the energy of the vibrational transition. Raman spectroscopy has been used extensively to characterize conjugated polymers and polymer-based materials,[77] and is a promising complement to electronic spectroscopies for interrogating the structural characteristics and dynamics of conjugated polymers in their excited states.[76] Given that excited states of conjugated oligomers and polymers are highly delocalized by nature, it is expected that C=C stretching frequencies of excited states should be highly sensitive to variations or evolution in the excited-state delocalization length.[78] The polymer chains can be regarded as made from a statistical distribution of segments with different conjugation lengths and hence different excitation energies. Therefore, the use of wavelength-dependent Raman excitation can enable the photo-selective interrogation of local structural features of conjugated polymers.[79]

Additionally, as mentioned above these Raman-active modes become intense infrared-active vibrational (IRAV) modes when charge carriers are generated onto the polymer chain, breaking the local spatial symmetry of the backbone.[80] Therefore, these are largely employed as a direct probe of polaron density in conjugated polymers, as mentioned above.

Understanding relationships between local structure and properties or behaviors of excitons will provide insights into how to manipulate their transport or charge separation in designer materials.[79]

2.5 π-Conjugated polyelectrolytes

Incorporation of ionic functionality as pendant groups on the conjugated backbone results in polymers known as conjugated polyelectrolytes (CPEs).[81–83] CPEs combine the intrinsic electronic and optical properties of the organic conjugated backbone and the charge interaction ability of polyelectrolytes (Figure 2.8).[84] Such unique characteristics provide excellent platforms for the development of chemo- and biosensors. In addition to their water solubility, the charged nature of CPEs facilitates their interaction with ionic species. For example, most CPE-based sensor approaches utilize the electrostatic interaction between the probes and the target species, such as metal ions, fluoride ions, polyelectrolytes, proteins, and oligo and polynucleic acids.[85]

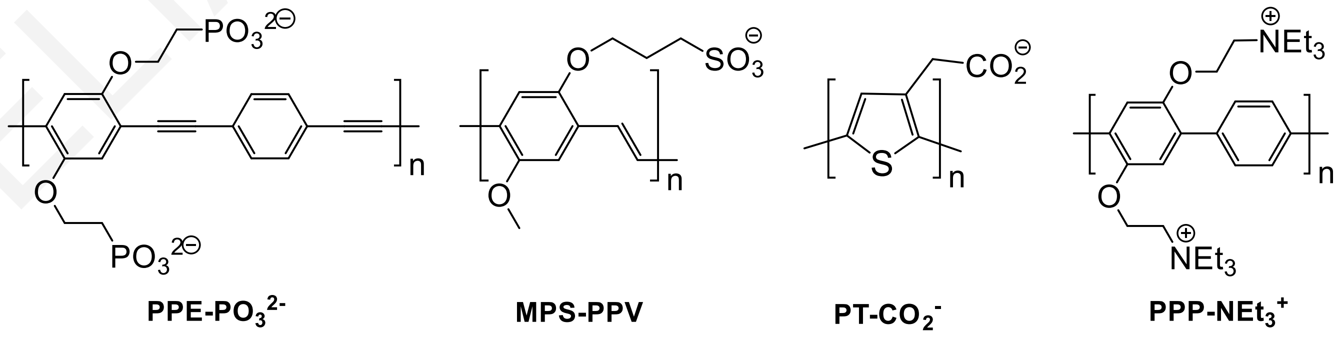

$PPE\text{-}PO_3^{2-}$ MPS-PPV $PT\text{-}CO_2^-$ $PPP\text{-}NEt_3^+$

Figure 2.8. Examples of structures of CPEs.[84]

2.5.1 Cationic polythiophenes

Within the family of water-soluble π-conjugated polyelectrolytes (CPEs), cationic polythiophenes (CPT) are a class of conjugated polymers with a flexible backbone that exhibits conformational variations in the presence of different ions and at different temperatures. Specifically, Xia et al.[86] found that the salting-in (chaotropic, weakly hydrated) anions like I^- develop strong hydrophobic interactions with the PMNT polymer chain, leading to a more extended and ordered backbone. In contrast, the salting-out (cosmotropic, strongly hydrated) anions like F^- strongly avoid the hydrophobic PMNT backbone, keeping a random-coiled configuration of the backbone (Figure 2.9). The existence of ordered and disordered backbone configurations is further verified by monitoring the main in-plane skeleton Raman modes (C-C and C=C stretch) of PMNT in various salt solutions.

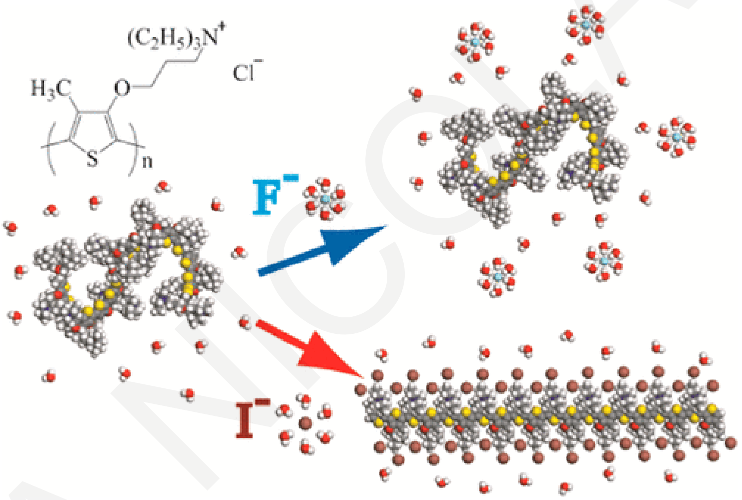

Figure 2.9. Representative illustration of the interaction between anions (F^- and I^-) and all-anti-PMNT oligomer (20 repeat units) in the presence of water molecules (light blue, F^- anion (upper); brown, I^- anion (lower)).[86]

Previous reports on the CPT polymer studied in this thesis, revealed that this polymer exhibits ionochromic behavior. The stationary absorption spectra for CPT in pure water and in PBS buffer solution are shown in Figure 2.10. In water, CPT displays an unstructured broad absorption band peaking at 402 nm, while CPT in solutions of the separate salts shows that mainly the Cl^- anions, which are present at a high concentration of 155 mM, are at the origin of the important spectral changes in the presence of the buffer.

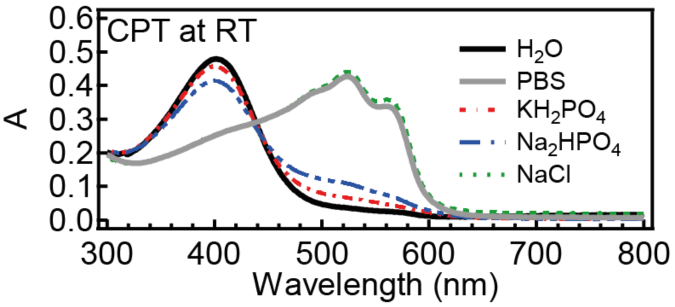

Figure 2.10. Absorption spectra of CPT in pure water, in PBS buffer and in different salt solutions at the relevant concentration of PBS (KH_2PO_4 1.06 mM, Na_2HPO_4 2.97 mM and NaCl 155 mM) at room temperature.[87]

This cationic polythiophene also displays thermochromic behavior.[87] At the higher investigated temperatures, CPT displays increased torsional disorder depicted by the blue-shifted broad spectra. As temperature decreases the absorption spectra red shift and begin to demonstrate vibronic structure, exhibiting an important increase of the relative intensity of the A_{0-0} peak with respect to the A_{0-1} peak. These observations indicate that the polymer chain adopts a less torsional-disordered conformation (leading to an increase in conjugation length) (Figure 2.11).

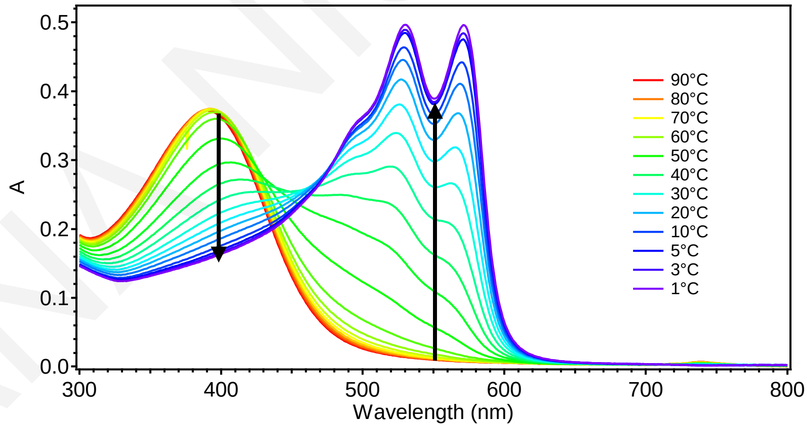

Figure 2.11. Absorption spectra of CPT in PBS at different temperatures between 1℃ and 90 ℃.[87]

Cationic polythiophenes are well known for their ability to form well-defined complexes with anionic single DNA strands. The solubility of cationic polythiophene in aqueous media and the remarkable optical properties hold great promise in the development of biosensors. Their fine sensitivity that reaches a scale of one change of nucleobase in the tested sequence, establishes them as among the most successful DNA biosensors.[88] The conformational changes induced in the polymer upon complexation with single-stranded DNA (ssDNA) are the lead cause for the exquisite sensitivity. Driven by this astonishing discovery, Charlebois et al.[89] performed a thorough investigation of sequence dependence of the polymer conformation using both homo-oligonucleotides and mixed sequences. Their work showed that the homo-oligonucleotides of the four bases induce completely different conformation on the polymer (Figure 2.12).

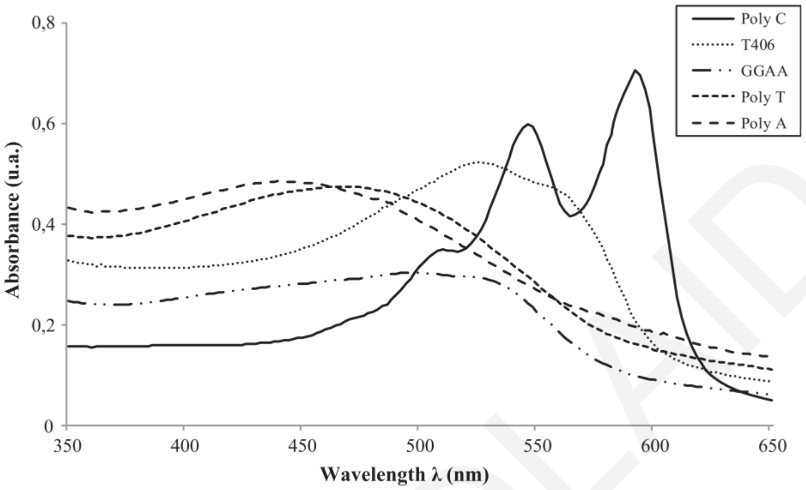

Figure 2.12 Absorbance UV-Vis spectra of polymer mixed with ssDNA oligonucleotides of 20 bases (polyC, T406, GGAA repeat, polyT and polyA).[89]

2.6 Templates

Directing the conformation of organic molecules in such a way as to produce desired properties is a promising approach that receives extensive interest from the scientific community.[90–92] An advantageous and straightforward way that enables the control of the conformation is self-assembly with appropriate templates.[93,94] Supramolecular self-assembly is the association of molecules that consist of specific functional groups, which promote the approach of each other through intermolecular, non-covalent interactions and induce a higher-order architecture with completely different properties than the individual molecules.[45] The selection of a powerful template to force organic molecules into a favorable conformation that could not be obtained otherwise can be challenging. This raises the need for a thorough, fundamental investigation with the aim to design the optimum self-assembly system.

The involvement of multiple interactions between the two components of a complex can lead to improvement of the performance of the studied molecule. Conjugated polymers with extended backbone and charged side chains can effectively template a planarized and oppositely charged polymer leading to excited states that are highly delocalized along the polymer backbone (Figure 2.13). A recent study[13] showed that multiple electrostatic interactions can be employed in order to organize the molecules in a functional architecture. In particular, the conjugated backbone and the charged side chains of the CPE were exploited so that excited states can migrate between molecules, ultimately delivering the energy more efficiently.

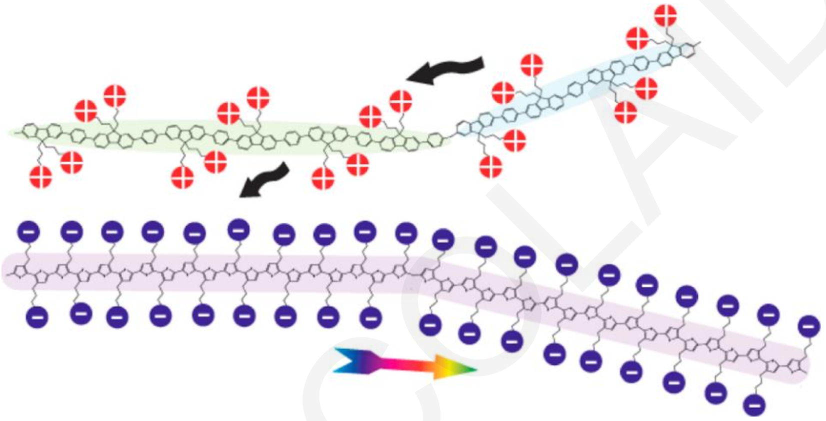

Figure 2.13. Schematic representation of the assembly of the two conjugated polyelectrolytes towards efficient electronic energy transfer.[13]

Other efficient templates for conformational control of conjugated polymers include macrocycles, such as cyclodextrines.[95–98] Formation of isolated polythiophene chains was achieved by encapsulation using an inclusion complex based on cyclodextrine molecules (Figure 2.14).[95] The structure of polythiophene in this nanotube was found to adopt near-planar geometry demonstrating suitability of such inclusion complexes in applications involving molecular circuits.

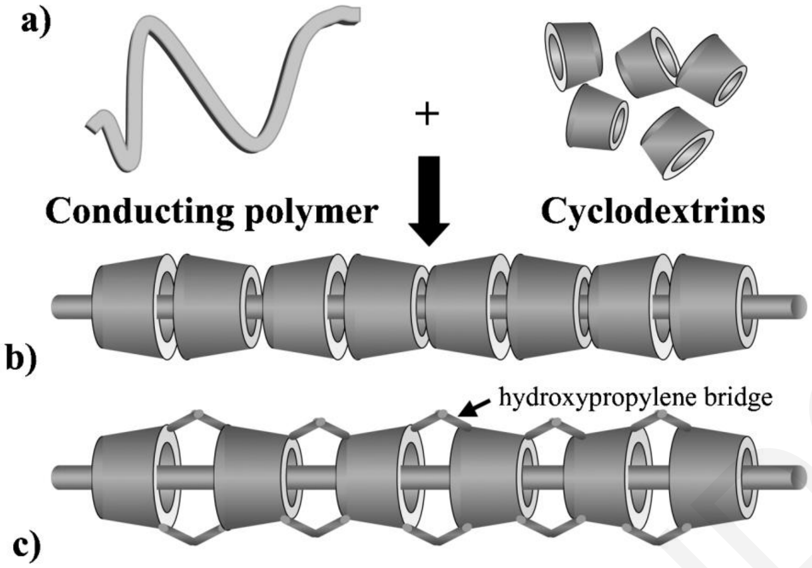

Figure 2.14. Schematic diagram of (a) the polymer and cyclodextrins; (b) inclusion complex formation of CDs and conducting polymer (c) polymer chain into a molecular nanotube of crosslinking a-cyclodextrines.[95]

Intriguing strategies have been developed to design insulated molecular wires, exploiting hydrophobic interactions, in order the conjugated polymer backbones to be encapsulated by a protective sheath, such as polysaccharides (such as s-SPG) (Figure 2.15),[99] cyclophanes,[100,101] wrapping them within dendrimeric wedges,[102] limiting the interchain interactions.

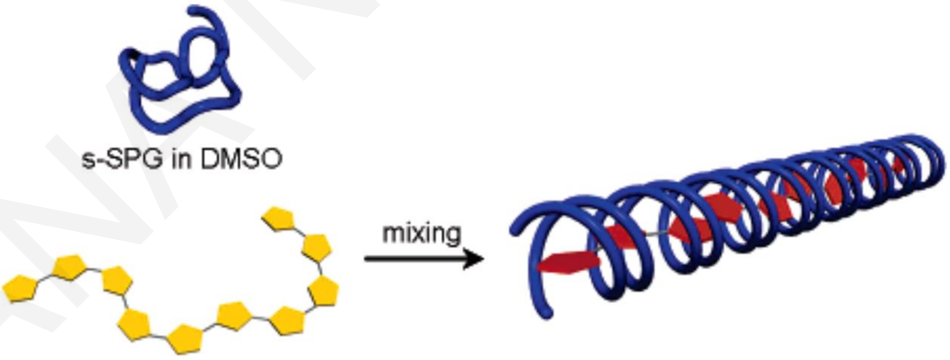

Figure 2.15. Schematic illustration of the chiral insulated wire formation.[99]

2.6.1 Nucleic acid-based templates

Key building blocks for templating conjugated polymers may be biological mimics, since nature has mastered the ability for highly predictable and programmable self-assembly. Nucleic acids, in particular, allow exquisite atomistic-level control of assembly interactions, leading to construction of reproducible, supramolecular structures. Recently DNA templating was used as a method for forming nanowires by extending the polymer and enhancing its conductivity.[103–105] One common and effective strategy involves a DNA-directed synthetic approach that enables the formation of conducting polymers by pre-organizing the monomers of conducting polymers through a covalent linkage to a nucleobase. Self-assembly aligns the monomers in the DNA major groove thus facilitating the programmed construction of specific conducting polymers. This approach is quite different however, as it involves strong covalent bonding between the CP and the DNA rather than supramolecular interactions.[106,107]

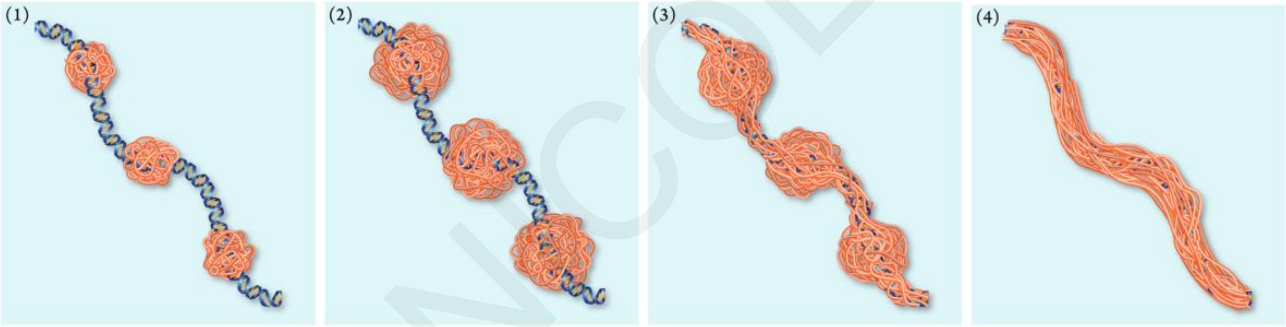

Figure 2.16. Stages in the growth mechanism of supramolecular DNA-templated polymer nanowires.[103]

The induction of extended polymers was also accomplished by exploiting the ability of DNA chains to assemble strongly only through non-covalent interactions. According to Watson et al.[103] the cationic polymer chains were involved in a supramolecular structure DNA that enable to undergo dynamic reconfiguration so as to elongate along the template axis (Figure 2.16)[103] and yield the highly regular, smooth morphology of the final nanowire. The assembly was formed by developing electrostatic interactions accompanied by additional noncovalent bonding (possibly Van der Waals). Therefore, the properties of conjugated polymers can be systematically and efficiently tailored using nucleic acids as scaffold by tuning their conformation.

The tuning of the conformation of conjugated molecules as well as the effect of the structural variation on the photophysics will be the main subject of the present doctoral dissertation, aiming to deliver an enriched, fundamental understanding to this research field.

References

(1) Qian, Y.; Zhang, X.; Xie, L.; Qi, D.; Chandran, B. K.; Chen, X.; Huang, W. Stretchable Organic Semiconductor Devices. *Adv. Mater.* **2016**, *28* (42), 9243–9265.

(2) Burroughes, J. H.; Bradley, D. D. C.; Brown, A. R.; Marks, R. N.; Mackay, K.; Friend, R. H.; Burns, P. L.; Holmes, A. B. Light-Emitting Diodes Based on Conjugated Polymers. *Nature* **1990**, *347* (6293), 539–541.

(3) Heeger, A. J. 25th Anniversary Article: Bulk Heterojunction Solar Cells: Understanding the Mechanism of Operation. *Adv. Mater.* **2014**, *26* (1), 10–28.

(4) Zhao, J.; Li, Y.; Yang, G.; Jiang, K.; Lin, H.; Ade, H.; Ma, W.; Yan, H. Efficient Organic Solar Cells Processed from Hydrocarbon Solvents. *Nat. Energy* **2016**, *1* (2), 15027.

(5) Lenz, J.; del Giudice, F.; Geisenhof, F. R.; Winterer, F.; Weitz, R. T. Vertical, Electrolyte-Gated Organic Transistors Show Continuous Operation in the MA Cm−2 Regime and Artificial Synaptic Behaviour. *Nat. Nanotechnol.* **2019**, *14* (6), 579–585.

(6) Zschieschang, U.; Klauk, H. Organic Transistors on Paper: A Brief Review. *J. Mater. Chem. C* **2019**, *7* (19), 5522–5533.

(7) Heeger, A. J.; Sariciftci, N. S.; Namdas, E. B. *Semiconducting and Metallic Polymers*; Oxford University Press, 2010.

(8) Thompson, B. C.; Fréchet, J. M. J. Polymer-Fullerene Composite Solar Cells. *Angew. Chemie - Int. Ed.* **2008**, *47* (1), 58–77.

(9) Li, Z. L.; Yang, S. C.; Meng, H. F.; Chen, Y. S.; Yang, Y. Z.; Liu, C. H.; Horng, S. F.; Hsu, C. S.; Chen, L. C.; Hu, J. P.; Lee, R. H. Patterning-Free Integration of Polymer Light-Emitting Diode and Polymer Transistor. *Appl. Phys. Lett.* **2004**, *84* (18), 3558–3560.

(10) Kim, Y.; Cook, S.; Tuladhar, S. M.; Choulis, S. A.; Nelson, J.; Durrant, J. R.;

Bradley, D. D. C.; Giles, M.; McCulloch, I.; Ha, C. S.; Ree, M. A Strong Regioregularity Effect in Self-Organizing Conjugated Polymer Films and High-Efficiency Polythiophene:Fullerene Solar Cells. *Nat. Mater.* **2006**, *5* (3), 197–203.

(11) Günes, S.; Neugebauer, H.; Sariciftci, N. S. Conjugated Polymer-Based Organic Solar Cells. *Chem. Rev.* **2007**, *107* (4), 1324–1338.

(12) Park, Y. D.; Lee, H. S.; Choi, Y. J.; Kwak, D.; Cho, J. H.; Lee, S.; Cho, K. Solubility-Induced Ordered Polythiophene Precursors for High-Performance Organic Thin-Film Transistors. *Adv. Funct. Mater.* **2009**, *19* (8), 1200–1206.

(13) Hollingsworth, W. R.; Segura, C.; Balderrama, J.; Lopez, N.; Schleissner, P.; Ayzner, A. L. Exciton Transfer and Emergent Excitonic States in Oppositely-Charged Conjugated Polyelectrolyte Complexes. *J. Phys. Chem. B* **2016**, *120* (31), 7767–7774.

(14) Panzer, F.; Bässler, H.; Köhler, A. Temperature Induced Order-Disorder Transition in Solutions of Conjugated Polymers Probed by Optical Spectroscopy. *J. Phys. Chem. Lett.* **2017**, *8* (1), 114–125.

(15) Raithel, D.; Simine, L.; Pickel, S.; Schötz, K.; Panzer, F.; Baderschneider, S.; Schiefer, D.; Lohwasser, R.; Köhler, J.; Thelakkat, M.; Sommer, M.; Köhler, A.; Rossky, P. J.; Hildner, R. Direct Observation of Backbone Planarization via Side-Chain Alignment in Single Bulky-Substituted Polythiophenes. *Proc. Natl. Acad. Sci. U. S. A.* **2018**, *115* (11), 2699–2704.

(16) Dyson, M. J.; Lariou, E.; Martin, J.; Li, R.; Erothu, H.; Wantz, G.; Topham, P. D.; Dautel, O. J.; Hayes, S. C.; Stavrinou, P. N.; Stingelin, N. Managing Local Order in Conjugated Polymer Blends via Polarity Contrast. *Chem. Mater.* **2019**, *31* (17), 6540–6547.

(17) Osaka, I.; Mccullough, R. D. Advances in Molecular Design and Synthesis of Regioregular Polythiophenes. *Acc. Chem. Res.* **2008**, *41* (9), 1202–1214.

(18) Grozema, F. C.; Van Duijnen, P. T.; Berlin, Y. A.; Ratner, M. A.; Siebbeles, L. D. A. Intramolecular Charge Transport along Isolated Chains of Conjugated Polymers: Effect of Torsional Disorder and Polymerization Defects. *J. Phys. Chem. B* **2002**, *106* (32), 7791–7795.

(19) Goel, M.; Heinrich, C. D.; Krauss, G.; Thelakkat, M. Principles of Structural Design of Conjugated Polymers Showing Excellent Charge Transport toward Thermoelectrics and Bioelectronics Applications. *Macromol. Rapid Commun.* **2019**, *40* (10), 1800915.

(20) Zhang, Z.; Liao, M.; Lou, H.; Hu, Y.; Sun, X.; Peng, H. Conjugated Polymers for Flexible Energy Harvesting and Storage. *Adv. Mater.* **2018**, *30* (13), 1704261.

(21) Correa, D. S.; Medeiros, E. S.; Oliveira, J. E.; Paterno, L. G.; Mattoso, L. H. C. Nanostructured Conjugated Polymers in Chemical Sensors: Synthesis, Properties and Applications. *J. Nanosci. Nanotechnol.* **2014**, *14* (9), 6509–6527.

(22) Mei, J.; Bao, Z. Side Chain Engineering in Solution-Processable Conjugated Polymers. *Chem. Mater.* **2014**, *26* (1), 604–615.

(23) Dikcal, F.; Ozturk, T.; Cinar, M. E. Fused Thiophenes: An Overview of the Computational Investigations. *Org. Commun.* **2017**, *10* (2), 56–71.

(24) Anthony, J. E. The Larger Acenes: Versatile Organic Semiconductors. *Angew. Chemie - Int. Ed.* **2008**, *47* (3), 452–483.

(25) Sun, Z.; Ye, Q.; Chi, C.; Wu, J. Low Band Gap Polycyclic Hydrocarbons: From Closed-Shell near Infrared Dyes and Semiconductors to Open-Shell Radicals. *Chem. Soc. Rev.* **2012**, *41* (23), 7857–7889.

(26) Portella, G.; Poater, J.; Bofill, J. M.; Alemany, P.; Sola, M. Local Aromaticity of [n]Acenes, [n]Phenacenes, and [n]Helicenes (n = 1−9). *J. Org. Chem.* **2005**, *70* (7), 2509–2521.

(27) Mori, T.; Nishimura, T.; Yamamoto, T.; Doi, I.; Miyazaki, E.; Osaka, I.; Takimiya, K. Consecutive Thiophene-Annulation Approach to π-Extended Thienoacene-Based Organic Semiconductors with [1]Benzothieno[3,2-b][1]Benzothiophene (BTBT) Substructure. *J. Am. Chem. Soc.* **2013**, *135* (37), 13900–13913.

(28) Gao, J.; Li, R.; Li, L.; Meng, Q.; Jiang, H.; Li, H.; Hu, W. High-Performance Field-Effect Transistor Based on Dibenzo[d,D′]Thieno[3,2-b;4,5-B′]Dithiophene, an Easily Synthesized Semiconductor with High Ionization Potential. *Adv. Mater.* **2007**, *19* (19), 3008–3011.

(29) Ni, W.; Wan, X.; Li, M.; Wang, Y.; Chen, Y. A–D–A Small Molecules for Solution-

Processed Organic Photovoltaic Cells. *Chem. Commun.* **2015**, *51* (24), 4936–4950.

(30) Cinar, M. E.; Ozturk, T. Thienothiophenes, Dithienothiophenes, and Thienoacenes: Syntheses, Oligomers, Polymers, and Properties. *Chem. Rev.* **2015**, *115* (9), 3036–3140.

(31) Zhou, N.; Prabakaran, K.; Lee, B.; Chang, S. H.; Harutyunyan, B.; Guo, P.; Butler, M. R.; Timalsina, A.; Bedzyk, M. J.; Ratner, M. A.; Vegiraju, S.; Yau, S.; Wu, C.; Chang, R. P. H.; Facchetti, A.; Chen, M.; Marks, T. J. Metal-Free Tetrathienoacene Sensitizers for High-Performance Dye-Sensitized Solar Cells. *J. Am. Chem. Soc.* **2015**, *137* (13), 3036–3140.

(32) Mishra, A.; Ma, C.-Q.; Bäuerle, P. Functional Oligothiophenes: Molecular Design for Multidimensional Nanoarchitectures and Their Applications. *Chem. Rev.* **2009**, *109* (3), 1141–1276.

(33) McCullough, R. D. The Chemistry of Conducting Polythiophenes. *Adv. Mater.* **1998**, *10* (2), 93–116.

(34) Sirringhaus, H.; Brown, P. J.; Friend, R. H.; Nielsen, M. M.; Bechgaard, K.; Langeveld-Voss, B. M. W.; Spiering, A. J. H.; Janssen, R. A. J.; Meijer, E. W.; Herwig, P.; de Leeuw, D. M. Two-Dimensional Charge Transport in Self-Organized, High-Mobility Conjugated Polymers. *Nature* **1999**, *401,* 685–688.

(35) Qiu, M.; Long, S.; Li, B.; Yan, L.; Xie, W.; Niu, Y.; Wang, X.; Guo, Q.; Xia, A. Toward an Understanding of How the Optical Property of Water-Soluble Cationic Polythiophene Derivative Is Altered by the Addition of Salts: The Hofmeister Effect. *J. Phys. Chem. C* **2013**, *117* (42), 21870–21878.

(36) Osaka, I.; Akita, M.; Koganezawa, T.; Takimiya, K. Quinacridone-Based Semiconducting Polymers: Implication of Electronic Structure and Orientational Order for Charge Transport Property. *Chem. Mater.* **2012**, *24* (6), 1235–1243.

(37) Mehmood, U.; Al-Ahmed, A.; Hussein, I. A. Review on Recent Advances in Polythiophene Based Photovoltaic Devices. *Renew. Sustain. Energy Rev.* **2016**, *57,* 550–561.

(38) Guo, X.; Baumgarten, M.; Müllen, K. Designing π-Conjugated Polymers for Organic Electronics. *Prog. Polym. Sci.* **2013**, *38* (12), 1832–1908.

(39) He, X.; Shan, T.; Tang, X.; Gao, Y.; Li, J.; Yanga, B.; Lu, P. Highly Efficient Organic Light Emitting Diodes Based on a D–A–D Type Dibenzothiophene Derivative Exhibiting Thermally Activated Delayed Fluorescence with Small ΔE_{ST}. *J. Mater. Chem. C* **2016**, *4* (43), 10205–10208.

(40) Cheng, Y.; Wang, C.; Wu, J.; Hsu, C. *Progress in High-Efficient Solution Process Organic Photovoltaic Devices*; 2015; Vol. 130.

(41) Lu, L.; Zheng, T.; Wu, Q.; Schneider, A. M.; Zhao, D.; Yu, L. Recent Advances in Bulk Heterojunction Polymer Solar Cells. *Chem. Rev.* **2015**, *115* (23), 12666–12731.

(42) Jiang, L.; Hirst, J. D.; Do, H. Structure-Property Relationships in Amorphous Thieno[3,2- b]Thiophene-Diketopyrrolopyrrole-Thiophene-Containing Polymers. *J. Phys. Chem. C* **2022**, *126* (26), 10842–10854.

(43) Scholes, G. D.; Rumbles, G. Excitons in Nanoscale Systems. *Nat. Mater.* **2015**, *5*, 683–696.

(44) Fratini, S.; Nikolka, M.; Salleo, A.; Schweicher, G.; Sirringhaus, H. Charge Transport in High-Mobility Conjugated Polymers and Molecular Semiconductors. *Nat. Mater.* **2020**, *19* (5), 491–502.

(45) Wilson, A. J. *Supramolecular Chemistry*; John Wiley & Sons, Ltd., 2009; Vol. 103.

(46) Ying, L.; Huang, F.; Bazan, G. C. Regioregular Narrow-Bandgap-Conjugated Polymers for Plastic Electronics. *Nat. Commun.* **2017**, *8*, 14047.

(47) Tong, M.; Sheng, C. X.; Vardeny, Z. V. Nonlinear Optical Spectroscopy of Excited States in Polyfluorene. *Phys. Rev. B - Condens. Matter Mater. Phys.* **2007**, *75* (12), 1–10.

(48) Zhao, H.; Mazumdar, S.; Sheng, C. X.; Tong, M.; Vardeny, Z. V. Photophysics of Excitons in Quasi-One-Dimensional Organic Semiconductors: Single-Walled Carbon Nanotubes and π -Conjugated Polymers. *Phys. Rev. B - Condens. Matter Mater. Phys.* **2006**, *73* (7), 1–11.

(49) Vardeny, Z.; Ehrenfreund, E.; Brafman, O.; Horovitz, B. Resonant Raman Scattering from Amplitude Modes in Trans-(CH)x and -(CD)X. *Phys. Rev. Lett.* **1983**, *51* (25), 2326–2329.

(50) Ehrenfreund, E.; Vardeny, Z.; Brafman, O.; Horovitz, B. Amplitude and Phase Modes in Trans-Polyacetylene: Resonant Raman Scattering and Induced Infrared Activity. *Phys. Rev. B* **1987**, *36* (3), 1535–1553.

(51) Kersting, R.; Lemmer, U.; Deussen, M.; Bakker, H. J.; Mahrt, R. F.; Kurz, H.; Arkhipov, V. I.; Bässler, H.; Göbel, E. O. Ultrafast Field-Induced Dissociation of Excitons in Conjugated Polymers. *Phys. Rev. Lett.* **1994**, *73* (10), 1440–1443.

(52) Kolle, P.; Schnappinger, T.; De Vivie-Riedle, R. Deactivation Pathways of Thiophene and Oligothiophenes : Internal Conversion versus Intersystem Crossing. *Phys. Chem. Chem. Phys.* **2016**, *18*, 7903–7915.

(53) Harrison, N. T.; Hayes, G. R.; Phillips, R. T.; Friend, R. H. Singlet Intrachain Exciton Generation and Decay in Poly (p-Phenylenevinylene). *Phys. Rev. Lett.* **1996**, *77* (9), 1881–1884.

(54) Kahmann, S.; Loi, M. A.; Brabec, C. J. Delocalisation Softens Polaron Electronic Transitions and Vibrational Modes in Conjugated Polymers. *J. Mater. Chem. C* **2018**, *6* (22), 6008–6013.

(55) Wilson, M. W. B.; Rao, A.; Clark, J.; Kumar, R. S. S.; Brida, D.; Cerullo, G.; Friend, R. H. Ultrafast Dynamics of Exciton Fission in Polycrystalline Pentacene. *J. Am. Chem. Soc.* **2011**, *133* (31), 11830–11833.

(56) Zimmerman, P. M.; Zhang, Z.; Musgrave, C. B. Singlet Fission in Pentacene through Multi-Exciton Quantum States. *Nat. Chem.* **2010**, *2* (8), 648–652.

(57) Miranda, P. B.; Moses, D.; Heeger, A. J. Ultrafast Photogeneration of Charged Polarons on Conjugated Polymer Chains in Dilute Solution. *Phys. Rev. B - Condens. Matter Mater. Phys.* **2004**, *70* (8), 1–9.

(58) Yu, W.; Donohoo-Vallett, P. J.; Zhou, J.; Bragg, A. E. Ultrafast Photo-Induced Nuclear Relaxation of a Conformationally Disordered Conjugated Polymer Probed with Transient Absorption and Femtosecond Stimulated Raman Spectroscopies. *J. Chem. Phys.* **2014**, *141* (4).

(59) Wang, C.; Angelella, M.; Doyle, S. J.; Lytwak, L. A.; Rossky, P. J.; Holliday, B. J.; Tauber, M. J. Resonance Raman Spectroscopy of the T 1 Triplet Excited State of Oligothiophenes. *J. Phys. Chem. Lett.* **2015**, *6* (18), 3521–3527.

(60) Thomas, A. K.; Brown, H. A.; Datko, B. D.; Garcia-Galvez, J. A.; Grey, J. K. Interchain Charge-Transfer States Mediate Triplet Formation in Purified Conjugated Polymer Aggregates. *J. Phys. Chem. C* **2016**, *120* (40), 23230–23238.

(61) Tatchen, J.; Gilka, N.; Marian, C. M. Intersystem Crossing Driven by Vibronic Spin – Orbit Coupling : A Case Study on Psoralen W. *Phys. Chem. Chem. Phys.* **2007**, *9*, 5209–5221.

(62) Fesser, K.; Bishop, A. R.; Campbell, D. K. Optical Absorption from Polarons. *Phys. Rev.* **1983**, *27* (8), 4804–4825.

(63) Wohlgenannt, M.; Jiang, X. M.; Vardeny, Z. V. Confined and Delocalized Polarons in π-Conjugated Oligomers and Polymers: A Study of the Effective Conjugation Length. *Phys. Rev. B - Condens. Matter Mater. Phys.* **2004**, *69* (24), 1–4.

(64) Campbell, D. K.; Bishop, A. R.; Fesser, K. Polarons in Quasi-One-Dimensional Systems. *Phys. Rev. B* **1982**, *26* (12), 6862–6874.

(65) Österbacka, R.; An, C. P.; Jiang, X. M.; Vardeny, Z. V. Two-Dimensional Electronic Excitations in Self-Assembled Conjugated Polymer Nanocrystals. *Science (80-.).* **2000**, *287* (5454), 839–842.

(66) Österbacka, R.; Jiang, X. M.; An, C. P.; Horovitz, B.; Vardeny, Z. V. Photoinduced Quantum Interference Antiresonances in π-Conjugated Polymers. *Phys. Rev. Lett.* **2002**, *88* (22), 4.

(67) Sirringhaus, H.; Brown, P. J.; Friend, R. H.; Nielsen, M. M.; Bechgaard, K.; Langeveld-Voss, B. M. W.; Spiering, A. J. H.; Janssen, R. A. J.; Meijer, E. W.; Herwig, P.; de Leeuw, D. M. Two-Dimensional Charge Transport in Self-Organized, High-Mobility Conjugated Polymers. *Nature* **1999**, *401*, 685–688.

(68) Jiang, X. M.; Österbacka, R.; Korovyanko, O.; An, C. P.; Horovitz, B.; Janssen, R. A. J.; Vardeny, Z. V. Spectroscopic Studies of Photoexcitations in Regioregular and Regiorandom Polythiophene Films. *Adv. Funct. Mater.* **2002**, *12* (9), 587–597.

(69) Jeng, K. S.; Chu, C. W.; Liu, C. L.; Jean, W. M.; Chen, H. L.; Chen, J. T. Orientation Preferences of Interchain Stackings for Poly(3-Hexylthiophene) Nanowires Prepared Using Template-Based Wetting Methods. *Macromol. Chem. Phys.* **2018**, *219* (11), 1800078.

(70) Cravino, A.; Neugebauer, H.; Luzzati, S.; Catellani, M.; Serdar Sariciftci, N. Vibrational Spectroscopy on PDTT3-a Low Band Gap Polymer Based on Dithienothiophene. *J. Phys. Chem. B* **2001**, *105* (1), 46–52.

(71) Cravino, A.; Neugebauer, H.; Luzzati, S.; Catellani, M.; Petr, A.; Dunsch, L.; Serdar Sariciftci, N. Positive and Negative Charge Carriers in Doped or Photoexcited Polydithienothiophenes: A Comparative Study Using Raman, Infrared, and Electron Spin Resonance Spectroscopy. *J. Phys. Chem. B* **2002**, *106* (14), 3583–3591.

(72) Cravino, A.; Neugebauer, H.; Petr, A.; Skabara, P. J.; Spencer, H. J.; McDouall, J. J. W.; Dunsch, L.; Sariciftci, N. S. Spectroelectrochemistry of Poly(Ethylenedithiathiophene)-the Sulfur Analogue of Poly(Ethylenedioxythiophene). *J. Phys. Chem. B* **2006**, *110* (6), 2662–2667.

(73) Dereka, B.; Svechkarev, D.; Rosspeintner, A.; Aster, A.; Lunzer, M.; Liska, R.; Mohs, A. M.; Vauthey, E. Solvent Tuning of Photochemistry upon Excited-State Symmetry Breaking. *Nat. Commun.* **2020**, *11* (1), 1–11.

(74) Yin, J.; Wang, Z.; Fazzi, D.; Shen, Z.; Soci, C. First-Principles Study of the Nuclear Dynamics of Doped Conjugated Polymers. *J. Phys. Chem. C* **2016**, *120* (3), 1994–2001.

(75) Kendrick, W. J.; Jirásek, M.; Peeks, M. D.; Greetham, G. M.; Sazanovich, I. V.; Donaldson, P. M.; Towrie, M.; Parker, A. W.; Anderson, H. L. Mechanisms of IR Amplification in Radical Cation Polarons. *Chem. Sci.* **2020**, *11* (8), 2112–2120.

(76) Yu, W.; Zhou, J.; Bragg, A. E. Exciton Conformational Dynamics of Poly(3-Hexylthiophene) (P3HT) in Solution from Time-Resolved Resonant-Raman Spectroscopy. *J. Phys. Chem. Lett.* **2012**, *3*, 1321–1328.

(77) Miller, S.; Fanchini, G.; Lin, Y. Y.; Li, C.; Chen, C. W.; Su, W. F.; Chhowalla, M. Investigation of Nanoscale Morphological Changes in Organic Photovoltaics during Solvent Vapor Annealing. *J. Mater. Chem.* **2008**, *18* (3), 306–312.

(78) Yu, W.; Donohoo-Vallett, P. J.; Zhou, J.; Bragg, A. E. Ultrafast Photo-Induced Nuclear Relaxation of a Conformationally Disordered Conjugated Polymer Probed with Transient Absorption and Femtosecond Stimulated Raman Spectroscopies. *J. Chem. Phys.* **2020**, *141*, 044201.

(79) Yu, W.; Magnanelli, T. J.; Zhou, J.; Bragg, A. E. Structural Heterogeneity in the Localized Excited States of Poly(3-Hexylthiophene). *J. Phys. Chem. B* **2016**, *120*, 5093–5102.

(80) Bredas, J. L.; Street, G. B. Polarons, Bipolarons, and Solitons in Conducting Polymers. *Acc. Chem. Res.* **1985**, *18* (10), 309–315.

(81) Duarte, A.; Pu, K.-Y.; Liu, B.; Bazan, G. C. Recent Advances in Conjugated Polyelectrolytes for Emerging Optoelectronic Applications. *Chem. Mater.* **2011**, *23* (Copyright (C) 2013 American Chemical Society (ACS). All Rights Reserved.), 501–515.

(82) Liu, Y.; Ogawa, K.; Schanze, K. S. Conjugated Polyelectrolytes as Fluorescent Sensors. *J. Photochem. Photobiol. C Photochem. Rev.* **2009**, *10* (4), 173–190.

(83) Rubio-Magnieto, J.; Azene, E. G.; Knoops, J.; Knippenberg, S.; Delcourt, C.; Thomas, A.; Richeter, S.; Mehdi, A.; Dubois, P.; Lazzaroni, R.; Beljonne, D.; Clement, S.; Surin, M. Self-Assembly and Hybridization Mechanisms of DNA with Cationic Polythiophene. *Soft Matter* **2015**, *11*, 6460–6471.

(84) Liu, Y.; Ogawa, K.; Schanze, K. S. Conjugated Polyelectrolytes as Fluorescent Sensors. *J. Photochem. Photobiol. C Photochem. Rev.* **2009**, *10* (4), 173–190.

(85) Thomas, S. W.; Joly, G. D.; Swager, T. M. Chemical Sensors Based on Amplifying Fluorescent Conjugated Polymers. *Chem. Rev.* **2007**, *107* (4), 1339–1386.

(86) Qiu, M.; Long, S.; Li, B.; Yan, L.; Xie, W.; Niu, Y.; Wang, X.; Guo, Q.; Xia, A. Toward an Understanding of How the Optical Property of Water-Soluble Cationic Polythiophene Derivative Is Altered by the Addition of Salts: The Hofmeister Effect. *J. Phys. Chem. C* **2013**, *117* (42), 21870–21878.

(87) Peterhans, L.; Alloa, E.; Sheima, Y.; Vannay, L.; Leclerc, M.; Corminboeuf, C.; Hayes, S. C.; Banerji, N. Salt-Induced Thermochromism of a Conjugated Polyelectrolyte. *Phys. Chem. Chem. Phys.* **2017**, *19* (42), 28853–28866.

(88) Duan, X. R.; Liu, L. B.; Feng, F. D.; Wang, S. Cationic Conjugated Polymers for Optical Detection of DNA Methylation, Lesions, and Single Nucleotide Polymorphisms. *Acc. Chem. Res.* **2010**, *43* (2), 260–270.

(89) Charlebois, I.; Gravel, C.; Arrad, N.; Boissinot, M.; Bergeron, M. G.; Leclerc, M.

Impact of DNA Sequence and Oligonucleotide Length on a Polythiophene-Based Fluorescent DNA Biosensor. *Macromol. Biosci.* **2013**, *13* (6), 717–722.

(90) Zhu, C.; Fang, L. Locking the Coplanar Conformation of π-Conjugated Molecules and Macromolecules Using Dynamic Noncovalent Bonds. *Macromol. Rapid Commun.* **2018**, *39* (2), 1700241.

(91) Zhu, C.; Mu, A. U.; Lin, Y. H.; Guo, Z. H.; Yuan, T.; Wheeler, S. E.; Fang, L. Molecular Coplanarity and Self-Assembly Promoted by Intramolecular Hydrogen Bonds. *Org. Lett.* **2016**, *18* (24), 6332–6335.

(92) Yao, W.; Zhao, Y. S. Tailoring the Self-Assembled Structures and Photonic Properties of Organic Nanomaterials. *Nanoscale* **2014**, *6* (7), 3467–3473.

(93) Surin, M.; Janssen, P. G. A.; Lazzaroni, R.; Leclère, P.; Meijer, E. W.; Schenning, A. P. H. J. Supramolecular Organization of Ssdna-Templated p-Conjugated Oligomers via Hydrogen Bonding. *Adv. Mater.* **2009**, *21* (10–11), 1126–1130.

(94) Hollingsworth, W. R.; Segura, C.; Balderrama, J.; Lopez, N.; Schleissner, P.; Ayzner, A. L. Exciton Transfer and Emergent Excitonic States in Oppositely-Charged Conjugated Polyelectrolyte Complexes. *J. Phys. Chem. B* **2016**, *120* (31), 7767–7774.

(95) Belosludov, R. V.; Sato, H.; Farajian, A. A.; Mizuseki, H.; Kawazoe, Y. Theoretical Study of Molecular Enamel Wires Based on Polythiophene-Cyclodextrin Inclusion Complexes. *Mol. Cryst. Liq. Cryst.* **2003**, *406*, 1–10.

(96) Van Den Boogaard, M.; Bonnet, G.; Van't Hof, P.; Wang, Y.; Brochon, C.; Van Hutten, P.; Lapp, A.; Hadziioannou, G. Synthesis of Insulated Single-Chain Semiconducting Polymers Based on Polythiophene, Polyfluorene, and β-Cyclodextrin. *Chem. Mater.* **2004**, *16* (23), 4383–4385.

(97) Shimomura, T.; Akai, T.; Fujimori, M.; Heike, S.; Hashizume, T.; Ito, K. Conductivity Measurement of Insulated Molecular Wire Formed by Molecular Nanotube and Polyaniline. *Synth. Met.* **2005**, *153* (1–3), 497–500.

(98) Masai, H.; Terao, J. Stimuli-Responsive Functionalized Insulated Conjugated Polymers. *Polym. J.* **2017**, *49* (12), 805–814.

(99) Li, C.; Numata, M.; Bae, A. H.; Sakurai, K.; Shinkai, S. Self-Assembly of

Supramolecular Chiral Insulated Molecular Wire. *J. Am. Chem. Soc.* **2005**, *127* (13), 4548–4549.

(100) Buey, J.; Swager, T. M. Three-Strand Conducting Ladder Polymers: Two-Step Electropolymerization of Metallorotaxanes. *Angew. Chem. Int. Ed* **2000**, *39*, 608–612.

(101) Sauvage, J.-P.; Kern, J.-M.; Bidan, G.; Divisia-Blohorn, B.; Vidal, P.-L. Conjugated Polyrotaxanes : Improvement of the Polymer Properties by Using Sterically Hindered Coordinating Units. *New J. Chem.* **2002**, *26*, 1287–1290.

(102) Hecht, S.; Frechet, J. M. J. Dendritic Encapsulation of Function : Applying Nature s Site Isolation Principle from Biomimetics to Materials Science. *Angew. Chem. Int. Ed.* **2001**, *40*, 74–91.

(103) Watson, S. M. D.; Galindo, M. A.; Horrocks, B. R.; Houlton, A. Mechanism of Formation of Supramolecular DNA-Templated Polymer Nanowires. *J. Am. Chem. Soc.* **2014**, *136* (18), 6649–6655.

(104) Hamedi, M.; Elfwing, A.; Gabrielsson, R.; Inganäs, O. Electronic Polymers and DNA Self-Assembled in Nanowire Transistors. *Small* **2013**, *9* (3), 363–368.

(105) Knudsen, J. B.; Liu, L.; Kodal, A. L. B.; Madsen, M.; Li, Q.; Song, J.; Woehrstein, J. B.; Wickham, S. F. J.; Strauss, M. T.; Schueder, F.; Vinther, J.; Krissanaprasit, A.; Gudnason, D.; Smith, A. A. A.; Ogaki, R.; Zelikin, A. N.; Besenbacher, F.; Birkedal, V.; Yin, P.; Shih, W. M.; Jungmann, R.; Dong, M.; Gothelf, K. V. Routing of Individual Polymers in Designed Patterns. *Nat. Nanotechnol.* **2015**, *10* (10), 892–898.

(106) Chen, W.; Schuster, G. B. Precise Sequence Control in Linear and Cyclic Copolymers of 2,5-Bis(2-Thienyl)Pyrrole and Aniline by DNA-Programmed Assembly. *J. Am. Chem. Soc.* **2013**, *135* (11), 4438–4449.

(107) Surin, M. From Nucleobase to DNA Templates for Precision Supramolecular Assemblies and Synthetic Polymers. *Polym. Chem.* **2016**, *7* (25), 4137–4150.

CHAPTER 3

EXPERIMENTAL AND COMPUTATIONAL ANALYSIS

3.1 Introduction to Raman spectroscopy

Raman spectroscopy is a technique that provides highly chemical-specific information about samples based on the fundamental vibrational modes of the molecules. In Raman spectroscopy, the sample is irradiated by intense laser beams in the UV-visible region (ν_0), and the scattered light consists of two types: Rayleigh scattering (elastic), which is strong and has the same energy as the incident beam (ν_0) and Raman scattering (inelastic), which is very weak and it is due to the light interaction with vibrating molecules.[1] The difference in energy between the incident photons and the scattered photons is called Raman Shift. Figure 3.1a represents the conceptual picture associated with Raman scattering involving two vibrational states m and n. The upward and downward arrows represent the transitions associated with the incident and scattered photons, respectively. In the case of Stokes scattering, the initial state is lower in energy than the final state, and the scattered frequency ν_{en} is lower than the incident frequency ν_{me}. Anti-Stokes scattering, on the other hand, results when the initial state is higher in energy than the final, and consequently ν_{em} is greater than ν_{ne}. According to quantum mechanics, only those transitions involving $\Delta v = \pm 1$ are allowed for a harmonic oscillator. However, transitions involving $\Delta v = \pm 2, \pm 3, \ldots$ (overtones) are also weakly allowed by selection rules when anharmonicity exists in the system. Among many $\Delta v = \pm 1$ transitions, that of $v = 0 \rightarrow 1$ (fundamental) appears most strongly in Raman spectra.[1]

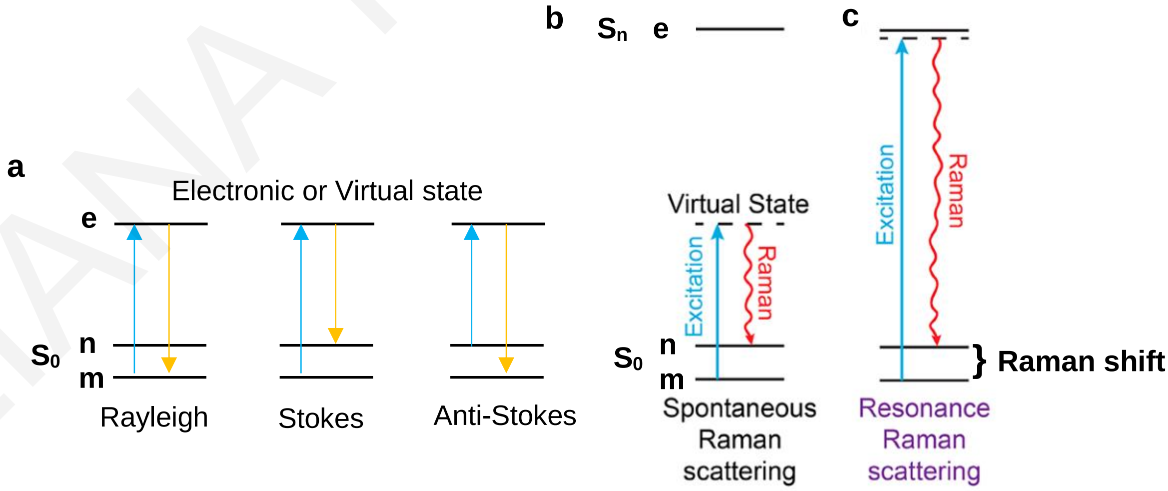

Figure 3.1. Energy diagrams for the processes involved in Raman spectroscopy.[2]

Vibrational activity in Raman scattering depends on the change in polarizability (α) during a vibration. Specifically, the Raman activity depends on $(\partial\alpha/\partial Q)_0$, which is evaluated at the equilibrium geometry. According to the two graphs of polarizability versus normal coordinate (Q_0) shown in Figure 3.2, the slope of the graph in Figure 3.2a is zero at the equilibrium geometry, so the mode is Raman inactive, while when $(\partial\alpha/\partial Q)_0 \neq 0$ (Figure 3.2b) for a type of vibration (such as a symmetric stretch), it is Raman active.[3]

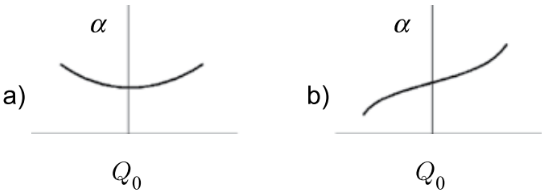

Figure 3.2. Polarizability versus normal coordinate for (a) Raman-inactive and (b) Raman-active normal modes.[3]

Resonance Raman (RR) spectroscopy in contrast to the off-resonance technique, which excites a molecule to a virtual state (Figure 3.1b), exploits an excitation energy that coincides with an electronic transition (Figure 3.1c) of the investigated molecule, in order to selectively enhance the vibrational Raman signatures that are coupled to the specific electronic transition. This results in the high sensitivity of RR spectroscopy that is able to detect analytes even with very low concentration. Figure 3.3 illustrates the beneficial influence of resonance in RR spectroscopy to enhance the vibrational signal of a specific component or molecular system. For example, the RR spectrum of tetracene nanocrystals was efficiently discriminated from the corresponding spectrum of the tetracene monomer (Figure 3.3b) by using different excitation wavelengths resonant with the absorption of each system (Figure 3.3a).[4]

This correlation is expressed by Equation 1, according to which the intensity of the vibrational bands is proportional to the $\left(a_{p\sigma}\right)_{mn}^{2}$, where $\left(a_{p\sigma}\right)_{mn}$ represents the change in polarizability caused by the m→e→n transition (Figure 3.1) (ρ, σ refers to the x, y and z components of the polarizability tensor).[1]

$$I_{mn} = constant \cdot I_0 \cdot (\nu_0 - \nu_{mn})^4 \sum\nolimits_{p\sigma} \left|\left(a_{p\sigma}\right)_{mn}\right|^2 \tag{1}$$

I_0, is the intensity of the incident laser beam of frequency ν_0.

$$\left(a_{p\sigma}\right)_{mn} = \frac{1}{h}\sum\nolimits_e \left(\frac{M_{me}M_{en}}{\nu_{em}-\nu_0+i\Gamma_e} + \frac{M_{me}M_{en}}{\nu_{en}+\nu_0+i\Gamma_e}\right) \tag{2}$$

where ν_{em} and ν_{en} are the frequencies corresponding to the energy differences between the states subscribed and h is Planck's constant. M_{me}, etc., are the electronic transition moments, such as $M_{me} = \int \Psi_m^* \mu_\sigma \Psi_e d\tau$, ($\Psi_m$ and Ψ_e are the total wavefunctions of the m and e states, respectively, and μ_σ is the σ component of the electric dipole moment), Γ_e is the band width of the e^{th} state, and the $i\Gamma_e$ term is called the damping constant. When $\nu_0 \approx \nu_{mn}$ the denominator $\nu_{em} - \nu_0 + i\Gamma_e$ decreases, and subsequently $\left(a_{p\sigma}\right)_{mn}$ increases, resulting in enhanced intensity I_{mn}. Hence, in this case, the first term of $\left(a_{p\sigma}\right)_{mn}$ is named as the "resonance term". According to the Born-Oppenheimer approximation, the electronic and vibrational states can be considered separable and can be expressed by different wavefunctions. The "resonance term" of the polarizability, if higher terms of the transition dipole moment are considered that depend on the normal coordinate Q, can be expressed as (Eq. 3)[1]:

$$\left(a_{p\sigma}\right)_{mn} \cong A + B \qquad (3)$$

The A-term is expressed by Eq. 4, where M_e is the pure electronic transition moment for the resonant excited state e, of which ν is the vibrational level of bandwidth Γ, $\nu_{\nu i}$ is the transition frequency from the ground state vibrational level i to the excited state vibrational level ν,

$$A \cong M_e^2 \frac{1}{h} \sum_\nu \frac{\langle j|\nu\rangle\langle \nu|i\rangle}{\nu_{\nu i} - \nu_0 + i\Gamma_\nu} \qquad (4)$$

and B-term by Eq. 5:[1]

$$B \cong M_e M_e{}' \frac{1}{h} \sum_\nu \frac{\langle j|Q|\nu\rangle\langle \nu|i\rangle + \langle j|\nu\rangle\langle \nu|Q|i\rangle}{\nu_{\nu i} - \nu_0 + i\Gamma_\nu} \qquad (5)$$

Usually the B-term is small and only the A-term contributes to the transition polarizability. Therefore, according to equation 4, the transition polarizability vanishes unless the excited state potential is displaced with respect to that of the ground state, as the two overlap integrals of vibrational wavefunctions of the numerator (Franck-Condon overlaps) are equal to 0. Thus, vibrational modes which are not Franck−Condon active are not allowed by the A term. Conversely, totally-symmetric modes that contribute to the vibrational progression of the ground to excited electronic state transition are active in resonance Raman. Thus, the totally-symmetric modes that are enhanced in the resonance Raman spectrum are those which correspond to the geometry change of the molecule. These modes are said to be "A-term enhanced" or "Franck−Condon enhanced".[3]

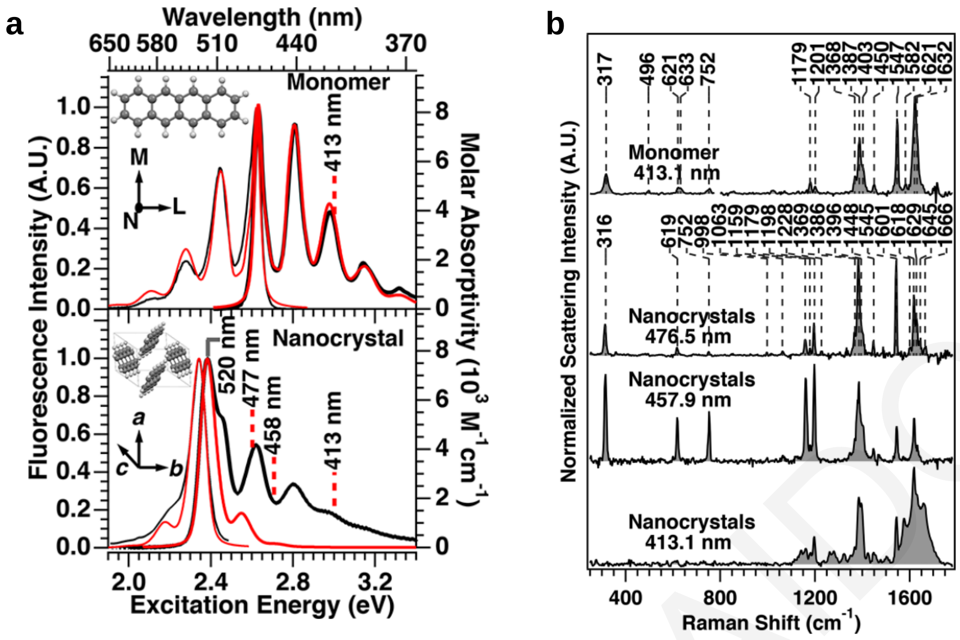

Figure 3.3. (a) Absorption and emission spectra (black lines) of tetracene monomer in acetone and nanocrystal suspension in water. (b) Comparison of Raman spectra of tetracene monomer and nanocrystal using different excitation wavelengths.[4]

3.1.1 Experimental setup

A schematic representation of the experimental setup used in our lab for Raman measurements is illustrated in Figure 3.4.

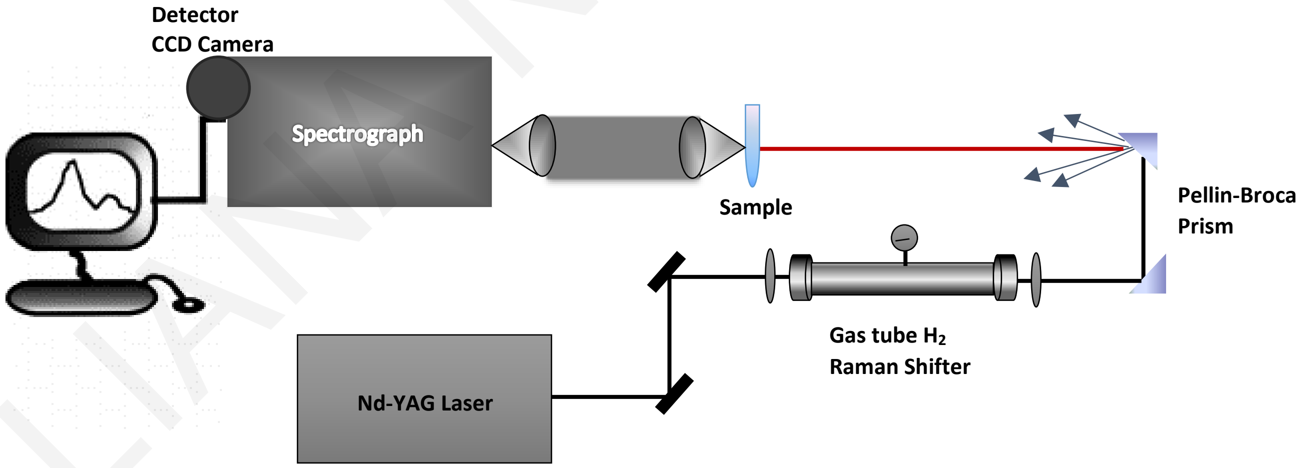

Figure 3.4. Schematic representation of the Resonance Raman setup.

Resonance Raman (RR) spectra were obtained with resonant excitation for each molecule tested and the excitation wavelengths employed were mostly provided by the second and fourth harmonics of a Q-switched Nd:YAG laser (PRO-230, 30 Hz, Spectra Physics) or via Raman shifting in a 1 m tube containing H_2 gas. Also, 473 nm excitation was obtained from a CW diode laser (Ultralasers, 50 mW OEM DPSS Laser). The excitation light was focused into a spinning cell consisting of an EPR suprasil tube (diameter: 4 mm) attached to a rheostat-controlled motor for choice of rotation speed. Use of the spinning cell prolonged the lifetime of the samples. Modest excitation energies were employed according to the used excitation wavelength to avoid decomposition of the sample, which was monitored by obtaining the absorption spectrum of the sample before and after exposure. The Raman scattered light was collected in a backscattering geometry and delivered to a 0.75 m focal-length Czerny–Turner spectrograph, equipped with a 1200-grooves/mm holographic grating for the visible wavelengths and a 2400 grooves/mm holographic grating for excitation at 266 nm. The slit width was set to 100 μm for all wavelengths used in this work. The scattered light was detected by a LN_2-cooled 2048 x 512 pixel, back-illuminated UV-enhanced CCD detector (Spec10:2KBUV/LN, Princeton Instruments). Frequency calibration of the spectra was accomplished with the use of cyclohexane. MATLAB and ORIGIN software were used for spectral treatment and analysis.

3.2 Theory of resonant Raman intensities

3.2.1 Determination of Absolute Resonance Raman Cross Sections

Absolute resonance Raman cross sections (σ_R) were determined for all the vibrational modes of the studied molecule observed in the RR spectra at an excitation wavelength close to the absorption maximum. In the calculation of the σ_R's the 801 cm^{-1} mode of cyclohexane (9.245 M) was used as an external standard. The intensities of the Raman bands were corrected for the spectral response of the instrument using a calibrated tungsten/halogen lamp and for self-absorption according to Equation 6:[5]

$$\frac{I_{s,corrected}}{I_{r,corrected}} = \frac{I_s\, c_r(\varepsilon_s+\varepsilon_0)}{I_r c_s(\varepsilon_r+\varepsilon_0)} \tag{6}$$

where c is the concentration of the reference or sample and ε is the extinction coefficient of the sample at the reference or sample peak, or laser line wavelength (subscripts r, s and 0, respectively). The intensities of the Raman bands were determined by deconvolution, due to spectral congestion, and the area of the Voigt peaks used for the fitting was subsequently calculated.

Absolute RR cross sections as a function of excitation wavelength were determined using Eq. 7 for the most intense bands in the spectra:[6]

$$\sigma_{R(v(x))} = \frac{I_{v(x)} C_i \left(\frac{1+2\rho}{1+\rho}\right)_{v(x)}}{I_i C_{v(x)} \left(\frac{1+2\rho}{1+\rho}\right)_i} \sigma_i \qquad (7)$$

In Eq. 7, σ_R is the Raman scattering cross section of mode v(x), ρ is the depolarization ratio, C is the concentration, and $I_{v(x)}$ and I_i are the experimentally determined intensities for the mode of interest and the external standard, respectively. The absolute Raman cross section and depolarization ratio for the 801 cm^{-1} mode of cyclohexane were previously measured or obtained from an A-term fit to the experimental cross sections (σ_R(473 nm)=1×10^{-12} cm^2, σ_R(532 nm)=6.68×10^{-13} cm^2, and ρ=0.09. A-term fit parameters: coupling constant K=1.3×10^{-9} Å^2 and ν_e=125000 cm^{-1}).[6–8] The depolarization ratios for the modes were taken as 1/3.

3.2.2 Resonance Raman Intensity Analysis (RRIA)

RR band intensities can provide detailed information regarding excited-state structure and dynamics that can be extracted through resonance Raman intensity analysis. As the intensities of RR bands are related to the displacements between the ground and excited state potential energy surface minima in each mode, i.e. the change in molecular structure upon excitation, which in turn determine the shape of the absorption spectrum, simultaneous modelling of the latter and RR excitation profiles (REPs) can provide access to a quantitative picture of the excited state structure. Here, RRIA was employed to provide insights on the significantly different vibronic structures in the absorption spectra of the tested molecules. In our analysis we used expressions from the time-dependent formalism for absorption (Eq. 8) and Resonance Raman scattering (Eq. 9) derived from second order perturbation theory:[9]

$$\sigma_A(E_L) = \frac{4\pi e^2 E_L M^2}{6\hbar^2 cn} \int_{-\infty}^{\infty} dE_{00} H(E_{00}) \times \left[\int_{-\infty}^{\infty} \langle i|i_1(t)\rangle exp\left[\frac{i(E_L+\epsilon_i)t}{\hbar}\right] D(t)\, dt\right] \qquad (8)$$

$$\sigma_{i\to f}(E_L) = \frac{8\pi e^4 E_S E_L M^4}{9\hbar^6 c^4} \int_{-\infty}^{\infty} \partial E_{00} H(E_{00}) \left|\int_0^{\infty} \langle f|i_1(t)\rangle exp\left(\frac{i(E_L+\epsilon_i)t}{\hbar}\right) D(t) dt\right|^2 \qquad (9)$$

The corresponding equations (Eq. 8 and 9 for absorption and Raman, respectively) for a model that includes transitions to two different electronics states are[10]:

$$\sigma_A(E_L) = \frac{4\pi e^2 E_L}{6\hbar^2 cn} \sum_u P_u \int_{-\infty}^{\infty} dE_{00} H(E_{00})$$

$$\times \left[\int_{-\infty}^{\infty} M_1^2 \langle i|i_1(t)\rangle exp\left[\frac{i(E_L+\epsilon_i)t}{\hbar}\right] D_1(t)\, dt\right.$$

$$+ \int_{-\infty}^{\infty} M_2^2 \langle i|i_2(t)\rangle exp\left[\frac{i(E_L+\epsilon_i)t}{\hbar}\right] D_2(t)\, dt\Big] \tag{10}$$

$$\sigma_{t\to f}(E_L) = \frac{8\pi e^4 E_S E_L}{9\hbar^6 c^4} \sum_u P_u \int \partial E_{00} H(E_{00})$$

$$\times \left| M_1^2 \int_0^{\infty} \langle f|i_1(t)\rangle \exp\left[\frac{i(E_L+\epsilon_t)}{\hbar}\right] e^{-\Gamma_1 t/\hbar} dt\right.$$

$$\left. + M_2^2 \int_0^{\infty} \langle f|i_2(t)\rangle \exp\left[\frac{i(E_L+\epsilon_t)}{\hbar}\right] e^{-\Gamma_2 t/\hbar} dt\right|^2 \tag{11}$$

In the above equations E_S and E_L are the scattered and incident photon energies, respectively (in cm^{-1}), *c* is the speed of light, and *n* is the solvent index of refraction. The magnitude of the transition dipole moment for the electronic transition is given by M (in Å) and ϵ_i is the energy of the initial vibrational state. Γ is the homogeneous line width of the excited state (in cm^{-1}), and is given by the damping function D(t). In this analysis the homogeneous broadening was taken to be Gaussian ($D(t) = e^{-\frac{\Gamma^2 t^2}{\hbar^2}}$). E_{00} is the energy difference between the $v = 0$ vibrational state in the ground and excited electronic state and H(E_{00}) is the contribution of inhomogeneous broadening, which corresponds to the presence of different solvent sites that are static on the time scale of Raman scattering, thus altering E_{00}. Θ represents the standard deviation of this distribution (in cm^{-1}) ($H(E_{00})$). The expression $\langle f|i_n(t)\rangle$ represents the time-dependent overlap of the final state in the scattering process with the initial state propagating under the influence of the excited state Hamiltonian in state *n*. Similarly, the expression $\langle i|i_j(t)\rangle$ in Eq. 3 and 5 is the time-dependent overlap of the initial ground vibrational state with the same state propagating on the excited state *j* potential energy surface.

In the case where both ground and excited states normal coordinates are identical and harmonic, the multidimensional overlaps $\langle i|i(t)\rangle$ and $\langle f|i(t)\rangle$ can be described by one-dimensional overlaps in each normal coordinate. Furthermore, in fundamental Raman scattering, where the final state differs from the initial state only in one coordinate, the multidimensional overlaps $\langle f|i(t)\rangle$ can be decomposed into $\langle f|i(t)\rangle$ for the Raman active mode and $\langle i|i(t)\rangle$ that refers to all other modes (Eq. 12 and 13).[9]

$$\langle i|i(t)\rangle = \prod_{k=1}^{8} \langle i_k|i_k(t)\rangle \tag{12}$$

$$\langle f|i(t)\rangle = \langle f_1|i_1(t)\rangle \prod_{k=2}^{8} \langle i_k|i_k(t)\rangle \tag{13}$$

Here, for example eight vibrational degrees of freedom of frequency ω are included in the model representing the most intense bands observed in the RR spectra. Explicit expressions have been derived for the one-dimensional overlaps and are available from the literature, where the dependence on the displacement, Δ, between the ground and excited state potential energy surface minima along each coordinate, (Figure 3.5) is apparent ($s = \Delta^2/2$, s: Huang-Rhys parameter):

$$\langle i|i(t)\rangle = exp\left[-s\left(1-e^{-i\omega t}\right)-\frac{i\omega t}{2}-\frac{iE_0 t}{\hbar}\right] \tag{14}$$

$$\langle f|i(t)\rangle = \pm s^{1/2}\left(e^{-i\omega t}-1\right)\langle i|i(t)\rangle \tag{15}$$

The time-dependent overlaps here were calculated using the methodology of Yan and Mukamel,[11] using a time step of 0.1 fs for a total of 5000 points.

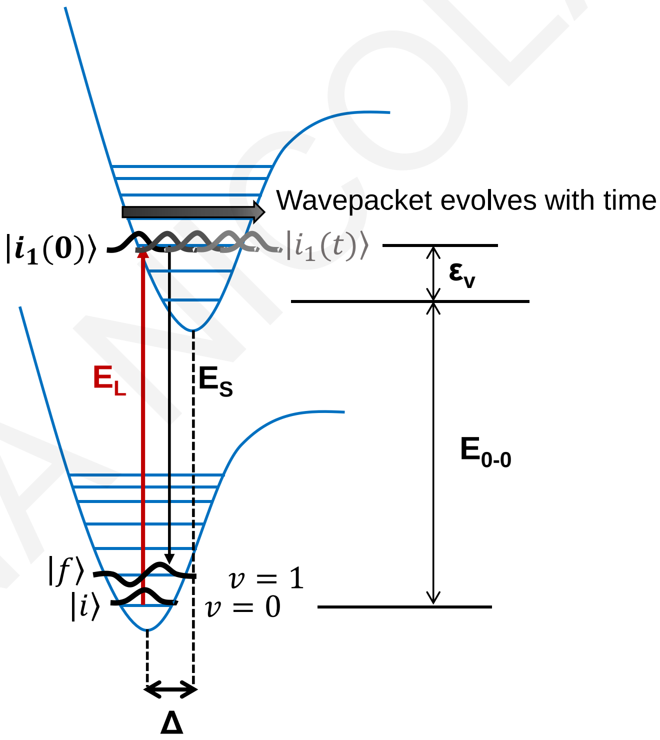

Figure 3.5. Wave packet dynamics on a displaced excited state potential surface.[3]

3.2.3 Stimulated Emission modeling

The stimulated emission spectra were simulated using Eq. 16, which resembles Eq. 8, with the difference that now χ are the electronic excited state vibrational eigenfunctions propagated by the ground state Hamiltonian and the inverse Fourier transform is taken.[12]

$$I_{SE}(\omega_L) \propto \sum_{\omega_L} \int_0^{\infty} \langle \chi|\chi_1(t)\rangle exp\left(i\left(-\omega+\omega_{eg}+\omega_1\right)t\right)D(t)dt \tag{16}$$

where $|1\rangle$ is a vibrational eigenstate of the excited electronic surface, ω_1 is its vibrational energy, ω_{eg} is the electronic zero-zero transition frequency and $|\chi_1(t)\rangle = \exp(-iH_g t/\hbar)|\chi_1\rangle$, where H_g is the ground state Hamiltonian.

3.3 Transient absorption spectroscopy

Transient absorption spectroscopy employs an ultrafast light pulse (the "pump" pulse) to prepare an excited electronic or vibrational state, followed by a probe pulse that is delayed by time τ. A schematic of the experiment in shown in Figure 3.6.

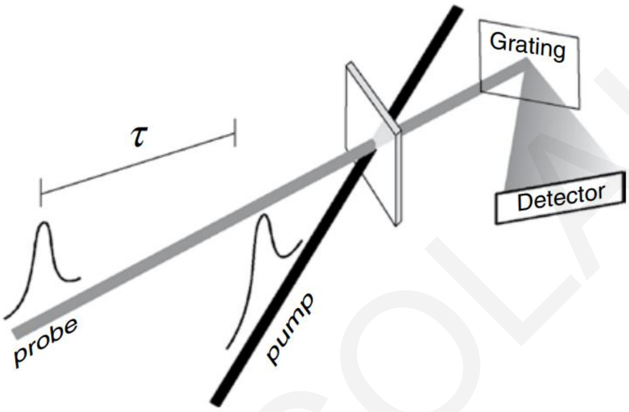

Figure 3.6 Basic pump-probe experimental arrangement.[3]

The time delay stems from a variable pathlength for the probe pulse compared to the pump. The time delay for a given pathlength difference derives from the speed of light, about 300 nm/fs. The extra length of the probe path relative to the pump path may be as long as 30 cm to achieve a delay of 1 ns, or as short as 3 μm for a delay of 10 fs. This technique is used to study dynamic processes in materials by monitoring the change in concentration of species produced following excitation. In femtosecond broad-band pump-probe experiments, the probe is a spectrally broadened, white light pulse.

The resulting spectra illustrate the change in absorbance (ΔA) (Figure 3.7a) of an excited sample compared to the sample in the ground state and its evolution in time. Upon excitation by the pump, a specific population is promoted to an excited state, and is detected by a negative band attributed to the ground state bleaching (GSB). Its sign is negative because less light is absorbed by the excited sample ($I_{pump} > I_{no\ pump}$) (Eq. 17).

$$\Delta A = -log\frac{I_{pump}}{I_{no\ pump}} \tag{17}$$

The GSB has mirror image relation with the steady-state absorption. The stimulated emission (SE) band is also negative and is located at higher wavelengths. The radiative relaxation of the molecules in the first excited state (S_1) is stimulated by the probe beam and more light arrives on the detector. Positive bands result from the absorption of the transient species. One of them is the excited absorption (ESA), which is the absorption from the state directly populated by the pump (S_1) to the higher excited states (S_n). In addition, positive bands could signify the existence of triplet state T_1 or charged species such as polarons. TA spectroscopy gives access to a large amount of information regarding these excited species and their formation and relaxation rates.

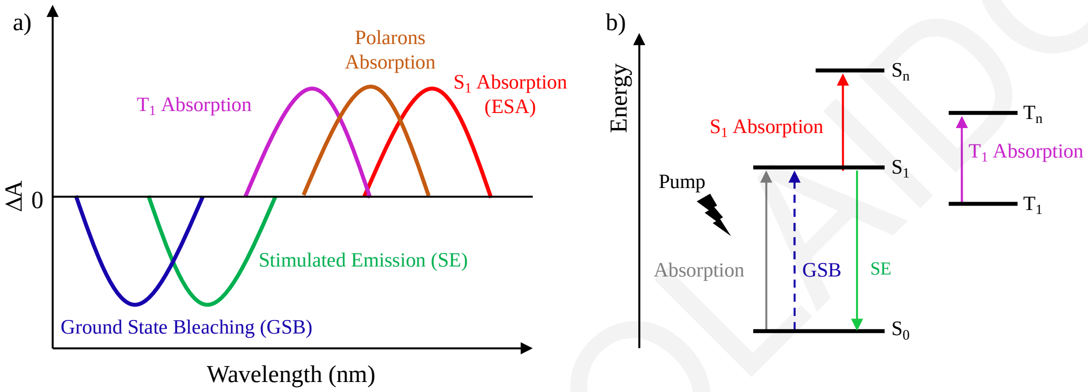

Figure 3.7: Electronic transitions underlying the different spectral features observed in transient absorption spectroscopy.

3.4 Transient vibrational spectroscopy

Investigation of molecular structural dynamics can be achieved through transient vibrational spectroscopy, which offers several advantages over time-resolved electronic spectroscopy. In the spectra of the latter, diffuse bands are frequently observed and overlapping electronic transitions are difficult to be resolved. In contrast, vibrational transitions, can display resolved spectral signatures and therefore can help distinguish the processes that occur by observing the structural evolution after photoexcitation.

3.4.1 Time-resolved Infrared spectroscopy

Transient infrared spectroscopy is becoming a widespread approach utilised to study the ultrafast dynamics of excited molecules. Structural changes of a wide range of molecules or molecular complexes were monitored with femtosecond pulses in the mid-IR directly in the time domain by means of transient absorption of prominent molecular vibrations.[13] A schematic representation of the experimental LIFEtime setup for TRIR measurements, that we used during our visit at the Central Laser Facility (CLF) of the Rutherford Lab is illustrated in Figure 3.8.

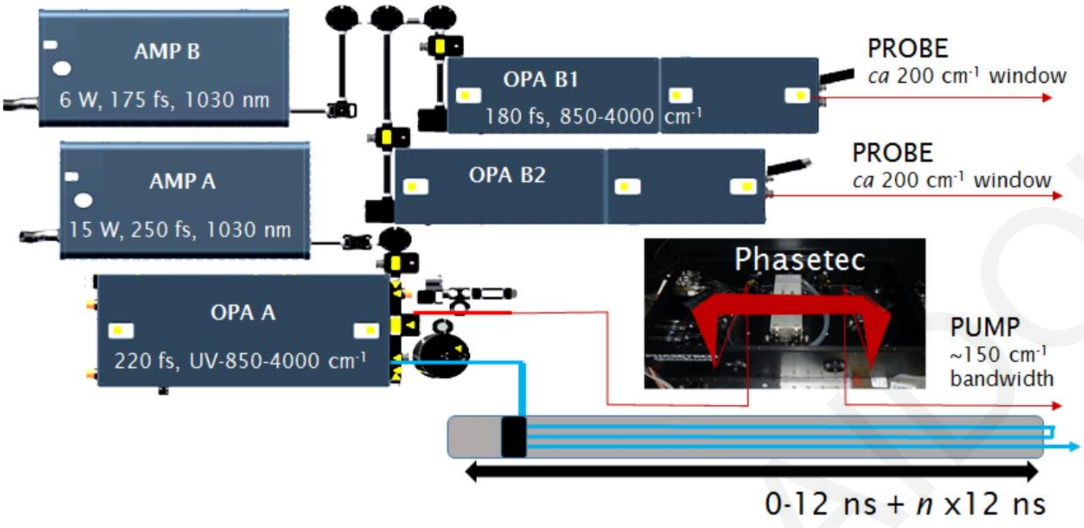

Figure 3.8 Experimental setup and laser system for femtosecond TRIR spectroscopy.

TRIR measurements performed at the LIFEtime setup consist two 100 kHz Pharos lasers and three optical parametric amplifiers (Light Conversion Systems), which provided 266 and 532 nm excitation with narrow bandwidth, and 220 fs-long pulses (150 cm^{-1}). The pump pulses at the sample had a fluence of 62 $\mu J/cm^2$ for 532 nm and 56.6 $\mu J/cm^2$ for 266 nm. The IR probe beam (pulse length of 180 fs (200 cm^{-1})) was split to form the reference and probe beams, which were dispersed in spectrographs and detected by MCT array detectors (IR Associates). The 50 kHz 532 nm pump beam was focused (~ 200 μm spot sizes) and overlapped with the probe beam (~50 μm spot size) in the sample cell. The high-speed data acquisition system allowed 100 kHz acquisition and processing of the probe and reference pulses to generate a pump-on pump-off infrared absorption difference signal. The difference signal was calibrated using the characteristic polystyrene IR absorption spectrum. The sample was raster scanned in x- and y- directions and constantly recycled in order to preserve the sample.

3.4.2 Impulsive Stimulated Raman Scattering

To track vibrations in real time, impulsive stimulated Raman scattering (ISRS), a third-order ($\chi^{(3)}$) nonlinear technique, was developed where a pair of ultrashort (typically, 10-15 fs) pulses, having temporal width less than the period of the vibration to be observed (or, equivalently, having spectral width more than the vibrational frequency to be recorded) are used. The pump pulse impulsively creates a time-dependent modulation (a vibrational coherence), which is subsequently interrogated by a time-delayed probe pulse, and the Raman spectrum is obtained by Fourier transform of the temporal interferogram.[14] A distinct advantage of impulsive over frequency domain Raman is that the full vibrationally coherent evolution of the system is measured. Photoexcitation of the molecular system on resonance with a ground-state electronic absorption band, impulsively generates vibrational coherences on the excited electronic state. When probing a transient electronic band at a particular wavelength, the time-dependent excited-state signals result in oscillations at the frequencies of the initially excited coherent nuclear motion.[15] Therefore, this technique enables the isolation of the spectral contribution of a distinct population.

3.4.3 Femtosecond Stimulated Raman Spectroscopy

Femtosecond stimulated Raman experiment (FSRS) is a time-resolved technique capable of following vibrationally resolved excited state dynamics.[16] FSRS is a three-pulse experiment. An actinic pump pulse of duration of ~30 fs excites the molecule in the usual way and initiates the photochemical reaction. The instantaneous structure of the molecule, represented by its Raman spectrum, is then read out at various time delays (Δt, see Figure 3.9)[3] by the two pulses, an intense 3 ps Raman pulse and a weaker 20 fs broadband probe pulse.[17]

The time resolution for the photochemical event is given by the time delay between the fs actinic pump and the fs probe pulses, while the frequency-resolution is given by the bandwidth of the ps Raman pump pulse, the vibrational dephasing time, the lifetime of the transient species, and the spectrograph resolution.[18] Thus, FSRS can provide dynamic information at fast timescales and with high spectral resolution. Consequently, this technique prevails over the typical time-resolved vibrational spectroscopic techniques, which employ picosecond pulses in order to achieve sufficient spectral resolution. Therefore, the time and spectral resolutions offered are limited because the Raman bands are at least as spectrally broad as the probe pulse, which is typically in the ns or ps regime.

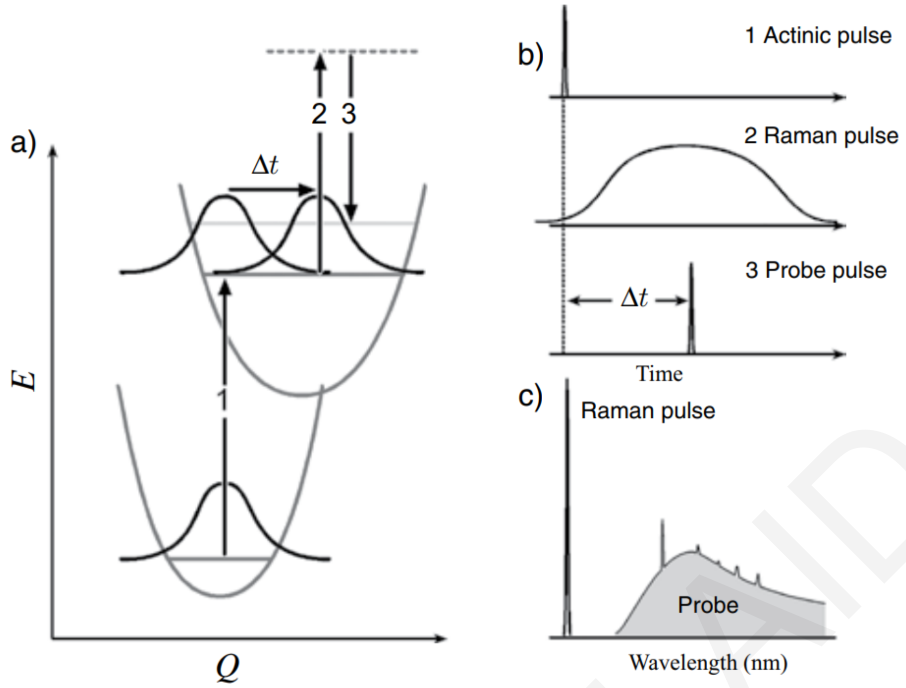

Figure 3.9: Pulse sequence (a and b) and resulting spectrum (c) for femtosecond stimulated Raman spectroscopy.[3]

References

(1) Ferraro, J. R.; Nakamoto, K.; Brown, C. W. *Introductory Raman Spectroscopy: Second Edition*; 2003.

(2) Wei, L.; Min, W. Electronic Preresonance Stimulated Raman Scattering Microscopy. *J. Phys. Chem. Lett.* **2018**, *9* (15), 4294–4301.

(3) McHale, J. L. *Molecular Spectroscopy, Second Edition*; 2017.

(4) Ellis, S. R.; Dietze, D. R.; Rangel, T.; Brown-Altvater, F.; Neaton, J. B.; Mathies, R. A. Resonance Raman Characterization of Tetracene Monomer and Nanocrystals: Excited State Lattice Distortions With Implications For E Ffi Cient Singlet Fission. *J. Phys. Chem. A* **2019**, *123*, 3863–3875.

(5) Bailey, S. E.; Cohan, J. S.; Zink, J. I. Interference Effects of Multiple Excited States in the Resonance Raman Spectroscopy of CpCoCOD. *J. Phys. Chem. B* **2000**, *104* (46), 10743–10749.

(6) Foster, C. E.; Barham, B. P.; Reid, P. J. Resonance Raman Intensity Analysis of Chlorine Dioxide Dissolved in Chloroform : The Role of Nonpolar Solvation. *J. Chem. Phys.* **2001**, *114* (19), 8492–8504.

(7) Trulson, M. O.; Mathies, R. A. Raman Cross Section Measurements in the Visible and Ultraviolet Using an Integrating Cavity: Application to Benzene, Cyclohexane, and Cacodylate. *J. Chem. Phys.* **1986**, *84* (4), 2068–2074.

(8) Esposito, A. P.; Foster, C. E.; Beckman, R. A.; Reid, P. J. Excited-State Dynamics of Chlorine Dioxide in the Condensed Phase from Resonance Raman Intensities. *J.*

Phys. Chem. A **1997**, *101* (29), 5309–5319.

(9) Myers, A. B.; Mathies, R. A.; Spiro, T. G. *Biological Applications of Raman Spectroscopy: Resonance Raman Spectra of Polyenes and Aromatics*; John Wiley & Sons, Ltd., 1987; Vol. 2.

(10) Trimithioti, M.; Hayes, S. C. Resonance Raman Intensity Analysis of ClNO2 Dissolved in Methanol. *J. Phys. Chem. A* **2013**, *117*, 300–310.

(11) Yan, Y. J.; Mukamel, S. Eigenstate-Free , Green Function , Calculation of Molecular Absorption and Fluorescence Line Shapes. *J. Chem. Phys.* **1986**, *85* (10), 5908–5923.

(12) Kulinowski, K.; Gould, I. R.; Myers, A. B. Absorption, Fluorescence, and Resonance Raman Spectroscopy of the Hexamethylbenzene/ Tetracyanoethylene Charge-Transfer Complex: Toward a Self-Consistent Model. *J. Phys. Chem.* **1995**, *99*, 9017–9026.

(13) Kendrick, W. J.; Jirásek, M.; Peeks, M. D.; Greetham, G. M.; Sazanovich, I. V.; Donaldson, P. M.; Towrie, M.; Parker, A. W.; Anderson, H. L. Mechanisms of IR Amplification in Radical Cation Polarons. *Chem. Sci.* **2020**, *11* (8), 2112–2120.

(14) Dhamija, S.; Bhutani, G.; Jayachandran, A.; De, A. K. A Revisit on Impulsive Stimulated Raman Spectroscopy : Importance of Spectral Dispersion of Chirped Broadband Probe. *J. Phys. Chem. A* **2022**, *126*, 1019–1032.

(15) Liebel, M.; Schnedermann, C.; Wende, T.; Kukura, P. Principles and Applications of Broadband Impulsive Vibrational Spectroscopy. *J. Phys. Chem. A* **2015**, *119*, 9506–9517.

(16) Kukura, P.; Mccamant, D. W.; Mathies, R. A. Femtosecond Stimulated Raman Spectroscopy. *Annu. Rev. Phys. Chem.* **2007**, *58*, 461–488.

(17) Lee, S.-Y.; Zhang, D.; Mccamant, D. W.; Kukura, P.; Mathies, R. A. Theory of Femtosecond Stimulated Raman Spectroscopy. *J. Chem. Phys.* **2004**, *121*, 3632.

(18) Dietze, D. R.; Mathies, R. A. Femtosecond Stimulated Raman Spectroscopy. *ChemPhysChem* **2016**, *17*, 1224–1251.

CHAPTER 4

STRUCTURAL AND PHOTOPHYSICAL TEMPLATING OF CONJUGATED POLYELECTROLYTES WITH SINGLE-STRANDED DNA*

The ability of polythiophene to adopt different conformations can act as an advantage in directing its conformation in ways that could produce desired properties. Templating is the main strategy investigated in this doctoral dissertation and our focus is oriented towards the exploration of the templating effect of single-stranded DNA oligomers (ssDNA) on conjugated polyelectrolytes (CPEs), specifically on cationic polythiophenes. In this chapter, the main goal is to uncover the intermolecular interactions that direct the polymer backbone conformation and shed light on the key parameters that need to be considered for the design of an efficient template, as well as the structural aspects of cationic polythiophenes that contribute to the optimization of the self-assembly system. We aim to comprehensively characterize the optical behavior and structure of the polythiophenes in conformationally distinct complexes depending on the sequence of nucleic bases. From this study derives a detailed atomistic-level understanding of the structure−property correlations. We find that electrostatic and other noncovalent interactions direct the assembly with the polymer, and we identify that optimal templating is achieved with (ideally 10−20) consecutive cytosine bases through numerous π-stacking interactions with the thiophene rings and side groups of the polymer, leading to a rigid assembly with ssDNA, with highly ordered chains and unique optical signatures. Our insights are an important step forward in an effective approach to structural templating and optoelectronic control of conjugated polymers and organic materials in general. For this work we collaborated with Prof. Natalie Banerji' s research group (University of Bern), who conducted absorption, circular dichroism and transient absorption measurements and Prof. Ursula Rothlisberger's research group (EPFL), who performed molecular dynamics simulations.

---

*Adapted from the paper "Structural and Photophysical Templating of Conjugated Polyelectrolytes with Single-Stranded DNA" published in Chemistry of Materials **2020**, *32*, 7347−7362.

4.1 Introduction

Control over the conformation of functional molecules in order to tailor their optoelectronic properties has tremendous potential for technological applications, especially for organic π-conjugated polymers that have gained extensive interest over the past few decades.[1–5] In particular, the strong correlation of the photophysical properties of conjugated polythiophenes to their backbone conformation has been under intensive investigation.[6–10] The random-coiled form of conjugated polythiophenes is typically more favored in solutions and thin films, limiting the desired extended π-conjugation along the backbone. Strategies to induce extended backbone conformations range from chemical modification of the polymer (mostly the side chains),[11,12] to noncovalent approaches, such as control of the electronic coupling through processing protocols,[13] dilution within an inactive solid polymer matrix (polyethylene or polypropylene),[10] or supramolecular assembly with templating molecules. Templates under consideration include cyclodextrins[14–17] and polysaccharides[18] for the formation of rod-like inclusion complexes, as well as extending charged polythiophenes through electrostatic interactions.[9] Recently, nucleic acids (NAs) have emerged as particularly advantageous in directing molecular conformation, since they can conveniently induce a broad range of higher-order architectures in chiral nanoassemblies with unique and readily controllable properties.[19–22] Complexation of conjugated polymers with NAs is facilitated by the presence of charged side groups on the backbone of conjugated polyelectrolytes. The strong electrostatic interactions that develop between ssDNA and CPEs, together with more specific and directional supramolecular effects, allow precise manipulation of the CPE conformation. Moreover, intermolecular packing between polymer backbones is in this case removed due to strong assembly with ssDNA,[23] allowing access to the properties of isolated conducting polymer chains with superior ease compared to other methods.[10,16,24,25] In the present work, we focus on complexes of ssDNA with cationic poly(1H-imidazolium,1-methyl(-3-[2-[(4-methyl-3-thienyl)oxy}-ethyl]-chloride, abbreviated here as CPT (Figure 4.1). Cationic polythiophenes such as CPT are successful optical sensors of DNA chains in numerous biological assays,[26–28] whereby the strong conformational changes induced in CPT upon complexation with ssDNA are the lead cause for exquisite sensitivity.[29] Intriguingly, the previous biosensing work has revealed a tremendous impact of the ssDNA sequence on the conformational and optical response of the polymer.[30] The complex formed of CPT and homonucleotide oligocytosine (dC) strands (Table S4.1) is especially noteworthy. Here, the exceptionally high ratio of the first to second vibronic peaks in the absorption spectrum points to uncommon intrachain coherence in

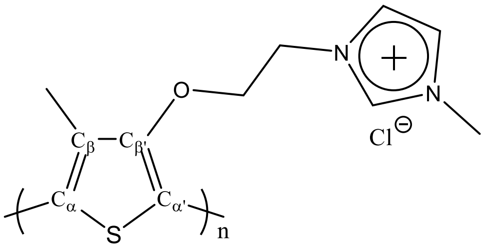

Figure 4.1. Molecular structure of cationic poly(1H-imidazolium,1- methyl-3-[2-[(4-methyl-3-thienyl)oxy]-ethyl]-chloride) (CPT).

highly ordered and extended chains.[30] To fundamentally understand the atomic-level interactions that direct this unique and very desirable templating effect, we combine stationary absorption, circular dichroism (CD) and resonance Raman (RR) spectroscopy with resonance Raman intensity analysis (RRIA) and molecular dynamics (MD) simulations. We compare different ssDNA sequences, different lengths of dC strands, and various side chains on the polythiophene backbone. This establishes the structure−property correlations that link the degree of order in the backbone, the chirality of the induced conformation, and the specific interactions that develop between the cationic polythiophenes and each ssDNA strand to the optical behavior of the complexes. Our study provides predictive understanding in an effective approach of structurally templating the optoelectronic properties of organic molecules.

4.2 Results and discussion

4.2.1 Optical response of CPT/ssDNA

The first crucial insights on the templating ability of ssDNAs were gained by placing the focus on the effect of ssDNA sequence to the optical properties of CPT. We correlate this to the CPT conformation in each complex. Figure 4.2 shows the stationary absorption of different CPT/ssDNA. The ssDNAs only absorb in the UV region,[31,32] where CPT also absorbs but to a lesser extent. On the other hand the signal in the visible region corresponds to the π−π* transition of the polymer,[33] illustrating the sensitivity of CPT backbone conformation on the ssDNA sequence. The tail of the absorption observed above the 650 nm is attributed to scattering effects, due to partial agglomeration that was observed to occur after ~20 min at high concentrations of all complexes (e.g. $1.5x10^{-4}$ M). In order to prevent agglomeration from affecting the results of the following spectroscopic methods, a new sample was prepared for long-lasting acquisition measurements (greater than 20 min).

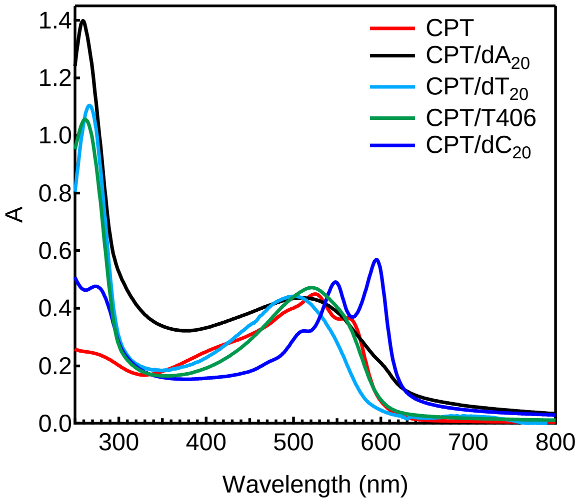

Figure 4.2. Absorption of CPT and its complexes with dA_{20} (black), dT_{20} (cyan), mixed sequence T406 (green) and dC_{20} (blue). All solutions were in PBS buffer with a concentration of $1.5x10^{-4}$ M (monomeric basis).

When dA_{20} is mixed with CPT at 20 °C (Figure 4.2), an unstructured broad band appears around 510 nm. This is different from the structured absorption band of CPT alone at 20 °C (also pictured in Figure 4.2), which was previously attributed to significant H-aggregation in relatively ordered chains.[33] This suggests that assembly with dA_{20} disrupts intermolecular CPT stacking but does not support ordering of the polymer chains. Indeed, the broadness of the band indicates an ensemble of disordered backbone conformations in the complex.[34,35] This is similar to the broad band at 398 nm of CPT alone at 55 °C, which was assigned according to the literature to random coiled chains at high temperature.[33] The strong red shift of disordered CPT/dA_{20} compared to disordered CPT alone is likely due to local environment effects (e.g., change in polarity) caused by the interactions with ssDNA.[34]

The absorption band of CPT/T406 and CPT/dT_{20} in the visible region is in both cases narrower than CPT/dA_{20}, which means that the polymer is less flexible in these complexes. A closer look at these two spectra reveals that in the case of CPT/T406 the spectrum is more structured, occupying the higher wavelength range (centered at 522 nm) compared to CPT/dT_{20} (centered at 501 nm), indicating that the polymer in CPT/T406 is more extended and planar than in CPT/dT_{20}.

In stark contrast to the absorption spectrum of CPT/dA_{20}, the spectrum of the CPT/dC_{20} complex shows a red-shifted absorption, strong vibronic structure and a predominant 0−0 transition at 594 nm (Figure 4.2), as generally observed for extended polythiophene chains with a large degree of order.[36,37] Here, the A_{0-0}/A_{0-1} ratio is 1.16 at 20 °C. This is, to the best of our knowledge, the highest ratio observed so far, even higher than for P3HT in nanofibers.[13] In addition, once formed, the CPT/dC$_{20}$ complex is very rigid, as the absorption band shape remains largely unaffected by temperature variations (e.g. at 55 °C, see Figure S4.1), in contrast to CPT/dA$_{20}$, as the absorption band blue-shifts as the temperature increases (Figure S4.2), verifying the conformational flexibility of CPT.

CPT/dA$_{20}$ and CPT/dC$_{20}$ were chosen to be studied more thoroughly, as we consider them to be the two extreme cases, based on the absorption studies, where the homonucleotide ssDNA sequence of dC$_{20}$ and dA$_{20}$ either strongly templates the CPT conformation (dC$_{20}$) or does not lead to significant ordering (dA$_{20}$) respectively.

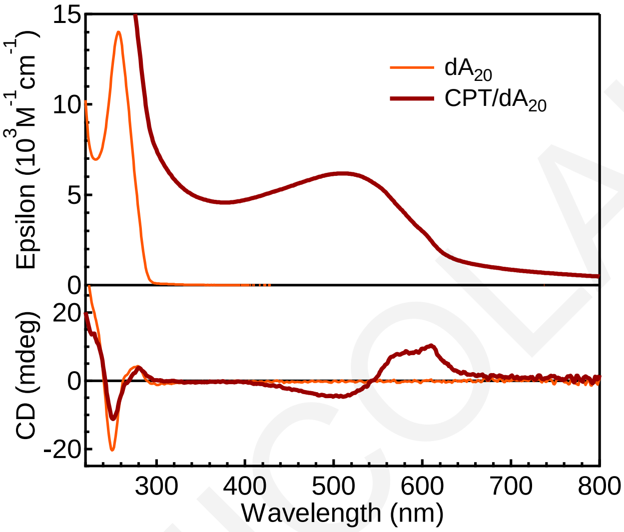

Figure 4.3. Experimental absorption (top left axis) and CD (bottom left axis) spectra of dA$_{20}$ (orange) and CPT/dA$_{20}$ (red) at 20 °C. All solutions were in PBS buffer with a concentration of 7.3x10^{-5} M (monomeric basis).

The chirality of these two complexes was investigated by CD spectroscopy, which measures the difference in the absorption of left-handed (LCP) (A_L) or right-handed circularly polarised (RCP) (A_R) light, following the equation, $\Delta\varepsilon = \varepsilon_L - \varepsilon_R = \frac{A_L - A_R}{lc}$. The characteristic CD signatures, are most commonly observed as bisignate signal, which is a couple of a positive and negative signal, called the Cotton effect. A (+/-) signal, where the positive signal is at longer wavelengths, while the negative one is at shorter wavelengths, originates from a right-handed twist between interacting chromophores. In an opposite way, a (-/+) signal (blue curve), is attributed to a left-handed helical structure. CPT/dA$_{20}$ at 20 °C shows a (+/−) CD signature (Figure 4.3) with a positive band centered at 593 nm and a negative band at around 500 nm (unlike achiral CPT alone, Figure S4.2), meaning that the complexation with dA$_{20}$ induces some chirality to the polymer with a preferential right-handed helical structure.[31,38–43] This conformation is however flexible and varies with temperature with simultaneous increase in chain disorder (blue-shift of absorption band) and disappearance of chirality (e.g. no evident CD signature in the visible region at 55 °C, Figure S4.2).[30] On the other hand, the CD signal due to dA_{20} in the UV region, indicating a right-handed helical conformation, changes only slightly upon complexation with CPT at any temperature, in agreement with the UVRR results below, implying that the secondary structure of dA_{20} is largely unaffected by assembly with CPT,[44] pointing to weak interactions in the complex.

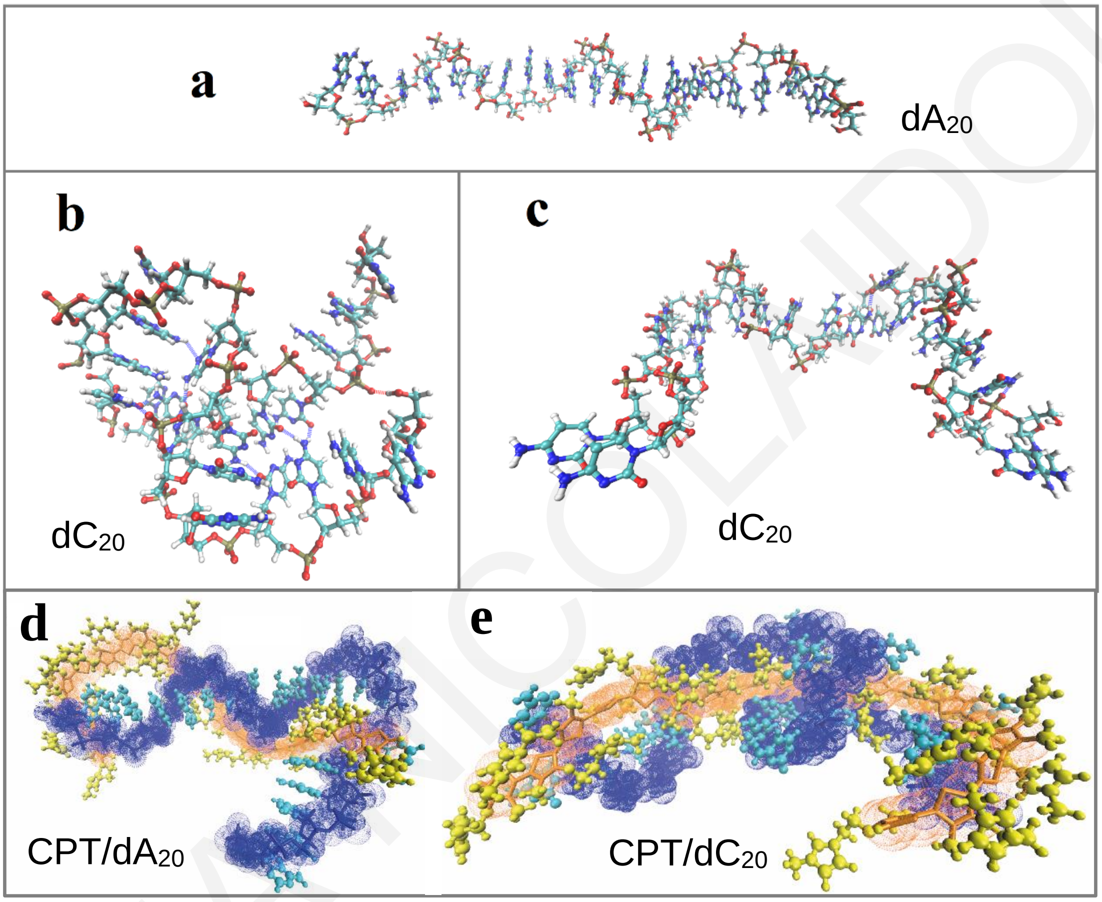

Figure 4.4. Representative structures of (a) single-stranded dA_{20}, (b and c) dC_{20} fragments where phosphorus atoms are in dark yellow, carbons in green, hydrogens in white, nitrogens in blue, and oxygens in red color. (d) CPT/ dA_{20} and (e) CPT/dC_{20} assemblies obtained by MD simulations. The ssDNA and the CPT chains in the complexes are represented as follows: i) CPT backbone: orange licorice surrounded by an orange dotted surface, ii) CPT side chains: yellow licorice, iii) DNA backbone (phosphate + sugar): blue licorice surrounded by a blue dotted surface, and iv) DNA bases: cyan licorice.

The experimental findings are strongly supported by MD simulations. Those show that dA_{20} either noncomplexed or when complexed with CPT, maintains a rigid conformation throughout the simulation, stabilized by stacking interactions between adenine bases (Figure 4.4a and close contact analysis (Figure 4.4d), in agreement with the literature[44,45]), while

CPT displays flexibility (in agreement with the broad unstructured absorption spectrum). In addition, MD runs show limited specific interactions between the polymer and dA_{20}.

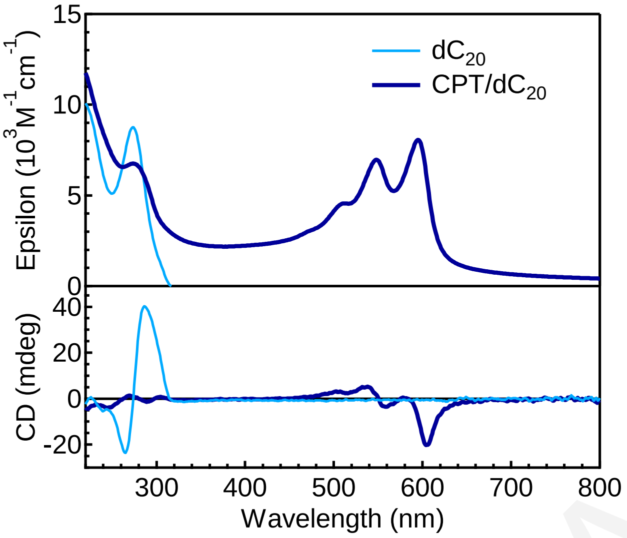

Figure 4.5. Experimental absorption (top left axis) and CD (bottom left axis) spectra of dC_{20} (cyan) and CPT/dC_{20} (blue) at 20 °C (complex formed at 55 °C). All solutions were in PBS buffer with a concentration of 7.3×10^{-5} M (monomeric basis).

Moreover, an induced CD signal due to CPT in a left-handed helical conformation appears in CPT/dC_{20} between 450 and 670 nm (Figure 4.5), suggesting the induction of different helical structures upon complexation with each of the ssDNA chains. The conformation of the ssDNA strand is also significantly affected in the complex. dC_{20} alone has a characteristic CD signal with a dominant positive band at 288 nm and a negative band at 265 nm, suggesting the presence of a moderate portion of i-motif structure (Figure 4.6), as expected for cytosine-rich DNA strands at pH 7.3. Cytosine-rich DNAs form an unusual quadruplex structure (“i-motif DNA”) consisting of two parallel-stranded intercalated duplexes, associated in head-to-tail fashion, made up of hemiprotonated base pairs. The i-motif formation is generally more important at slightly acidic pH (pKa ~ 6-6.5), when hemiprotonation of cytosines favors the formation of hydrogen bonds between them.[32,46,47] Therefore, this base pair is less stable at pH 7.3,[47] but as derived by CD measurements, this reduced stability at neutral pH does not prevent i-motif from partially forming. The portion of i-motif at different pHs was roughly calculated by probing the evolution of the ~290 nm peak intensity as a function of pH (assuming 100% i-motif formation for maximum ~290 nm intensity). As a result, we estimate that ~37% of dC_{20} strands form i-motif at the relevant conditions (pH 7.3). We also examined the effect of ionic strength on the stability of i-motif by estimating the i-motif fraction in the absence of salts, in the presence of 155 mM NaCl (as in PBS buffer) and in PBS buffer (Figure 4.6b). According to the CD spectra, the i-motif

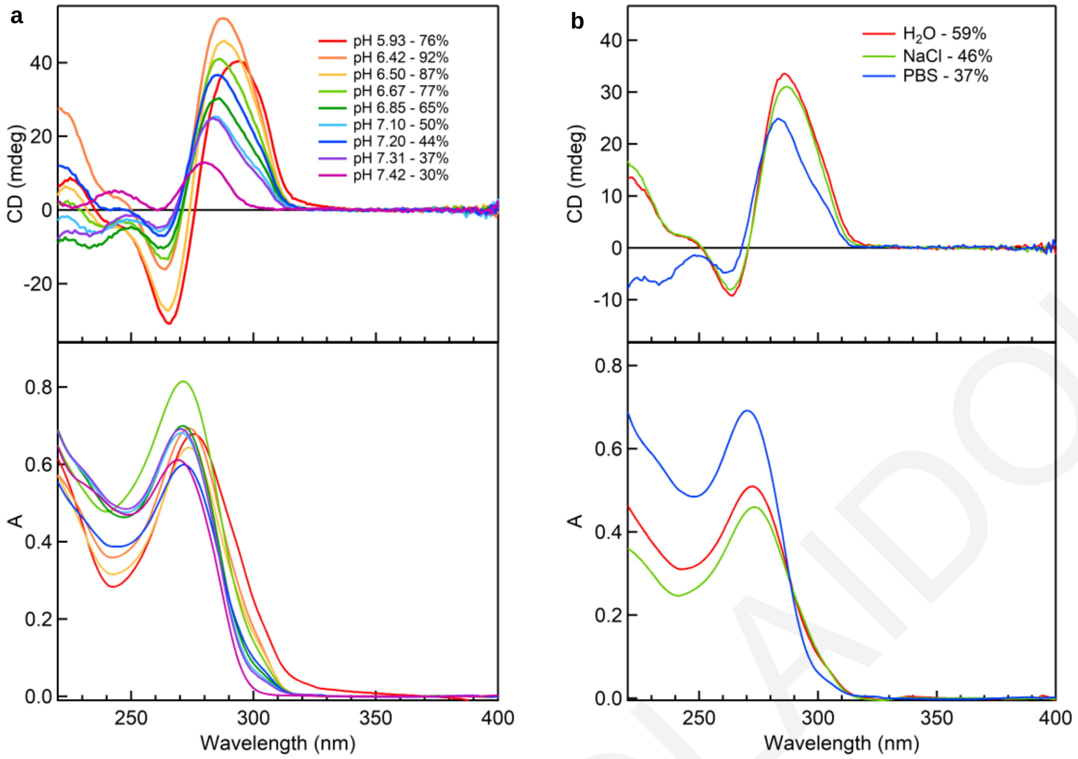

Figure 4.6. CD (top) and absorption spectra (bottom) of (a) pH titration of dC_{20} in PBS buffer and (b) at pH 7.3 in H_2O, NaCl and PBS buffer with calculation of the fraction of i-motif adopted by dC_{20}.

stability is decreased as the ionic strength increases. Thus, CD studies reveal that a mixture of secondary structures including i-motif must be present under the experimental conditions. This clarifies the flexibility of the conformation of dC_{20}, which renders cytosines available for involvement in non-covalent interactions with thiophene moieties. Ultimately, the CD feature of dC_{20} in the complex with CPT is dramatically changed (Figure 4.5), indicating that the strong assembly with CPT leads to the easy disruption of any secondary structure dC_{20} alone can adopt, forcing the ssDNA chain into a completely different conformation (see also UVRR results below). The absorption peak at 274 nm is also less intense in the complex, possibly due to hypochromism induced by a partial alignment of the transition dipole moments when the bases are stacked.[48] This phenomenon is known for double stranded DNA, which absorbs less compared to the denatured form.[49]

MD simulations show that dC_{20} has a high degree of flexibility and adopts several different structures, including both extended and compact configurations (Figures 4.4b, c), but the i-motif structure is not evidenced by MD simulations since the simulations were performed with fixed protonation states. Nevertheless, the mixture of secondary structures is theoretically demonstrated as well. This is in stark contrast to the more rigid dA_{20} and likely favours the assembly of dC_{20} with CPT.

4.2.2 Backbone planarity of CPT in the complexes CPT/ssDNA

A more in-depth experimental investigation of the backbone planarity of CPT upon complexation with the different ssDNA chains was achieved by using resonance Raman (RR) spectroscopy. Figure 4.7 presents the fingerprint region of the RR spectra of CPT complexes with visible excitation (for the extended range spectra, see Figure S4.3), which were normalized with respect to the intensity of the band at ~1487 cm^{-1}. At the used wavelengths (435.69, 473 and 532 nm), we are on resonance with the π–π* absorption of CPT, therefore we observe only contributions associated with vibrations of the conjugated polymer (mainly the thiophene backbone).

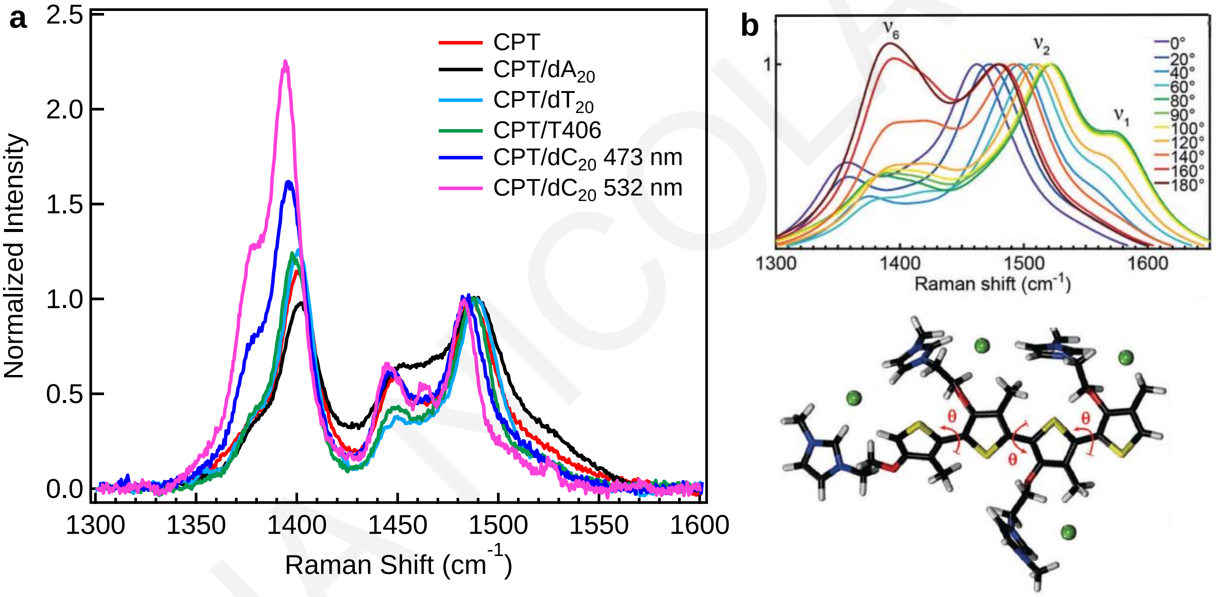

Figure 4.7. (a) Resonance Raman (RR) spectra with visible excitation at 435.69 nm for CPT/dT_{20}, at 473 nm for CPT, CPT/dA_{20}, CPT/T406 and CPT/dC_{20} and at 532 nm for CPT/dC_{20} in PBS buffer with a concentration of 1.5×10^{-4} M (monomeric basis) at 20 °C. (b) [†] Top: Raman spectra of the CPT tetramer computed at the B3LYP/6-31G* level; energies corrected using an empirical scaling factor for B3LYP (0.97). Geometries were optimized at the B3LYP-D3(BJ)/6-31G* level, keeping the three SCCS dihedral angles (θ) frozen at the color-coded value. Bottom: Geometry optimized at θ =160˚ with the "wobble" torsion mode indicated.

The deconvolution of the RR spectra is shown in Figure S4.4, and the band assignment is summarized in Table 4.1. The position, intensity, and line width of the Raman bands are strongly dependent on the ssDNA participating in the complex. In the case of CPT/ dA_{20}, the bands appear essentially at the same position as in the case of the polymer alone, while a 3-4 cm^{-1} downshift is observed in the case of CPT/dC_{20}. Moreover, the relative intensities of the C-C (~1400 cm^{-1}) and C=C (1487 cm^{-1}) stretches in CPT/dC_{20} are distinctly different than in the other complexes or the polymer alone, with the C-C intensity dominating.

The spectra are similar to the RR spectra of CPT that have been reported before and assigned based on DFT calculations.[33] According to these calculations, when the CPT conformation is characterized by high planarity (SCCS dihedral angle (θ)~ 0° or 180°, see Figure 4.7b), these are the main observations: 1) downshift of $C_\alpha=C_\beta$ symmetric stretch caused by the higher inter-ring electronic conjugation when adjacent thiophene rings become planar, thus weakening the $C_\alpha=C_\beta$ bond and decreasing its associated frequency, 2) sharper bands as fewer polymer segments of different conjugation lengths are involved (homogeneous distribution of conjugation lengths), 3) increase of $I_{C\text{-}C}/I_{C=C}$ Raman intensity ratio, (in agreement with computations for P3HT by Tsoi et al.[50]) and 4) a strongly enhanced shoulder observed experimentally at 1448 cm^{-1}.

Table 4.1. Comparison of the frequencies (cm^{-1}) of RR bands of pure CPT in various duplexes.

Frequency (cm^{-1})					**Assignment**
CPT	**CPT/dA_{20}**	**CPT/T406**	**CPT/dC_{20} $\lambda_{exc}=473$ nm**	**CPT/dC_{20} $\lambda_{exc}=532$ nm**	
1376	1378	1378	1376	1376	Mixed $C_\beta–C_{\beta'}$ and $C_\alpha–C_{\alpha'}$ stretching
1400	1400	1399	1397	1394	Mixed $C_\beta–C_{\beta'}$ and $C_\alpha–C_{\alpha'}$ stretching
1449	1448	1448	1448	1448	$C_\alpha=C_\beta$(O) ring stretching
1464	1465	1468	1464	1463	$C_\alpha=C_\beta$(Me) ring stretching
1487	1486	1487	1484	1484	$C_\alpha=C_\beta$(Me) ring stretching
1514	1518	1512	1510	1510	$C_\alpha=C_\beta$ ring stretching (anti)

Taken in conjunction with the downshifts in the bands, this signifies an increase in the electronic conjugation of the CPT backbone caused by a greater inter-ring planarity, demonstrating a more extended conformation for CPT in the CPT/dC_{20} complex.[33] The intensity of the C-C band increases further with excitation at 532 nm, due to resonance with even more planar and lower energy chain segments. In addition, the spectrum of CPT/dA_{20} exhibits broader line widths, showing inhomogeneity and torsional disorder of the CPT conformation. In contrast, the narrow peaks observed in the CPT/dC_{20} spectrum reflect the rigidity and homogeneity of the CPT conformation in the complex. The spectrum of CPT/T406 corresponds to an intermediate situation between the dA_{20} and dC_{20} complexes. CPT/dT_{20} spectrum is more similar with T406 complex but the broader linewidth and the blue shifted C=C band indicate again the larger disorder in the backbone of this complex.

With the help of MD simulations, the distribution of the S-C-C-S dihedral angles (between adjacent thiophene rings) was calculated for CPT alone and compared to the corresponding values in the two complexes (Figure S4.5 in Appendix). Overall, the occurrence of a dihedral angle corresponding to a planar conformation (around -180° or +180°) follows the trend CPT/dC_{20} $\gg$ CPT/dA_{20} > CPT alone, which agrees with the increased degree of planarity for CPT/dC_{20} witnessed by RR spectroscopy with visible excitation.

The aforementioned information extracted by RR spectroscopy enabled to address experimentally the ground state conformation of CPT in CPT/ssDNA complexes, through the interpretation of the RR spectra. Further exploitation of these spectra through RRIA, offers an initial glimpse of the structural impact of templating on the excited state behavior, especially for the extended CPT conformation in the complex with dC_{20}, as a starting point for assessing suitability for technological applications involving e.g. extended intrachain exciton delocalization or directional long-range exciton migration. Therefore, we use RRIA to evaluate the early-time excited state structural evolution of CPT in the various complexes in the Franck-Condon region, as the band intensities are associated with specific geometrical changes upon excitation.[51] RRIA requires first the quantification of resonance Raman cross sections (σ_R) (Section 3.2.1, Eq.2). The intensities of the Raman bands were determined by deconvolution (see Figure S4.4), due to spectral congestion, and the area of the Voigt peaks was subsequently calculated. The absolute σ_R's for all the RR bands of CPT were calculated for excitation at 473 nm for CPT/T406 and CPT/dA_{20} and at 532 nm for CPT/dC_{20} (Table 4.2), which is always ~1900 cm^{-1} to the blue side of the λ_{max} of the absorption spectrum.

Table 4.2. Absolute Resonance Raman cross sections for the major bands in the three complexes.

CPT/dA$_{20}$		**CPT/T406**		**CPT/dC$_{20}$ excitation at 532 nm**	
Frequency (cm^{-1})	**σ_R (x10^{-9}) (Å^2)**	**Frequency (cm^{-1})**	**σ_R (x10^{-9}) (Å^2)**	**Frequency (cm^{-1})**	**σ_R (x10^{-9}) (Å^2)**
885	0.27±0.07	886	1.39±0.28	885	3.34±1.80
968	1.45±0.41	959	2.30±0.58	977	4.62±2.62
1378	1.19±0.30	1378	3.45±0.96	1376	9.12±5.57
1400	12.24±2.46	1399	18.93±3.61	1394	21.68±10.25
1448	9.09±2.56	1448	6.07±0.63	1448	5.73±1.25
1465	1.87±0.77	1468	4.27±0.38	1463	3.26±1.33
1486	10.78±2.02	1488	10.56±1.62	1484	10.55±4.13
1518	3.98±1.91	1512	3.71±0.30	1510	0.83±0.23

These cross sections along with the absorption cross section for each complex were then simultaneously modeled (Section 3.2.2 Eq. 8 and 9). The fits to the absorption spectra are shown in Figure 4.8a-c, while Figures 4.8d and S4.6-S4.7 show the RR excitation profiles (REP's) for CPT in all the complexes, i.e. the calculated σ_R as a function of excitation energy.

A good fit was obtained for the red edge of the absorption spectra of the complexes (Figure 4.8a-c), with a corresponding excellent fit to the REPs of all the prominent bands in the RR spectra of the polymer (Figures 4.8d and S4.6-S4.7). Higher electronic transitions to higher singlet states or due to more disordered polymer populations were not included in the calculation, explaining the deviation from the blue side of the experimental absorption bands, which however did not affect the calculation of the REPs. Even though we choose to simplify the model used in this study, the parameters obtained still provide a self-consistent comparative picture of the conformational changes occurring in the three complexes.

The fitting parameters are reported in Table 4.3. The parameters used in the modelling include the ground and excited state frequencies (ω_g and ω_e) and the displacements (Δ) along each normal coordinate, the electronic transition dipole moment (M), the homogeneous (Γ) and inhomogeneous broadening (Θ) and the difference between the v = 0 in the ground and excited electronic states (E_{00}). We find that the C_β-$C_{\beta'}$ stretch exemplifies the highest displacement (Δ) in CPT/dC$_{20}$ compared to other modes, i.e. the largest change in bond length upon excitation, while the C_α=C_β symmetric stretch (also reflecting the transition

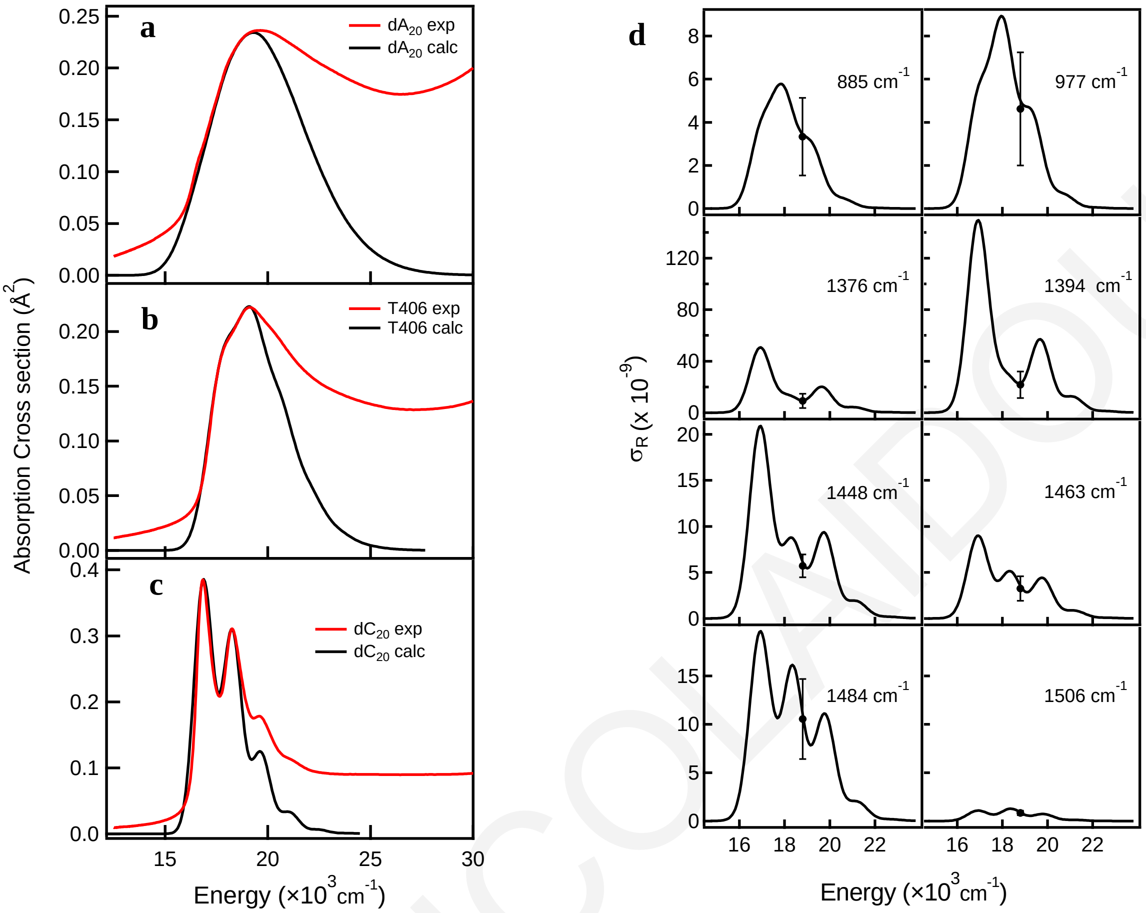

Figure 4.8. Experimental (red) and calculated (black) electronic absorption spectra of (a) CPT/dA$_{20}$, (b) CPT/T406 and (c) CPT/dC$_{20}$. (d) Calculated Raman excitation profiles (REPs) for the most prominent vibrational modes of CPT/dC$_{20}$ complex. The points with error bars denote the experimentally calculated absolute RR cross sections at 532 nm.

towards a quinoidal state) becomes increasingly important as we move from CPT/dC$_{20}$ to CPT/dA$_{20}$, with Δ about three times as large in the latter complex (Figure 4.9). The total reorganization energy, λ, calculated from mode-specific reorganization energies $\left(\lambda_{tot} = \sum \lambda_i = \sum_i \omega_i \frac{\Delta_i}{2}\right)$, also demonstrates a three times larger structural evolution on going from the ground to the excited state in the case of dA$_{20}$ (λ = 1119 cm^{-1} for dC$_{20}$, 1627 cm^{-1} for T406 and 3024 cm^{-1} for dA$_{20}$, see Figure 4.9). In addition, we see doubling of the inhomogeneous broadening from 450 cm^{-1} (56 meV) in CPT/dC$_{20}$ to 900 cm^{-1} (112 meV) in CPT/dA$_{20}$, indicating the larger number of energetic sites available due to conformational disorder. Simultaneously, an increase in the homogeneous broadening from 45 cm^{-1} in CPT/dC$_{20}$ to 100 cm^{-1} in CPT/dA$_{20}$ corresponded to a decrease in total dephasing from 118 to 53 fs, which includes contributions from excited state lifetime and pure dephasing (e.g. due to collisions with the solvent). This illustrates an overall larger conformational rearrangement in response to the change of electron density in the excited state for the more flexible complexes, where our RR measurements and the MD simulations show that the polymer is less tightly bound to the ssDNA and the CPT conformation is less planar in the ground state with more torsional disorder.

Table 4.3. Parameters used in the RRIA for the three complexes of CPT.

Transition	ω_g (cm^{-1})	ω_e (cm^{-1})	Δ_k	ω_g (cm^{-1})	ω_e (cm^{-1})	Δ_k	ω_g (cm^{-1})	ω_e (cm^{-1})	Δ_k	ω_g (cm^{-1})	ω_e (cm^{-1})	Δ_k
		CPT/dC_{20} (20ºC)			CPT/dC_{20} (55ºC)			CPT/T406			CPT/dA_{20}	
ν_1	885	885	0.14	885	885	0.13	885	885	0.12	885	885	0.055
ν_2	977	977	0.17	977	977	0.16	969	969	0.16	968	968	0.125
ν_3	1376	1376	0.56	1376	1376	0.54	1378	1378	0.38	1378	1378	0.31
ν_4	1394	1394	0.93	1394	1394	0.94	1399	1399	0.97	1400	1400	1.11
ν_5	1448	1448	0.40	1448	1448	0.35	1448	1448	0.59	1448	1448	1.00
ν_6	1463	1463	0.25	1463	1463	0.23	1468	1468	0.46	1465	1465	0.48
ν_7	1484	1484	0.38	1484	1484	0.33	1488	1487	0.70	1486	1486	1.11
ν_8	1510	1510	0.11	1510	1510	0.09	1512	1512	0.40	1518	1518	0.60
Γ (cm^{-1})		45			45			85			100	
Θ (cm^{-1})		480			450			755			900	
E_{00} (cm^{-1})		16875			16900			17900			16650	
M (Å)		0.822			0.87			0.881			0.975	

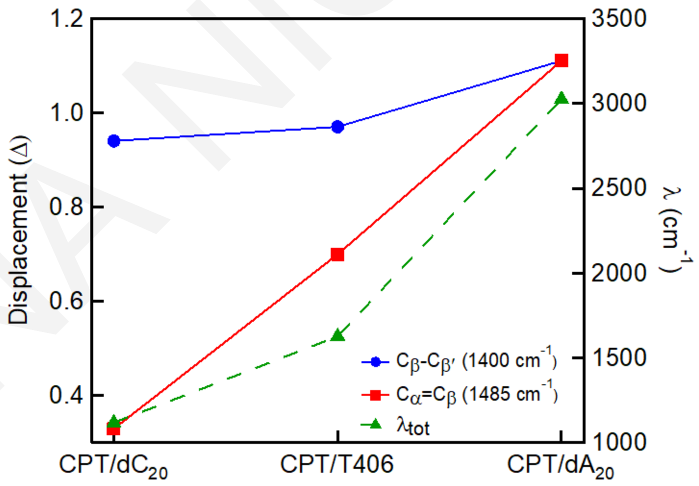

Figure 4.9. Dependence of the displacement (Δ) along the C_β-$C_{\beta'}$ and C_α=C_β normal coordinates on the CPT/ssDNA complex, as obtained from modeling the absorption and Raman cross sections.

4.2.3 Atomistic-level details of the CPT-ssDNA interactions

As already shown above, dA_{20} does not induce strong conformational changes in CPT, while dC_{20} leads to a tighter structure for the CPT/dC_{20} complex, with pronounced optical signatures of the polymer. To understand this selective response to different ssDNA bases, we have investigated the atomistic-level interactions in the complexes, concerning 1) intra-DNA interactions, 2) intra-CPT interactions between thiophenes (backbone) and/or side chains and 3) CPT/DNA interactions (between groups of the nucleobases and CPT). This is experimentally studied through RR spectroscopy with excitation in the UV (266 nm), which interrogates structural changes that occur in the various ssDNAs upon complexation with CPT. Also, a theoretical evaluation was achieved through MD simulations.

Figure 4.10 presents the UVRR spectra of each ssDNA alone and in the complex (extended spectral range in Figure S4.8). The spectra of the ssDNAs are similar to those previously reported (see Tables 4.4 and S4.1 for the assignment of the main bands).[52–55] Characteristic bands of ssDNA are associated with in-plane vibrational modes of the base rings and exocyclic bonds. Sugar and phosphate vibrations are not enhanced at this excitation wavelength and are therefore not identified in the UVRR spectra. As reported in the past,[45] the vibrational bands in the UVRR spectra of NAs are highly sensitive to structural changes.

Table 4.4. Frequencies (cm^{-1}) and assignments of dominant RR bands in UVRR spectra of ssDNA.

dA_{20}		**dC_{20}**	
Frequency (cm^{-1})	**Assignment[1]**	**Frequency (cm^{-1})**	**Assignment**
1258	N1C6, C6N6	1246	δC6H, C4N4
1309	N9C8, N3C2, δC8H, δC2H	1297	N1C6, C5C6
1338	N7C5, C8N7	1381	C4N4, N1C2
1377	C1N9, C6N6	1532	N3C4, N1C2
1425	C4N9, δC8H	1618	δNH_2, C4N4
1484	δC2H, N9C8, δC8H	1656	C2O, C2N3
1506	N7C8		
1581	C5C4, C4N3		
1603	δNH_2, C5C6, C6N6		

[1] Stretching vibrations, unless denoted δ (bending vibrations)

Thus, the great similarity displayed between the Raman spectra of dA_{20} and CPT/dA_{20} reflects the resistance to deformation due to the intrinsic rigidity of single-stranded dA_{20}, which is stabilized by the stacking interactions between adenine bases.[44,45] This is confirmed through MD simulations, which show that the pronounced intra-DNA π-stacking (between neighboring adenine bases) prevail over the stacking between the ssDNA and CPT units (adenine-thiophene/imidazole), leading to conformational flexibility of CPT in the complex.[56]

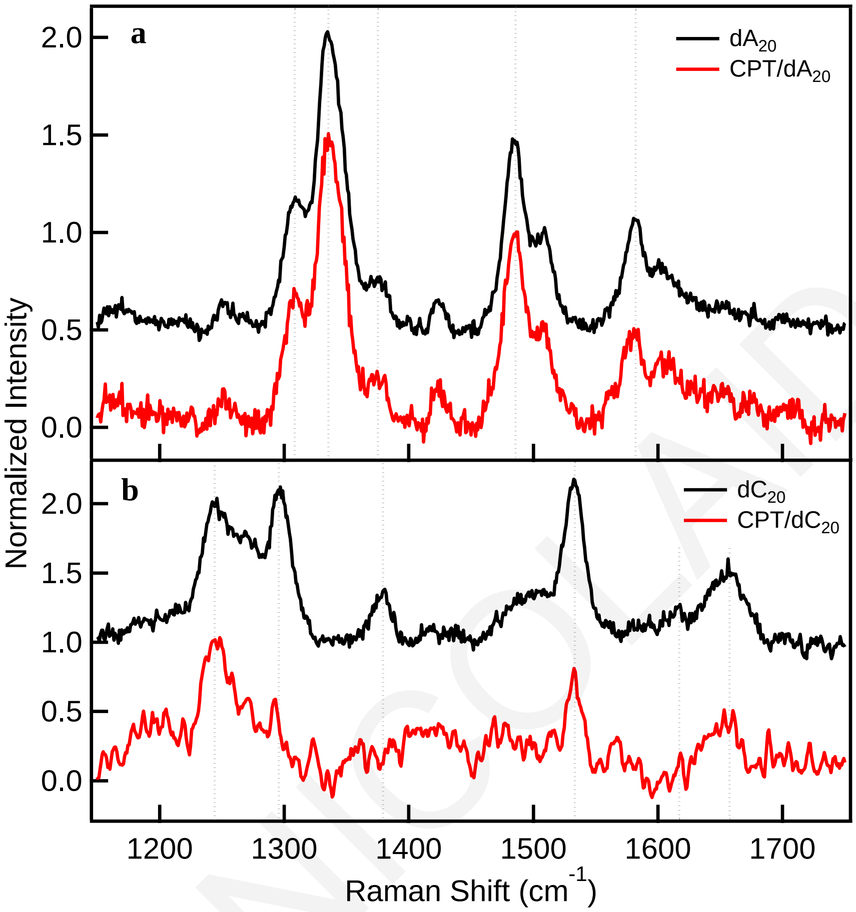

Figure 4.10. UVRR spectra of (a) dA$_{20}$ and CPT/dA$_{20}$ in PBS buffer with a concentration of $1.5 \cdot 10^{-4}$ M and (b) dC$_{20}$ and CPT/dC$_{20}$ in PBS buffer with a concentration of $3 \cdot 10^{-4}$ M (monomeric basis) at room temperature with excitation at 266 nm (normalized with respect to the intensity of the band at ~1484 and ~1246 cm^{-1} respectively).

In contrast, the Raman bands at 991, 1297, 1381, and 1532 cm^{-1}, which correspond to vibrational modes of cytosine localized near the glycosidic bond, experience an intensity decrease when dC$_{20}$ assembles with CPT (Figures 4.10 and S4.8). Previous work has shown that those base vibrations are affected by the deoxyribose ring puckering and the glycosidic bond orientation defined by the torsion angle (χ).[45,57–59] The conformational sensitivity of the in-plane base vibrations derives from vibrational coupling with the adjacent C(1′)-H bend from the deoxyribose ring (see Figure 4.11a). Therefore, the intensity changes observed are likely associated with a transition in sugar puckering and alteration of the dihedral angle between the base ring and the sugar induced by specific interactions between dC$_{20}$ and CPT that are absent in CPT/dA$_{20}$. Indeed, according to our MD analysis, the distribution of dihedral angles between the base and the sugar for dC$_{20}$ alone and assembled with CPT shifts by 20°

(Figure 4.11d), while no such difference is seen for the sugar-base dihedral angle of dA_{20} (Figure 4.11c). Moreover, the MD close contact analysis shows that strong π-stacking develops between the cytosines of dC_{20} and the thiophenes and imidazoles of CPT (Figure 4.12).[56] These π-stacking interactions are responsible for the modification in the deoxyribose ring puckering and/or twist of the glycosidic bond. They are also the main

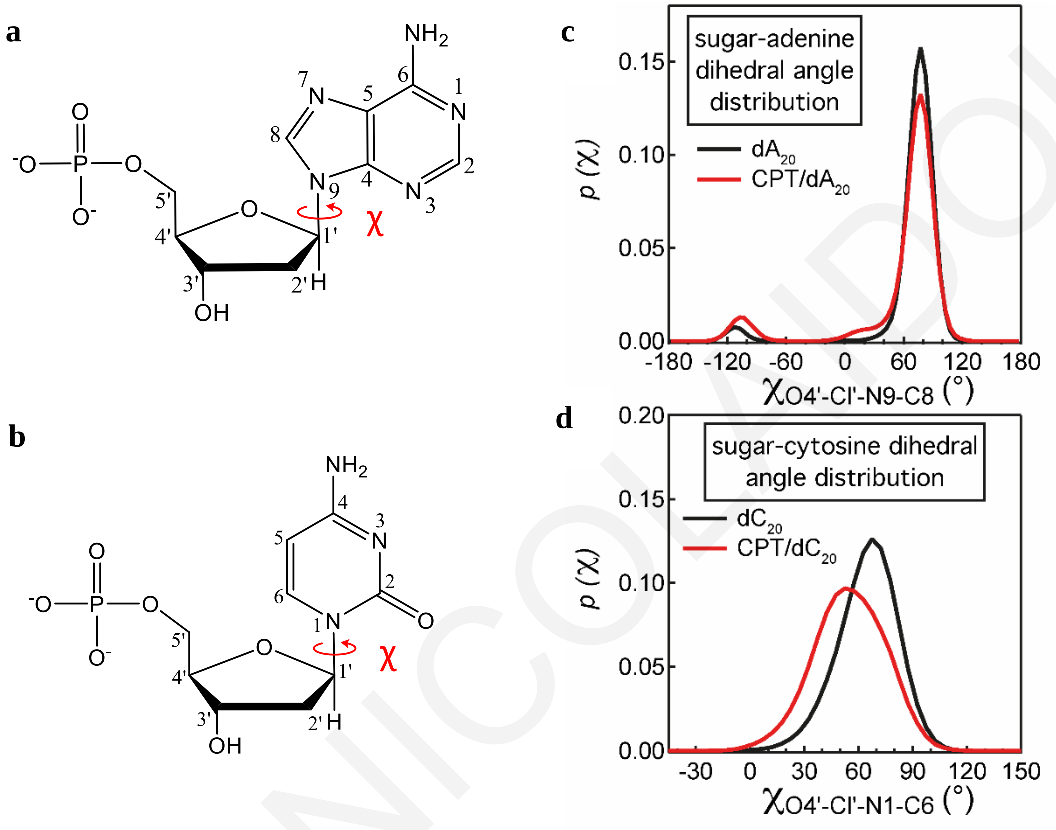

Figure 4.11. Structure of the deoxyribonucleotides of (a) adenine and (b) cytosine in which the glycosidic torsional angle χ is depicted, defined by O4′-C1′-N9-C8 atoms for deoxyadenosine and O4′-C1′-N1-C6 atoms for deoxycytidine. (c-d) Distributions of the dihedral angle between the sugar (deoxyribose) and the base in ssDNA alone and assembled with CPT obtained by the MD simulations ((c) adenine in dA_{20} and (d) cytosine in dC_{20}).

reason for the important differences observed between the CPT/dC_{20} and CPT/dA_{20} complexes. As depicted in Figure 4.12, the cytosines stack with every other thiophene in the sequence, due to the long distance between bases imposed by the phosphodiester bond. The close contact analysis also shows that nucleobase-imidazole interactions in CPT/dC_{20} are much more abundant than in CPT/dA_{20}.[56] Both π−π interactions thus play a decisive role in defining the compact structure of CPT/dC_{20} and are further complemented by thiophene−imidazole stacking within the CPT backbone (Figure 4.12). Intra-DNA cytosine stacking in dC_{20} is not as strong as the adenine interactions in dA_{20} [56,60,61] rendering the cytosines available for π-stacking with the thiophenes and imidazoles from CPT. Moreover, the MD close contact analysis demonstrates a significant decrease in cytosine stacking once CPT is added.[56] Any secondary structure that dC_{20} can adopt on its own is thus disrupted, and the ssDNA chain is forced into a different conformation during complex formation as attested by the CD signature in the UV and UVRR (see Figures 4.5 and 4.10). The UVRR spectra of T406 at Figure S4.8b (assignment of the main bands, Table S4.1) show a distinct similarity with dA_{20} (Figures 4.10a and S4.8a) and again no conformational changes are observed upon complexation with CPT. Adenosines and cytosines constitute the larger part of T406 sequence in equal amount (Table 4.5, Figure 4.17), so it is expected that the contribution of these nucleotides to the spectra to be larger. Nevertheless, cytosine bands do not appear in these spectra and we observe modes attributed mainly to adenosine. This is due to the fact that adenosines exhibit higher extinction coefficient at this wavelength and consequently their bands are enhanced to such an extent that they overshadow cytosine bands, which appear at similar wavenumbers. As a result, no significant changes are observed between the spectra of the oligonucleotide and the duplex, since any expected changes due to interaction of the polymer with the cytosines cannot be distinguished.

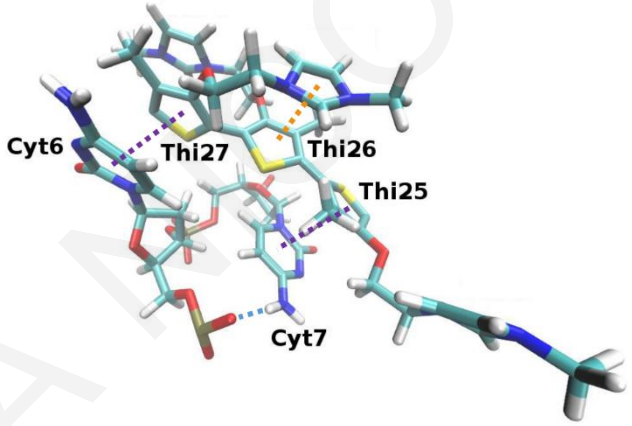

Figure 4.12. Image of non-covalent interactions occurring between CPT and dC_{20} as observed in MD simulations. π-stacking interactions between cytosine and thiophene rings are shown in purple dotted lines, while stacking interactions between the imidazole group from a neighbouring thiophene and a thiophene ring are shown in orange. A hydrogen bond between the N-H proton from the cytosine and the oxygen from a phosphate group is also apparent in this snapshot (cyan dotted line).

MD simulations show numerous electrostatic interactions between the negatively charged phosphate groups of the ssDNA and the positively charged imidazole side-chains of CPT. The MD simulations also display limited CPT-DNA H-bonds in each CPT/ssDNA complex. Intra-DNA H-bonding interactions in dA_{20} are also negligible, while in dC_{20} commonly occur in conjunction with cytosine-thiophene stacking interactions, as depicted in Figure

4.12, contributing to the overall conformational stability of CPT/dC_{20}.[56] Moreover, chalcogen bonds within CPT, between the sulfur atoms of the thiophenes and the oxygen atoms of the alkoxy side chains,[62] are found to have a negligible effect.[56] Thus, electrostatic interactions are crucial to bringing the CPT and ssDNA strands together and play a significant role in both the CPT/dA_{20} and CPT/dC_{20} complexes. This agrees experimentally with the efficient assembly of CPT with both ssDNA strands, evidenced by the different optical properties and polymer conformation of each CPT/ssDNA complex. Nevertheless, the limited π-stacking and H-bonds in CPT/dA_{20} reveal that electrostatic interactions are principally responsible for the assembly of CPT/dA_{20}, but are unable to induce rigidity to the CPT conformation. On the other hand, the numerous stacking interactions of CPT/dC_{20}, are the key ingredient to structurally direct CPT into a rigid and more planar conformation.

4.2.4 Effect of dC length on CPT/dC complex formation

Since the cytosines of the ssDNA strand stack with every second thiophene of CPT (Figure 4.12), this suggests that consecutive sequences of cytosines favor maximal π-stacking occurrence and chain extension. We thus investigate what length of dC induces the best templating of CPT, which consists of an average of 42 thiophene units (estimated using the number-averaged molecular weight, Mn). Absorption and CD spectra of CPT complexed to dC strands of 5 to 80 bases (Table 4.6) show that the strong templating effect is observed for ssDNA oligomers with 10 units or more, yielding the characteristically structured absorption and CD spectra of CPT at a thiophene/nucleobase ratio of 1:1 (maximal A_{0-0}/A_{0-1} ratio and induced CD signal of CPT between 450 nm and 670 nm, result of the superposition of several distinct (-/+) CD signals, one for each vibronic peak, see Figure 4.13). However, for longer ssDNA segments (dC_{40}, dC_{80}), the assembly over the entire length is more challenging, as illustrated by the reduced A_{0-0}/A_{0-1} ratio. This might be due to increased intra-DNA interactions for longer chains, as their CD signal in the UV region before and after complexation is similar but with reduced ellipticity (Figure 4.14), meaning that their initial secondary structure does not completely unfold upon interaction with CPT, thus part of the DNA does not complex with CPT. Moreover, we find that complex formation with dC_5 is rather slow and unfavourable, requiring excess ssDNA (2.25 cytosine monomers for 1 thiophene unit) and leaving the solution for 1 day to be completed due to modified cooperativity. Figure 4.15b shows a plot of the normalized CD signal at 604 nm as a function of dC concentration for the various dC lengths. We observe differences in the slope of the sigmoidal curve as a function of dC length, alluding to a change in the cooperativity of the system, which can explain the slower complex formation in the case of dC_5.

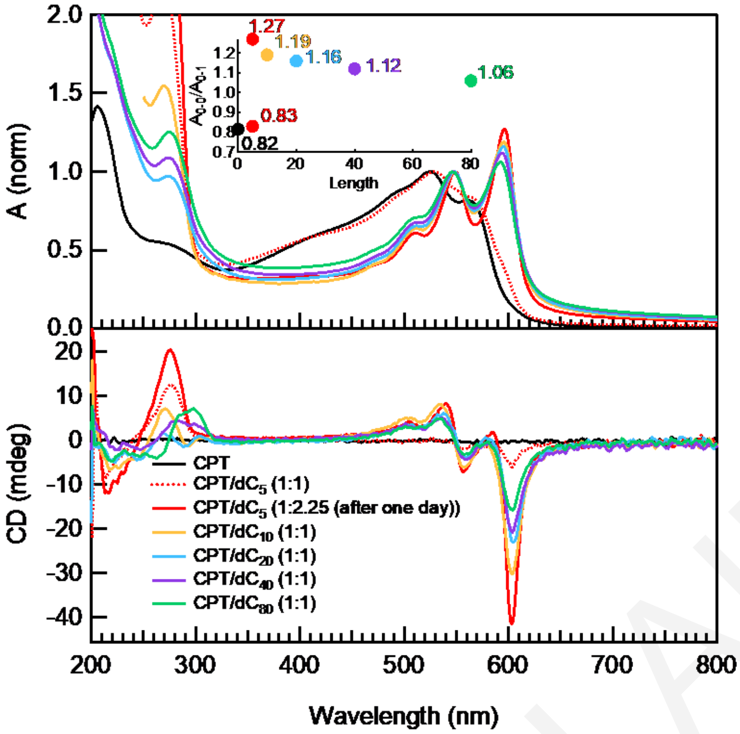

Figure 4.13. Stationary absorption and CD spectra of CPT complexed to dC strands of 5, 10, 20, 40 and 80 nucleobase units at 20°, obtained by adding monomeric equivalence of the ssDNAs to a solution of CPT in PBS buffer (7.3x10^{-5} M, monomeric basis). The inset shows the A_{0-0}/A_{0-1} ratio of the CPT absorption band as a function of dC length.

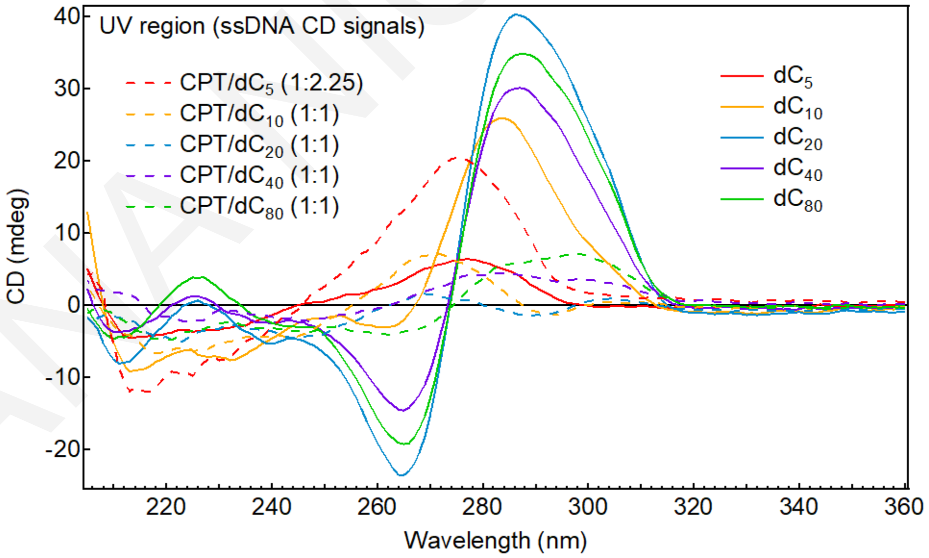

Figure 4.14. CD spectra of the different dCs (solid lines) and the corresponding CPT/dC complexes (dashed lines) in PBS at 20 °C. The spectra are zoomed in the UV region to show the CD signals that are mainly from dCs (even though an induced CD signal from CPT and possible coupling or charge transfer to the ssDNA cannot be completely excluded). Concentration: 7.3·10^{-5} M (monomeric basis of cytosine bases for dCs alone and of CPT for CPT/dCs).

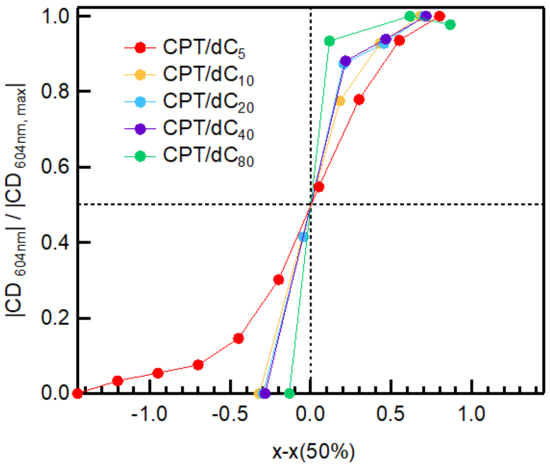

Figure 4.15. Normalized CD signal as a function of the dC equivalents titrated in CPT solution for the various dC lengths. The x axis has been shifted relative to the position of 50% CD signal.

Titrating concentrated CPT into a dilute dC$_5$ solution (Figure 4.16a) (instead of vice versa) does not lead to any templating (while the titration order is irrelevant for the longer dC chains, Figure 4.16b), highlighting the inability of the short dC$_5$ chains to disrupt CPT aggregates in the concentrated stock solution used for the titration. Finally, complexes with dC$_{10}$ and dC$_{20}$ display the highest A_{0-0}/A_{0-1} ratio (Figure 4.13), denoting the most effective templating, while the CD signal of these oligonucleotides in the UV region (Figure 4.14) changes after complexation, showing that complex formation alters completely the ssDNA conformation, as also confirmed from our MD simulations and the UVRR data. Therefore, we suggest that 10-20 nucleobase units are ideal to wrap around segments of CPT forming a compact structure via mainly electrostatic and π-stacking interactions as shown in Figure 4.4e, leading to significant local ordering and intrachain coherence.

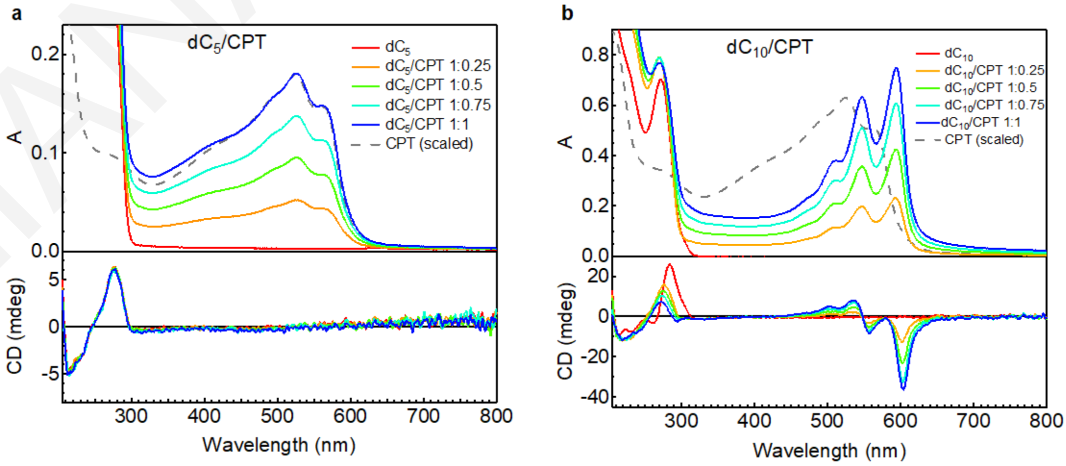

Figure 4.16. Absorption and CD spectra of (a) dC$_5$ and (b) dC$_{10}$ with different relative amounts of CPT (in PBS buffer with a dC concentration of $7.3 \cdot 10^{-5}$ M, monomeric basis, 20 °C). The scaled absorption spectrum of CPT alone is added as reference (dashed grey line).

4.2.5 Generalization to other ssDNA and polythiophene systems

Having understood the specific interactions that induce characteristic conformations in complexes of CPT with dA_{20} and dC_{20}, we generalize our findings to different homonuclear and mixed ssDNA sequences, as well as to thiophene polyelectrolytes carrying different side chains. We confirm that the CPT/dC_{20} combination is the most effective in templating an extended polymer conformation. The absorption spectra of CPT complexed to different ssDNA sequences (20-base length) are shown in Figure 4.17. The homonucleotides dT_{20} and dG_{20} cause weak templating similar to dA_{20}, while dC_{20} stands out from all other investigated sequences. The behavior of dT_{20} agrees with previous work and with our RR measurements (Figure 4.7), which indicate that thymine bases do not stack strongly with thiophenes, possibly due to the extra methyl group compared to cytosine.[31] The templating strength of mixed ssDNA oligomers (Table 4.5) is highly variable and does not necessarily correlate with the number of cytosines in the sequence. For example, the assembly of CPT with d[$(TTCC)_5$] (50% cytosine bases) leads to unstructured and blue-shifted absorption of CPT, possibly due to the weak stacking of the intermittent cytosine pairs with thiophenes, or due to strong intra-DNA interactions. This confirms that the excellent templating of dC_{20} via extended cytosine-thiophene stacking relies on consecutive cytosine sequences, not just pairs interspersed between other bases. Nevertheless, for biologically more relevant sequences containing the four natural DNA bases in random order (T406 and T406RC, with 30% and 10% cytosines, respectively),[30] an intermediate templating effect can be achieved, with an optical response between those of CPT/dA_{20} and CPT/dC_{20} (Figure S4.9 for

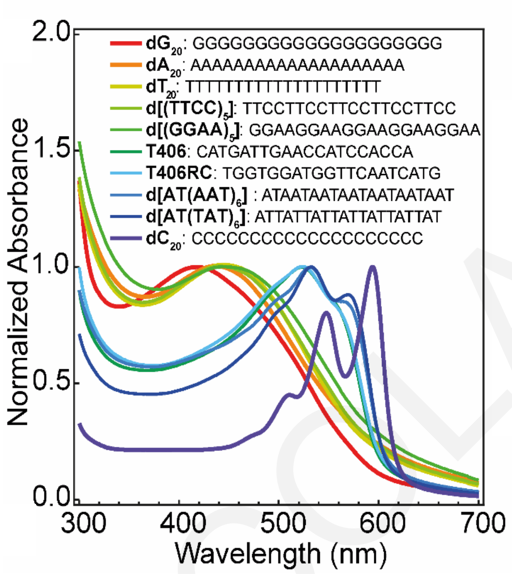

Figure 4.17. Absorption spectra of CPT complexed to various 20-base ssDNA strands (sequences shown in the legend) at 55 °C.

CPT/T406 and 4.17). The visible RR spectrum of CPT/T406 in Figure 4.7, shows that the polymer adopts a more ordered conformation in the relatively rigid complex with T406 but does not reach the level of CPT/dC_{20}. Interestingly, d[(AT(TAT)$_6$] and d[AT(AAT)$_6$], that contain adenines separated by thymines (but no cytosines), result in a more structured absorption spectrum than T406 when complexed with CPT. We suggest that the adenines π-stack in this case with CPT, since our MD simulations evidence some adenine-thiophene stacking in CPT/dA_{20}, which competes with strong interactions between the adenine bases.[56] Disruption of the adenine-adenine stacking by the thymine bases in d[(AT(TAT)$_6$] and d[AT(AAT)$_6$] can therefore explain the better complexation with CPT. However, having guanine bases between adenine pairs (d[(GGAA)$_5$]) does not lead to the same effect, showing the intricate interplay of ssDNA-CPT and intra-DNA interactions that leads to efficient conformational templating in the complexes.

With the aim to examine whether the interactions responsible for templating in the CPT/dC_{20} system can extend to other thiophene polyelectrolytes, we chose two other polymers that were previously studied in DNA complexes[31,38,63,64] (Figure 4.18). P3HT-Im and P3HT-PMe_3 have different cationic side groups (phosphonium and imidazole, Figure 4.18a), which are attached to the $C_{\beta'}$ position of the thiophene backbone via a six-carbon chain (without the oxygen atom present in CPT). Moreover, the methyl group from the C_β position is missing. Even though the counterion in these polymers is bromide, its concentration is 4 orders of magnitude lower than the chloride concentration in the PBS buffer, and therefore was not considered to affect the conformation of the polymer. The RR spectra of these two polymers resemble the well-known P3HT Raman spectrum,[13,65] but differ from the one of CPT, where the C=C stretching mode is split due to alkoxy substitution at the $C_{\beta'}$ position.[65,66] According to the literature, a more prominent peak around 1378 cm^{-1} (C-C stretching mode), a red-shift of the C=C symmetric stretching band toward ~1450 cm^{-1}, a reduction of the full-width-half-maximum (fwhm) of this C=C mode and a less prominent peak at ~1520 cm^{-1} (antisymmetric stretching mode of C=C) are all indications for a more planar P3HT backbone. These characteristic changes are most pronounced for both complexes of P3HT-PMe_3 and P3HT-Im with dC_{20}, while dA_{20} has the opposite effect on the conformation of each polymer (broad RR bands, less intense C-C peak, C=C mode shifted to higher wavenumbers, Figure 4.18a, b).

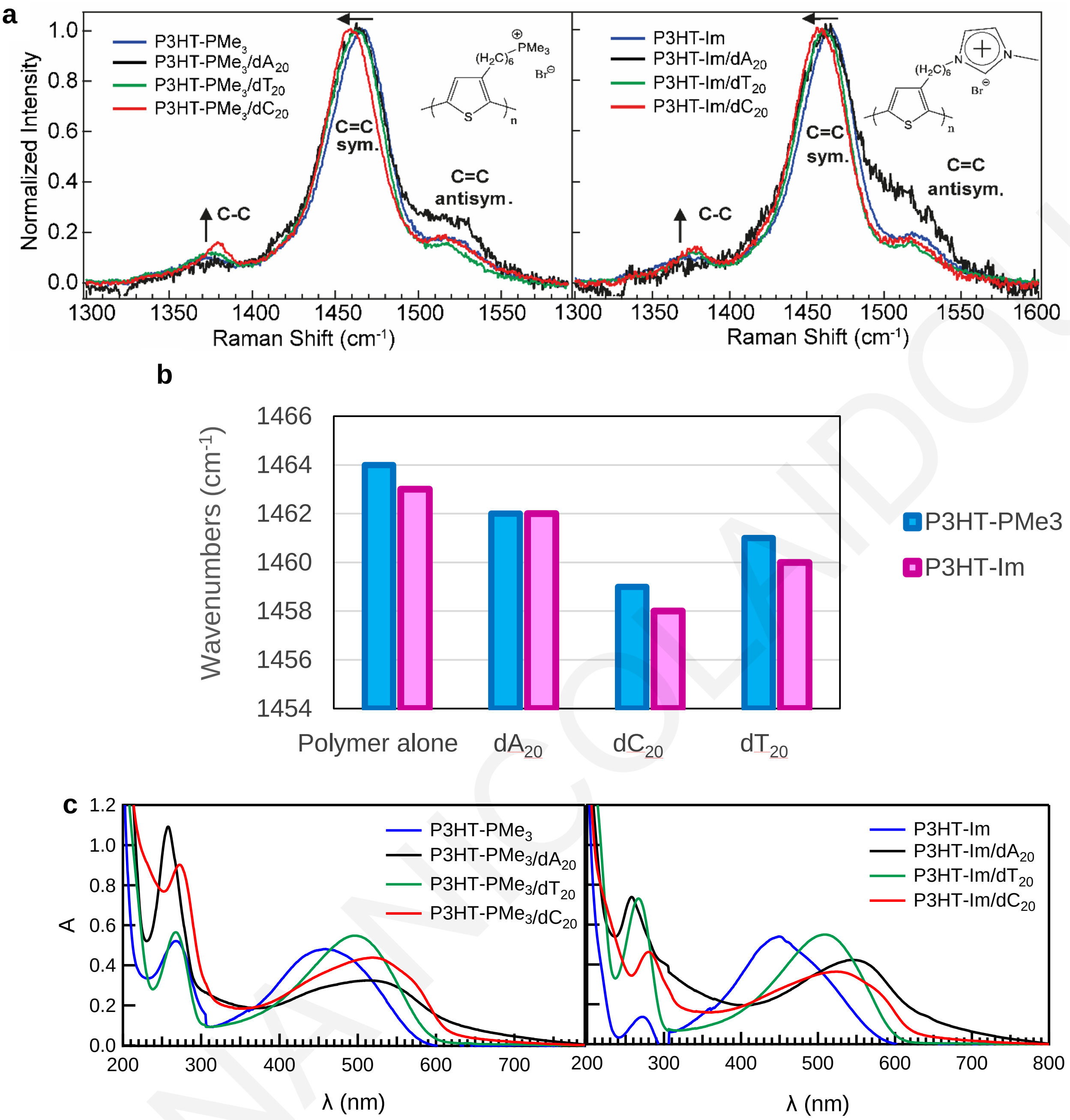

Figure 4.18. (a) RR spectra normalized with respect to the intensity of the band at ~1460 cm^{-1} with excitation at 473 nm for (left) P3HT-PMe$_3$ or (right) P3HT-Im (blue) and its complexes with dA$_{20}$ (black), dT$_{20}$ (green) and dC$_{20}$ (red) in PBS buffer with a concentration of 1.5x10^{-4} M (monomeric basis) at room temperature. (b) Graphical comparison of the wavenumbers of C=C symmetric band of P3HT-PMe$_3$ (blue) or P3HT-Im (magenta) and its complexes with dA$_{20}$, dC$_{20}$ and dT$_{20}$ extracted from the corresponding RR spectra. (c) Absorption spectra of (left) P3HT-PMe$_3$ or (right) P3HT-Im (blue) and its complexes with dA$_{20}$ (black), dT$_{20}$ (green) and dC$_{20}$ (red) in PBS buffer with a concentration of 1.5·10^{-4} M (monomeric basis) at room temperature.

UVRR spectra of dC_{20} with these polythiophenes display an intensity decrease of the bands 1297 cm^{-1}, 1381 cm^{-1} and 1532 cm^{-1}, (Figure 4.19) upon complexation with CPT. It is possible that, as in the case of CPT, the changes are mostly associated with π-π stacking interactions between cytosines and thiophenes, which induce the conformational changes in dC_{20}. Furthermore, a red-shift observed in the 1656 cm^{-1} mode, assigned to the carbonyl group of cytosine, must be related to some interaction of the oxygen, possibly a hydrogen bond, causing the C=O bond to be elongated. This shift is observed in both complexes (P3HT-Im/dC_{20} and P3HT-PMe$_3$/dC_{20}).

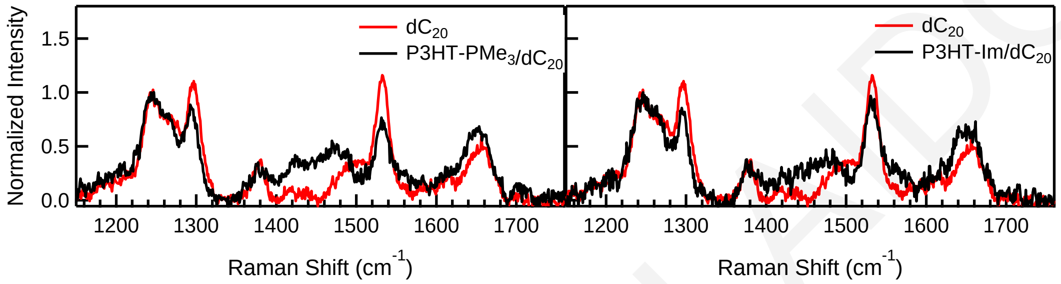

Figure 4.19. UVRR spectra of dC_{20} alone and assembled with (a) P3HT-PMe$_3$ and (b) P3HT-Im.

However, even though the effect of the ssDNA sequence on the conformation of the polymer is similar across a variety of cationic polythiophenes, with dC_{20} having the largest tendency to enhance backbone torsional order, its templating ability is significantly reduced with P3HT-Im and P3HT-PMe$_3$ (see absorption spectra, Figures 4.18c and 4.20). Their weak

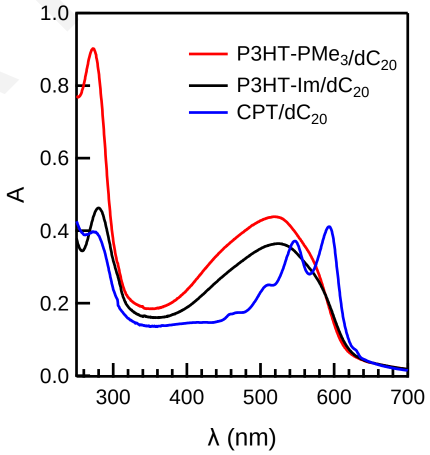

Figure 4.20. Absorption spectra of dC_{20} complexed to CPT, P3HT-PMe$_3$, and P3HT-Im in PBS buffer with a concentration of 1.5×10^{-4} M (monomeric basis) at room temperature.

templating must result either from the longer alkyl group in the cationic side chain and/or the absence of the C_β methyl substituent, since our MD simulations show that chalcogen interactions (involving the alkoxy oxygen) have no decisive effect on the CPT conformation.[56] Indeed, the methyl substituent in CPT restricts the possibility of cisoid (syn-syn) conformations between neighboring thiophenes, which were found quite preponderant for the interactions of P3HT-PMe_3 with ssDNA or dsDNA.[31,63] Such cisoid conformations contribute to steric repulsion between the side chains inducing overall more torsional backbone disorder. Moreover, the longer alkyl chains occupy a larger volume than in CPT, possibly limiting the essential polymer-DNA π-stacking in the complexes.

4.3 Conclusions

We have investigated here the templating effect of ssDNA oligomers with different sequences on cationic polythiophenes. The conformational and photophysical behaviour of the polymer/ssDNA complexes was studied using a powerful combination of spectroscopic techniques supported by MD simulations, leading to significant expansion of knowledge and understanding of the systems. We find that in all complexes, strong electrostatic interactions develop between the two components, leading to reduced polymer aggregation so that the properties of isolated chains can be accessed. However, large variations in the templating effect between different polymer/ssDNA combinations show the importance of additional noncovalent interactions. We identify CPT/dC as the complex displaying the most pronounced templating effect, highlighted by the most extensive intrachain coupling as seen from the optical response of the polymer. The first key to this effective templating is the extensive succession of cytosines in dC (ideally 10−20 bases), which favors π-stacking with the thiophene/imidazole rings of CPT over strong intra-DNA interactions, inducing a more planar and tighter conformation of the polymer. In contrast, CPT interacts mainly electrostatically with dA_{20} (π-stacking is weak), allowing conformational flexibility of the polymer, while dA_{20} maintains a rigid helical structure in the complex due to strong adenine-adenine stacking. Mixed ssDNA sequences induce a variable degree of order in CPT, depending on the intricate interplay of ssDNA-CPT and intra-DNA interactions, but never approaching the one of dC_{20}. We find that the second key to effective templating resides in the nature of the polymer side chains. Substituting CPT with another imidazole-based polythiophene (P3HT-Im) causes poor templating even with dC_{20}, because the cationic side chains are in this case too long to induce a good conformational fit with the ssDNA, and the absence of an additional methyl group on the thiophenes enhances torsional disorder on the backbone. Finally, excited-state structural relaxation is significantly reduced, with the rigid CPT/dC_{20} complex having a particularly small reorganization energy. This maintains intrachain exciton delocalization, favouring (possibly coherent) directional exciton migration along the chains. Linearity of the conjugated chain previously allowed isolated polydiacetylene (PDA) to function as electrical conductive nanowires due to the ability to transmit charge over long distances by coherent tunnelling,[67,68] or to exhibit efficient and unidirectional coherent excitonic energy transfer due to delocalized states over the chain.[69] In a comparable approach, the templating effect of ssDNA can provide access to versatile applications in optoelectronics ranging from artificial light-harvesting to single-molecule circuits based on careful design of supramolecular assemblies with conjugated polymers.

4.4 Experimental section

4.4.1 Materials and Sample Preparation

Cationic poly(1H-imidazolium,1-methyl-3-[2-[(4-methyl-3-thienyl)oxy]ethyl]-, chloride) (CPT), was synthesised as previously described (Figure 1).[29,70] It has a molecular weight (M_w) of 22 kDa (M_n = 11 kDa), with a polydispersity index (PDI) of 2.0. Each monomer unit of 262.8 g/mol contains one positive charge on the ionic side-chain, compensated by a Cl^- counter ion. Cationic poly[3-(6´-(trimethylphosphonium)hexyl)thiophene-2,5-diyl] ($P3HT-PMe_3$) and poly[3-(6´-(imidazolium)hexyl)thiophene-2,5-diyl] (P3HT-Im) (Figure 5d) were synthesized as previously described.[38] $P3HT-PMe_3$ and P3HT-Im have number-averaged molecular weight (Mn) of 17.7 kDa and 18.1 kDa (PDI=1.27) and the molecular weight of each monomer unit is 320.01 g/mol and 326.117 g/mol respectively. Each monomer unit is compensated by a Br^- counter ion. A stock solution of each polymer (monomeric concentration of $2 \cdot 10^{-3}$ M) was prepared in water (purified through a Synergy water purification system) and stored in the freezer. Single-stranded oligonucleotides (ssDNAs) were purchased from Sigma-Aldrich. The ssDNAs with a length of 20 monomers are named dA_{20}, dG_{20} (homopurine), T406, T406RC, $d[(GGAA)_5]$, $d[(TTCC)_5]$, $d[(AT(TAT)_6]$, $d[AT(AAT)_6]$ (mixed sequence), dT_{20} and dC_{20} (homopyrimidine). All oligonucleotides were previously used by Charlebois et al.[30] and their sequences are listed in Table 4.5. A stock solution of each ssDNA (monomeric concentration of $2 \cdot 10^{-3}$ M) was prepared in water and stored in the freezer. Phosphate buffered saline (PBS) was purchased from Thermo Fisher Scientific (catalogue number: 10010-031, pH 7.4, KH_2PO_4 1.06 mM, Na_2HPO_4 2.97 mM, NaCl 155 mM) and was used to dilute polymer and ssDNA stock solutions to different monomeric concentrations depending on the experiment: $7.3 \cdot 10^{-5}$ M for stationary absorption and CD measurements, $1.5 \cdot 10^{-4}$ M for RR experiments in dA_{20} and T406, and $3 \cdot 10^{-4}$ M for RR experiments in dC_{20}. For cationic polythiophene/ssDNA experiments, solutions with monomeric equivalence were prepared, with one positive charge from cationic polythiophene for one negative charge of ssDNA in order to have a complete formation of the complex form.[29,30] The order of addition for all the solutions was the following: PBS (solvent), cationic polythiophene, ssDNA. We note that the CPT/dC$_{20}$ complex was formed and studied at 55 °C only for the stationary absorption and CD measurements. In order to avoid precipitation effects during the longer RR measurements, the CPT/dC$_{20}$ complex was formed and studied at 20 °C, although this decreases the A_{0-0}/A_{0-1} ratio to 1.16 (see Figure S4.1b).

Table 4.5: Name, length and sequence of the ssDNAs employed in this study.

Name	Length	Sequence (5'-3')
dA$_{20}$	20	AAAAAAAAAAAAAAAAAAAA
dG$_{20}$	20	GGGGGGGGGGGGGGGGGGGG
dC$_{20}$	20	CCCCCCCCCCCCCCCCCCCC
dT$_{20}$	20	TTTTTTTTTTTTTTTTTTTT
T406	20	CATGATTGAACCATCCACCA
T406RC	20	TGGTGGATGGTTCAATCATG
d[(GGAA)$_5$]	20	GGAAGGAAGGAAGGAAGGAA
d[(TTCC)$_5$]	20	TTCCTTCCTTCCTTCCTTCC
d[(AT(TAT)$_6$]	20	ATTATTATTATTATTATTAT
d[AT(AAT)$_6$]	20	ATAATAATAATAATAATAAT

For experiments with different lengths of dC, aqueous solutions (0.1 mM, oligomer concentration) of homocytosine of five different lengths (5, 10, 20, 40 and 80 bases) were also purchased from Sigma-Aldrich. The homocytosine oligomers and their monomeric concentrations are listed in Table 4.6. PBS was used to dilute the CPT and ssDNA stock solutions. CPT first: 58.4 μL of CPT ($2\cdot10^{-3}$ M) were added to 1540 μL of PBS to obtain a final concentration of $7.3\cdot10^{-5}$ M, on monomeric basis. Then several portions of dC (each portion corresponding to ¼ of the total monomeric concentration of CPT) where added to the CPT solution. dC first: a volume of dC stock solution (different for each dC) was added to 1540 μL of PBS to obtain a final concentration of $7.3\cdot10^{-5}$ M, on monomeric basis. Then several portions of 14.6 μL of CPT ($2\cdot10^{-3}$ M, corresponding to ¼ of the total monomeric concentration of dC) were added to the dC solution. After each addition of every titration, the solution was left to equilibrate for at least 5-10 minutes before recording the steady-state absorption and CD spectra. The temperature was set at 20 °C.

For the study of the pH dependence of the stability of i-motif conformation for dC$_{20}$, minor portions of 0.1 M HCl or NaOH were added, either to lower or raise pH respectively. The pH titrations were carried out at 20° C using H_2O, NaCl or PBS buffer as solvent for salt-dependence studies. The reported pH values (measured with accuracy of ± 0.05 pH units) are those obtained before the CD spectra were taken.

Table 4.6: Name, length, sequence and monomeric concentration of the five homocytosine oligomers employed in this study.

Name	Length	Sequence (5'-3')	Monomeric concentration (mM)
dC$_5$	5	CCCCC	0.5
dC$_{10}$	10	(CCCCC)$_2$	1
dC$_{20}$	20	(CCCCC)$_4$	2
dC$_{40}$	40	(CCCCC)$_8$	4
dC$_{80}$	80	(CCCCC)$_{16}$	8

4.4.2 Experimental details

Absorption spectroscopy. Absorption spectra were recorded with a UV/VIS/NIR Lambda 900 spectrometer (Perkin-Elmer). A quartz cuvette with an optical path length of 10 mm was placed inside the stand-alone Peltier-based temperature-controlled cuvette holder (Flash300/E, Quantum Northwest) and the temperature was allowed to stabilize for 5-10 min. A small magnetic stir bar was placed in the cuvette and the stirring speed could be controlled with the cuvette holder.

Circular Dichroism spectroscopy. CD spectra were recorded with a J-715 spectropolarimeter (Jasco). A quartz cuvette with an optical path length of 10 mm was placed inside the temperature-controlled holder of the spectropolarimeter. For the pH titration of dC$_{20}$, CD spectra were recorded with a Jasco J-815 CD Spectrometer using EPR suprasil tubes (diameter: 4 mm).

Resonance Raman Studies. Resonance Raman (RR) spectra of cationic polythiophene/ssDNA complexes were obtained with excitation at 435.69, 473, 532 and 266 nm. The 532 and 266 nm excitation wavelengths employed in the RR experiments were provided by the second and fourth harmonics of a Q-switched Nd:YAG laser (PRO-230, 30 Hz, Spectra Physics) and the 435.69 nm was produced via Raman shifting at 532 nm in a 1 m tube containing H_2 gas. The 473 nm excitation was obtained from a CW diode laser (Ultralasers, 50 mW OEM DPSS Laser). The excitation light was focused into a spinning cell consisting of an EPR suprasil tube (diameter: 4 mm) attached to a rheostat-controlled motor for choice of rotation speed. Use of the spinning cell prolonged the lifetime of the samples. Modest excitation energies (2.1 mW at 473 nm and 435.69 nm, 0.1 mW (3.3 μJ per pulse) at 532 nm, and 0.07 mW at 266 nm (~2.5 μJ per pulse)) were employed to avoid decomposition of the sample, which was monitored by obtaining the absorption spectrum of the sample before and after exposure. The Raman scattered light was collected in a backscattering geometry and delivered to a 0.75m focal-length Czerny−Turner spectrograph, equipped with a 1200-grooves/mm holographic grating for the visible wavelengths and a 2400 grooves/mm holographic grating for excitation at 266 nm. The slit width was set to 100 μm providing for 5 cm^{-1} spectral resolution at the visible wavelengths used in this work and 7 cm^{-1} at 266 nm. The scattered light was detected by a LN_2-cooled 2048 x 512 pixel, back-illuminated UV-enhanced CCD detector (Spec10:2KBUV/LN, Princeton Instruments). Each spectrum with excitation in the visible is the accumulation of 6 × 5 min spectra, while 20 × 10 min spectra were required in the UV. Frequency calibration of the spectra was accomplished with the use of cyclohexane. MATLAB and ORIGIN software were used for spectral treatment and analysis.

References

(1) Guo, X.; Baumgarten, M.; Müllen, K. Designing π-Conjugated Polymers for Organic Electronics. *Prog. Polym. Sci.* **2013**, *38* (12), 1832–1908.

(2) Jeng, K. S.; Chu, C. W.; Liu, C. L.; Jean, W. M.; Chen, H. L.; Chen, J. T. Orientation Preferences of Interchain Stackings for Poly(3-Hexylthiophene) Nanowires Prepared Using Template-Based Wetting Methods. *Macromol. Chem. Phys.* **2018**, *219* (11), 1800078.

(3) Van Den Eede, M. P.; Van Gestel, L.; Koeckelberghs, G. Expression of Chirality in Tailor-Made Conjugated Polymers. *Macromolecules* **2018**, *51* (17), 6602–6608.

(4) Zhu, C.; Fang, L. Locking the Coplanar Conformation of π-Conjugated Molecules and Macromolecules Using Dynamic Noncovalent Bonds. *Macromol. Rapid Commun.* **2018**, *39* (2), 1700241.

(5) Zhu, C.; Mu, A. U.; Lin, Y. H.; Guo, Z. H.; Yuan, T.; Wheeler, S. E.; Fang, L. Molecular Coplanarity and Self-Assembly Promoted by Intramolecular Hydrogen Bonds. *Org. Lett.* **2016**, *18* (24), 6332–6335.

(6) Raithel, D.; Simine, L.; Pickel, S.; Schötz, K.; Panzer, F.; Baderschneider, S.; Schiefer, D.; Lohwasser, R.; Köhler, J.; Thelakkat, M.; Sommer, M.; Köhler, A.; Rossky, P. J.; Hildner, R. Direct Observation of Backbone Planarization via Side-Chain Alignment in Single Bulky-Substituted Polythiophenes. *Proc. Natl. Acad. Sci. U. S. A.* **2018**, *115* (11), 2699–2704.

(7) Dyson, M. J.; Lariou, E.; Martin, J.; Li, R.; Erothu, H.; Wantz, G.; Topham, P. D.; Dautel, O. J.; Hayes, S. C.; Stavrinou, P. N.; Stingelin, N. Managing Local Order in

Conjugated Polymer Blends via Polarity Contrast. *Chem. Mater.* **2019**, *31* (17), 6540–6547.

(8) Sugimoto, T.; Ebihara, Y.; Ogino, K.; Vacha, M. Structure-Dependent Photophysics Studied in Single Molecules of Polythiophene Derivatives. *ChemPhysChem* **2007**, *8* (11), 1623–1628.

(9) Hollingsworth, W. R.; Segura, C.; Balderrama, J.; Lopez, N.; Schleissner, P.; Ayzner, A. L. Exciton Transfer and Emergent Excitonic States in Oppositely-Charged Conjugated Polyelectrolyte Complexes. *J. Phys. Chem. B* **2016**, *120* (31), 7767–7774.

(10) Kanemoto, K.; Sudo, T.; Akai, I.; Hashimoto, H.; Karasawa, T.; Aso, Y.; Otsubo, T. Intrachain Photoluminescence Properties of Conjugated Polymers as Revealed by Long Oligothiophenes and Polythiophenes Diluted in an Inactive Solid Matrix. *Phys. Rev. B* **2006**, *73* (23), 235203.

(11) Sun, C.; Mroz, M. M.; Castro Smirnov, J. R.; Luer, L.; Hermida-Merino, D.; Zhao, C.; Takeuchi, M.; Sugiyasu, K.; Cabanillas-Gonzalez, J. Amplified Spontaneous Emission in Insulated Polythiophenes. *J. Mater. Chem. C* **2018**, *6* (24), 6591–6596.

(12) Kim, H. J.; Skinner, M.; Yu, H.; Oh, J. H.; Briseno, A. L.; Emrick, T.; Kim, B. J.; Hayward, R. C. Water Processable Polythiophene Nanowires by Photo-Cross-Linking and Click-Functionalization. *Nano Lett.* **2015**, *15* (9), 5689–5695.

(13) Niles, E. T.; Roehling, J. D.; Yamagata, H.; Wise, A. J.; Spano, F. C.; Moule, A. J.; Grey, J. K. J-Aggregate Behavior in Poly-3-Hexylthiophene Nanofibers. **2012**, 0–4.

(14) Belosludov, R. V.; Sato, H.; Farajian, A. A.; Mizuseki, H.; Kawazoe, Y. Theoretical Study of Molecular Enamel Wires Based on Polythiophene-Cyclodextrin Inclusion Complexes. *Mol. Cryst. Liq. Cryst.* **2003**, *406*, 1–10.

(15) Van Den Boogaard, M.; Bonnet, G.; Van’t Hof, P.; Wang, Y.; Brochon, C.; Van Hutten, P.; Lapp, A.; Hadziioannou, G. Synthesis of Insulated Single-Chain Semiconducting Polymers Based on Polythiophene, Polyfluorene, and β-Cyclodextrin. *Chem. Mater.* **2004**, *16* (23), 4383–4385.

(16) Shimomura, T.; Akai, T.; Fujimori, M.; Heike, S.; Hashizume, T.; Ito, K. Conductivity Measurement of Insulated Molecular Wire Formed by Molecular Nanotube and Polyaniline. *Synth. Met.* **2005**, *153* (1–3), 497–500.

(17) Masai, H.; Terao, J. Stimuli-Responsive Functionalized Insulated Conjugated Polymers. *Polym. J.* **2017**, *49* (12), 805–814.

(18) Li, C.; Numata, M.; Bae, A. H.; Sakurai, K.; Shinkai, S. Self-Assembly of Supramolecular Chiral Insulated Molecular Wire. *J. Am. Chem. Soc.* **2005**, *127* (13), 4548–4549.

(19) Hamedi, M.; Elfwing, A.; Gabrielsson, R.; Inganäs, O. Electronic Polymers and DNA Self-Assembled in Nanowire Transistors. *Small* **2013**, *9* (3), 363–368.

(20) Watson, S. M. D.; Galindo, M. A.; Horrocks, B. R.; Houlton, A. Mechanism of Formation of Supramolecular DNA-Templated Polymer Nanowires. *J. Am. Chem. Soc.* **2014**, *136* (18), 6649–6655.

(21) Knaapila, M.; Costa, T.; Garamus, V. M.; Kraft, M.; Drechsler, M.; Scherf, U.; Burrows, H. D. Conjugated Polyelectrolyte (CPE) Poly{3-[6-(N -Methylimidazolium)Hexyl]-2, 5-Thiophene} Complexed with DNA: Relation between Colloidal Level Solution Structure and Chromic Effects. *Macromolecules* **2014**, *47* (12), 4017–4027.

(22) Knudsen, J. B.; Liu, L.; Kodal, A. L. B.; Madsen, M.; Li, Q.; Song, J.; Woehrstein, J. B.; Wickham, S. F. J.; Strauss, M. T.; Schueder, F.; Vinther, J.; Krissanaprasit, A.; Gudnason, D.; Smith, A. A. A.; Ogaki, R.; Zelikin, A. N.; Besenbacher, F.; Birkedal, V.; Yin, P.; Shih, W. M.; Jungmann, R.; Dong, M.; Gothelf, K. V. Routing of Individual Polymers in Designed Patterns. *Nat. Nanotechnol.* **2015**, *10* (10), 892–898.

(23) Björk, P.; Persson, N. K.; Peter, K.; Nilsson, R.; Åsberg, P.; Inganäs, O. Dynamics of Complex Formation between Biological and Luminescent Conjugated Polyelectrolytes - A Surface Plasmon Resonance Study. *Biosens. Bioelectron.* **2005**, *20* (9), 1764–1771.

(24) Dubin, F.; Melet, R.; Barisien, T.; Grousson, R.; Legrand, L.; Schott, M.; Voliotis, V. Macroscopic Coherence of a Single Exciton State in an Organic Quantum Wire. *Nat. Phys.* **2006**, *2*, 32–35.

(25) Cacialli, F.; Wilson, J. S.; Michels, J. J.; Daniel, C.; Silva, C.; Friend, R. H.; Severin, N.; Samori, P.; Rabe, J. P.; O’connell, M. J.; Taylor, P. N.; Anderson, H. L. Cyclodextrin-Threaded Conjugated Polyrotaxanes as Insulated Molecular Wires with Reduced Interstrand Interactions. *Nat. Mater.* **2002**, *1*, 160–164.

(26) Béra-Abérem, M.; Najari, A.; Ho, H.-A.; Gravel, J. F.; Nobert, P.; Boudreau, D.; Leclerc, M. Protein Detecting Arrays Based on Cationic Polythiophene-DNA-Aptamer Complexes. *Adv. Mater.* **2006**, *18* (20), 2703–2707.

(27) Guan, H.; Cai, M.; Chen, L.; Wang, Y.; He, Z. Label-Free DNA Sensor Based on Fluorescent Cationic Polythiophene for the Sensitive Detection of Hepatitis B Virus Oligonucleotides. *Luminescence* **2010**, *25* (4), 311–316.

(28) Zhan, R.; Fang, Z.; Liu, B. Naked-Eye Detection and Quantification of Heparin in Serum with a Cationic Polythiophene. *Anal. Chem.* **2010**, *82* (4), 1326–1333.

(29) Ho, H.-A.; Boissinot, M.; Bergeron, M. G.; Corbeil, G.; Doré, K.; Boudreau, D.; Leclerc, M. Colorimetric and Fluorometric Detection of Nucleic Acids Using Cationic Polythiophene Derivatives. *Angew. Chem. Int. Ed.* **2002**, *41* (9), 1548–1551.

(30) Charlebois, I.; Gravel, C.; Arrad, N.; Boissinot, M.; Bergeron, M. G.; Leclerc, M. Impact of DNA Sequence and Oligonucleotide Length on a Polythiophene-Based Fluorescent DNA Biosensor. *Macromol. Biosci.* **2013**, *13* (6), 717–722.

(31) Rubio-Magnieto, J.; Azene, E. G.; Knoops, J.; Knippenberg, S.; Delcourt, C.; Thomas, A.; Richeter, S.; Mehdi, A.; Dubois, P.; Lazzaroni, R.; Beljonne, D.; Clement, S.; Surin, M. Self-Assembly and Hybridization Mechanisms of DNA with Cationic Polythiophene. *Soft Matter* **2015**, *11*, 6460–6471.

(32) Kypr, J.; Kejnovská, I.; Renčiuk, D.; Vorlíčková, M. Circular Dichroism and Conformational Polymorphism of DNA. *Nucleic Acids Res.* **2009**, *37* (6), 1713–1725.

(33) Peterhans, L.; Alloa, E.; Sheima, Y.; Vannay, L.; Leclerc, M.; Corminboeuf, C.; Hayes, S. C.; Banerji, N. Salt-Induced Thermochromism of a Conjugated Polyelectrolyte. *Phys. Chem. Chem. Phys.* **2017**, *19* (42), 28853–28866.

(34) Banerji, N.; Cowan, S.; Vauthey, E.; Heeger, A. J. Ultrafast Relaxation of the Poly(3-Hexylthiophene) Emission Spectrum. *J. Phys. Chem. C* **2011**, *115* (19), 9726–9739.

(35) Sun, C.; Mróz, M. M.; Castro Smirnov, J. R.; Lüer, L.; Hermida-Merino, D.; Zhao, C.; Takeuchi, M.; Sugiyasu, K.; Cabanillas-González, J. Amplified Spontaneous Emission in Insulated Polythiophenes. *J. Mater. Chem. C* **2018**, *6* (24), 6591–6596.

(36) Spano, F. C.; Silva, C. H- and J-Aggregate Behavior in Polymeric Semiconductors. *Annu. Rev. Phys. Chem.* **2014**, *65* (1), 477–500.

(37) Yamagata, H.; Spano, F. C. Interplay between Intrachain and Interchain Interactions in Semiconducting Polymer Assemblies: The HJ-Aggregate Model. *J. Chem. Phys.* **2012**, *136* (18), 184901.

(38) Rubio-Magnieto, J.; Thomas, A.; Richeter, S.; Mehdi, A.; Dubois, P.; Lazzaroni, R.; Clément, S.; Surin, M. Chirality in DNA–π-Conjugated Polymer Supramolecular Structures: Insights into the Self-Assembly. *Chem. Commun.* **2013**, *49* (48), 5483.

(39) Digennaro, A.; Wennemers, H.; Joshi, G.; Schmid, S.; Mena-Osteritz, E.; Bäuerle, P. Chiral Suprastructures of Asymmetric Oligothiophene-Hybrids Induced by a Single Proline. *Chem. Commun.* **2013**, *49* (93), 10929–10931.

(40) Nilsson, K. P. R.; Rydberg, J.; Baltzer, L.; Inganäs, O. Twisting Macromolecular Chains: Self-Assembly of a Chiral Supermolecule from Nonchiral Polythiophene Polyanions and Random-Coil Synthetic Peptides. *PNAS* **2004**, *101* (31), 11197–11202.

(41) Ewbank, P. C.; Nuding, G.; Suenaga, H.; McCullough, R. D.; Shinkai, S. Amine Functionalized Polythiophenes : Synthesis and Formation of Chiral , Ordered Structures on DNA Substrates. *Tetrahedron Lett.* **2001**, *42*, 155–157.

(42) Langeveld-Voss, B. M. W.; Christiaans, M. P. T.; Janssen, R. A. J.; Meijer, E. W. Inversion of Optical Activity of Chiral Polythiophene Aggregates by a Change of Solvent. *Macromolecules* **1998**, *31* (19), 6702–6704.

(43) Balaz, M.; Tannir, S.; Varga, K. Chiral Multichromophoric Supramolecular Nanostructures Assembled by Single Stranded DNA and RNA Templates. *Coord. Chem. Rev.* **2017**, *349*, 66–83.

(44) Mills, J. B.; Vacano, E.; Hagerman, P. J. Flexibility of Single-Stranded DNA: Use of Gapped Duplex Helices to Determine the Persistence Lengths of Poly(DT) and Poly(DA). *J. Mol. Biol.* **1999**, *285* (1), 245–257.

(45) Konorov, S. O.; Schulze, H. G.; Addison, C. J.; Haynes, C. A.; Blades, M. W.; Turner, R. F. B. Ultraviolet Resonance Raman Spectroscopy of Locked Single-Stranded Oligo(DA) Reveals Conformational Implications of the Locked Ribose in LNA. *J. Raman Spectrosc.* **2009**, *40* (9), 1162–1171.

(46) Antao, V. P.; Gray, D. M. CD Spectral Comparisons of the Acid-Induced Structures of Poly[d(A)], Poly[r(A)], Poly[d(C)], and Poly[r(C)]. *J. Biomol. Struct. Dyn.* **1993**, *10* (5), 819–839.

(47) Saxena, S.; Joshi, S.; Shankaraswamy, J.; Tyagi, S.; Kukreti, S. Magnesium and Molecular Crowding of the Cosolutes Stabilize the I-Motif Structure at Physiological PH. *Biopolymers* **2017**, *107* (7), 1–11.

(48) Smith, K. C.; Hanawalt, P. C. *Molecular Photobiology: Inactivation and Recovery*; Academic Press, 1969.

(49) Davis, T. M.; McFail-Isom, L.; Keane, E.; Williams, L. D. Melting of a DNA Hairpin without Hyperchromism. *Biochemistry* **1998**, *37* (19), 6975–6978.

(50) Tsoi, W. C.; James, D. T.; Kim, J. S.; Nicholson, P. G.; Murphy, C. E.; Bradley, D. D. C.; Nelson, J.; Kim, J. S. The Nature of In-Plane Skeleton Raman Modes of P3HT and Their Correlation to the Degree of Molecular Order in P3HT:PCBM Blend Thin Films. *J. Am. Chem. Soc.* **2011**, *133*, 9834–9843.

(51) Myers, A. B.; Mathies, R. A.; Spiro, T. G. *Biological Applications of Raman Spectroscopy: Resonance Raman Spectra of Polyenes and Aromatics*; John Wiley & Sons, Ltd., 1987; Vol. 2.

(52) Fodor, S. P. A.; Rava, R. P.; Hays, T. R.; Spiro, T. G. Ultraviolet Resonance Raman-Spectroscopy Of The Nucleotides With 266-, 240-, 218-, And 200-Nm Pulsed Laser Excitation. *J. Am. Chem. Soc.* **1985**, *107* (6), 1520–1529.

(53) Wen, Z. Q.; Thomas, G. J. UV Resonance Raman Spectroscopy of DNA and Protein Constituents of Viruses: Assignments and Cross Sections for Excitations at 257, 244, 238, and 229 Nm. *Biopolymers* **1998**, *45* (3), 247–256.

(54) Benevides, J. M.; Kang, C.; Thomas, G. J. Raman Signature of the Four-Stranded Intercalated Cytosine Motif in Crystal and Solution Structures of DNA Deoxycytidylates d(CCCT) and d(C8). *Biochemistry* **1996**, *35* (18), 5747–5755.

(55) Wen, Z. Q.; Overman, S. A.; Thomas, G. J. Structure and Interactions of the Single-Stranded DNA Genome of Filamentous Virus Fd: Investigation by Ultraviolet Resonance Raman Spectroscopy. *Biochemistry* **1997**, *36* (25), 7810–7820.

(56) Peterhans, L.; Nicolaidou, E.; Diamantis, P.; Alloa, E.; Leclerc, M.; Surin, M.; Clément, S.; Rothlisberger, U.; Banerji, N.; Hayes, S. C. Structural and

Photophysical Templating of Conjugated Polyelectrolytes with Single-Stranded DNA. *Chem. Mater.* **2020**, *32* (17), 7347–7362.

(57) Toyama, A.; Takino, Y.; Takeuchi, H.; Harada, I. Ultraviolet Resonance Raman Spectra of Ribosyl C(1′)-Deuterated Purine Nucleosides: Evidence of Vibrational Coupling between Purine and Ribose Rings. *J. Am. Chem. Soc.* **1993**, *115* (24), 11092–11098.

(58) Miskovsky, P.; Tomkova, A.; Chinsky, L.; Turpin, P. Y. Conformational Transitions of Poly(Dl-Dc)in Aqueous Solution as Studied by Ultraviolet Resonance Raman Spectroscopy. *J. Biomol. Struct. Dyn.* **1993**, *11* (3), 655–669.

(59) Tomkova, A.; Miskovsky, P.; Chinsky, L.; Turpin, P.-Y. UV Resonance Raman Contribution to Structure Determination of the X Form of Double-Stranded Poly (DA-DT). *J. Mol. Struct.* **1995**, *344* (1–2), 11–20.

(60) Hunter, C. A. Sequence-Dependent DNA Structure The Role of Base Stacking Interactions. *J. Mol. Biol.* **1993**, *230*, 1025–1054.

(61) Guckian, K. M.; Schweitzer, B. A.; Ren, R. X.-F.; Sheils, C. J.; Tahmassebi, D. C.; Kool, E. T. Factors Contributing to Aromatic Stacking in Water: Evaluation in the Context of DNA. *J. Am. Chem. Soc.* **2000**, *122* (10), 2213–2222.

(62) Pascoe, D. J.; Ling, K. B.; Cockroft, S. L. The Origin of Chalcogen-Bonding Interactions. *J. Am. Chem. Soc.* **2017**, *139* (42), 15160–15167.

(63) Fossépré, M.; Trévisan, M. E.; Cyriaque, V.; Wattiez, R.; Beljonne, D.; Richeter, S.; Clément, S.; Surin, M. Detection of the Enzymatic Cleavage of DNA through Supramolecular Chiral Induction to a Cationic Polythiophene. *ACS Appl. Bio Mater.* **2019**, *2* (5), 2125–2136.

(64) Leclercq, M.; Rubio-Magnieto, J.; Mohammed, D.; Gabriele, S.; Leclercq, L.; Cottet, H.; Richeter, S.; Clément, S.; Surin, M. Supramolecular Self-Assembly of DNA with a Cationic Polythiophene: From Polyplexes to Fibers. *ChemNanoMat* **2019**, *5*, 703–709.

(65) Louarn, G.; Trznadel, M.; Buisson, J. P.; Laska, J.; Pron, A.; Lapkowski, M.; Lefrant, S. Raman Spectroscopic Studies of Regioregular Poly(3-Alkylthiophenes). *J. Phys. Chem.* **1996**, *100* (30), 12532–12539.

(66) Pron, A.; Louarn, G.; Lapkowski, M.; Zagorska, M.; Glowczyk-Zubek, J.; Lefrant,

S. “In Situ” Raman Spectroelectrochemical Studies of Poly(3,3′-Dibutoxy-2,2′-Bithiophene). *Macromolecules* **1995**, *28*, 4644–4649.

(67) Okawa, Y.; Mandal, S. K.; Hu, C.; Tateyama, Y.; Goedecker, S.; Tsukamoto, S.; Hasegawa, T.; Gimzewski, J. K.; Aono, M. Chemical Wiring and Soldering toward All-Molecule Electronic Circuitry. *J. Am. Chem. Soc.* **2011**, *133* (21), 8227–8233.

(68) Yamagata, H.; Spano, F. C. Vibronic Coupling in Quantum Wires: Applications to Polydiacetylene. *J. Chem. Phys.* **2011**, *135* (5).

(69) Holcman, J.; Al Choueiry, A.; Enderlin, A.; Hameau, S.; Barisien, T.; Legrand, L. Coherent Control of the Optical Emission in a Single Organic Quantum Wire. *Nano Lett.* **2011**, *11* (10), 4496–4502.

(70) Dore, K.; Dubus, S.; Ho, H. A.; Levesque, I.; Brunette, M.; Corbeil, G.; Boissinot, M.; Boivin, G.; Bergeron, M. G.; Boudreau, D.; Leclerc, M. Fluorescent Polymeric Transducer for the Rapid, Simple, and Specific Detection of Nucleic Acids at the Zeptomole Level. *J. Am. Chem. Soc.* **2004**, *126* (13), 4240–4244.

CHAPTER 5

UNRAVELLING EXCITED STATE DYNAMICS OF A ssDNA-ASSEMBLED CONJUGATED POLYELECTROLYTE

In the previous chapter, we have addressed the ground state conformation of polymer/ssDNA complexes. However, the sequence-dependent templating effect of single-stranded DNAs (ssDNAs) on the conformation of conjugated polyelectrolytes has the prospect of transmitting properties to the excited state dynamics that optoelectronic applications rely on. Therefore, it is imperative to understand the impact of templating on the excited state behavior, especially for the extended cationic polythiophene (CPT) conformation in the complex with dC_{20}, to assess the suitability for technological applications involving e.g. extended intrachain exciton delocalization or directional long-range exciton migration. Here, we explore structurally the CPT/ssDNA complexes, in order to differentiate the impact of each ssDNA on the excited state properties of the complex. According to transient absorption (TA) measurements in the vis-NIR spectral range, all complexes exhibited similar photophysical behavior regardless of ssDNA sequence, detecting only excitons with fast dynamics. In addition, long-lived polaron states or triplet states were absent, in contrast to CPT alone, which forms interchain aggregates. Therefore, to access more structural information, we use ultrafast time-resolved infrared spectroscopy (TRIR) to study the excited state processes of CPT polymer assembled with ssDNA, assuming (according to chapter 4) either a flexible disordered structure (in complex with dA_{20}) or forming a more rigid complex with increased polymer backbone planarity (with dC_{20}). We find that intrachain polarons are produced in both cases upon selective excitation of the polymer, but to a larger extent when the templating induces greater torsional order. Polaron formation was monitored through the temporal evolution of the intensified vibrational bands known as IR active vibrational modes (IRAVs) that interfere with mid-IR polaron electronic absorption giving rise to Fano antiresonances (FA). Femtosecond stimulated Raman spectroscopy (FSRS) was also exploited with selective excitation of the polymer, reinforcing the assumption of ultrafast polaron formation at segments with larger conjugation. TRIR spectroscopy via selective excitation of ssDNA, revealed that the stacking interactions between the thiophene rings and the nucleic acid bases can promote the formation of an intermolecular charge transfer complex. Therefore, in the design of functional templated conjugated polymers, one needs to not only consider the effect of ssDNA on directing their conformation but also the involvement in the photophysics, to assess the suitability of such structures for optoelectronic applications. For this work we collaborated with Natalie Banerji' s research group (University of Bern), who conducted transient absorption spectroscopy. The TRIR data were obtained during our visit at the Central Laser Facility (CLF) of the Rutherford Lab in the United Kingdom. The FSRS measurements were conducted by Tullio Scopigno's group at Sapienza University of Rome. The FSRS experiments were prepared during our visit to their lab.

5.1 Introduction

DNA can be seen as a scaffold for tuning the optoelectronic properties of conjugated polymers, when appropriate interactions during self-assembly direct their backbone conformation. This DNA-based approach relies on the strong correlation of photophysical properties with polymer backbone conformation.[1–4] Understanding the nature of the structure of the complex and the way it influences the photophysical properties makes studying both their ground state and excited state properties by structurally probing each partner of equal importance. In particular, having a deeper fundamental understanding of ultrafast photo-induced processes is of utmost importance to further advance the molecular design of such nanostructures, since optoelectronic functionality is deeply governed by the formation and decay dynamics of charged and neutral excitations.

Among π-conjugated polymers, cationic π-conjugated polyelectrolytes facilitate the complexation with nucleic acids through electrostatic interactions of positively charged polymer side chains with the negatively charged phosphodiester groups in the nucleic acid backbone.[5] An intriguing example is the cationic polythiophene polymer (CPT) with imidazolium side chains.[6–8] According to our previous work[9] (see Chapter 4), this polymer can adopt an extended polythiophene chain when assembled with homonucleotide oligocytosine (dC_n) strands, following a mechanism of complexation that involves extensive π-stacking interactions between thiophene and cytosine rings, further enhanced by π-stacking with the imidazolium cation, that leads to improved backbone planarization.

Optically excited charge carriers on a π-conjugated chain display absorption bands in the near-IR and mid-IR due to new energy levels inside the optical band gap compared to their ground state counterparts.[10] These polaron bands were detected experimentally for a range of polymers through a quasi-steady state measurement, known as photoinduced absorption (PIA).[11] Spectroscopically in the near-IR region, the polaron band P_2, corresponding to the transition from the HOMO to the highest polaron energy level in the gap,[12–15] is detected in the case of polythiophenes at ~10000 cm^{-1} (1000 nm) and formation after optical excitation can therefore be monitored through transient absorption (TA) spectroscopy. The intensity of P_2 is a key indicator of the existence of interchain interactions (between polymer chains), exhibiting moderate intensity when interchain interactions are weak.[12,13] Previous knowledge, obtained by TA measurements on CPT (Figure 5.1) conducted in a previous study,[16] revealed that polymer chains alone favor the generation of long-lived polaron states (P_2 band at ~950 nm) at low temperatures and triplet states (observed at ~730 nm) at higher temperatures, detected in the near-IR spectra region.[16]

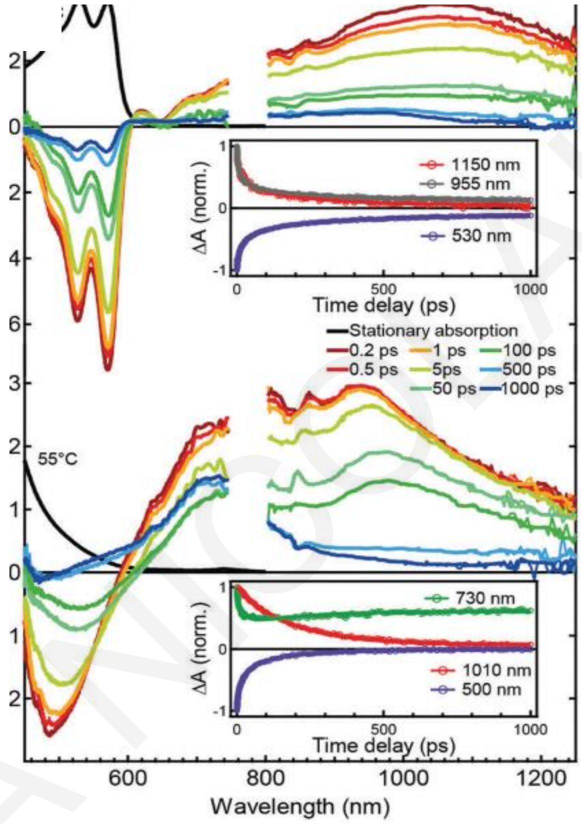

Figure 5.1. TA data for CPT in solution following excitation at 400 nm (1.5×10^{-4} M on a monomeric unit basis in PBS). TA spectra recorded at selected time delays for CPT at 5 ˚C (top) and 55 ˚C (bottom) with the corresponding stationary absorption (black curves). The two insets show the TA dynamics probed at selected wavelengths.

In the mid-IR range of PIA of positively charged polythiophene chains, two bands are observed known as A and B. Band A (also referred to as a combination of the delocalized polaron band (DP_1) or charge transfer (CT)[17] and P_0 band[18,19]) is composed of overlapping interchain and intrachain components. One component can dominate over the other, depending on the effectiveness of polaron delocalization over several chains due to significant interchain coupling, or along the polymer (intrachain) in the presence of non-interacting chains.[20,21] Band B (also known as P_1) corresponds to the transition from the HOMO to the lowest polaron energy level in the gap.[13,15,20] According to the PIA spectra, the polaron bands A and B can be detected at ~1000 and 4000 cm^{-1}, respectively.[10,21] Therefore, band A can overlap with strong vibrational IR bands, which are originally Raman-active (Ag) modes coupled to the π-electron system that become strongly absorbing infrared active vibrations, referred to as IRAVs. IRAVs occur through structural distortion stemming from localized charge carriers on the π-conjugated chain creating large changes in bonding dipole moments.[22–25] When overlap of IRAV modes and polaron electronic absorption exists, Fano anti-resonances (FA) emerge.[11,21,26–29] The FA bands can be interrogated by TRIR, enabling monitoring of the photogenerated excited state species and simultaneously accessing crucial information on structural evolution that occurs during the rapid relaxation processes,[29,30] often inaccessible by conventional spectroscopy. In particular, this is clearly demonstrated through picosecond time-resolved photoinduced IRAV studies of Mizrahi et al.[31,32] and Miranda et al.[33], in which photogenerated polarons were detected selectively using IRAV modes of PPV polymer chains as a direct measure, avoiding interference with overlapping bands from neutral excitations, such as excitons and excimers as is the case with transient absorption measurements in the visible/near/IR. Similar studies on polythiophene films, enabled monitoring of polaron diffusion, charge carrier separation and recombination, as well as detection of structural modifications attributed to polaron relaxation processes of the polymer.[34,35]

Structural characterization by using transient Raman, has been also increasingly employed over the years for interrogating the excited state local structure and dynamics of conjugated polymers with improved spectral and temporal resolution.[36–38] The combination of TA, TRIR and transient Raman can enable the detection of the structural changes from ground to the excited state and the electron-density distribution, which are linked to the excited species generated and therefore shed light on the processes that occur after photoexcitation.

Here, we firstly examined the ultrafast excited-state relaxation through femtosecond TA measurements on CPT/ssDNA[9] in solution, where CPT demonstrate, regardless of the sequence, a comparable photophysical behavior, described by the formation of excitons with similar dynamics. This raises the question as to why the complexation that induces different polymer conformations does not seem to affect the excited state behaviour of the polymer, and whether the TA measurements simply could not detect some other excited species formed due to the spectral range investigated. Therefore, we then employed TRIR in the mid-IR as a structural probe to compare the excited state behaviour of the loosely bound CPT/DNA-base complexes with the more rigid and ordered systems. The excited state dynamics were investigated for solutions of the pure compounds and their corresponding complexes in deuterated PBS buffer through selective excitation of each compound at 532 nm and 266 nm, coinciding with the polymer and oligonucleotide absorption, respectively. Following excitation at 532 nm we observe the formation of intrachain polarons in both complexes, which, in the case of the rigid system, perturb the environment of the π-stacked cytosine base, while with excitation at 266 nm we observe charge transfer between the polymer and the closely interacting ssDNA. Results from both excitation wavelengths were dependent on the strength and nature of interactions that is strongly controlled by the sequence of ssDNA. We also proceed to a more detailed evaluation of the conformational evolution of CPT backbone of the more intriguing complex, which is CPT/dC$_{20}$, in the excited state by using impulsive stimulated Raman scattering (ISRS), stimulated Raman spectroscopy (SRS) and femtosecond stimulated Raman spectroscopy (FSRS). We aimed to selectively determine the vibrational dynamics of modes associated with backbone planarization and therefore examine more thoroughly the conformational changes that the excited-state species undergo during relaxation. This study demonstrates the power of combining transient electronic and vibrational spectroscopy in expanding the knowledge on the excited state mechanisms.

5.2 Results and discussion

5.2.1 Transient absorption studies and stimulated emission simulation

Interestingly, even though the ssDNA sequences induce different CPT conformations, the nature and lifetime of the excited state are roughly similar in the different complexes. Figure 5.2 shows a selection of TA spectra for the CPT/dA$_{20}$ and CPT/dC$_{20}$ complexes at different time delays following excitation at 400 nm. For all complexes, a positive broad band centered at ~1050 nm is ascribed to the excited state absorption (ESA) of the S$_1$ singlet exciton,[16] and a negative feature below 800 nm is attributed to ground state bleaching (GSB) and stimulated emission (SE), with the differences in band shape associated to different degrees of order in CPT as also reflected in the absorption spectra. The broad and red-shifted ESA is characteristic of delocalized excitons (as observed for ordered CPT alone at low temperature,[16] while the ESA of more localized excitons in random-coiled CPT chains is narrower and centered around 950 nm).[15,39] Moreover, the TA features decay in all complexes with lifetimes of a few picoseconds (2.5-4 ps) and a few tens of picoseconds (22-28 ps, Table 5.1), with the dynamics of the ESA and GSB bands mirroring each other, meaning that the same exciton population is probed (Figures 5.2b). Finally, no long-lived species are formed in the complexes contrary to CPT alone in solution, where long-lived

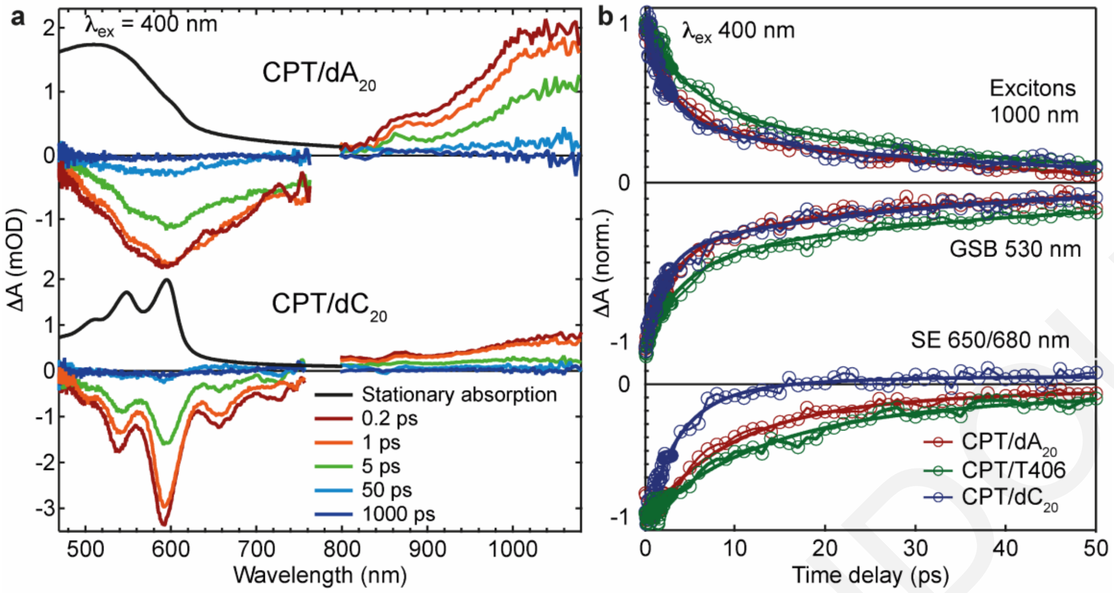

Figure 5.2. (a) TA spectra recorded following excitation at 400 nm at selected time delays with the corresponding stationary absorption (black curves) for two complexes (top: CPT/dA$_{20}$, bottom: CPT/dC$_{20}$) in solution at 20 °C (1.5x10^{-4} M on a monomeric unit basis in PBS). The features at around 740 and 860 nm are artefacts due to the white light generation near the fundamental 800 nm laser output. (b) TA dynamics at selected probe wavelengths for the three complexes (dA$_{20}$, T406, and dC$_{20}$). Solid lines correspond to the biexponential global fit.

polarons are generated at low temperature and intersystem crossing populates the triplet state at high temperature (decay time at ~450 and 400 ps respectively).[16] Along with the fast exciton quenching, this is additional proof that the assembly of CPT with the different ssDNA sequences is always achieved and leads to isolated CPT chains, as polaron formation is usually observed in polythiophenes with interchain interactions.[16] The absence of triplet generation provides additional support for the higher torsional order of CPT in all complexes, as intersystem crossing is aided by torsional disorder.[40–43]According to the early-time structural evolution of CPT investigated using resonance Raman intensity analysis (RRIA), which is presented in chapter 4 (section 4.2.2), the homogeneous broadening increases from 45 cm^{-1} to 100 cm^{-1}, which corresponds to a decrease in total dephasing from 118 to 53 fs. Since Γ includes contributions from excited state lifetime and pure dephasing, one can use the exciton lifetime determined from the TA measurements to calculate the contribution from pure dephasing. The average lifetime is on the order of 15 ps, therefore pure dephasing (e.g. due to collisions with the solvent) seems to play the dominant role in the excited state deactivation.

Table 5.1. Lifetimes (τ_1, τ_2) with the associated amplitude percentage (%), offset (y_0) and average lifetime (τ) obtained with a biexponential global fit of selected TA dynamics for CPT/dA$_{20}$, CPT/T406 and CPT/dC$_{20}$ following 400 nm excitation.

λ_{ex} = 400 nm	λ_{probe}	τ_1 (ps)	τ_2 (ps)	y_0	Average τ (ps)
CPT/dA$_{20}$	1000 nm	3.0 (60%)	22 (40%)	0.02	11
	680 nm	3.0 (31%)	22 (69%)	0.02	16
	530 nm	3.0 (62%)	22 (38%)	-0.04	10
CPT/T406	1000 nm	4.0 (48%)	28 (52%)	0.06	17
	650 nm	4.0 (30%)	28 (70%)	0.00	21
	530 nm	4.0 (48%)	28 (52%)	-0.15	17
CPT/dC$_{20}$	1000 nm	2.5 (66%)	25 (34%)	0.07	10
	680 nm	2.5 (77%)	25 (23%)	0.06	8
	530 nm	2.5 (63%)	25 (37%)	-0.04	11

Structural changes in the excited state can also be extracted from TA spectroscopy by monitoring the temporal evolution of the spectral band shapes. In particular, the clear vibronic structure of the TA spectra of CPT/dC$_{20}$ in the GSB/SE region allows one to isolate the time-dependent SE spectra after subtracting the properly scaled calculated absorption (from RRIA) (Figure 5.3) and to use a similar methodology as RRIA to analyze them (Figure 5.4-5.5, Table 5.2). The earliest SE spectrum accessible within the time resolution of the TA experiment (at 200 fs) already displays a Stokes shift of 52 meV (~70% of the total Stokes shift) with respect to the absorption. Such behavior in conjugated polymers is typically related to ultrafast dynamic localization of the initial photoexcitation, caused by electronic relaxation and coupling to nuclear modes.[44–49] However, the initial Stokes shift observed for CPT/dC$_{20}$ is less pronounced than in other systems and (in contrast to e.g. P3HT)[46] the

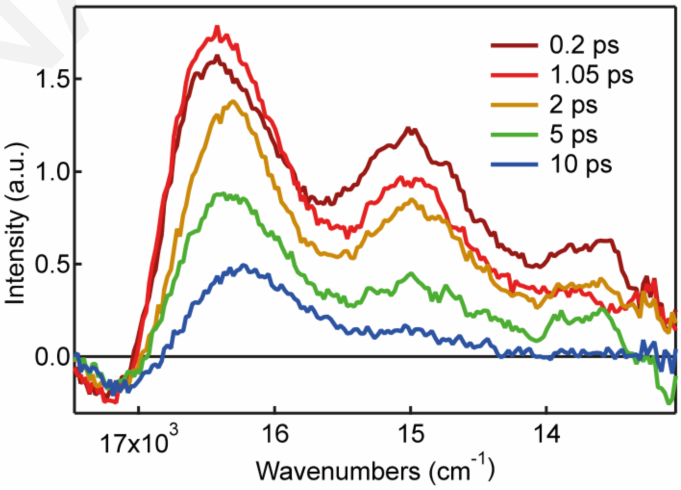

Figure 5.3. Extracted stimulated emission spectra at different time delays after photoexcitation for CPT/dC$_{20}$.early emission spectrum is a mirror image of the absorption that can be reproduced with identical parameters.

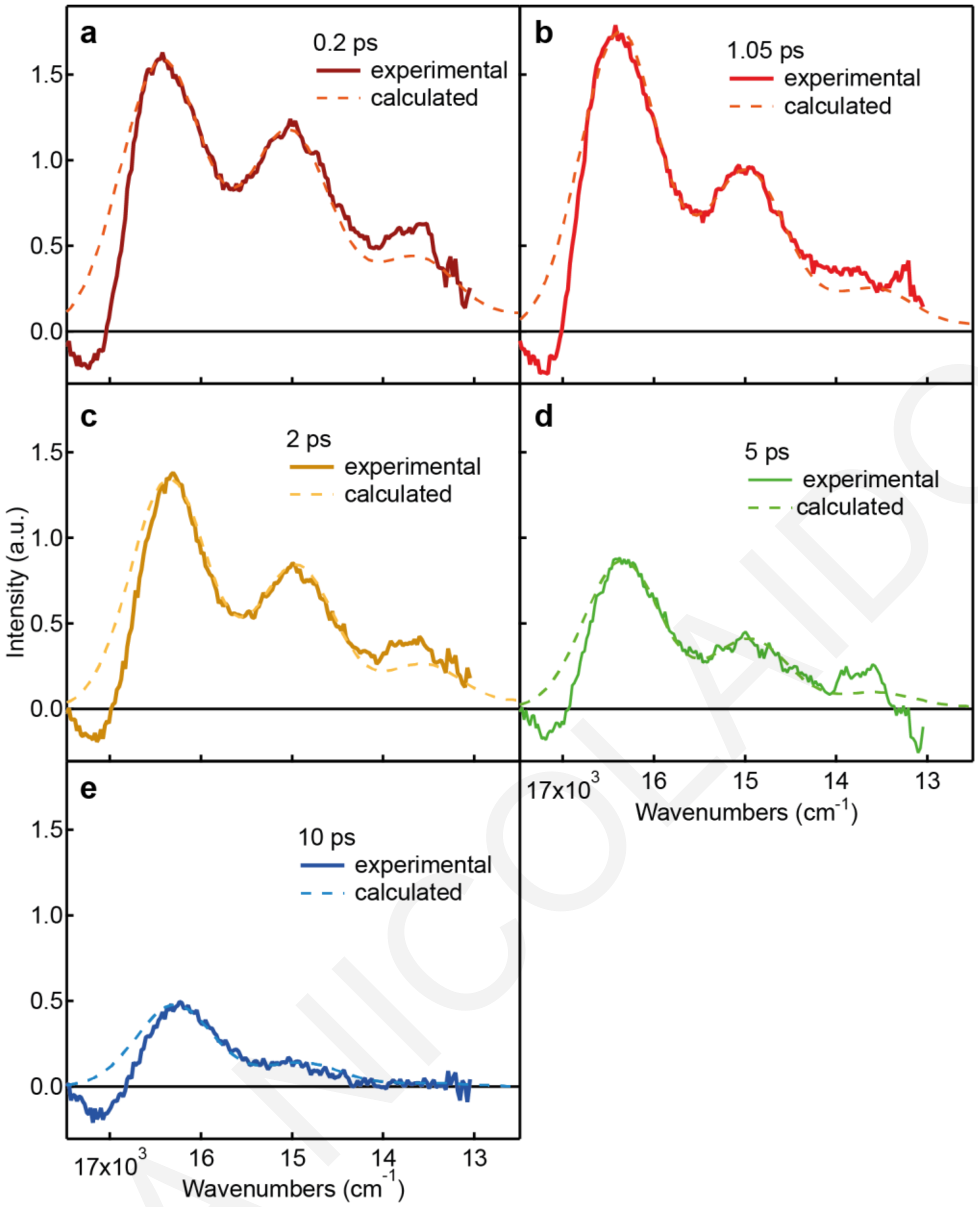

Figure 5.4. Experimental and calculated stimulated emission spectra for CPT/dC$_{20}$ at selected time delays.

This points to limited (mainly electronic) relaxation within < 200 fs, maintaining delocalization of the excited state and possibly favoring the occurrence of coherent exciton migration along the chain.[47,49–51] At longer time delays (> 200 fs), the SE spectrum of CPT/dC$_{20}$ undergoes a red-shift of the 0-0 band (by ~22 meV, leading to a total Stokes shift of 74 meV), and an increase of the vibronic band intensity ratio (I_{0-0}/I_{0-1}) from 1.34 at 0.2 ps to 3.41 at 10 ps (Figure 5.3). Fitting of the SE spectra reveals that the geometrical relaxation of the polymer involves mainly the C_β-$C_{\beta'}$ stretch, as this exhibits the highest contribution to the SE vibronic progression and sustains the largest reduction in Δ with time (Figure 5.4-5.5, Table 5.2). A concomitant decrease of the inhomogeneous broadening, which indicates a narrower distribution of chromophores, occurs within the first 2 ps. Based on previous literature about polythiophenes, this slower relaxation is ascribed to mainly incoherent exciton migration to lower energy chain segments (longer, more planar), accompanied by

Table 5.2. Parameters used in the stimulated emission fitting of the complex CPT/dC$_{20}$ for different time delays.

Transition	ω_g (cm^{-1})	ω_e (cm^{-1})	Δ_k				
			0.2 ps	1.05 ps	2 ps	5 ps	10 ps
ν_1	885	885	0.13	0.13	0.13	0.13	0.23
ν_2	977	977	0.16	0.16	0.16	0.16	0.16
ν_3	1376	1376	0.54	0.54	0.54	0.48	0.24
ν_4	1394	1394	0.93	0.68	0.80	0.63	0.53
ν_5	1448	1448	0.35	0.35	0.35	0.35	0.25
ν_6	1463	1463	0.23	0.23	0.23	0.23	0.23
ν_7	1484	1484	0.34	0.34	0.34	0.34	0.30
ν_8	1510	1510	0.10	0.10	0.10	0.10	0.10
Γ (cm^{-1})			45	45	45	45	45
Θ (cm^{-1})			450	425	415	415	415
E_{00} (cm^{-1})			16480	16440	16360	16360	16300
M (Å)			0.513	0.475	0.430	0.320	0.218

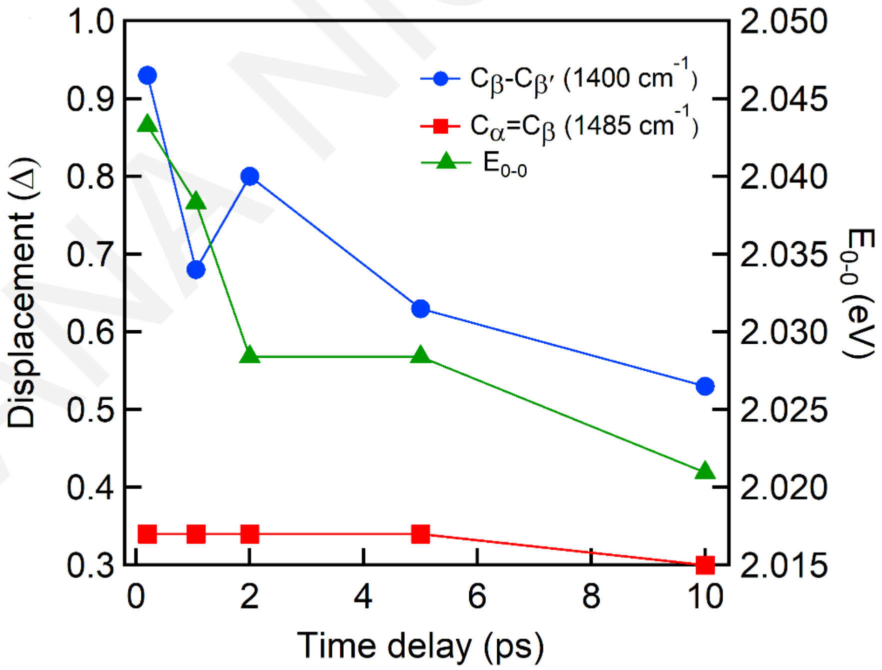

Figure 5.5. Dependence of the displacement (Δ) along the C$_\beta$-C$_{\beta'}$ and C$_\alpha$=C$_\beta$ normal coordinates and E$_{0\text{-}0}$ on the delay time, as obtained from modeling the stimulated emission spectra.

torsional relaxation of the backbone.[46,52–55] Again, the effect in CPT/dC_{20} is weaker and faster than generally observed (e.g. the total Stokes shift for polythiophene solutions is usually twice as large and spectral relaxation proceeds up to 100-200 ps).[46,52] The limited geometrical relaxation in the complex agrees with the small reorganization energy calculated by RRIA (~140 meV, section 4.2.2) and the fact that dC_{20} induces a more planar and tighter conformation of CPT already in the ground state, hindering large reorganization of the excited state. Moreover, exciton migration is limited to intrachain processes and likely concerns a more homogenous distribution of chain segments with similar energy. Going to CPT/dA_{20}, a slightly more important spectral red-shift is observed in the negative TA features (from 593 nm at 0.2 ps to 600 nm at 5 ps, *vs.* from 591 nm to 594 nm in CPT/dC_{20}), as predicted by the higher reorganization energy in the more flexible complex. This is still much less than the red-shift of the TA bands observed for random-coiled CPT alone at 55 °C (40 nm shift over 100 ps),[16] suggesting that even for CPT/dA_{20} the excited-state relaxation is restricted by the complexation with ssDNA.

5.2.2 Time-Resolved Infrared spectroscopy

The TRIR spectra of CPT alone with excitation at 532 nm are shown in Figure 5.6a. A prominent feature is the large contribution from background absorption (appearing as a baseline offset) to the spectra, clearly observed at the earliest delay times, decreasing steadily with time and seeming to correlate with the decrease in IR mode intensities. We assign this background to an electronic absorption due to polaron formation within the instrument response (~200 fs), supported by the observation of polaron absorption in the near-IR TA spectra of CPT in the ordered phase reported previously,[16] corresponding to the P_2 polaron band (10470 cm^{-1}). The background absorption observed in the TRIR spectra is therefore attributed to band A, which is expected to be located in the region ~800-1600 cm^{-1} according to the literature for rr-P3HT,[19,20] coinciding with the spectral region we collected the spectra. We can conclude that in the absence of ssDNA, excitation of ordered CPT chains at 532 nm leads to interchain polaron delocalization.

Generally, the existence of such a broad background hinders the discrimination of vibrational ground state bleaches and transient bands (negative and positive bands, respectively). Nonetheless, we observe significant spectral dips in the TRIR spectra at wavenumbers that are similar to the resonance Raman spectra of the ground state (Figure 5.6b). The intensity of these bands is strongly indicative of IRAV modes, which here spectrally coincide with

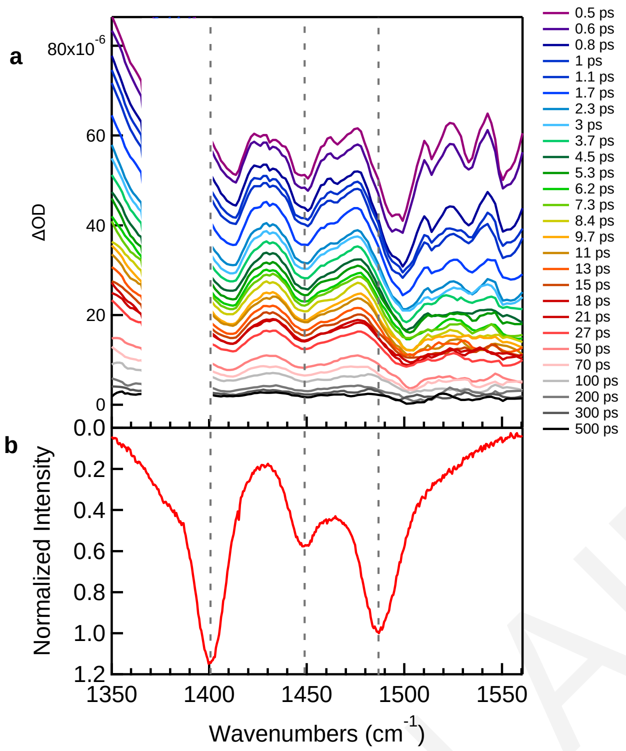

Figure 5.6. (a) TRIR spectra of CPT following excitation at 532 nm. The spectral region 1370-1400 cm^{-1}, is dominated by an experimentally-induced artifact feature and has been omitted. No extra vibrational features are expected in this region as seen in Fig. 5.7a and S5.1a. (b) Ground state Raman spectrum of CPT with excitation at 532 nm with inverted y axis.

the electronic absorption band A and therefore these dips are attributed to Fano-antiresonances.[19,27,28,56] This concept is also evidenced in the TRIR spectra of P3HT we collected (Figure S5.1c), for which photoinduced absorption in the mid-IR spectral range is widely reported in the literature, facilitating the interpretation of the data. The similarity of the PIA spectrum (Figure S5.1d, reproduced from the literature) with apparent Fano-antiresonances, with the TRIR spectra provides strong validation for the occurrence of overlap between the electronic band and IRAV modes. The existence of coupling between the absorption background and the various vibrational signals is graphically demonstrated (Figure 5.7) by the linear relationship between the intensity of each vibrational dip and the intensity of a point in the spectra considered as background at various delay times. The reduction in background absorption due to polaron recombination is correlated with the observed loss in intensity of the FA modes.

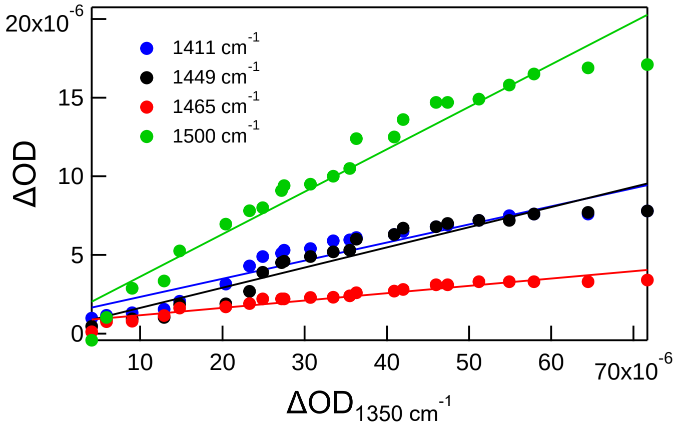

Figure 5.7. Linear correlation of the intensity of each vibrational band in the TRIR spectra of CPT alone and the intensity of a point (1350 cm^{-1}) considered as background as a function of delay time (between 1.7-200 ps).

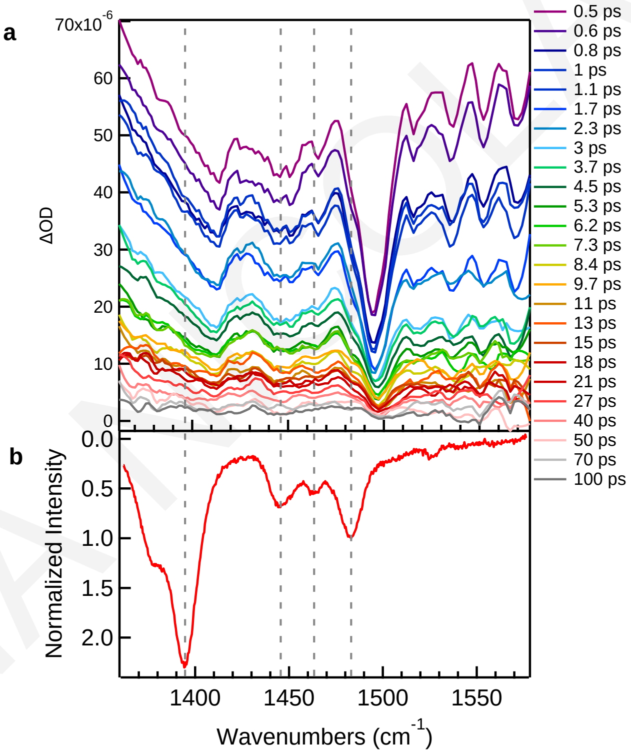

Figure 5.8. (a) TRIR spectra of CPT/dC$_{20}$ with excitation at 532 nm (b) Ground state Raman spectrum of CPT/dC$_{20}$ with excitation at 532 nm with reversed y axis.

Similar behaviour is observed in the TRIR spectra of the CPT/ssDNA complexes (Figure 5.8a and Figure S5.2b) showing a broad background absorption signal, assigned to band A, and vibrational dips assigned to FA. In the case of CPT/ssDNA complexes, TA spectroscopy was unable to depict polaron formation, since in the spectral region used the only indication of the existence of polarons is the P$_2$ polaron band, which was not evident in any of the TA spectra of the complexes. Nonetheless, the absence of the P$_2$ band is a key sign for weak interchain interactions. This subsequently suggests that the intrachain contribution in band A of the TRIR spectra of the complexes is stronger.[18–21] Therefore, we can deduce that when CPT is assembled with ssDNA, this is non-aggregated, confirming that the interactions between ssDNA with CPT are strong enough to isolate a single conducting polymer chain.

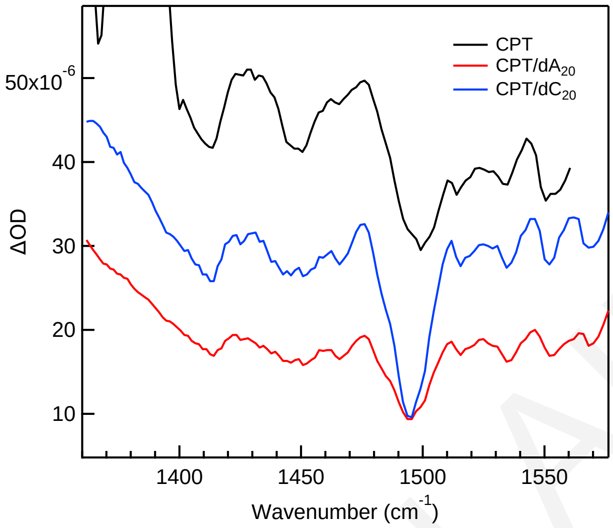

Figure 5.9. TRIR spectra at 1 ps of CPT (black), CPT/dA$_{20}$ (red) and CPT/dC$_{20}$ (blue). The latter spectrum was divided by 1.25 to adjust for concentration differences.

Figure 5.9 compares TRIR spectra of CPT and when complexed with two different ssDNAs, dA$_{20}$ and dC$_{20}$. We observe a significant difference in the intensity of the background absorption between the two ssDNAs (Figure 5.9). The ~30% decrease in the background absorption signal in CPT/dA$_{20}$ can be attributed to the increased disorder of the backbone conformation that leads to attenuation of the oscillator strength for band A,[14] as well as to the smaller relative portion of ordered polymer chain segments excited at 532 nm, according to the absorption spectrum of CPT in this complex (Figure S5.2).[9] As seen in our previous work on CPT with resonance Raman spectroscopy, excitation at 532 nm probes the more planar polymer chain segments, which are the ones that facilitate polaron formation.[9] Therefore, these more torsionally-ordered segments are expected to contribute the most to the TRIR spectra shown herein. In contrast to the signal in CPT/dA$_{20}$, the increased electronic absorption of CPT/dC$_{20}$ is attributed to intrachain order, while in the case of CPT alone to interchain long-range order.

The intensity of IRAV modes is linked to the extent of polaron delocalization along the polymer chain and the associated charge displacement during vibrational motion, as well as the proximity with a low-lying electronic transition leading to strong vibronic coupling.[29,57] Increased delocalization of positive charge carriers is evidenced by higher intensity.[23,24] Therefore, the largest intensity of the FAs in CPT/dC$_{20}$ (Figure 5.9) is associated with a more delocalized intrachain polaron. The dramatic change in the 1498 cm^{-1} FA intensity, assigned to the C=C symmetric stretching of the thiophene ring,[9] is attributed to the sensitivity of this mode to changes in charge density during the oscillation that displace the polaron along the long axis of the conjugated molecule generating an increased dipole moment with large variations.[23,56,58] This means, that in the case of CPT/dC_{20}, both the largest population of polarons and the greatest delocalization length is derived among the samples tested, which is facilitated by the increased degree of planarity of the polymer backbone.[9] As seen earlier, the intensity of the FA bands also varies with the intensity of the broad absorption background, which could contribute to the reduced FA intensity in the CPT/dA_{20} complex. However, in the case of CPT alone with known reduced torsional order compared to CPT/dC_{20},[9] the electronic absorption background is significant due to contributions to the electronic band from interchain interactions, while the 1498 cm^{-1} FA lacks in intensity, alluding to reduced intrachain exciton delocalization.

In addition to the intensity, the position of IRAVs can be sensitive to the π-electron configuration due to the strong electron-phonon coupling.[23] The position of IRAVs reported in the literature usually stems from quasi-steady state spectra obtained either through PIA or charge modulation spectroscopy (CMS), or from chemically/electrochemically-doped samples. TRIR, as a direct probe for polarons, reveals the timescale for their formation through monitoring the temporal evolution of IRAVs and can provide insights on the excited state processes at play. Interestingly, in all cases, TRIR spectra at early times (e.g. 300 fs) display a prominent shift between the C_β-C_β and C_α=C_β(Me) (1414 and 1498 cm^{-1}, respectively) symmetric stretching IRAV bands (Figure 5.6a, 5.8a and S5.2b) and the corresponding resonance Raman (RR) bands (1400 and 1487 cm^{-1} respectively, Figure 5.6b, 5.8b and S5.2c) with excitation at 532 nm.[9] The position of the C_β-C_β stretch band is harder to determine accurately due to its broadness and asymmetric shape. Focusing on the C_α=C_β stretch, the position at 1498 cm^{-1} is reminiscent of the position in the resonance Raman spectrum recorded for the neutral CPT with 405 nm excitation,[16] i.e. for CPT chains that are torsionally disordered, with reduced conjugation length. As previously noted in the literature,[23,27] the density of photoinduced charge carriers is smaller than what can be chemically produced. Therefore, the polymers can host both neutral and charged segments. The structural distortion due to polaron formation reduces the conjugation length of these planar charged segments causing a blue shift in the position of the IR-activated C_α=C_β stretch.

At later delay times the 1498 cm^{-1} FA band upshifts, but to a different extent and with different dynamics in CPT alone and the CPT/dA$_{20}$ and CPT/dC$_{20}$ complexes. This C=C symmetric stretching band is known to be sensitive to chain conformation.[9,27,59–61] Polaron localization accompanied by conformational relaxation could be at the origin of the shift.[62] The smallest shift is observed in the case of CPT/dC$_{20}$ (3 cm^{-1}), compared to CPT/dA$_{20}$ (7 cm^{-1}) or CPT alone (9 cm^{-1}). This reflects the rigidity of the CPT/dC$_{20}$ complex, allowing for the smallest conformational reorganization (bond length change). This observation follows the same trend with the total reorganization energy (λ_{tot}) calculated for these three cases using Resonance Raman Intensity Analysis (RRIA) (section 4.2.2), which reflects the overall magnitude of the conformational rearrangement in the excited state and subsequently the rigidity of chain conformation. This argues that conformational relaxation is influenced by the rigidity that characterizes each case. This is also reflected in the timescale of the observed shift (Figure S5.3). In CPT alone, the full extent of the shift occurs in the first 8 ps (time constant 1.2 ± 0.4 ps), after which no more changes are observed, except reduction in the intensity of the band due to recombination. In CPT/dA$_{20}$ where electrostatic interactions with the ssDNA limit relaxation to some extent, spectral evolution of this band occurs over 30 ps (time constant 19 ± 4 ps), albeit to a lesser extent than CPT alone, while in CPT/dC$_{20}$, with extensive interactions with the ssDNA bases, minimal evolution (2-3 cm^{-1}) occurs over the first 40 ps.

Moreover, fitting of the dynamics of the ~1498 cm^{-1} band intensity (after elimination of the background contribution, see Figure S5.4, Table 5.3) with a biexponential model gives time constants for CPT alone of 2.6 $\pm$ 0.55 and 38.5 $\pm$ 6.8 ps, similar to the case of the CPT/dC$_{20}$ complex (2.7 $\pm$ 0.42 and 33 $\pm$ 5 p), whereas the same band for the CPT/dA$_{20}$ complex decays significantly faster (2.34 $\pm$ 0.35 and 16.8 $\pm$ 3.6 ps) (Figure S5.5 and S5.6). The slightly

Table 5.3. Time constants (τ_1, τ_2) obtained with a biexponential global fit of dynamics of background and the intensity of 1498 cm^{-1} band for CPT alone, CPT/dC$_{20}$ and CPT/dAC$_{20}$ following 532 nm excitation.

	Background (ps)		**1498 cm^{-1} band (ps)**	
CPT	2.2±0.2	31±4	2.6±0.6	38±7
CPT/dC$_{20}$	3.3±0.1	35±10	2.7±0.6	33±7
CPT/dA$_{20}$	2.0±0.5	16±4	2.3±0.3	17±4

slower decay kinetics for CPT alone due to polaron recombination could be attributed to the two-dimensional nature of polaron delocalization due to simultaneous intra and interchain interactions even in solution.[21,35] While a longer-lived polaronic species (due to interchain interactions) was observed in the TA spectra at 950 nm in our previous study[16] that should follow the same dynamics as the species observed in the mid-IR, the shorter temporal observation window in the present experiments (0.5 ns) hinders direct comparison, even though a small offset is also observed here. However, the large majority of the signal (95%) decays by 200 ps, possibly due to intrachain recombination. This might explain the similarity of the recombination dynamics to the case of the CT/dC_{20} complex where interchain interactions are excluded. The faster recombination dynamics observed in the dA_{20} complex can be attributed to the polymer backbone disorder, due to the limited interactions between CPT and the ssDNA, which limits carrier diffusion. Therefore, the similarity of the vibrational bands in the TRIR spectra of CPT alone with those of the complexes indicate their common origin, while the difference in lifetimes reflect the modification of the interactions that the polymer experiences that consequently affect its conformation. The difference in the lifetimes and the generally faster decay dynamics in the dA_{20} complex is also evident in the background absorption (polaron band A) kinetics confirming that the electronic and vibrational features belong to the same species (Table 5.3, Figures S5.7-S5.9).

To gain more information about the excited state dynamics of the complexes we focus on the second component of the complexes, the oligonucleotides, by conducting time- resolved IR measurements with excitation at 266 nm. While at this wavelength we expect excitation of the ssDNAs, the CPT absorption spectrum (Figure S5.2a) indicates that the polymer also absorbs in this spectral region, possibly contributing to the TRIR spectra. In the case of CPT/dC_{20}, a very prominent feature of the TRIR spectra is the background absorption (Figure 5.10a). The background is also observed in the TRIR spectra of CPT alone with UV excitation (Figure S5.10) but not of dC_{20} alone (Figure S5.11) and therefore the background cannot be attributed to changes in the cytosine bases upon excitation. Thus, the background absorption in the case of CPT alone can be attributed as above to intra- and interchain polaron formation after excitation to higher and more delocalized electronic states.[59,63] Additionally, the simultaneous absorption of CPT at 266 nm to a comparable extent as dC_{20} leads to complicated vibrational spectra consisting of signals ascribed to both components. To disentangle the contribution of each component, bands were assigned to dC_{20} in agreement with the literature,[64–66] with the remaining bands attributed to the polymer. Assignment of the ground state bleaches was performed by considering both literature FTIR spectra, as well as ATR-FTIR spectra taken from drop-casted films of dC_{20}, CPT, and the complex (Figure S5.12). Even though some contribution from the water bend band at ~1650 cm^{-1} overlaps the carbonyl region, the contribution from the base vibrations can still be discerned.

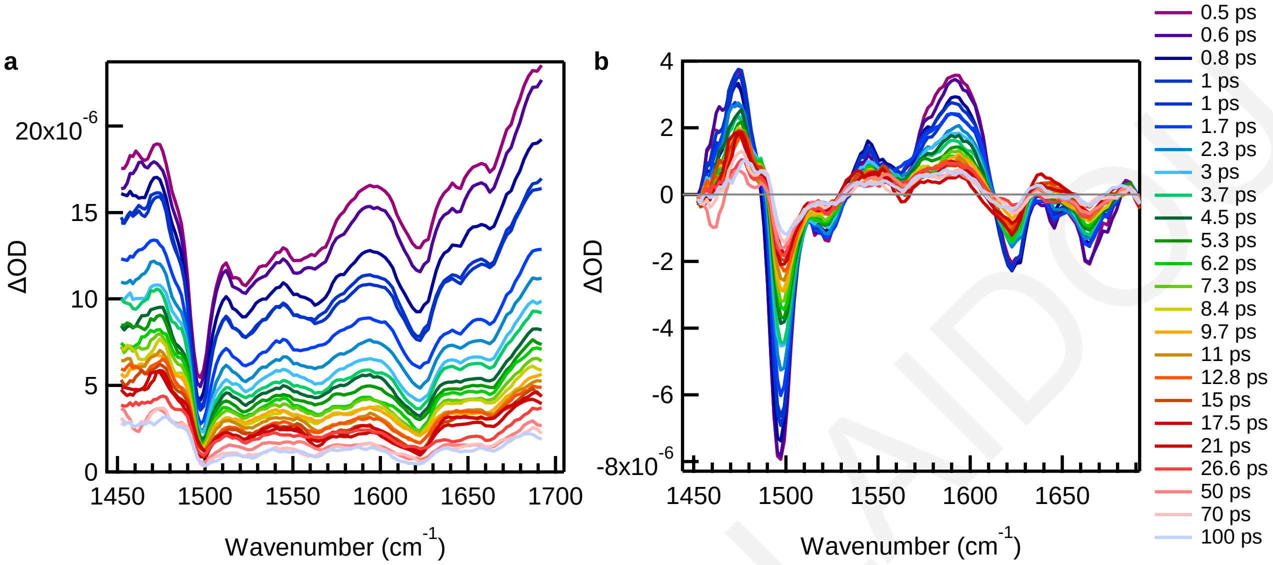

Figure 5.10. TRIR spectra of CPT/dC_{20} (a) before and (b) after background subtraction with excitation at 266 nm.

Subtracting the background absorption (Figure 5.10b) reveals rich vibrational signatures that evolve with time. Comparison of the TRIR spectrum of CPT/dC_{20} with the TRIR spectrum of dC_{20} alone at the same time delay (2 ps) (Figure 5.11) helps identify any bands that correspond to CPT, as well as detect the influence of the interaction of the two components on the ssDNA structure and dynamics. The TRIR spectra of the CPT/dC_{20} complex appear significantly different to those of the oligonucleotide. Nonetheless, we can discern characteristic signatures of the base in the TRIR spectrum of CPT/dC_{20}, both in the ground state bleaches as well as the transient bands. It is important to note here that in the case of bands associated with dC_{20}, the dips are considered as bleaches rather than FAs as above, both because of the similarity with the dC_{20} alone spectra and the ground state FTIR spectra, and the fact that the electronic background absorption must be associated with the polymer, which thus remains uncoupled with the ssDNA vibrations. The ground state bleaches that relate to dC_{20} appear at 1520 cm^{-1}, attributed to in-plane ring modes and at 1665 cm^{-1} due to the carbonyl group.[65] As previously reported, the detection of carbonyl peaks at 1665 and 1695 cm^{-1}, indicates that polycytosine chains could form an i-motif structure.[65] We do not expect dC_{20} to adopt this configuration in the CPT/dC_{20} complex due to monomeric equivalence (1:1) between CPT and dC_{20} (for which the best templating ability is achieved as previously observed[9]), and therefore, we consider the possibility of these peaks to be signatures of protonated cytosines in dC$_{20}$ chains that do not necessarily fold into i-motif configuration when complexed with CPT. This assumption is supported by the fast kinetics of 1545 and 1574 cm^{-1} bands, which will discussed more thoroughly further below. According to Keane et al.,[65] long-lived species are not produced due to simple protonation of cytosine but is rationalised in terms of the specific structural features of the i-motif. The absence of these species could indicate that i-motif is not formed. Nevertheless, i-motif could be observed if, for example, the end of the dC$_{20}$ chain is not associated with CPT in the case the two chains are not perfectly registered, or if some dC$_{20}$ chains remain uncomplexed. Observation of some i-motif populations is supported by similarities with the spectral signature observed in the dC$_{20}$ alone spectrum. Firstly, comparison of the later spectrum at pH 7 to the TRIR spectrum of dC$_{30}$ at the same pH value reproduced from the literature[65] (Figure 5.11), reveals great similarities. Then relating these spectra to the ones of dC$_{30}$ in the random[30] and i-motif configuration[65] we can conclude that dC$_{20}$ at pH 7 adopts the i-motif structure to a limited extent, in agreement with our previous CD measurements.[9] In addition, two known transient bands for polycytosines are clearly observed, in the 1545 cm^{-1} and 1585 cm^{-1} region, where the latter can be deconvoluted into 1574 and 1590 cm^{-1} bands. According to the literature, the characteristic transient band at 1574 cm^{-1} has only been observed previously in the spectra of nucleotides and polymeric strands but not in those of the single base, and has been attributed to the carbonyl stretching mode in the n$_O\pi^*$ state of dC$_{20}$.[64–66] From the above we therefore assign the band at 1545 cm^{-1} to a charge transfer between neighboring protonated and non-protonated cytosines (C$^-$:CH$^+$), as would be expected in the case of the i-motif where the bases are closely packed.[65]

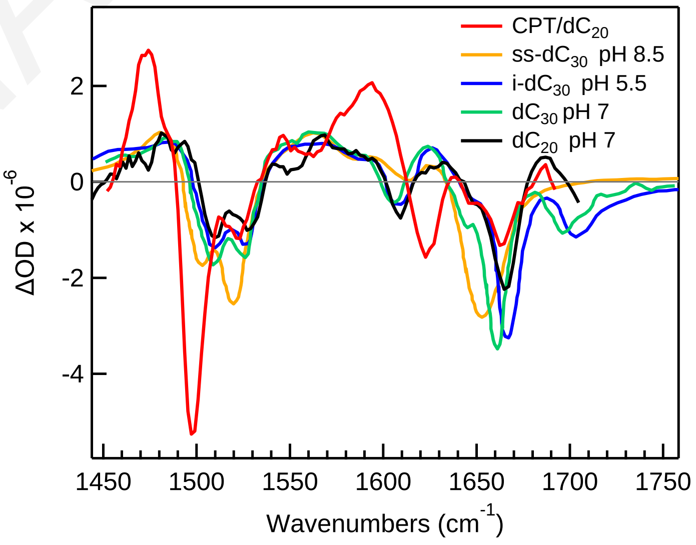

Figure 5.11. TRIR spectra after the subtraction of the background of CPT/dC$_{20}$ (red) and dC$_{20}$ at pH 7 (black) and dC$_{30}$ at pH 8.5 (yellow), 5.5 (blue) and 7 (green) (TRIR spectra of dC$_{30}$ were reproduced from the literature) at 2 ps.

Close observation of the TRIR spectra of CPT/dC$_{20}$ with excitation at 266 nm in the region 1550 to 1570 cm^{-1} shows some spectral evolution. Deconvolution of this region (Figure S5.17) revealed a new transient at 1558 cm^{-1}. According to the cytosine literature,[67] this band most likely corresponds to the formation of the cytosine anion, which could be a marker for the formation of a charge transfer state between the polymer and the ssDNA. The redox potentials of thiophene (ionization potential (IP): 4.85 eV; electron affinity (EA): 3.15 eV)[68] and cytosine (IP: 8.68 eV, EA: 0.56 eV)[69] confirm the direction of oxidation, with an electron transferring from thiophene to cytosine, with the π-stacking between thiophene and cytosine facilitating the charge transfer.[67,70,71] This new band at 1558 cm^{-1}, which corresponds to a carbonyl stretching mode of the cytosine, decays with lifetime of ~3 ps (Figure S5.24) and exhibits a 5 cm^{-1} downshift within the first ~10 ps (Figure S5.17), possibly due to a vibrational Stark effect[72] upon charge recombination, as this band is very sensitive to the electric environment.

Two other intense negative bands stand out at 1498 cm^{-1} and 1627 cm^{-1} in the TRIR spectrum of CPT/dC$_{20}$. The band at 1498 cm^{-1} is attributed to a FA of the same C=C stretch of the polymer as seen with excitation at 532 nm (Figure 5.8a) facilitated by the overlap with the polaron electronic transition. The temporal behaviour of this band is similar, with a 3 cm^{-1} shift with time. The assignment is further supported by the appearance of this FA in the spectra of CPT alone with excitation at 266 nm (Figure S5.10). The band located at 1627 cm^{-1}, however, cannot be assigned to any expected bands from the polymer. The highest wavenumber vibrations predicted for CPT from DFT calculations (Figure S5.13) are various imidazole ring vibrations and these fall in the 1570 cm^{-1} region as seen from the ATR-FTIR spectrum of the polymer (Figure S5.12). These bands do not carry any strong intensity in the Raman spectrum to lead to noticeable FA bands (see Figure S5.14), in addition to the fact they overlap strong transient bands in the TRIR spectra. Observing though the ATR-FTIR spectrum of CPT/dC$_{20}$ (Figure S5.12), a band ~1618 cm^{-1} is visible as a shoulder to the more prominent water bend band at 1650 cm^{-1}. Therefore, this band must correspond to a base vibration. Based on literature,[73,74] the cytosine ring stretching vibration expected in this region is the ring mode stretch $\nu(C_5{=}C_6) + \nu(N_3{=}C_4) + \nu(C_2{=}O_7)$. Π-π stacking of the thiophene and cytosine rings in the complex found in our previous work[9] followed by generation of the charge-transfer complex upon photoexcitation must perturb the environment of the base ring leading to enhanced bleach intensity of this band compared to the 266 nm excited TRIR spectra of dC$_{20}$ alone. Interestingly this band is observed in the TRIR spectra of CPT/dC$_{20}$ with excitation at 532 nm (Figure S5.15a) but not in the TRIR spectra of CPT alone at 532 nm and 266 nm (Figure S5.16 and S5.10b respectively), further excluding this as a polymer vibration. This suggests that even without direct excitation of the ssDNA, because of π-π stacking between the base and thiophene rings and the generation of a charged species on the polymer chain, the ring environment is severely perturbed, leading to significant bleaching of the base ring vibration, rather than the usually more strongly appearing carbonyl bands (Figure S5.15b). Similar signatures of DNA bleaching bands were observed in TRIR spectra of excited metal complexes bound to different DNA sequences and were used as indicators of the binding site on the DNA.[75,76]

The kinetics of CPT/dC_{20} and dC_{20} alone (Table 5.4) are tremendously different, revealing the strong effect of complexation on ssDNA dynamics. Specifically, starting with dC_{20} alone, the 1574 cm^{-1} band exhibits slow kinetics on the scale of hundreds of ps and the 1545 cm^{-1} band decays even more slowly. Even though the kinetic traces of these two bands are noisy, the difference in the kinetics of these two bands (see Figure S5.18 and S5.19) is in line with the literature (lifetime of ~150 ps for 1574 cm^{-1} and ~240 ps for 1545 cm^{-1} band).[65] Surprisingly, the respective cytosine bands when complexed with CPT recover much faster than expected (~4 and 30 ps, respectively, Figure S5.20 and S5.21), suggesting that complexation contributes to faster relaxation of cytosine to the ground state. This explains the larger ground state population, evidenced by the transient peak at ~1590 cm^{-1} due to ground state vibrational absorption and subsequent relaxation of dC_{20}, which is more intense in the CPT/dC_{20} spectrum.

Table 5.4. Time constants (τ_1, τ_2) obtained with a biexponential global fit of dynamics of background and the intensity of bands for dC_{20} and CPT/dC_{20} following 266 nm excitation.

	dC_{20}		**CPT/dC_{20}**	
Background (ps)	-	-	0.45±0.01	12±1
1498 cm^{-1} band (ps)	-	-	1.5±0.3	10±2
1627 cm^{-1} band (ps)	-	-	2.2±0.3	35±34
1558 cm^{-1} band (ps)	-	-	0.2±0.2	3.3±1.8
1545 cm^{-1} band (ps)	2.4±1.0	300±70	0.5±0.1	40±10
1577 cm^{-1} band (ps)	4.7±2.4	150±30	0.1±0.1	3.7±0.6

The occurrence of charge transfer between dC_{20} and CPT is also evidenced by the existence of background absorption, attributed to a charge transfer state. The kinetics of the background and the vibrational bands were analysed, revealing that the FA at 1498 cm^{-1} and the background absorption undergo a double exponential decay with time constants ~1.5 and 10 ps (Figures (S5.22-S5.23), Table 5.4) in both cases, which suggests they are associated with the same excited state process. These two markers combined with the formation of cytosine anion and its decay on a similar timescale (lifetime ~3 ps, see Figure S5.24), strongly support we are observing an electronic charge-transfer state in the mid-IR spectra.

TRIR measurements in CPT/dA$_{20}$ and dA$_{20}$ demonstrate a close similarity (Figure 5.12), as the spectra in both cases are consistent with the known peaks of adenosine reported in the literature, e.g. the intense bleach at ~1630 cm^{-1} (C=N, C=C ring stretches),[77] suggesting that the complex does not disturb the adenosine structure or dynamics. This is consistent with the weak binding between the polymer and dA$_{20}$ as was implied by our previous UVRR results.[9] In this case, we do not observe any evidence of charge transfer that could lead to new transient peaks due to the charged species, broad electronic absorption background and Fano antiresonances of CPT such as the one at 1498 cm^{-1} in the TRIR spectra of CPT/dC$_{20}$. Charge transfer must be restricted due to the absence of π-stacking interactions between thiophenes and adenines. In addition, the fact that the absorption of dA$_{20}$ at 266 nm is five times larger than the absorption of CPT, explains the absence of any signal attributed to CPT.

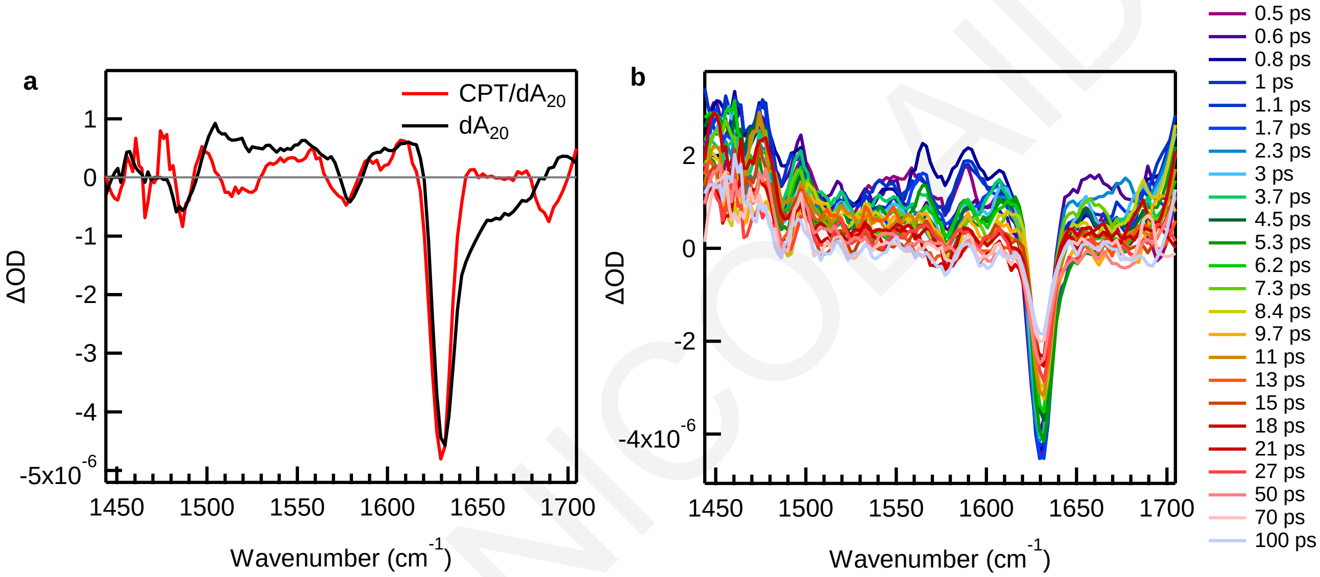

Figure 5.12. (a) TRIR spectra after the subtraction of the background of CPT/dA$_{20}$ (red) and dA$_{20}$ at pH 7 (black) at 2 ps (b) TRIR spectra of CPT/dA$_{20}$ without background subtraction with excitation at 266 nm.

5.2.3 Time-resolved Raman spectroscopy

In order to avoid the complication coming from the existence of polaron absorption in the TRIR spectra, we also attempt to exploit the advantages of Raman Spectroscopy by using Impulsive Stimulated Raman Scattering (ISRS) and Femtosecond Stimulated Raman Spectroscopy (FSRS). This is because, time-resolved Raman spectroscopy enables background-free resonantly enhanced recording of ground- and excited-state Raman spectra, which can offer new and detailed perspective on the structural properties and dynamics of conjugated polymers.

Since CPT/dC$_{20}$ display the most noteworthy templating ability among the ssDNA tested, it is very interesting to explore more thoroughly the structural evolution of the polymer in this complex in the excited state using Raman spectroscopy. This could complement the knowledge gained from TA and TRIR measurements, with the aim of identifying the excited state species (excitons and charge carriers) produced after photoexcitation, their influence on the structure of the polymer backbone and the kinetics of the processes in which they are involved. To track the photogenerated excitons and/or charges in the polymer backbone, selective probing of the transient structural changes of the polymer backbone is necessary during its photoexcited evolution.[63] The requirement for selectivity in excitation wavelength stems from the fact that the intrachain structure is normally characterized by a distribution of segments of variable conjugation lengths, that can host localized excitations.[60] Therefore, selective excitation would provide further insights into how the nature of the local structure impacts the excited state processes and address the mechanisms that drive nonequilibrium relaxation of photoexcited polymer.

As previously mentioned, the primary phases for the excited state relaxation are (1) exciton localization on ~100 fs timescale, (2) long-range torsional reorganization, that planarizes and stabilizes the quinoidal structure of the excited state and (3) excitonic energy transfer (EET) through which energy migrates to lower energy sites, characterized by different degrees of conjugation length. Both the latter processes occur on subpicosecond and picosecond timescales and are expected to planarize the polymer backbone of the exciton.[61,78] These processes are difficult to be interrogated experimentally, due to the fast timescale on which they occur and the required sensitive probe of ultrafast nuclear dynamics to detect the details of the relaxation process between the initially created and subsequently relaxing states.[61,79]

Time-resolved resonance enhanced Raman spectroscopy has been reportedly exploited as a direct method for interrogating evolution in conformation and photogenerated species in conjugated polymers that occurs through the course of excited-state relaxation.[27,60,61,63,78,80,81] The vibrational frequencies of various Raman-active modes and most notably the symmetric C=C stretching mode, similarly as in TRIR spectroscopy, are directly sensitive to the extent of excited state delocalization along a polymer backbone.[61,78] Taking into consideration, that the excited states of conjugated polymers are known to be highly delocalized by nature,[60,61,63,80,81] we expect that the Raman spectral region of C-C and C=C stretching bands collected in resonance with transitions between singlet excited states will exhibit frequency and intensity trends ascribed to variation in the local effective conjugation length, revealing heterogeneities among excited state species (excitons of different conjugation length and/or polarons).[60]

5.2.3.1 Impulsive Stimulated Raman Spectroscopy (ISRS)

Two femtosecond pulses are exploited in each case presented below for measuring the impulsive stimulated Raman spectra (ISRS), as mentioned in section 3.4.2, a Raman pump pulse and a probe pulse. The vibrational frequencies of the resulting Raman spectra are retrieved after Fourier-transformation.[82–86] In this work, ISRS measurements were conducted using three different sets of pulses, interrogating with each set different species. These are: (1) Raman pump at 500-600 nm (on resonance with absorption) and probe pulse at 600-700 nm (on resonance with SE) (see spectra at Figure 5.13), (2) Raman pump at 600-700 nm (on resonance with SE) and probe pulse at 500-600 nm (on resonance with absorption) (Figure 5.15) and (3) Raman pump at 500-600 nm (on resonance with absorption) and probe pulse at near-IR 800-970 nm (on resonance with excited-state absorption) (Figure 5.16).

The pump pulse used in case (1) was chosen to be in-resonance selectively with only the $S_0 \rightarrow S_1$ transition to impulsively generate vibrational coherences on the excited state.

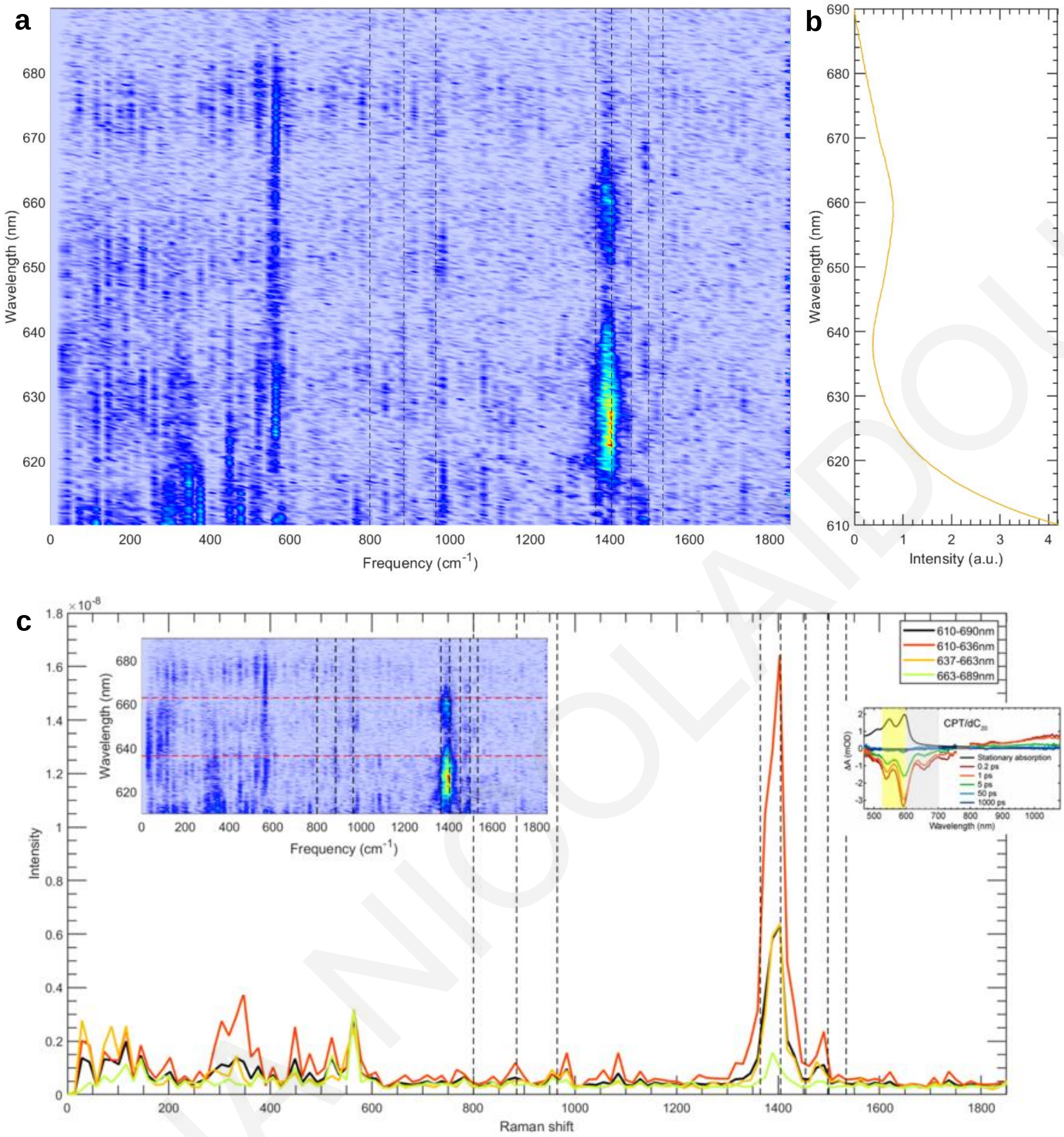

Figure 5.13. (a) 2D broadband ISRS spectrum of CPT/dC$_{20}$ as a function of the probe wavelength and the Raman frequency. (b) Stimulated emission spectrum (c) Comparison of ISRS spectra integrated over different probe wavelength regions (see legends) from 610 to 689 nm (stimulated emission), after Fourier transform of the coherent oscillations. The different probe wavelength regions and all the prominent bands are displayed by red and black dashed lines, respectively, in the 2D broadband ISRS spectrum (left inset) in panel c. The inset on the right side of panel c corresponds to TA spectra, recorded following excitation at 400 nm at selected time delays (adopted by Figure 5.2), where the yellow box marks the region of pump excitation wavelengths (on resonance with absorption: 500-600 nm) and the grey box marks the region of probe wavelengths (on resonance with SE: 600-700 nm).

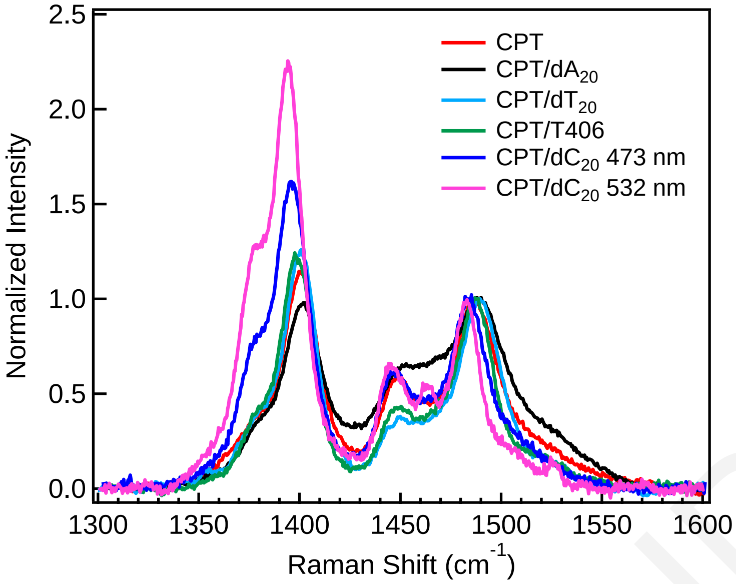

Figure 5.14. Ground state Resonance Raman (RR) spectra with visible excitation at 435.69 nm for CPT/dT$_{20}$, at 473 nm for CPT, CPT/dA$_{20}$, CPT/T406 and CPT/dC$_{20}$ and at 532 nm for CPT/dC$_{20}$ in PBS buffer with a concentration of 1.5x10^{-4} M (monomeric basis) at 20 °C.

The ISRS spectra at Figure 5.13 exhibit an intense band at 1350-1400 cm^{-1} and a band with modest intensity at 1450-1500 cm^{-1} attributed to C-C and C=C stretching modes respectively, according to the corresponding ground state modes with excitation at 532 nm (1394 cm^{-1} and 1484 cm^{-1} see section 4.2.2 and Figure 5.14) and the reported Raman spectra of polythiophenes with alkoxy side chain in the literature.[87,88] The expected splitting of the latter band induced by the existence of alkoxy side chain is not observed in the ISRS spectra probably due to limited spectral resolution of the method. According to Batignani et al.,[89] ISRS can monitor vibrational coherences over only a restricted temporal window, upper bounded by a maximum time delay (T_M) between the Raman pulse and probe pulse and therefore the ISRS lineshapes are generally affected by a limited spectral resolution $\Delta\tilde{\nu} = \frac{1}{cT_M}$. We observe that the relative intensity of C-C to C=C stretching bands is increased, as well as a small red-shift (~3 cm^{-1}, more distinct in Figure S5.25) of these bands as the probe wavelength is increased. These changes are consistent with the presence of enhanced planarity of backbone conformation, attributed to the fact that we are probing selectively more planar moieties when the probe wavelength increases. The position of the bands does not differ significantly from the ground state wavenumbers of the respective bands. We would expect larger shifts stemming from the greater delocalized character relative to the ground state, leading to increased conjugation length. Furthermore, we observe a band at ~560 cm^{-1} attributed to the thiophene breathing mode, which is also evident in the ground state spectrum (Figure S5.26).

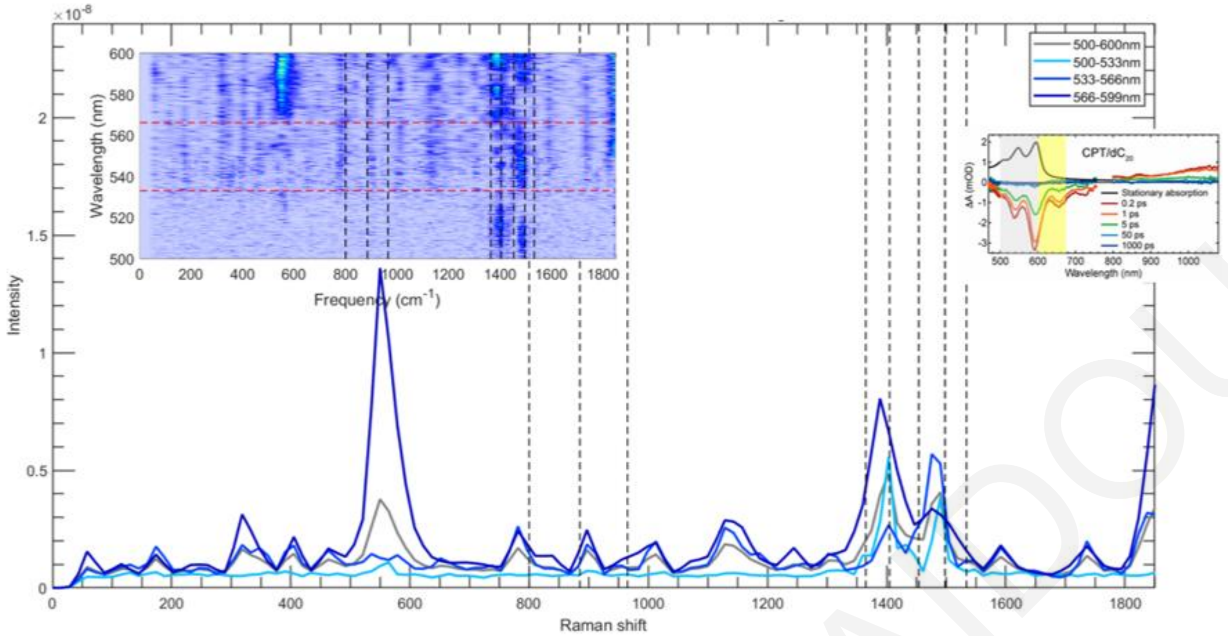

Figure 5.15. Comparison of ISRS spectra of CPT /dC$_{20}$ integrated over different probe wavelength regions (see legends) from 500 to 599 nm (absorption), after Fourier transform of the coherent oscillations. The different probe wavelength regions and all the prominent bands are displayed by red and black dashed lines respectively in the 2D broadband ISRS spectrum (left inset). The inset on the right side corresponds to TA spectra, recorded following excitation at 400 nm at selected time delays (adopted by Figure 5.2), where the yellow box marks the region of pump excitation wavelengths (on resonance with SE: 600-700 nm) and the grey box marks the region of probe wavelengths (on resonance with absorption: 500-600 nm).

Correspondingly, in case (2) the excitation wavelength is in resonance with $S_1 \rightarrow S_0$ transition, meaning that is a preresonant pulse with respect to ground state absorption ensuring that no excited-state population is generated and therefore vibrations in the ground electronic state are expected to be isolated. In the range of 1300-1550 cm^{-1} of the spectra shown at Figure 5.15 and S5.27 we observe analogous spectral shape to the ground state (Figure 5.14). We could not detect variations in the position of the peaks in this spectral range when probing at 500-566 nm and any possible shifts are not distinguishable due to the limited resolution.[59] The spectrum with the highest probe wavelength at 566-599 nm seems to be the only one that exhibits red-shift of both C-C (10 cm^{-1}) and C=C (15 cm^{-1}) stretching bands compared to ground state spectrum, with the C-C band to become also more intense relatively to C=C band, in accordance with the trend observed at Figure 5.13. This is expected as this range of probe wavelengths (566-599 nm) almost falls into the SE region and we are probing different population with increased contribution of excited state. The variations of the position of the peaks in the probe range of 500-566 nm compared to the excited state Raman spectra at Figure 5.13 are more distinct in Figure S5.28. There are also clear discrepancies in the relative intensity of C-C to C=C, which is increased drastically, as previously mentioned, when we excite CPT/dC$_{20}$ in resonance with absorption, compared to the spectra when we excite in preresonance relative to absorption, reminiscing the ground state ratios of these bands. The ~560 cm^{-1} is again evident in Figure 5.15, with its intensity in the spectrum of 566-599 nm probing range to largely exceed the intensity of the bands at the spectral range of 1300-1550 cm^{-1}. The fact that this band is intensified when the excited state contribution is significant, indicates that this band is also affected by the increasing contribution of the quinoid structure. The higher planarity of polymer backbone in the excited state could be linked to larger polarizability along the polymer chains that may result in enhancement of this band (~560 cm^{-1}) that arises from a ring breathing mode.[63] All the above data support the fact that the backbone planarization is a result of various collective motions in the polymer.

In Figure 5.16 the excitation wavelength is on resonance with $S_0 \rightarrow S_1$ transition and the probe wavelength region is resonant with excited state absorption, enhancing the vibrational coherences on the excited state. The fact that we detect changes in regard to the ground state (Figure 5.14 and 5.15), which are increase of the relative intensity of C-C to C=C stretching bands and red shift of these bands, indicates greater delocalized character of the excited state. We would expect that as the Raman pump in the case (1) and (3) is the same and in resonance with the absorption the same population would be probed. However, comparing these spectra (Figure 5.16) with the Raman spectra at Figure 5.13, we observe that the shifts are larger for both bands (~20 cm^{-1} for C-C band and ~10 cm^{-1} for C=C band) compared to the shifts observed at Figure 5.13. (~7 cm^{-1} for both bands). We also observe no shifts or clear differences in the relative intensities of C-C to C=C bands by varying the probe wavelength region, which could mean that the probed segments, when in resonance with excited state absorption, are different than in case (1) and have not only greater delocalized character relative to the ground state but also exhibit the largest possible conjugation length, probably indicating the existence of polarons. Furthermore, in the spectral region of interest (1350-1550 cm^{-1}), a distinct peak stands out at ~1535 cm^{-1}, which could be ascribed to antisymmetric C=C stretching band.[27,90]

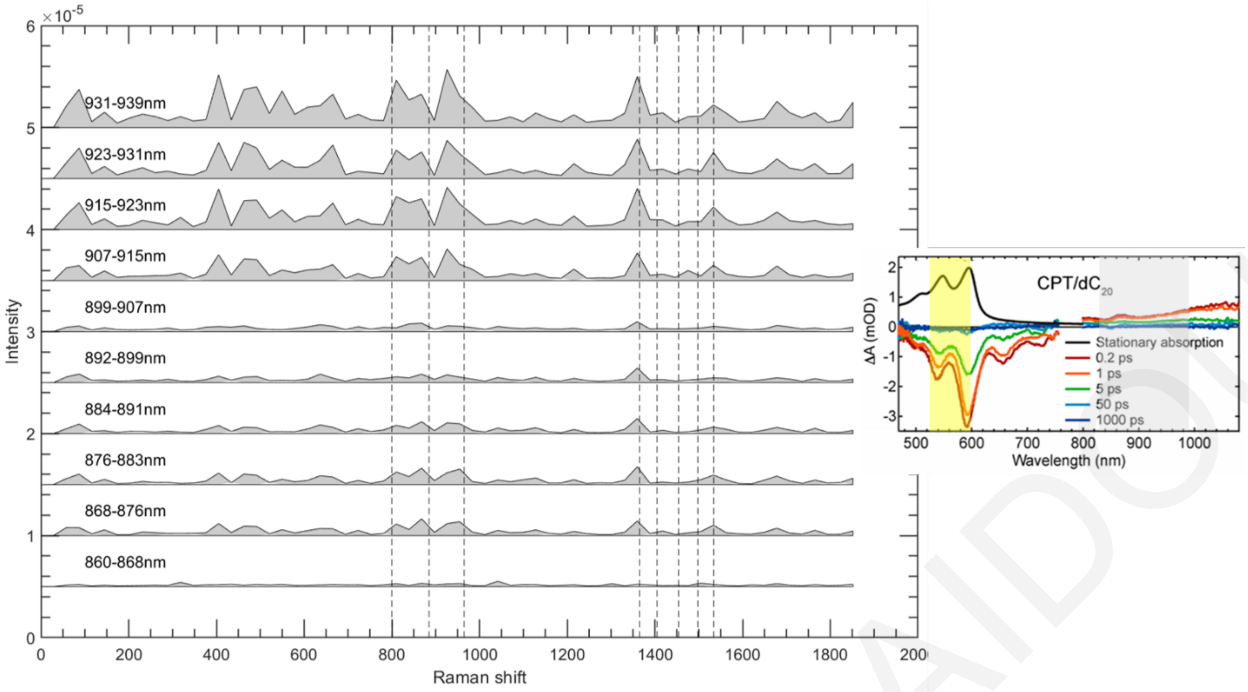

Figure 5.16. Comparison of ISRS spectra of CPT /dC$_{20}$ integrated over different probe wavelength regions (specified on the left of each spectrum) from 860 to 939 nm (excited-state absorption (ESA)), after Fourier transform of the coherent oscillations. The inset at the right side corresponds to TA spectra, recorded following excitation at 400 nm at selected time delays (adopted by Figure 5.2), where the yellow box marks the region of pump excitation wavelengths (on resonance with absorption: 500-600 nm) and the grey box marks the region of probe wavelengths (on resonance with excited-state absorption: IR 800-970 nm).

However, according to the literature,[9,27,90–92] this peak is usually located at lower wavenumbers (between 1510-1520 cm^{-1}) and the increase of this band indicates an evolution in the dihedral angle between monomers in the direction of a less planar geometry along the polymer backbone.[27,90,92] This contradicts with the previous observations leading to opposite conclusions about the conformational changes. Combining the fact that the excited state is reportedly characterized as more delocalized by nature[60,61,63,80,81] and that the spectra have low signal to noise ratio in general, as several bands emerge (such as ~1600-1800 cm^{-1}), that cannot be ascribed to any vibrational modes according to the calculated spectra of CPT (Figure S5.13), we suspect that the band at 1535 cm^{-1} is part of noise as well.

5.2.3.2 Stimulated Raman Spectroscopy (SRS)

In Stimulated Raman Scattering (SRS), Raman enhancement and greater sensitivity is achieved using two incident laser beams, a narrowband picosecond Raman pump pulse and a broadband femtosecond Stokes or anti-Stokes (red and blue side respectively) probe pulse and when their energy difference coincides specific vibrational frequencies, the Raman signal of the corresponding modes amplifies.[93] The red (Stokes) side of the spectrum measured in the region at longer wavelength with respect to the Raman pump display only positive peaks, while the blue (anti-Stokes) side of the spectrum measured in the region at lower wavelength with respect to the Raman pump constitutes of both positive and negative peaks, that correspond to Raman gain and loss signals after excitation.[94] The SRS spectra of the red side shown in Figure 5.17 (see Figure S5.29, S5.30 and S5.31 for temporal evolution of these spectra) using Raman pump pulse at 599, 614 and 644 nm (599 and 614 nm on resonance with A_{0-0} while 644 nm is located on at the red edge of the absorption, see Figure S5.2a), exhibit the same number of vibrational bands with spontaneous Raman spectra at 532 nm of CPT/dC_{20} (Figure 5.14). The differences of the SRS spectra with the Raman pump excitation wavelength are linked to the planarity of the excited moieties. Hence, the Raman pump wavelengths used for excitation (599, 614 and 644 nm) interrogate excited state

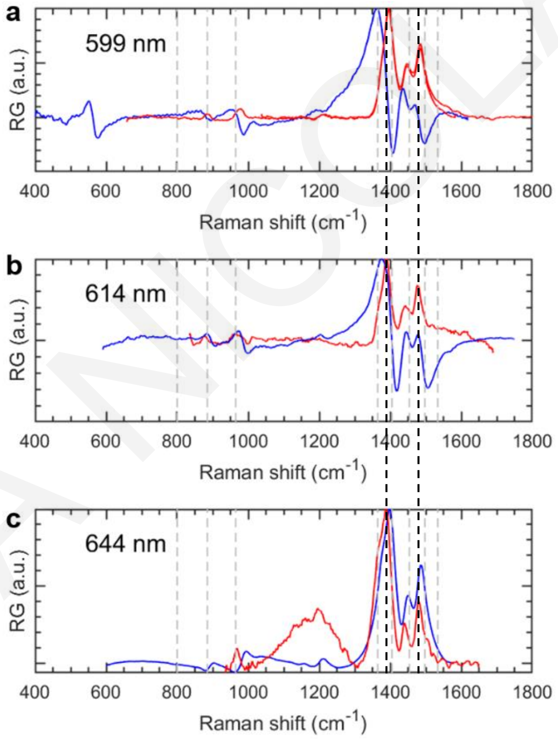

Figure 5.17. Comparison SRS spectra of CPT /dC_{20} when probing at blue and red side of Raman pump wavelength (indicated by the colour of each spectrum) using (a) 599 nm, (b) 614 nm and (c) 644 nm as Raman pump wavelengths.

subpopulations characterized by different degrees of delocalization. Higher-energy Raman excitation probes sub-populations characterized by shorter effective conjugation length and low energy Raman excitation probes segments with longer conjugation lengths.[61] This is reflected by the greater red shift of the C=C stretching band and relative intensity ratio of C-C to C=C stretching modes, as we move from 599 to 644 nm Raman pump, when probing at the red side. On the other hand, the SRS spectra with excitation at 599 and 614 nm, when probing on the blue side, display a dispersive feature centered at ~1390 cm^{-1}. Dispersive features are observed when the Raman pulse and the probe pulse are no longer well separated, the Raman pump wavelength is on resonance[95] and are centered around the original peak position, altering the position and the line shape of the corresponding Raman mode.[94] The fact that the spectrum with excitation at 644 nm consists of only positive peaks could be attributed to the fact that the excitation wavelength is located far the absorption maximum of CPT/dC_{20}. This is in accordance with the studies of Lim et al.,[93] who have investigated the dependence of the stimulated Raman loss signal on Raman pump intensity and demonstrated that pronounced spectral modulation in stimulated Raman loss is observed in the strong pump regime.

5.2.3.3 Femtosecond Stimulated Raman Spectroscopy (FSRS)

We then have measured the stimulated Raman spectrum with the same narrow picosecond Raman pump and broad-band femtosecond probe wavelengths used for SRS spectroscopy, after selective photoexcitation of the polymer in the CPT/dC_{20} complex with a third pulse, the femtosecond actinic pump beam at 550 nm. This three-pulse Raman measurement is known as Femtosecond stimulated Raman scattering (FSRS). FSRS offers the possibility to collect structural information with high spectral resolution (10 cm^{-1}) and explore processes at sub-picosecond timescale, by improving the temporal precision, as it is limited to the femtosecond actinic pump and probe pulse durations ($\Delta t > 50$ fs).[36–38] This enables monitoring of the ultrafast process that occur immediately after photoexcitation and determine the conformational changes that the polymer backbone undergoes, that could be assigned to production of specific excited state species.

Photoexcitation of polythiophene in solution has been reported to result in the generation of singlet excitons as major species.[63,78] However, according to TRIR measurements and in agreement with the literature,[96] a considerable fraction of polarons is generated even after photoexcitation of the sample in a solution, when the appropriate conditions are met. These conditions include increased delocalization length of polymer backbone and ultrafast dissociation of hot excitons (on the <500 fs timescale), in order to prevent the occurrence of exciton relaxation, by having enough excess energy to lower the binding energy between the hole and its respective counterpart and achieve delocalization of the produced charge carriers. The backbone planarization is the key aspect that drives the generation of the delocalized hot-polaron, meaning that ground state planarity plays a critical role in determining the charge generation yields in the excited state.[63,80,96–98]

Figures 5.18a-5.19a show the SRS spectra of Stokes bands when Raman pump is at 599, 614 and 644 nm respectively with or without the excitation with actinic pump. Normalization of these spectra with respect to the actinic pump off intensity was conducted (Figures 5.19c,

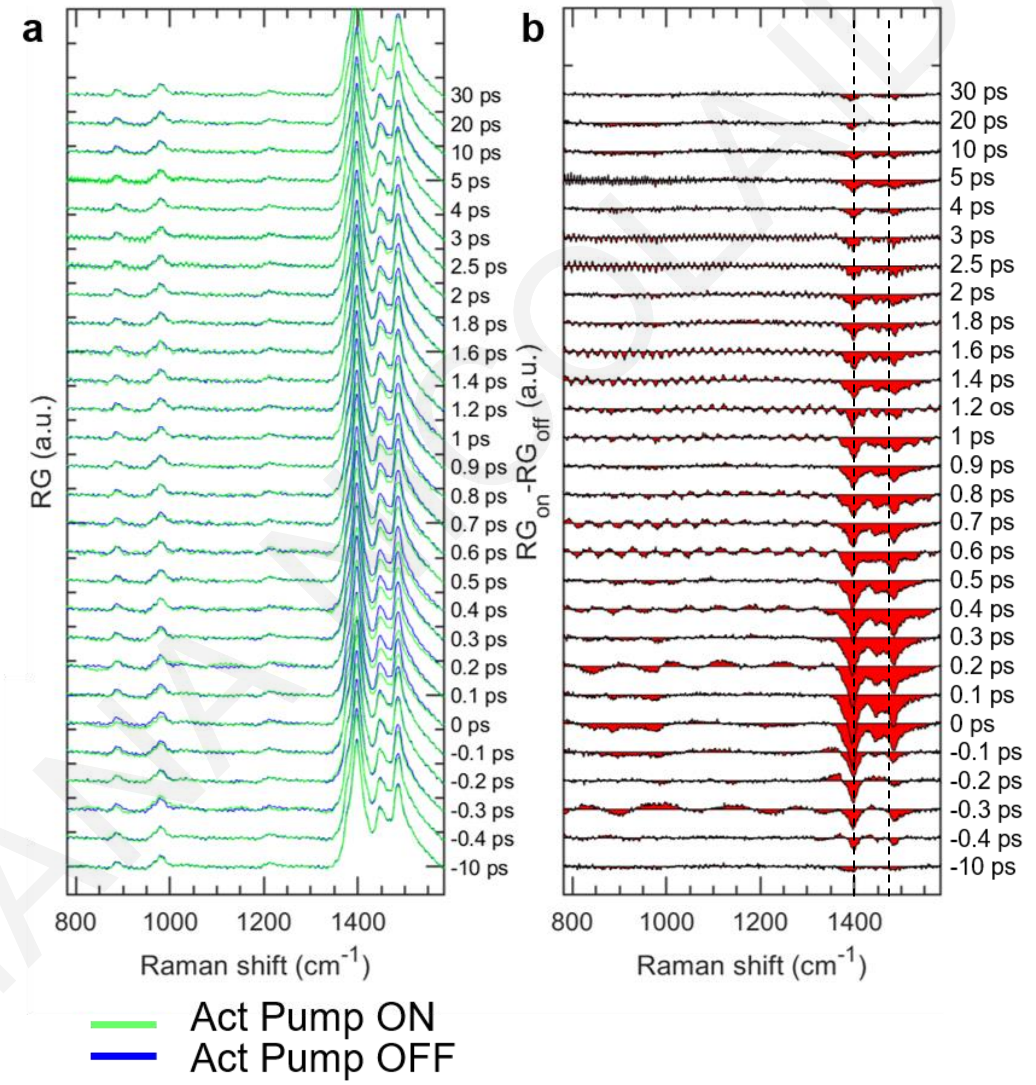

Figure 5.18. (a) Temporal evolution of actinic pump on and pump off spectra (green and blue spectra respectively) of CPT /dC_{20} using 599 nm as Raman pump wavelength, when probing on the red side of Raman pump wavelength (center of spectral region: 643 nm). (b) Difference of actinic pump on – pump off spectra in panel (a) at different time delays.

S5.32a, S5.38a), but only in the spectra collected via Raman excitation at 614 nm we could distinguish some bandwidth variations that produce temporal signatures. Therefore, from the difference of the pump on – pump off SRS spectra on the red side before (Figure 5.19b) and after (Figure 5.19c) normalization by the actinic pump off intensity via Raman excitation at 614 nm (red), we could detect apparent variations as time evolves that are linked to the conformational planarization after photoexcitation.[81] The changes in the spectra before normalization (Figure 5.19b) include a red shift of the bleach peaks C-C and C=C by ~7 cm^{-1} compared to ground state spectrum and increase of the relative intensity of C-C to C=C stretching bands until 0.3 ps and then gradually decreases concurrently with the blue shift towards the initial position of ground state (changes are finalized at ~1 ps). In the spectra after normalization (Figure 5.19c) we observe a positive feature at ~1370 cm^{-1}, ascribed to C-C stretching bond, which is ~20 cm^{-1} red shifted, compared to the ground state spectrum.

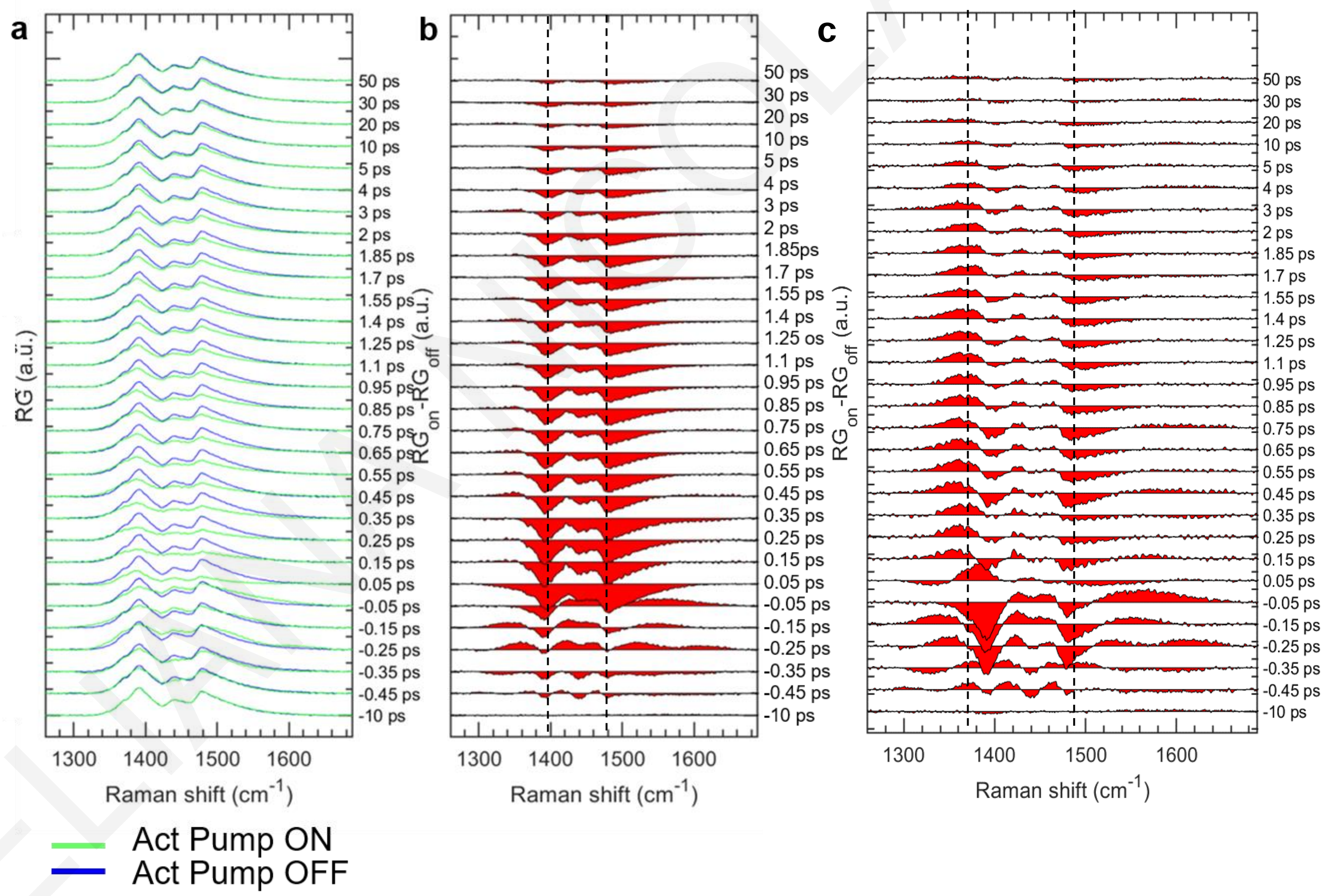

Figure 5.19. (a) Temporal evolution of actinic pump on and pump off spectra (green and blue spectra respectively) of CPT /dC$_{20}$ using 614 nm as Raman pump wavelength, when probing at red side of Raman pump wavelength (center of spectral region: 666 nm). (b) Non-normalized and (c) normalized difference of actinic pump on – pump off spectra in panel a at different time delays.

The position of this positive peak and the observed shift resemble the ISRS spectra in Figure 5.16. For excited polythiophene backbone, which has greater delocalized character relative to its ground state,[27,60,81] the red shift can be interpreted as the lengthening of the effective delocalization. According to the literature[27,63,80] a possible mechanism after photoexcitation could involve either ultrafast exciton localization, or hot and delocalized polaron formation indicated by red shift of the aforementioned bands due to reorganization from the ground-state geometry to a more planar configuration. The subsequent blue shift of these modes is assigned to vibrational cooling[63,81] or polaron localization (in accordance with the blue shift of 1498 cm^{-1} band in the TRIR spectra of CPT/dC$_{20}$).

The Raman spectroscopic signatures that indicate polaron formation is a prominent red shift of C=C stretching mode as large as ~20 cm^{-1} (in polythiophene films) and increased relative intensity of C-C to C=C, while the exciton features show a small red-shift of 3-4 cm^{-1} compared to the ground state modes.[21,37] The red-shift indicates quinoidal contribution as assigned by Bragg and co-workers previously.[81] When the polymer adopts this structure, electron density shifts away from C=C bonds, resulting in a red shift and an increase near the inter-ring stretch.[78] Even though the shift can be attributed to polaron formation, we have to consider that the sample is in solution, so the generation of these species is limited compared to films studied in the literature.

Further exploitation of the FSRS data led to the analysis of the kinetics (Figures S5.32, S5.34, S5.35, S5.37, S5.38, S5.40) of integrated difference signal of the actinic pump on-pump off spectra. The extracted time constants support the assumption of polaron formation after photoexcitation. According to TA measurements mentioned above the average lifetime of excited state absorption of the S$_1$ singlet exciton at ~1000 nm is very short, equal to 14 ps for CPT/dC$_{20}$ (Table 5.1). In contrast, the kinetics of the main indications of polaron formation within TRIR spectra, which are the Fano-antiresonance peak at 1498 cm^{-1} and the existence of background due to polaron absorption exhibit larger time constants of 33 and 35 ps respectively. Excitons are known to relax faster than polarons, while polarons exhibit longer lifetimes due to slower recombination rate in comparison with that for excitons.[63] Thereby, the fact that the time constants extracted by the fit of kinetics of FSRS spectra are above 30 ps, indicate strongly the generation of polarons and confirm the above argument. Nevertheless, the existence of considerable amount of short-lived excitons is certain and contributes significantly to the extracted time constants and the variations of the FSRS spectra. Hole-polarons in P3HT neat films have been reported to have a lifetime of 800 ps, much slower than what we observe in our spectroscopic analysis of the CPT-ssDNA complexes.

The FSRS spectra of Stokes bands in Figure 5.20 with Raman pump excitation at 644 nm have very small signal, making it difficult to extract any information. The origin of the low signal is still unknown. On the other hand, the anti-Stokes side of FSRS spectra via Raman pump wavelength at 599 and 614 nm, depicted in Figures S5.34, S5.37 show a dispersive feature at ~1390 cm^{-1}, that resembles the SRS spectra with the Raman pump pulse selection mentioned above. The normalized FSRS spectra in Figures S5.33, S5.36, S5.39 are very noisy and did not contribute to the structural characterization. The spectra on the blue side via Raman pump at 644 nm (Figure S5.40) are different than the FSRS spectra at 599 and 614 nm, being increasingly intense and resemble closely the ground state spectrum (Figure 5.14) with only subtle variations at different time delays. The lack of significant changes in the band shape and the modest red shifts of the loss C-C and C=C stretching bands with time of the spectra, as well as the resemblance with the ground state spectrum indicates that with

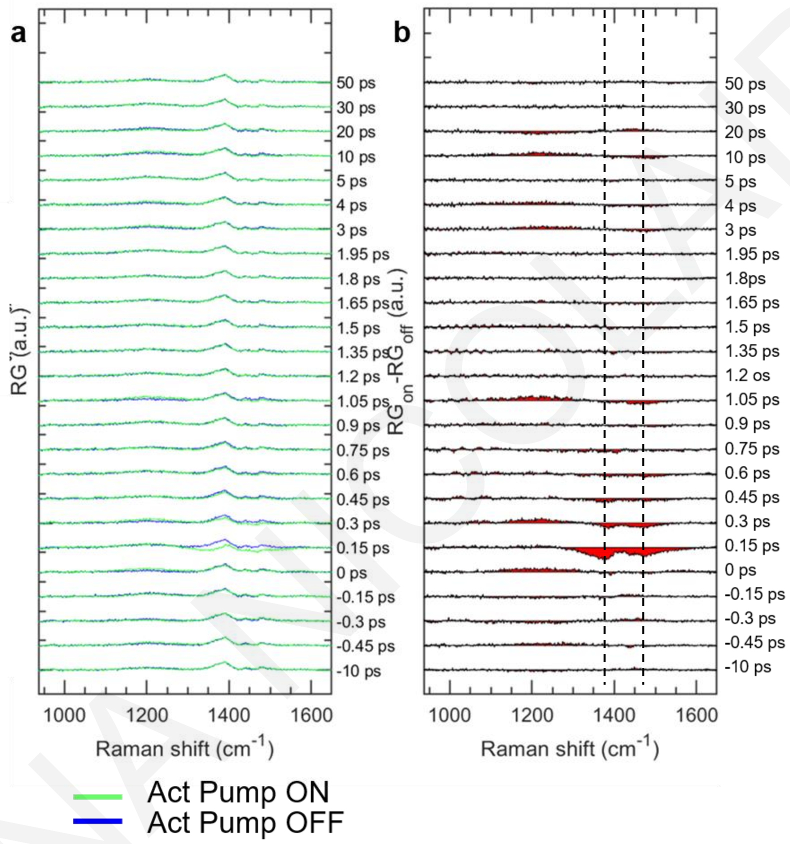

Figure 5.20. (a) Temporal evolution of actinic pump on and pump off spectra (green and blue spectra respectively) of CPT /dC$_{20}$ using 644 nm as Raman pump wavelength, when probing on the red side of Raman pump wavelength (center of spectral region: 704 nm). (b) Difference of actinic pump on – pump off spectra in panel a at different time delays.

this Raman pump wavelength, probing of polaron formation was not successful as no enhancement of the signal of this population through resonance was achieved. Transient Raman of polythiophene samples has been previously reported to detect the presence of excitons and polarons by selectively exciting these species using pump wavelengths on resonance with their absorption, which are ~900 nm for polarons and ~1100 nm for excitons.[63] Therefore, new sets of three-pulse experiments including these wavelengths could result in better discrimination between the Raman signals of excitons and polarons.

5.3 Conclusions

In summary, TA spectroscopy displayed the formation of intrachain delocalized excitons with a relatively short lifetime and the absence of any long-lived polaron or triplet states. Subsequently, TRIR measurements on complexes of a CPT polymer with ssDNA provided greater detail and largely enhanced the knowledge on the excited state behaviour. We find that both complexes, CPT/dC$_{20}$, a rigid complex with limited geometric relaxation and CPT/dA$_{20}$, a flexible complex, form intrachain polarons following visible excitation, however, to a lesser extent for the latter due to increased intrachain disorder. This polaron decays faster than the delocalized polaron formed in the case of CPT alone and the CPT/dC$_{20}$ complex. Transient Raman contributed significantly to the detection of ultrafast polaron formation, which occur on the <0.3 ps timescale, even though excitons are still major contributors to the excited state population. On a timescale of few ps, vibrational cooling or polaron recombination result in a polymer backbone structure with shorter conjugation length resembling the ground state conformation.

The effective templating of CPT with ssDNA chains (such as dC$_{20}$) through non-covalent interactions modified the photophysical behaviour of both partners. UV excitation through TRIR spectroscopy revealed the modification of the excited state behavior of dC$_{20}$, facilitated by the existence of numerous π-stacking interactions between the two components. A new band associated with the cytosine anion was observed, which combined with background absorption point to the formation of a charge transfer complex between CPT and dC$_{20}$, in contrast to the CPT/dA$_{20}$ case, where the TRIR spectra solely reflect the excited state behaviour of the oligoadenosine. These results suggest that even though extensive interactions between the scaffold and the polymer are useful to control the conformation, the ssDNA is not a mere spectator scaffold and one needs to consider how this affects the photophysics that ultimately guide the application of these complexes in molecular electronics.

5.4 Experimental section

5.4.1 Materials and Sample Preparation

CPT characteristics, the three single-stranded oligonucleotides (ssDNAs) which are dA_{20}, T406 and dC_{20}, stock solutions preparation and PBS composition are described in section 4.4.1. 1.2 mg of P3HT (Mw~50 kDa, PDI=1.5) were dissolved in 1 mL of d-chlorobenzene and then diluted to produce a solution with concentration of 1 mM for TRIR measurements.

5.4.2 Experimental details

Ultrafast Transient Absorption (TA) spectroscopy. TA measurements were carried out in the research group of Prof. Natalie Banerji, at the Department of Chemistry at the University of Bern. The spectroscopic data were collected by Dr. Lisa Peterhans, who carried out the analysis and interpretation of the TA data as well. TA spectra were recorded using femtosecond pulsed laser pump−probe spectroscopy. The solutions were placed in a quartz cuvette with an optical path length of 2 mm (Starna Cells Inc.) placed inside the temperature-controlled holder and held by a piece of aluminum. Pump excitation at 400 nm (200 fs resolution) was achieved by frequency doubling the fundamental 800 nm laser output (from a Ti:sapphire laser system with regenerative amplification providing 35 fs pulses at a repetition rate of 1 kHz, Astrella, Coherent). The pump diameter was about 1 mm, and the pump intensity was 400 nJ with the 400 nm excitation (fluence: 13 $\mu J/cm^2$). The probe beam consisted of a white light continuum (∼450−1200 nm) generated by passing a portion of the 800 nm amplified Ti:sapphire output through a 5 mm thick sapphire window. Either 720 nm low pass filters or 850 nm long pass filters were used to remove the remaining fundamental intensity from the white light, when the visible and the near-infrared (nIR) parts of the spectrum were recorded separately. The probe intensity was negligible compared to the pump intensity, and the spot size was much smaller (probe energy of <5 nJ, probe diameter of about 160 μm). The probe pulses were time-delayed with respect to the pump pulses by means of a computer-controlled translation stage. The probe beam was split before the sample into a signal beam (transmitted through the sample and overlapped with the pump beam) and a reference beam. The signal and reference beams were detected separately using a pair of spectrographs (home-built prism spectrometers) equipped with 512 × 58 pixel back-thinned CCDs (Hamamatsu S07030−0906) and assembled by Entwicklungsbüro Stresing, Berlin. The pump beam was chopped at half the amplifier frequency to improve the sensitivity of the setup. The transmitted intensity of the signal beam was recorded shot-by-shot, and it was corrected for laser intensity fluctuations using the reference beam. The single shot TA spectra measured time delays (between −4 ps and 1 ns) was scanned five times, without any noticeable signs of degradation. Wavelength calibration was accomplished with a series of 10 nm bandpass filters. To avoid polarization effects, the relative polarization of the probe and pump pulses was set at the magic angle. All spectra were corrected for the chirp of the white-light probe. MATLAB and IgorPro software were used for data analysis.

Time resolved IR (TRIR) Spectroscopy. TRIR measurements were performed at the LIFEtime setup, which is an ultrafast infrared absorption facility at the Rutherford Appleton Laboratory. Two 100 kHz Pharos lasers and three optical parametric amplifiers (Light Conversion Systems) provided 266 and 532 nm excitation with narrow band, long pulses which are 220 fs (150 cm^{-1}). The pump pulses at the sample have a fluence of 62 $\mu J/cm^2$ for 532 nm and 56.6 $\mu J/cm^2$ for 266 nm. The IR probe beam (pulse length of 180 fs (200 cm^{-1})) was split to form the reference and probe beams, which were dispersed in spectrographs and detected by MCT array detectors (IR Associates). The 50 kHz 532 nm pump pulses were focused (~ 200 μm spot sizes) and overlapped with the probe beam (~50 μm spot size) in the sample cell. The high-speed data acquisition system allowed 100 kHz acquisition and processing of the probe and reference pulses to generate a pump-on pump-off infrared absorption difference signal. The difference signal was calibrated using the characteristic polystyrene IR absorption spectrum. The sample was raster scanned in x- and y- directions and constantly recycled in order to preserve the sample.

Samples with an approximate volume of 0.8 mL were loaded onto a demountable liquid flow cell (Harrick Scientific Products, Inc) comprised of two 25-mm-diameter CaF_2 plates (Crystran Ltd), separated by a 100-micron Teflon Spacer. In all experiments, the sample solution was recirculated using a peristaltic pump.

The equation that was used for the fitting of the kinetics (Figures S5.3-S5.9, S5.17-S5.24, S5.32, S5.34-S5.35, S5.37-S5.38 and S5.40) is:

$$f(t) = y_0 + A_1 exp\left(\frac{-(t - t_0)}{\tau_1}\right) + A_2 exp\left(\frac{-(t - t_0)}{\tau_2}\right)$$

ATR-FTIR Spectroscopy. The FTIR measurements were performed on a Vertex 70 FTIR spectrometer (Bruker Optics, Ettlingen, Germany), equipped with a single-reflection ZnSe ATR accessory (Pike Technologies, Madison WI, USA) and a DTGS detector (Bruker Optics, Ettlingen, Germany). Spectra collection took place with the Opus 7.0 software (Bruker Optics, Ettlingen, Germany). Samples of $1 \cdot 10^{-3}$ M for ssDNA and CPT/ssDNA and of $7\cdot10^{-3}$ M for CPT were deposited on the crystal and allowed to dry for ~1 h until solvent was evaporated prior to the measurement. A background was recorded with a clean crystal before the start of the measurements. The background and sample spectra were acquired with 64 scans at an instrument resolution of 4 cm^{-1} over the spectral range between 400 to 4000 cm^{-1}. The contribution of PBS buffer was also subtracted from each sample spectrum. MATLAB and ORIGIN software were used for spectral treatment and analysis.

Impulsive Stimulated Raman Scattering (ISRS). ISRS measurements were carried out in the research group of Prof. Tullio Scopigno, at the Department of Physics at the Sapienza University of Rome. The spectroscopic data were collected by Dr. Giovanni Batignani and Dr. Miles Martinati, who carried out the analysis of the ISRS data as well. The experimental setup is based on a Ti:sapphire laser source that generates 3.6 mJ, 35 fs pulses at 800 nm and 1 kHz repetition rate. The Raman pulse is generated by a noncollinear optical parametric amplifier (NOPA) that produces tunable visible pulses in the range (500−700 nm) and compressed using chirped mirrors to ∼10 fs. The Raman pump and probe pulses exploited are 500-600, 600-700 and 800-970nm. The time interval between the Raman and probe pulses is defined by a computer-controlled delay line on the Raman pulse optical path. The WLC probe pulse is generated by focusing part of the source pulse on a nonlinear medium plate. The time duration of the Raman pulse is measured by second harmonic noncollinear autocorrelation, while the probe chirp can be estimated from the relative delay of the onset of oscillations at different probe wavelengths.

Femtosecond Stimulated Raman spectroscopy (FSRS). FSRS measurements were carried out in the research group of Prof. Tullio Scopigno, at the Department of Physics at the Sapienza University of Rome. The spectroscopic data were collected by Dr. Giovanni Batignani and Dr. Miles Martinati, who carried out the analysis of the FSRS data as well. A Ti:sapphire laser generates 3.6 mJ, 35 fs pulses at 800 nm and 1 kHz repetition rate. A portion of the laser fundamental drives a two-stage optical parametric amplifier (OPA) to generate a 550 nm, 60 fs actinic pump with 1 μJ energy on the sample. The Raman pulses are generated from a second two-stage OPA that produces tunable IR− visible pulses, followed by a spectral compression stage based on frequency doubling in a 25 mm β-barium borate crystal. Cleaning of the RP spectral profile is performed by a double-pass 2f spectral filter, which enables at the same time reducing the pulse bandwidth and rectifying its temporal profile, increasing its time duration. Raman pulses with 599, 614 and 644 nm wavelength, 630 nJ energy, and 3.5 ps time duration are focused on the sample. The AP and the RP pulses are collinear, while the PP is tilted by ∼2°. The femtosecond probe is a white-light continuum

(WLC), generated by focusing the laser fundamental into a sapphire crystal, and covers the 450−750 nm spectral range. The Raman features arise as positive gain on top of the transmitted WLC (center of spectral region of probe: 643, 666 and 704 nm) or negative loss (center of spectral region of probe: 566, 574 and 604 nm)), which is frequency dispersed by a spectrometer onto a CCD device, able to perform single-shot acquisitions. A synchronized chopper at 500 Hz blocks alternating RP pulses in order to obtain the Raman gain/loss using successive probe pulses, while a second chopper blocks the actinic pump at 250 Hz in order to obtain Raman gain spectra with and without actinic excitation. Notably, under the presented configuration, the stimulated Raman gain is calculated as the ratio of the PP with and without the RP in the presence of the AP, and hence eventual XPM effects on the PP do not affect the measured FSRS spectrum. The temporal delays between the three pulses used in the FSRS experiment can be tuned by means of two delay line stages (on the PP and AP beam paths).

References

(1) Hollingsworth, W. R.; Segura, C.; Balderrama, J.; Lopez, N.; Schleissner, P.; Ayzner, A. L. Exciton Transfer and Emergent Excitonic States in Oppositely-Charged Conjugated Polyelectrolyte Complexes. *J. Phys. Chem. B* **2016**, *120* (31), 7767–7774.

(2) Panzer, F.; Bässler, H.; Köhler, A. Temperature Induced Order-Disorder Transition in Solutions of Conjugated Polymers Probed by Optical Spectroscopy. *J. Phys. Chem. Lett.* **2017**, *8* (1), 114–125.

(3) Raithel, D.; Simine, L.; Pickel, S.; Schötz, K.; Panzer, F.; Baderschneider, S.; Schiefer, D.; Lohwasser, R.; Köhler, J.; Thelakkat, M.; Sommer, M.; Köhler, A.; Rossky, P. J.; Hildner, R. Direct Observation of Backbone Planarization via Side-Chain Alignment in Single Bulky-Substituted Polythiophenes. *Proc. Natl. Acad. Sci. U. S. A.* **2018**, *115* (11), 2699–2704.

(4) Dyson, M. J.; Lariou, E.; Martin, J.; Li, R.; Erothu, H.; Wantz, G.; Topham, P. D.; Dautel, O. J.; Hayes, S. C.; Stavrinou, P. N.; Stingelin, N. Managing Local Order in Conjugated Polymer Blends via Polarity Contrast. *Chem. Mater.* **2019**, *31* (17), 6540–6547.

(5) Rubio-Magnieto, J.; Azene, E. G.; Knoops, J.; Knippenberg, S.; Delcourt, C.; Thomas, A.; Richeter, S.; Mehdi, A.; Dubois, P.; Lazzaroni, R.; Beljonne, D.;

Clement, S.; Surin, M. Self-Assembly and Hybridization Mechanisms of DNA with Cationic Polythiophene. *Soft Matter* **2015**, *11*, 6460–6471.

(6) Ho, H. A.; Boissinot, M.; Bergeron, M. G.; Corbeil, G.; Dore, K.; Boudreau, D.; Leclerc, M. Colorimetric and Fluorometric Detection of Nucleic Acids Using Cationic Polythiophene Derivatives. *Angew. Chemie, Int. Ed.* **2002**, *41* (9), 1548–1551.

(7) Liu, Y.; Ogawa, K.; Schanze, K. S. Conjugated Polyelectrolytes as Fluorescent Sensors. *J. Photochem. Photobiol. C Photochem. Rev.* **2009**, *10* (4), 173–190.

(8) Duan, X. R.; Liu, L. B.; Feng, F. D.; Wang, S. Cationic Conjugated Polymers for Optical Detection of DNA Methylation, Lesions, and Single Nucleotide Polymorphisms. *Acc. Chem. Res.* **2010**, *43* (2), 260–270.

(9) Peterhans, L.; Nicolaidou, E.; Diamantis, P.; Alloa, E.; Leclerc, M.; Surin, M.; Clément, S.; Rothlisberger, U.; Banerji, N.; Hayes, S. C. Structural and Photophysical Templating of Conjugated Polyelectrolytes with Single-Stranded DNA. *Chem. Mater.* **2020**, *32* (17), 7347–7362.

(10) Österbacka, R.; An, C. P.; Jiang, X. M.; Vardeny, Z. V. Two-Dimensional Electronic Excitations in Self-Assembled Conjugated Polymer Nanocrystals. *Science (80-.).* **2000**, *287* (5454), 839–842.

(11) Österbacka, R.; Jiang, X. M.; An, C. P.; Horovitz, B.; Vardeny, Z. V. Photoinduced Quantum Interference Antiresonances in π-Conjugated Polymers. *Phys. Rev. Lett.* **2002**, *88* (22), 4.

(12) Mansour, A. E.; Lungwitz, D.; Schultz, T.; Arvind, M.; Valencia, A. M.; Cocchi, C.; Opitz, A.; Neher, D.; Koch, N. The Optical Signatures of Molecular-Doping Induced Polarons in Poly(3-Hexylthiophene-2,5-Diyl): Individual Polymer Chains: Versus Aggregates. *J. Mater. Chem. C* **2020**, *8* (8), 2870–2879.

(13) Arvind, M.; Tait, C. E.; Guerrini, M.; Krumland, J.; Valencia, A. M.; Cocchi, C.; Mansour, A. E.; Koch, N.; Barlow, S.; Marder, S. R.; Behrends, J.; Neher, D. Quantitative Analysis of Doping-Induced Polarons and Charge-Transfer Complexes of Poly(3-Hexylthiophene) in Solution. *J. Phys. Chem. B* **2020**, *124* (35), 7694–7708.

(14) Ghosh, R.; Spano, F. C. Excitons and Polarons in Organic Materials. *Acc. Chem.*

Res. **2020**, *53* (10), 2201–2211.

(15) Guo, J.; Ohkita, H.; Benten, H.; Ito, S. Near-IR Femtosecond Transient Absorption Spectroscopy of Ultrafast Polaron and Triplet Exciton Formation in Polythiophene Films with Different Regioregularities. *J. Am. Chem. Soc.* **2009**, *131* (46), 16869–16880.

(16) Peterhans, L.; Alloa, E.; Sheima, Y.; Vannay, L.; Leclerc, M.; Corminboeuf, C.; Hayes, S. C.; Banerji, N. Salt-Induced Thermochromism of a Conjugated Polyelectrolyte. *Phys. Chem. Chem. Phys.* **2017**, *19* (42), 28853–28866.

(17) Sirringhaus, H.; Brown, P. J.; Friend, R. H.; Nielsen, M. M.; Bechgaard, K.; Langeveld-Voss, B. M. W.; Spiering, A. J. H.; Janssen, R. A. J.; Meijer, E. W.; Herwig, P.; de Leeuw, D. M. Two-Dimensional Charge Transport in Self-Organized, High-Mobility Conjugated Polymers. *Nature* **1999**, *401*, 685–688.

(18) Pochas, C. M.; Spano, F. C. New Insights on the Nature of Two-Dimensional Polarons in Semiconducting Polymers: Infrared Absorption in Poly(3-Hexylthiophene). *J. Chem. Phys.* **2014**, *140* (24), 244902.

(19) Kahmann, S.; Loi, M. A.; Brabec, C. J. Delocalisation Softens Polaron Electronic Transitions and Vibrational Modes in Conjugated Polymers. *J. Mater. Chem. C* **2018**, *6* (22), 6008–6013.

(20) Ghosh, R.; Chew, A. R.; Onorato, J.; Pakhnyuk, V.; Luscombe, C. K.; Salleo, A.; Spano, F. C. Spectral Signatures and Spatial Coherence of Bound and Unbound Polarons in P3HT Films: Theory Versus Experiment. *J. Phys. Chem. C* **2018**, *122* (31), 18048–18060.

(21) Jiang, X. M.; Österbacka, R.; Korovyanko, O.; An, C. P.; Horovitz, B.; Janssen, R. A. J.; Vardeny, Z. V. Spectroscopic Studies of Photoexcitations in Regioregular and Regiorandom Polythiophene Films. *Adv. Funct. Mater.* **2002**, *12* (9), 587–597.

(22) Cravino, A.; Neugebauer, H.; Luzzati, S.; Catellani, M.; Serdar Sariciftci, N. Vibrational Spectroscopy on PDTT3-a Low Band Gap Polymer Based on Dithienothiophene. *J. Phys. Chem. B* **2001**, *105* (1), 46–52.

(23) Cravino, A.; Neugebauer, H.; Luzzati, S.; Catellani, M.; Petr, A.; Dunsch, L.; Serdar Sariciftci, N. Positive and Negative Charge Carriers in Doped or Photoexcited Polydithienothiophenes: A Comparative Study Using Raman, Infrared, and Electron

Spin Resonance Spectroscopy. *J. Phys. Chem. B* **2002**, *106* (14), 3583–3591.

(24) Cravino, A.; Neugebauer, H.; Petr, A.; Skabara, P. J.; Spencer, H. J.; McDouall, J. J. W.; Dunsch, L.; Sariciftci, N. S. Spectroelectrochemistry of Poly(Ethylenedithiathiophene)-the Sulfur Analogue of Poly(Ethylenedioxythiophene). *J. Phys. Chem. B* **2006**, *110* (6), 2662–2667.

(25) Dereka, B.; Svechkarev, D.; Rosspeintner, A.; Aster, A.; Lunzer, M.; Liska, R.; Mohs, A. M.; Vauthey, E. Solvent Tuning of Photochemistry upon Excited-State Symmetry Breaking. *Nat. Commun.* **2020**, *11* (1), 1–11.

(26) Chin, X. Y.; Yin, J.; Wang, Z.; Caironi, M.; Soci, C. Mapping Polarons in Polymer FETs by Charge Modulation Microscopy in the Mid-Infrared. *Sci. Rep.* **2014**, *4*, 1–6.

(27) Yin, J.; Wang, Z.; Fazzi, D.; Shen, Z.; Soci, C. First-Principles Study of the Nuclear Dynamics of Doped Conjugated Polymers. *J. Phys. Chem. C* **2016**, *120* (3), 1994–2001.

(28) Peeks, M. D.; Tait, C. E.; Neuhaus, P.; Fischer, G. M.; Hoffmann, M.; Haver, R.; Cnossen, A.; Harmer, J. R.; Timmel, C. R.; Anderson, H. L. Electronic Delocalization in the Radical Cations of Porphyrin Oligomer Molecular Wires. *J. Am. Chem. Soc.* **2017**, *139* (30), 10461–10471.

(29) Kendrick, W. J.; Jirásek, M.; Peeks, M. D.; Greetham, G. M.; Sazanovich, I. V.; Donaldson, P. M.; Towrie, M.; Parker, A. W.; Anderson, H. L. Mechanisms of IR Amplification in Radical Cation Polarons. *Chem. Sci.* **2020**, *11* (8), 2112–2120.

(30) Keane, P. M.; Wojdyla, M.; Doorley, G. W.; Kelly, J. M.; Clark, I. P.; Parker, A. W.; Greetham, G. M.; Towrie, M.; Magno, L. M.; Quinn, S. J. Ultrafast IR Spectroscopy of Polymeric Cytosine Nucleic Acids Reveal the Long-Lived Species Is Due to a Localised State. *Phys. Chem. Chem. Phys.* **2012**, *14* (18), 6307–6311.

(31) Mizrahi, U.; Ehrenfreund, E.; Gershoni, D.; Vardeny, Z. V. Time-Resolved Spectroscopy of Infrared Active Vibrations in 2,5-Dioctyloxy Poly(Phenylene Vinylene) Films. *Polymer (Guildf).* **2002**, *44* (3), 691–694.

(32) Mizrahi, U.; Shtrichman, I.; Gershoni, D.; Ehrenfreund, E.; Vardeny, Z. V. Picoseconds Time Resolved Photoinduced Absorption by Infrared Active Vibrations as a Probe for Charge Photogeneration in MEH-PPV/C60 Composites. *Synth. Met.*

1999, *102* (1–3), 1182–1185.

(33) Miranda, P. B.; Moses, D.; Heeger, A. J. Ultrafast Photogeneration of Charged Polarons on Conjugated Polymer Chains in Dilute Solution. *Phys. Rev. B - Condens. Matter Mater. Phys.* **2004**, *70* (8), 1–9.

(34) Meskers, S.; van Hal, P.; Spiering, A.; Hummelen, J. Time-Resolved Infrared-Absorption Study of Photoinduced Charge Transfer in a Polythiophene-Methanofullerene Composite Film. *Phys. Rev. B - Condens. Matter Mater. Phys.* **2000**, *61* (15), 9917–9920.

(35) Stallhofer, K.; Nuber, M.; Kienberger, R.; Körstgens, V.; Müller-Buschbaum, P.; Iglev, H. Dynamics of Short-Lived Polaron Pairs and Polarons in Polythiophene Derivatives Observed via Infrared-Activated Vibrations. *J. Phys. Chem. C* **2019**, *123* (46), 28100–28105.

(36) Lee, S.-Y.; Zhang, D.; Mccamant, D. W.; Kukura, P.; Mathies, R. A. Theory of Femtosecond Stimulated Raman Spectroscopy. *J. Chem. Phys.* **2004**, *121,* 3632.

(37) Kukura, P.; Mccamant, D. W.; Mathies, R. A. Femtosecond Stimulated Raman Spectroscopy. *Annu. Rev. Phys. Chem.* **2007**, *58,* 461–488.

(38) Dietze, D. R.; Mathies, R. A. Femtosecond Stimulated Raman Spectroscopy. *ChemPhysChem* **2016**, *17,* 1224–1251.

(39) Cook, S.; Furube, A.; Katoh, R. Analysis of the excited states of regioregular polythiophene P3HT. *Energy Environ. Sci.* **2008**, *1* (2), 294–299.

(40) R. S., L.; Vennapusa, S. R. Formation and Decay of Intersystem Crossing Receiver Triplet State in Terthiophene and Quaterthiophene. *Int. J. Quantum Chem.* **2021**, 1–10.

(41) Guo, L.; Qin, Y.; Gu, X.; Zhu, X.; Zhou, Q.; Sun, X. Spin Transport in Organic Molecules. *Front. Chem.* **2019**, *7*, 1–11.

(42) Skov, A. B.; Larsena, M. A. B.; Liisberga, M. B.; Hansen, T.; Sølling, T. I. Conformationally Controlled Ultrafast Intersystem Crossing in Bithiophene Systems. *Phys. Chem. Chem. Phys.* **2018**, *20*, 13412–13418.

(43) Kolle, P.; Schnappinger, T.; De Vivie-Riedle, R. Deactivation Pathways of Thiophene and Oligothiophenes : Internal Conversion versus Intersystem Crossing

†. *Phys. Chem. Chem. Phys.* **2016**, *18*, 7903–7915.

(44) Yang, X.; Dykstra, T. E.; Scholes, G. D. Photon-Echo Studies of Collective Absorption and Dynamic Localization of Excitation in Conjugated Polymers and Oligomers. *Phys. Rev. B - Condens. Matter Mater. Phys.* **2005**, *71* (4), 1–15.

(45) Wells, N. P.; Boudouris, B. W.; Hillmyer, M. A.; Blank, D. A. Intramolecular Exciton Relaxation and Migration Dynamics in Poly(3-Hexylthiophene). *J. Phys. Chem. C* **2007**, *111* (42), 15404–15414.

(46) Banerji, N.; Cowan, S.; Vauthey, E.; Heeger, A. J. Ultrafast Relaxation of the Poly(3-Hexylthiophene) Emission Spectrum. *J. Phys. Chem. C* **2011**, *115* (19), 9726–9739.

(47) Hwang, I.; Scholes, G. D. Electronic Energy Transfer and Quantum-Coherence in π-Conjugated Polymers. *Chem. Mater.* **2011**, *23* (3), 610–620.

(48) Tozer, O. R.; Barford, W. Exciton Dynamics in Disordered Poly(p-Phenylenevinylene). 1. Ultrafast Interconversion and Dynamical Localization. *J. Phys. Chem. A* **2012**, *116* (42), 10310–10318.

(49) Banerji, N. Sub-Picosecond Delocalization in the Excited State of Conjugated Homopolymers and Donor-Acceptor Copolymers. *J. Mater. Chem. C* **2013**, *1* (18), 3052–3066.

(50) Collini, E.; Scholes, G. D. Coherent Intrachain Energy Migration in a Conjugated Polymer at Room Temperature. *Science (80-.).* **2009**, *323* (5912), 369–373.

(51) Binder, R.; Lauvergnat, D.; Burghardt, I. Conformational Dynamics Guides Coherent Exciton Migration in Conjugated Polymer Materials: First-Principles Quantum Dynamical Study. *Phys. Rev. Lett.* **2018**, *120* (22), 2–5.

(52) Westenhoff, S.; Beenken, W. J. D.; Friend, R. H.; Greenham, N. C.; Yartsev, A.; Sundström, V. Anomalous Energy Transfer Dynamics Due to Torsional Relaxation in a Conjugated Polymer. *Phys. Rev. Lett.* **2006**, *97* (16), 166804.

(53) Gallaher, J. K.; Chen, K.; Huff, G. S.; Prasad, S. K. K.; Gordon, K. C.; Hodgkiss, J. M. Evolution of Nonmirror Image Fluorescence Spectra in Conjugated Polymers and Oligomers. *J. Phys. Chem. Lett.* **2016**, *7* (17), 3307–3312.

(54) Kim, T. W.; Kim, W.; Park, K. H.; Kim, P.; Cho, J. W.; Shimizu, H.; Iyoda, M.;

Kim, D. Chain-Length-Dependent Exciton Dynamics in Linear Oligothiophenes Probed Using Ensemble and Single-Molecule Spectroscopy. *J. Phys. Chem. Lett.* **2016**, *7* (3), 452–458.

(55) Park, K. H.; Kim, W.; Yang, J.; Kim, D. Excited-State Structural Relaxation and Exciton Delocalization Dynamics in Linear and Cyclic π-Conjugated Oligothiophenes. *Chem. Soc. Rev.* **2018**, *47* (12), 4279–4294.

(56) Anderson, M.; Ramanan, C.; Fontanesi, C.; Frick, A.; Surana, S.; Cheyns, D.; Furno, M.; Keller, T.; Allard, S.; Scherf, U.; Beljonne, D.; D'Avino, G.; Von Hauff, E.; Da Como, E. Displacement of Polarons by Vibrational Modes in Doped Conjugated Polymers. *Phys. Rev. Mater.* **2017**, *1* (5), 1–9.

(57) Nafie, L. A. Theory of Vibrational Circular Dichroism and Infrared Absorption: Extension to Molecules with Low-Lying Excited Electronic States. *J. Phys. Chem. A* **2004**, *108* (35), 7222–7231.

(58) Zamadar, M.; Asaoka, S.; Grills, D. C.; Miller, J. R. Giant Infrared Absorption Bands of Electrons and Holes in Conjugated Molecules. *Nat. Commun.* **2013**, *4*, 2818.

(59) Takaya, T.; Enokida, I.; Furukawa, Y.; Iwata, K. Direct Observation of Structure and Dynamics of Photogenerated Charge Carriers in Poly(3-Hexylthiophene) Films by Femtosecond Time-Resolved Near-IR Inverse Raman Spectroscopy. *Molecules* **2019**, *24*, 431.

(60) Yu, W.; Magnanelli, T. J.; Zhou, J.; Bragg, A. E. Structural Heterogeneity in the Localized Excited States of Poly(3-Hexylthiophene). *J. Phys. Chem. B* **2016**, *120*, 5093–5102.

(61) Yu, W.; Donohoo-Vallett, P. J.; Zhou, J.; Bragg, A. E. Ultrafast Photo-Induced Nuclear Relaxation of a Conformationally Disordered Conjugated Polymer Probed with Transient Absorption and Femtosecond Stimulated Raman Spectroscopies. *J. Chem. Phys.* **2020**, *141*, 044201.

(62) Magnanelli, T. J.; Bragg, A. E. Time-Resolved Raman Spectroscopy of Polaron Pair Formation in Poly(3-Hexylthiophene) Aggregates. *J. Phys. Chem. Lett.* **2015**, *6* (3), 438–445.

(63) Roy, P.; Anandan, G. T.; Nayak, N.; Kumar, A.; Dasgupta, J. Raman Snapshots of

Side-Chain Dependent Polaron Dynamics in PolyThiophene Films. *J. Phys. Chem. B* **2023**, *127*, 567–576.

(64) Keane, P. M.; Wojdyla, M.; Doorley, G. W.; Watson, G. W.; Clark, I. P.; Greetham, G. M.; Parker, A. W.; Towrie, M.; Kelly, J. M.; Quinn, S. J. A Comparative Picosecond Transient Infrared Study of 1-Methylcytosine and 5′-DCMP That Sheds Further Light on the Excited States of Cytosine Derivatives. *J. Am. Chem. Soc.* **2011**, *133* (12), 4212–4215.

(65) Keane, P. M.; Wojdyla, M.; Doorley, G. W.; Kelly, J. M.; Parker, A. W.; Clark, I. P.; Greetham, G. M.; Towrie, M.; Magno, L. M.; Quinn, S. J. Long-Lived Excited States in i-Motif DNA Studied by Picosecond Time-Resolved IR Spectroscopy. *Chem. Commun.* **2014**, *50* (23), 2990–2992.

(66) Keane, P. M.; Baptista, F. R.; Gurung, S. P.; Devereux, S. J.; Sazanovich, I. V.; Towrie, M.; Brazier, J. A.; Cardin, C. J.; Kelly, J. M.; Quinn, S. J. Long-Lived Excited-State Dynamics of i-Motif Structures Probed by Time-Resolved Infrared Spectroscopy. *ChemPhysChem* **2016**, *17* (9), 1281–1287.

(67) Bucher, D. B.; Pilles, B. M.; Carell, T.; Zinth, W. Charge Separation and Charge Delocalization Identified in Long-Living States of Photoexcited DNA. *Proc. Natl. Acad. Sci. U. S. A.* **2014**, *111* (12), 4369–4374.

(68) Park, B. N.; Uhlrich, J. J.; Kuech, T. F.; Evans, P. G. Electrical Properties of GaN/Poly(3-Hexylthiophene) Interfaces. *J. Appl. Phys.* **2009**, *106* (1), 013713.

(69) Wetmore, S. D.; Boyd, R. J.; Eriksson, L. A. Electron Affinities and Ionization Potentials of Nucleotide Bases. *Chem. Phys. Lett.* **2000**, *322* (1–2), 129–135.

(70) Santoro, F.; Barone, V.; Improta, R. Influence of Base Stacking on Excited-State Behavior of Polyadenine in Water, Based on Time-Dependent Density Functional Calculations. *Proc. Natl. Acad. Sci. U. S. A.* **2007**, *104* (24), 9931–9936.

(71) Ibele, L. M.; Sánchez-Murcia, P. A.; Mai, S.; Nogueira, J. J.; González, L. Excimer Intermediates En Route to Long-Lived Charge-Transfer States in Single-Stranded Adenine DNA as Revealed by Nonadiabatic Dynamics. *J. Phys. Chem. Lett.* **2020**, *11* (18), 7483–7488.

(72) Boxer, S. G. Stark Realities. *J. Phys. Chem. B* **2009**, *113*, 2972–2983.

(73) Banyay, M.; Sarkar, M.; Graslund, A. A Library of IR Bands of Nucleic Acids in

Solution. *Biophys. Chem.* **2003**, *104*, 477–488.

(74) Peng, C. S.; Jones, K. C.; Tokmakoff, A. Anharmonic Vibrational Modes of Nucleic Acid Bases Revealed by 2D IR Spectroscopy. *J. Am. Chem. Soc.* **2011**, *133* (39), 15650–15660.

(75) Keane, P. M.; O'Sullivan, K.; Poynton, F. E.; Poulsen, B. C.; Sazanovich, I. V.; Towrie, M.; Cardin, C. J.; Sun, X. Z.; George, M. W.; Gunnlaugsson, T.; Quinn, S. J.; Kelly, J. M. Understanding the Factors Controlling the Photo-Oxidation of Natural DNA by Enantiomerically Pure Intercalating Ruthenium Polypyridyl Complexes through TA/TRIR Studies with Polydeoxynucleotides and Mixed Sequence Oligodeoxynucleotides. *Chem. Sci.* **2020**, *11* (32), 8600–8609.

(76) Poynton, F. E.; Hall, J. P.; Keane, P. M.; Schwarz, C.; Sazanovich, I. V.; Towrie, M.; Gunnlaugsson, T.; Cardin, C. J.; Cardin, D. J.; Quinn, S. J.; Long, C.; Kelly, J. M. Direct Observation by Time-Resolved Infrared Spectroscopy of the Bright and the Dark Excited States of the [Ru(Phen)2(Dppz)]2+ Light-Switch Compound in Solution and When Bound to DNA. *Chem. Sci.* **2016**, *7* (5), 3075–3084.

(77) Doorley, G. W.; Wojdyla, M.; Watson, G. W.; Towrie, M.; Parker, A. W.; Kelly, J. M.; Quinn, S. J. Tracking DNA Excited States by Picosecond-Time-Resolved Infrared Spectroscopy: Signature Band for a Charge-Transfer Excited State in Stacked Adenine-Thymine Systems. *J. Phys. Chem. Lett.* **2013**, *4* (16), 2739–2744.

(78) Yu, W.; Zhou, J.; Bragg, A. E. Exciton Conformational Dynamics of Poly(3-Hexylthiophene) (P3HT) in Solution from Time-Resolved Resonant-Raman Spectroscopy. *J. Phys. Chem. Lett.* **2012**, *3*, 1321–1328.

(79) Wells, N. P.; Blank, D. A. Correlated Exciton Relaxation in Poly (3-Hexylthiophene). *Phys. Rev. Lett.* **2008**, *100*, 086403.

(80) Roy, P.; Jha, A.; Yasarapudi, V. B.; Ram, T.; Puttaraju, B.; Patil, S.; Dasgupta, J. Ultrafast Bridge Planarization in Donor-π-Acceptor Copolymers Drives Intramolecular Charge Transfer. *Nat. Commun.* **2017**, *8*, 1716.

(81) Bragg, A. E.; Yu, W.; Zhou, J.; Magnanelli, T. Ultrafast Raman Spectroscopy as a Probe of Local Structure and Dynamics in Photoexcited Conjugated Materials. *J. Phys. Chem. Lett.* **2016**, *7*, 3990–4000.

(82) Fumero, G.; Schnedermann, C.; Batignani, G.; Wende, T.; Liebel, M.; Bassolino,

G.; Ferrante, C.; Mukamel, S.; Kukura, P.; Scopigno, T. Two-Dimensional Impulsively Stimulated Resonant Raman Spectroscopy of Molecular Excited States. *Phys. Rev. X* **2020**, *10*, 011051.

(83) Liebel, M.; Schnedermann, C.; Wende, T.; Kukura, P. Principles and Applications of Broadband Impulsive Vibrational Spectroscopy. *J. Phys. Chem. A* **2015**, *119*, 9506–9517.

(84) Monacelli, L.; Batignani, G.; Fumero, G.; Ferrante, C.; Mukamel, S.; Scopigno, T. Manipulating Impulsive Stimulated Raman Spectroscopy with a Chirped Probe Pulse. *J. Phys. Chem. Lett.* **2017**, *8*, 966–974.

(85) Batignani, G.; Sansone, C.; Ferrante, C.; Fumero, G.; Mukamel, S.; Scopigno, T. Excited-State Energy Surfaces in Molecules Revealed by Impulsive Stimulated Raman Excitation Profiles. *J. Phys. Chem. Lett.* **2021**, *12*, 9239–9247.

(86) Dhamija, S.; Bhutani, G.; Jayachandran, A.; De, A. K. A Revisit on Impulsive Stimulated Raman Spectroscopy : Importance of Spectral Dispersion of Chirped Broadband Probe. *J. Phys. Chem. A* **2022**, *126*, 1019–1032.

(87) Pron, A.; Louarn, G.; Lapkowski, M.; Zagorska, M.; Glowczyk-Zubek, J.; Lefrant, S. "In Situ" Raman Spectroelectrochemical Studies of Poly(3,3′-Dibutoxy-2,2′-Bithiophene). *Macromolecules* **1995**, *28*, 4644–4649.

(88) Louarn, G.; Trznadel, M.; Buisson, J. P.; Laska, J.; Pron, A.; Lapkowski, M.; Lefrant, S. Raman Spectroscopic Studies of Regioregular Poly(3-Alkylthiophenes). *J. Phys. Chem.* **1996**, *100* (30), 12532–12539.

(89) Batignani, G.; Ferrante, C.; Fumero, G.; Scopigno, T. Broadband Impulsive Stimulated Raman Scattering Based on A. *J. Phys. Chem. Lett.* **2019**, *10*, 7789–7796.

(90) Arrigoni, A.; Brambilla, L.; Castiglioni, C.; Bertarelli, C. Conducting Electrospun Nanofibres: Monitoring of Iodine Doping of P3HT through Infrared (IRAV) and Raman (RaAV) Polaron Spectroscopic Features. *Nanomaterials* **2022**, *12*, 4308.

(91) Mosca, S.; Milani, A.; Castiglioni, C.; Jolín, V. H.; Meseguer, C.; Juan, T. L.; Zhao, C.; Sugiyasu, K.; Delgado, M. C. R. Raman Fingerprints of π - Electron Delocalization in Polythiophene- Based Insulated Molecular Wires. *Macromolecules* **2022**, *55*, 3458–3468.

(92) Mansour, A. E.; Valencia, A. M.; Lungwitz, D.; Wegner, B.; Tanaka, N.; Shoji, Y.; Fukushima, T.; Opitz, A.; Cocchi, C.; Koch, N. Understanding the Evolution of the Raman Spectra of Molecularly P-Doped. *Phys. Chem. Chem. Phys.* **2022**, *24*, 3109–3118.

(93) Lim, S.; Chon, B.; Rhee, H.; Cho, M. Spectral Modulation of Stimulated Raman Scattering Signal : Beyond Weak Raman Pump Limit. *J. Raman Spectrosc.* **2018**, *49*, 607–620.

(94) Batignani, G.; Fumero, G.; Pontecorvo, E.; Ferrante, C.; Mukamel, S.; Scopigno, T. Genuine Dynamics vs Cross Phase Modulation Artifacts in Femtosecond Stimulated Raman Spectroscopy. *ACS Photonics* **2019**, *6*, 492–500.

(95) Frontiera, R. R.; Shim, S.; Mathies, R. A.; Frontiera, R. R.; Shim, S.; Mathies, R. A. Origin of Negative and Dispersive Features in Anti-Stokes and Resonance Femtosecond Stimulated Raman Spectroscopy Origin of Negative and Dispersive Features in Anti-Stokes and Resonance Femtosecond Stimulated Raman Spectroscopy. **2008**, *064507*.

(96) Song, Y.; Clafton, S. N.; Pensack, R. D.; Kee, T. W.; Scholes, G. D. Vibrational Coherence Probes the Mechanism of Ultrafast Electron Transfer in Polymer–Fullerene Blends. *Nat. Commun.* **2014**, *5*, 4933.

(97) Provencher, F.; Bérubé, N.; Parker, A. W.; Greetham, G. M.; Towrie, M.; Hellmann, C.; Côté, M.; Stingelin, N.; Silva, C.; Hayes, S. C. Direct Observation of Ultrafast Long-Range Charge Separation at Polymer-Fullerene Heterojunctions. *Nat. Commun.* **2014**, *5*, 4288.

(98) Grancini, G.; Maiuri, M.; Fazzi, D.; Petrozza, A.; Egelhaaf, H.-J.; Brida, D.; Cerullo, G.; Lanzani, G. Hot Exciton Dissociation in Polymer Solar Cells. *Nat. Mater.* **2013**, *12*, 29–33.

CHAPTER 6

EFFECT OF STRUCTURAL CONFORMATION OF CONJUGATED POLYMERS ON SPIN TRANSPORT*

The origin and yield of charge in the excited state of conjugated polymers has been an intensively studied research field of organic semiconductors for many years. However, it is rarely found that a neat conjugated polymer can exhibit charges in the ground state. This type of polymer has been reported to possess spin-based properties that can be exploited in molecular spintronics. Organic semiconductors consisting mainly of relatively light chemical elements were expected to exhibit low spin-orbit coupling (SOC) and large spin relaxation time, making them attractive as spin conveyors in spintronic devices. However, a series of theoretical and experimental spin diffusion length and spin Hall angle results contradicting this expectation have triggered an ongoing discussion to understand the coupling of spins to their environment in these systems. In this context we use the prototype material poly(3,4-ethylenedioxythiophene):polystyrene sulfonate as a model conducting polymer system to monitor the impact of chemical doping and the resulting modification of the polymer's backbone conformation on the spin diffusion length. The increased spin diffusion length during dedoping of the polymer, indicating a reduction of the SOC strength, is associated with an increased planarity at the dedoped level monitored by Raman spectroscopy. This reveals that spin transport is inextricably linked to the structural conformation of the organic semiconductor. Spin phenomena of a conjugated polymer can be modified through control of the polymer's structural conformation, paving the way for a new functionality for spintronic based devices. For this work we collaborated with Assistant Prof. Theodossis Trypiniotis' s research group in the Department of Physics of the University of Cyprus.

---

*Adapted from the paper "Effect of structural conformation of conjugated polymers on spin transport" published in Physical Review Materials **2022**, *6*, 095601.

6.1 Introduction

Organic semiconductors (OSCs) have been recently studied for organic spintronics, aiming to understand the spin relaxation and spin transport mechanisms in organic materials and to exploit their particular properties to invent new spintronic functionalities and devices.[1,2] The spin relaxation time, spin diffusion length (SDL), and spin Hall angle (θ_{SH}) are interconnected crucial figures of merit which determine the spin "conductivity" of a material and whether it is more suitable as a conveyor or a detector of spin. The spin relaxation time is controlled by two principal factors, the spin-orbit coupling (SOC) and the hyperfine interaction.[2] Since organic materials mainly consist of elements with small atomic numbers (e.g., H, C, O), very long spin diffusion lengths and spin relaxation times are expected, with associated small spin Hall angles.[3,4] Many experimental reports, however, demonstrated spin diffusion lengths ranging from about 1 nm to approximately 1 μm in organic structures with similar light elements, which implies that in some cases the SOC strength is higher than expected.[4–7] The origin of such unexpected results in these systems is still under investigation and remains a very active research area both theoretically and experimentally.[2,8,9] The strength of the SOC is reflected in the spin-admixture parameter γ, which is a measure of the influence of spin-orbit coupling on spin dynamics.[10–13] The conformation of the polymer structure is believed to affect γ since it depends on the relative orientation of neighbouring π orbitals. More specifically, higher SOC is obtained for greater torsional angles along the polymer backbone of an OSC.[7] Raman spectroscopy is an excellent structural probe as it is particularly sensitive to π-electrons, which are highly polarizable under photoexcitation and thus gives information on polymer conformation and structure.[14] Many studies have employed Raman spectroscopy to characterize a range of chemically doped polymers, mostly polythiophenes, showing that structural conformation stands out as one of the most significant parameters that influence the properties of conjugated polymers such as spin transport.[15]

In this work, we aim to elucidate the link between a polymer's backbone conformation and SOC using poly(3,4-ethylenedioxythiophene):poly(4-styrenesulfonate), most commonly referred to as PEDOT:PSS, as a model material. Therefore, we exploited the capability of Resonance Raman spectroscopy in experimentally probing the structural reorganization of PEDOT conjugated polymer. We firstly use chemical doping or dedoping to alter the polymer's structural conformation and we identify the vibrational modes associated with the formation of polarons/bipolarons in PEDOT, correlating the changes of these modes with the molecular order of the polymer. The observed trends are attributed to the variation of the degree of torsion between conjugated units along the polymer backbone of PEDOT, with the structural conformation and associated change in planarity monitored via Raman spectroscopy. We use this alongside with in situ spectro-electrochemical measurements to provide a comprehensive understanding of the electronic and vibrational structure of the polymer chain monitored via Raman spectroscopy. We finally estimate the spin-admixture parameter γ^2 and find that it reduces as the polymer planarity increases.

6.2 Results and discussion

6.2.1 Chemical doping

The series of samples with different doping levels, labelled P1–P6, as used throughout this study, is presented in Table 6.1. In order to have different degrees of doping for PEDOT:PSS we employed different amounts of DMSO or NaOH to respectively adjust the doping or dedoping of the polymer. Introducing an organic solvent with high solubility in water and high hydrophilicity, such as Dimethyl Sulfoxide (DMSO), which isolates uncoupled PSS, changes the film morphology, and improves the crystallinity, results in a significant increase of carrier concentration and conductivity.[16–18] The opposite outcome is achieved by the insertion of a dedopant, such as NaOH, that neutralizes PEDOT:PSS and disrupts the π conjugation of the PEDOT structure.[19,20] The ability to tune the doping level was confirmed by conductivity and carrier concentration measurements, reported in our paper[21] and is further supported by optical absorbance measurements displayed in Figure 6.1, which shows the absorption spectra at the different doping levels covering a wide spectral range in UV-Vis-NIR.

Table 6.1. Labeling of the PEDOT:PSS samples in descending doping order with additive concentrations.

Sample ID	P1	P2	P3	P4	P5	P6
Additive	DMSO	-	NaOH	NaOH	NaOH	NaOH
Dopant Conc. (Vol%)	1	-	0.5	0.5	0.5	1
[NaOH] (M)			0.5	4	5	4

The distinct band at ~950 nm, more prominent in the sample with the lower doping i.e. P6 is related to polymer polaronic states.[22–24] The spectra contain also a weaker feature at ~800 nm and a broad band extended to infrared with an apparent peak at ~1700 nm that are both attributed to bipolaron absorption.[22] The presence of bipolarons indicate that in the respective samples the PEDOT is in a high doped state.[22,25]

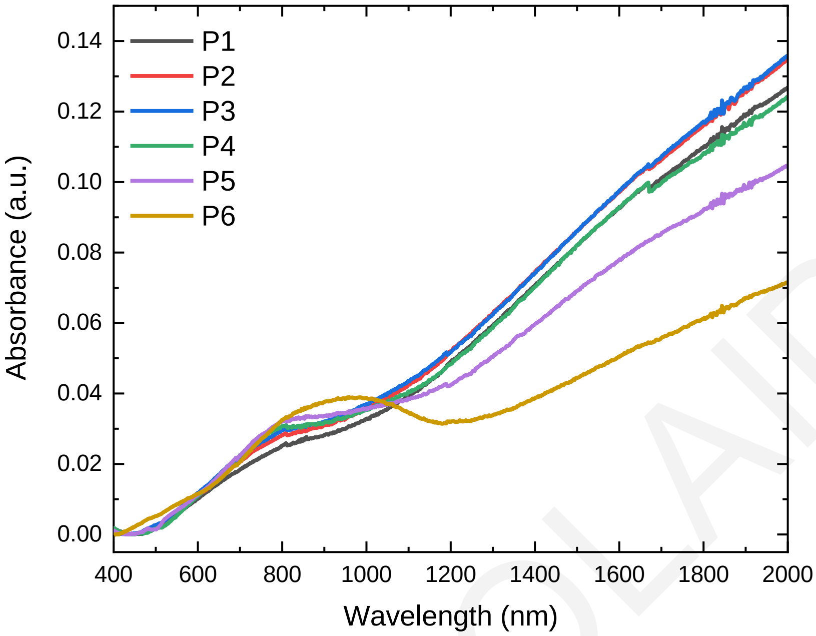

Figure 6.1. UV-vis-NIR absorption spectra for all samples of spin-coated films.

Addition of DMSO causes a significant reduction of trapped polaron population while simultaneously leading to spinless bipolaron formation.[26,27] Consequently, polarons and bipolarons coexist in PEDOT:PSS, the populations of which are modified during doping. It can be observed that as the concentration of NaOH increases causing dedoping, the bipolaron features quench at the expense of the polaron absorption at ~950 nm.[19,20,22,25]

Spin measurements, more specifically inverse spin Hall effect (ISHE) under Ferromagnetic Resonance (FMR) measurements employed in our paper[21] for estimation of spin diffusion length (SDL) and spin Hall angle (θ_{SH}), a measure of the efficiency of the spin-to-charge conversion, which are closely linked to the SOC strength in the material, revealed that the degree of doping is associated with changes in the SOC strength. Since the doping procedure does not affect the atomic composition, we expect that the variation of the SOC originates in a possible alteration of the PEDOT's structural conformation upon doping. Indeed, the interplay between changes of the polymer's backbone conformation and chemical doping has been widely reported for OSCs.[28–30] In such situations, the strength of the SOC can be conveniently parametrized via the spin-admixture parameter, which is directly proportional to the ratio of spin flipping to spin-conserving hopping events.[10,11,13] The magnitude of γ^2 is expected to be maximized for large thiophene-thiophene dihedral angles (orthogonal π-orbitals) and minimized for a planar backbone PEDOT.[12] We can estimate γ^2 for every PEDOT:PSS doping level using the theory proposed by Wang et al.[4] The spin-lattice relaxation time T_1 that is already obtained is affected by two principal contributions, SOC and hyperfine interaction (HFI), and is given by the relation $T_1 = (\omega_{HFI} + \omega_{SOC})^{-1} = (\, 2\Omega^2_{HFI}\,\tau/3 + 8\,\gamma^2/3\tau\,)^{-1}$. The spin relaxation rate due to the local HFI corresponds to the first term and HFI = 2×10^8 Hz is the Larmor frequency of the local hyperfine magnetic field, while the second corresponds to the spin relaxation rate due to the SOC. The dwell time τ of a spin on a molecule is given by $\tau = \left(2D_{\text{hop}}/\alpha^2 + 2D_{\text{exc}}/R^2\right)^{-1}$ where α = 0.37 nm[18] is the average hopping distance between polarons along the π-π stacking direction. Figure 6.2 shows the estimate of γ^2 for every sample. A clear gradual reduction of the spin admixture is observed during dedoping with an overall decline of approximately one order of magnitude (10^{-6}-10^{-5}), indicating that the PEDOT backbone becomes more planar with the insertion of NaOH. Furthermore, the absolute values of γ^2 obtained are in good agreement with the theoretical estimation for sexithiophene (T6), shown in Figure 6.2 as a blue dashed line for comparison, whose structure is similar with PEDOT:PSS.[12,31]

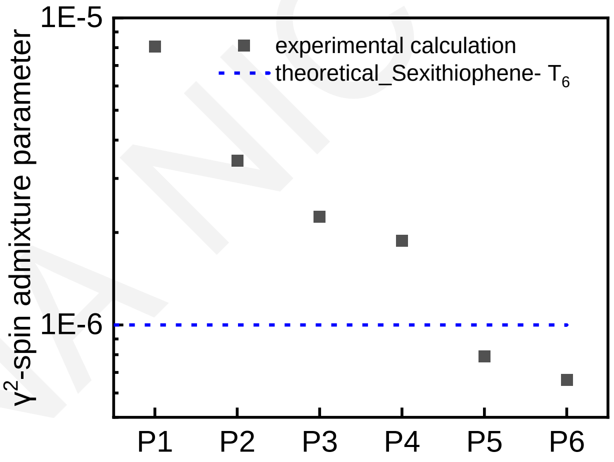

Figure 6.2. Estimation of the spin admixture parameter γ^2 for P1–P6. For comparison, we plot the theoretical value of sexithiophene (T6) (blue dashed line) a material with linear conformation and very similar structure with PEDOT.

We can experimentally verify the above conclusion via resonance Raman spectroscopy, which can provide information regarding the structural conformation of conjugated polymers. In a typical resonance Raman spectrum of PEDOT:PSS, four main peaks are distinguished.[32–34] Two of them are ascribed to the stretching modes of inter and intra-ring C–C single bonds of thiophene, centered at ~1250 and ~1360 cm^{-1}, and the other two to the symmetric and asymmetric stretches of C=C double bonds at ∼1430 and 1520 cm^{-1}, respectively. The assignment of the most prominent bands is summarized in Table 6.2. The most significant changes observed during the dedoping process are identified in the Raman band between 1400 and 1500 cm^{-1}, which is mainly due to C=C symmetric stretching. This band includes contributions from the symmetric stretching modes of the $C_α$–$C_β$(–O) bond in the quinoid structure and the $C_α$=$C_β$(–O) bond in the benzoid structure at ∼1430 and ∼1450 cm^{-1}, respectively, and the asymmetric $C_α$=$C_β$(–O) stretching at 1400 cm^{-1}.[34] The quinoid structure represents a more linear backbone with enhanced planarity, stemming from the double bond $C_α$=$C_α$ between the thiophene units, which locks the backbone dihedral angle to 180°, while the benzoid structure has a favored coil conformation, as the single bond $C_α$–$C_α$ facilitates inter-ring twisting (Figure 6.4b).[28] Consequently, Raman spectroscopy gives the opportunity for an in-depth understanding of PEDOT's structural change during chemical doping, by tracking the quinoid/benzoid ratio for every sample.

From the absorption spectra, we determine the laser excitation wavelength required for resonance Raman spectroscopy measurements.[35–37] At 532 nm, the neutral band can be resonantly excited and this would provide more sensitive structural characterization to the changes in the dedoped PEDOT. Figure 6.3 shows the Raman spectra with 532 nm excitation for every doping level. At high doping levels the C=C symmetric stretch band is broader, reflecting the conformational disorder of the polymer in mixed charge states (neutral, polaron, and bipolaron). The shorter conjugation length of the benzoid segments at these doping levels shifts the benzoid band to higher wavenumbers with enhanced contribution (see Figure 6.5).[38,39] A clear shift of the position of the C=C symmetric stretch band to lower wavenumbers is observed upon dedoping. This is more prominent in the Raman spectrum of P6, with a downshift of 7 cm$^{–1}$ of the quinoid C=C stretch band, which in combination with the pronounced narrowing of the C=C linewidth (full width at half maximum), constitutes a distinct signature of the increased planarity of PEDOT's backbone expected for the quinoid conformation.[39,40]

Table 6.2. Comparison of the frequencies (cm^{-1}) of Raman bands of P1-P6 extracted from deconvolution of RR spectra.

Frequency (cm^{-1})						**Assignment**
P1	**P2**	**P3**	**P4**	**P5**	**P6**	
1235	1235	1238	1240	1236	1209	C_a-C_a inter-ring stretching
1258	1258	1255	1255	1255	1268	C_a-C_a inter-ring stretching
1321	1321	1324	1320	1324	1332	C_b-C_b stretching
1366	1366	1363	1363	1364	1367	C_b-C_b stretching
1403	1403	1400	1400	1399	1402	Asymmetric C_a=C_b (-O) stretching
1436	1436	1432	1431	1432	1429	Quinoid symmetric C_a-C_b (-O) stretching
1456	1456	1453	1452	1453	1452	Benzoid symmetric C_a=C_b (-O) stretching
1495	1495	1492	1494	1497	1505	Asymmetric C=C stretching
1535	1533	1529	1529	1533	1519	Asymmetric C=C stretching
1565	1565	1562	1560	1562	1550	Asymmetric C=C stretching

The area, FWHM and the position of all Raman bands (see Table 6.1 and S6.1), including quinoid and benzoid bands were determined by deconvolution of Resonance Raman spectra (see Figure 6.5(a) and Table S6.1, as an example corresponding to P1 and Figure 6.5(b) for P6), which were modelled using Voigt peaks (a convolution of Lorentzian and Gaussian profiles). Specifically, the appropriate deconvolution of the C=C symmetric stretch peak shown in Figure 6.4a further confirms the gradual enhancement of the quinoid, more planar, structure when dedoped and especially its predominance in the case of P6, which along with its narrower linewidth indicates a smaller distribution of PEDOT structural conformations (Figure 6.4a).[39]

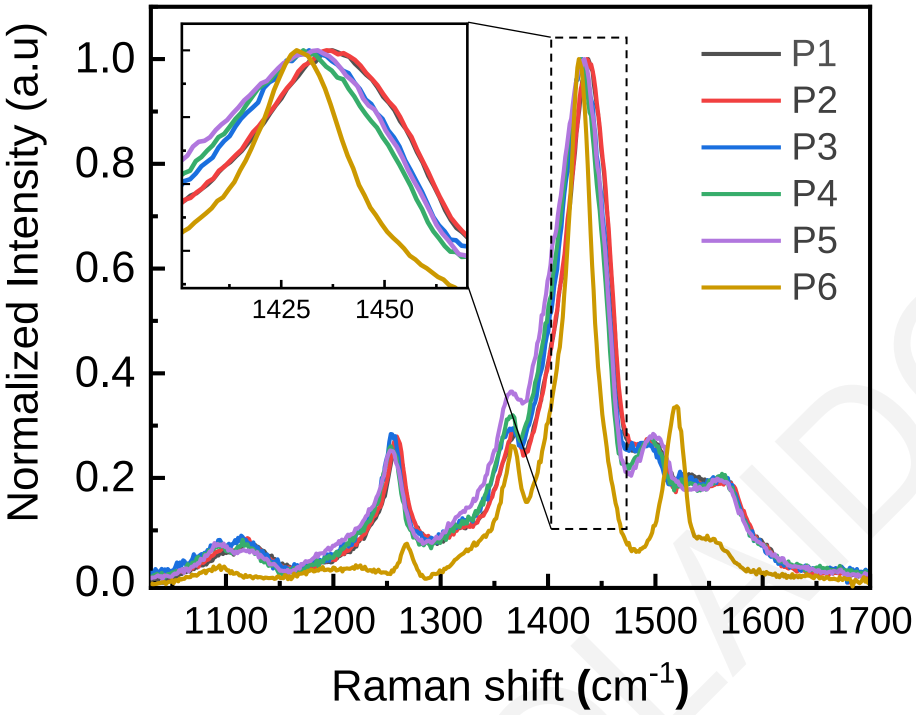

Figure 6.3 Normalized resonance Raman spectra of the PEDOT:PSS samples at different doping levels with excitation at 532 nm.

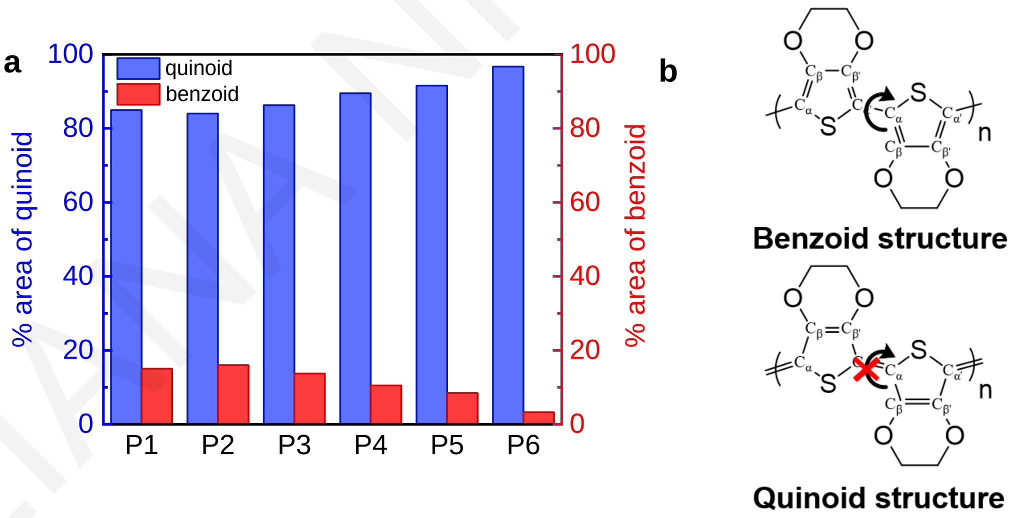

Figure 6.4. (a) Percentage of the quinoid and benzoid band within our different samples obtained from Raman data deconvolution, together with the corresponding structures (b).

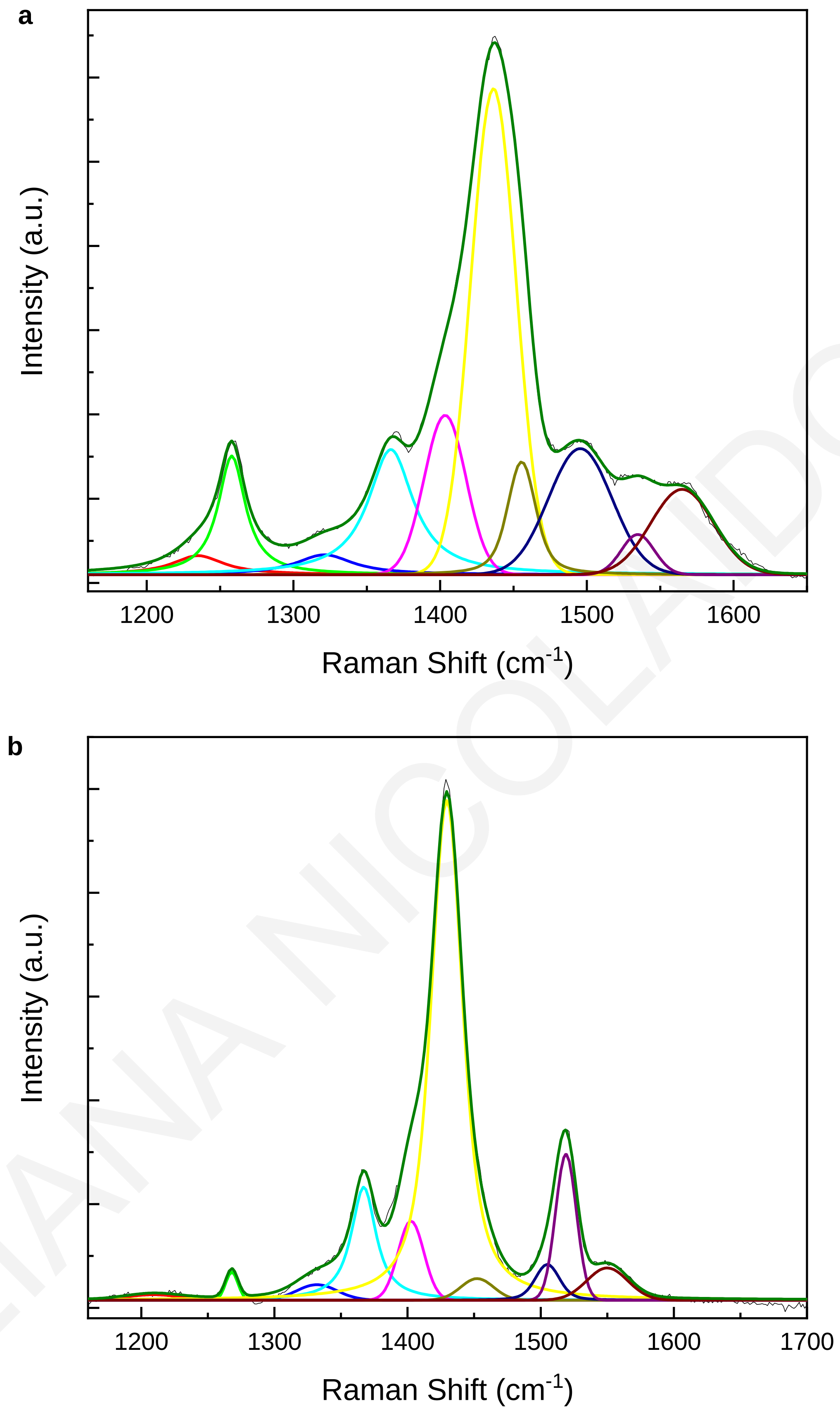

Figure 6.5. Deconvolution of RR spectra for (a) P1 and (b) P6 with excitation at 532 nm.

This tendency of the resonance Raman spectra after chemical doping agrees with the corresponding behaviour of Raman spectra during electrochemical doping and or dedoping. Polarons, regardless of how they are formed (can be formed by charge injection, chemical doping, or electrochemical doping, as well as by charge generation via photoexcitation,[41–43] are similar in nature and exhibit similar spectroscopic signatures.[44,45] Compared to photogeneration and chemical doping, electrochemical doping of PEDOT:PSS allows precise control of polaron formation in terms of its density.[46] Here, a layer of the ion gel (consisting of an ionic liquid (EMIM:BF_4) within a polymer matrix (PVDF-HFP)) was spin casted on top of the three electron structure PEDOT:PSS film, and the polaron density is controlled via an electrochemical potential to the film in a three-electrode cell configuration (see Figure S6.1), while Raman spectroscopic measurements are performed *in operando* (simultaneously) with excitation at 532 nm.[14]

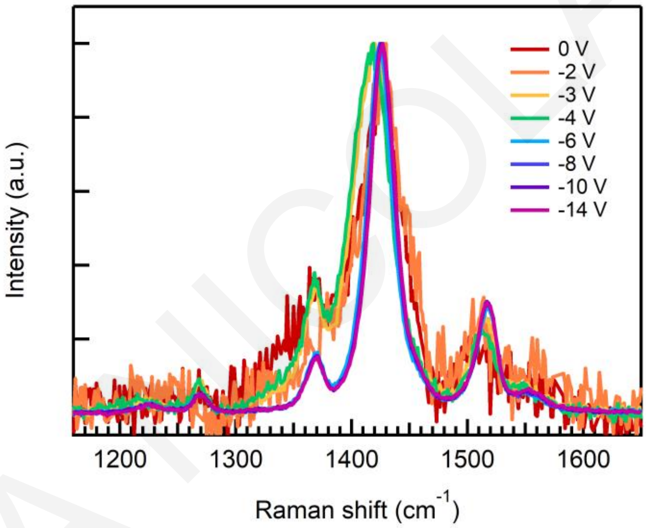

Figure 6.6. Normalized resonance Raman spectra of PEDOT:PSS upon electrochemical reduction (dedoping) with excitation at 532 nm.

The Raman spectra when reduction (dedoping) (from 0 to −14V) and oxidation (doping) potentials (from 0 to 4V) are applied are shown at Figures 6.6 and 6.7 respectively and agree with electrochemical doping/dedoping of PEDOT reported in the literature.[25,39] The spectra with applied reduction potential until -4 V exhibit the known signatures of increased planarity and therefore quinoid structure, which are a downshift of the C=C symmetric stretching band to ~1420 cm^{-1}, an increased intensity of the C-C band stretch at 1370 cm^{-1} until -4V and narrowing of FWHM. From -6V to -14V the C=C symmetric stretching band shifts back to higher wavenumbers, the intensity of C-C decreases and C=C asymmetric stretching band at ~1520 cm^{-1} increases, indicating that benzoid structure associated with the neutral polymer is involved more in the backbone conformation, due to diminution of the polaron concentration.

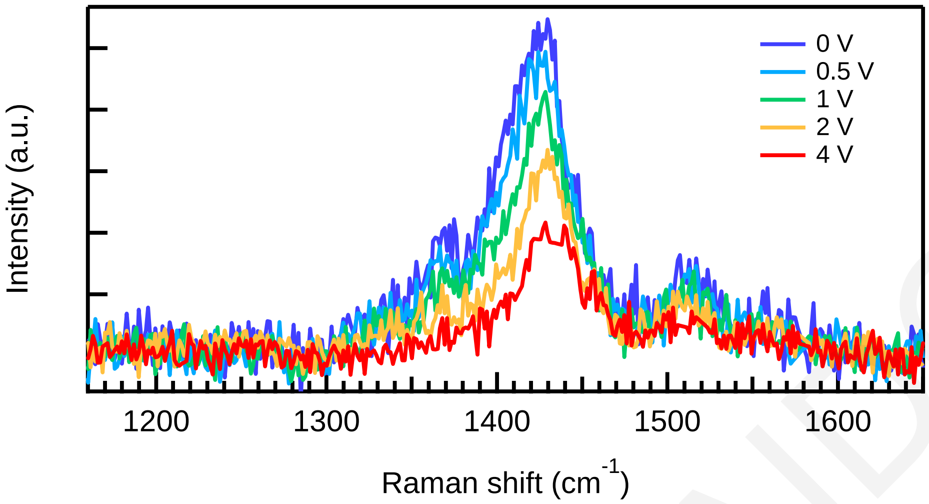

Figure 6.7. Resonance Raman spectra of PEDOT:PSS upon electrochemical oxidation (doping) with excitation at 532 nm.

Evolution towards a disordered benzoid structure is also observed when oxidation potentials are applied displaying a prominent blue shift of the C=C stretching band. These spectra are not normalized, showing an overall decrease of the intensity of the spectra as doping levels are increased due to the fact that at 532 nm we excite selectively the neutral population, which decreases as oxidation increases. This explains also the better signal to noise obtained at more negative potentials that generate an increasing neutral population on the polymer backbone.

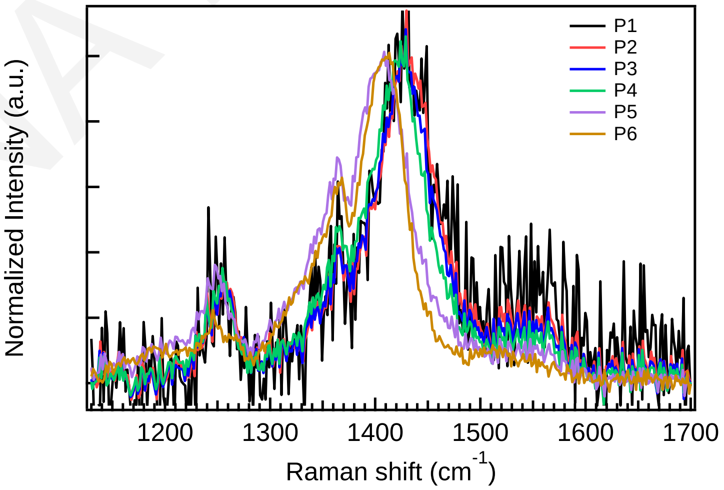

Figure 6.8. Normalized resonance Raman spectra of the PEDOT:PSS samples at different doping levels with excitation at 532 nm.

Figure 6.8 shows the normalized Raman spectra using 785 nm as excitation wavelength on resonance with the polymer polaronic transitions. We observe the increase of the relative intensity of C-C to C=C Raman intensity as the concentration of NaOH is increased. This due to an increasing amount of quinoid segments, which dominate the PEDOT conformation, while the smaller distribution of the PEDOT conformations is evidenced by the narrowing of the C=C FWHM, when the population of polarons increases due to dedoping.[39] We observe the opposite effect when oxidizing the film, with FWHM broadening induced by the higher degree of conformational disorder, as a mixture of charged states is present.

6.3 Conclusions

We have explored the influence of structural conformation of conjugated polymer on spin transport in PEDOT:PSS at different chemically defined doping levels. The increasing dedoping exhibits gradual reduction of the spin admixture parameter γ^2 by one order of magnitude and therefore indicates an associated SOC strength reduction. Since the chemical composition of the organic semiconductor remains the same by the doping procedure, we attribute the change of the SOC strength to the alteration of the structural conformation of the polymer. This is confirmed through resonance Raman spectroscopy with the predominance of the more planar quinoid structure at lower doping levels, indicating that enhanced planarity is associated with SOC strength reduction. The main spectral features related to dedoped PEDOT:PSS are the narrowing of the C=C stretching band FWHM, which shifts in peak position to lower energies, and the increase of the relative intensity of C-C to C=C stretching bands. This study offers an intrinsic way of controlling SOC by manipulating the OSC’s structural conformation, which can be used for future spin transport studies in these materials as well as to enhance functionality in spintronic devices.

6.4 Experimental section

6.4.1 Materials and Sample Preparation

Thin film preparation was carried out in the research group of Prof. Theodossis Trypiniotis, at the Department of Physics of the University of Cyprus by the PhD candidate Constantinos Nicolaides, who also estimated the spin admixture parameter γ^2, collected the absorption data and assisted in arranging the electrochemical doping setup for Raman measurements. Experiments were carried out at room temperature using solution-processed PEDOT:PSS (PH1000, PEDOT:PSS ratio=1:2.5) filtered using a 0.45-μm PVDF syringe filter as the starting material. The substrates were cleaned with deionized water and isopropanol in an ultrasonic bath and dried with nitrogen gas followed by UV-ozone treatment for 10 min before use. In order to have different degrees of doping for PEDOT:PSS we employed different amounts of DMSO or NaOH to respectively adjust the doping or dedoping of the polymer. The series of samples with different doping levels, labeled P1–P6, is presented in Table 6.1. For absorption measurements a volume of 20 μL of PEDOT:PSS solution was spin coated at 4000 rpm in ambient conditions and the resulting films were then annealed at 120 °C for 15 min. For Raman measurements the samples were prepared by drop-casting 20 μL of PEDOT:PSS solution and dried at 120 °C for 20 min. For electrochemical doping Au contact pads were thermally evaporated through a shadow mask and were used for the source, drain, and gate electrodes. The contacts were fabricated by using a top contact side-gate configuration (Figure S6.1) on the SiO_2 substrates. Part of the PEDOT:PSS layers were removed by cotton stick (for gate electrode deposition). After annealing at 150 ° C for 30 min in air, Au was evaporated by using electron beam evaporation. The ion gel from the ionic liquid 1-ethyl-3-methylimidazolium tetrafluoroborate ($EMIM:BF_4$) and the block copolymer poly(vinylidene fluoride-co-hexafluoropropylene (PVDF-HFP) dissolved in DMF solvent, were used as the electrolyte and dielectric. Electrochemical doping was achieved using the Sourcemeter KEITHLEY 2450.

6.4.2 Experimental details

Absorption spectroscopy. Optical absorbance measurements were performed over a wide spectral range in UV-Vis-NIR. Optical absorption data were recorded by employing a Perkin Elmer Lamda 1050 spectrophotometer equipped with a three-detector module covering the 300-3000 nm spectral range.

Resonance Raman Studies with excitation at 532 nm. For Resonance Raman experiments conducted with excitation at 532 nm we used a custom-made Raman microscope (Raman AlphaSource RLS4032, NanoBioAnalytics). A 20x objective was used to focus 35 mW of the laser light onto the film surface. The Raman scattered light was collected through an optical fiber and delivered to a 0.30m focal-length Czerny−Turner spectrograph (SpectraPro, SP2300i, Princeton Instruments), equipped with a 1200 grooves/mm classically-ruled grating. The slit width was set to 30 μm providing 2 cm^{-1} spectral resolution at 532 nm. The scattered light was detected by a LN2-cooled 1340 x 100 pixel, back-illuminated CCD detector (Spec10:100B/LN, Princeton Instruments). Each spectrum is the accumulation of 5 × 10 min spectra. Frequency calibration of the spectra was accomplished with the use of cyclohexane. MATLAB and ORIGIN software were used for spectral treatment and analysis. The percentage area of the quinoid and benzoid band was calculated using the following equation:

$$\%\, area\ of\ quinoid(or\ benzoid) = \frac{Area(quinoid\ or\ benzoid)}{Area(quinoid) + Area(benzoid)} * 100$$

Resonance Raman Studies with excitation at 785 nm. Raman spectra with excitation at 785 nm were obtained using a fibre-optic Raman Probe connected to a 475-mW CW 785-nm Multimode Laser and a FERGIE 1024BRX spectrograph equipped with a 50-μm slit, a 1200 gr/mm grating (550-nm blaze) a back-illuminated, deep depletion eXcelon sensor (Teledyne Princeton Instruments) and a thermoelectric cooling at −45 ˚C charged coupled device (CCD) controlled by Lightfield software (Princeton Instruments, Trenton, NJ, USA). Each spectrum for each position on the film is the accumulation of 5 × 10 min spectra and were collected without any observed damage. Cyclohexane was used as a frequency calibration standard.

References

(1) Dediu, V. A.; Hueso, L. E.; Bergenti, I.; Taliani, C. Spin Routes in Organic Semiconductors. *Nat. Mater.* **2009**, *8*, 707–716.

(2) Guo, L.; Qin, Y.; Gu, X.; Zhu, X.; Zhou, Q.; Sun, X. Spin Transport in Organic Molecules. *Front. Chem.* **2019**, *7*, 1–11.

(3) Tsurumi, J.; Matsui, H.; Kubo, T.; Häusermann, R.; Mitsui, C.; Okamoto, T.; Watanabe, S.; Takeya, J. Coexistence of Ultra-Long Spin Relaxation Time and Coherent Charge Transport in Organic Single-Crystal Semiconductors. *Nat. Phys.* **2017**, *13*, 994–998.

(4) Wang, S.; Venkateshvaran, D.; Mahani, M. R.; Chopra, U.; Mcnellis, E. R.; Pietro, R. Di; Schott, S.; Wittmann, A.; Schweicher, G.; Cubukcu, M.; Kang, K.; Carey, R.; Wagner, T. J.; Siebrecht, J. N. M.; Wong, D. P. G. H.; Jacobs, I. E.; Aboljadayel, R. O.; Ionescu, A.; Egorov, S. A.; Mueller, S.; Zadvorna, O.; Skalski, P.; Jellett, C.; Little, M.; Marks, A.; Mcculloch, I.; Wunderlich, J.; Sinova, J.; Sirri. Long Spin Diffusion Lengths in Doped Conjugated Polymers Due to Enhanced Exchange Coupling. *Nat. Electron.* **2019**, *2*, 98–107.

(5) Sun, D.; Schooten, K. J. Van; Kavand, M.; Malissa, H.; Zhang, C.; Groesbeck, M.;

Boehme, C.; Vardeny, Z. V. Inverse Spin Hall Effect from Pulsed Spin Current in Organic Semiconductors with Tunable Spin–Orbit Coupling. *Nat. Mater.* **2016**, *15*, 863–870.

(6) Watanabe, S.; Ando, K.; Kang, K.; Mooser, S.; Vaynzof, Y.; Kurebayashi, H.; Saitoh, E.; Sirringhaus, H. Polaron Spin Current Transport in Organic Semiconductors. *Nat. Phys.* **2014**, *10*, 308–313.

(7) Vetter, E.; VonWald, I.; Yang, S.; Yan, L.; Koohfar, S.; Kumah, D.; Yu, Z.-G.; You, W.; Sun, D. Tuning of Spin-Orbit Coupling in Metal-Free Conjugated Polymers by Structural Conformation. *Phys. Rev. Mater.* **2020**, *4*, 085603.

(8) Lu, Q.; Yin, S.; Gao, T.; Qin, W.; Xie, S.; Qu, F.; Saxena, A. Spin Transport Based on Exchange Coupling in Doped Organic Polymers. *J. Phys. Chem. Lett.* **2020**, *11*, 1087–1092.

(9) Lu, Q.; Xie, S.; Qu, F. Hopping-Dominated Spin Transport in Unintentionally Doped Organic Semiconductors. *J. Phys. Chem. Lett.* **2021**, *12*, 3540–3544.

(10) Chopra, U.; Egorov, S. A.; Sinova, J.; Mcnellis, E. R. Chemical and Structural Trends in the Spin-Admixture Parameter of Organic Semiconductor Molecules. *J. Phys. Chem. C* **2019**, *123*, 19112−19118.

(11) Chopra, U.; Shambhawi, S.; Egorov, S. A.; Sinova, J.; Mcnellis, E. R. Accurate and General Formalism for Spin-Mixing Parameter Calculations. *Phys. Rev. B* **2019**, *100*, 134410.

(12) Yu, Z. G. Spin-Orbit Coupling , Spin Relaxation , and Spin Diffusion in Organic Solids. *Phys. Rev. Lett.* **2011**, *106*, 106602.

(13) Yu, Z. G. Spin-Orbit Coupling and Its Effects in Organic Solids. *Phys. Rev. B* **2012**, *85*, 115201.

(14) Nightingale, J.; Wade, J.; Moia, D.; Nelson, J.; Kim, J. Impact of Molecular Order on Polaron Formation in Conjugated Polymers. *J. Phys. Chem. C* **2018**, *122*, 29129−29140.

(15) Francis, C.; Fazzi, D.; Grimm, S. .; Paulus, F.; Beck, S.; Hillebrandt, S.; Pucci, A.; Zaumseil, J. Raman Spectroscopy and Microscopy of Electrochemically and

Chemically Doped High-Mobility Semiconducting Polymers. *J. Mater. Chem. C* **2017**, *5*, 6176–6184.

(16) Crispin, X.; Jakobsson, F. L. E.; Crispin, A.; Grim, P. C. M.; Andersson, P.; Volodin, A.; Haesendonck, C. Van; Auweraer, M. Van Der; Salaneck, W. R.; Berggren, M. The Origin of the High Conductivity of Poly(3,4-Ethylenedioxythiophene)-Poly(Styrenesulfonate) (PEDOT-PSS) Plastic Electrodes. *Chem. Mater.* **2006**, *18*, 4354–4360.

(17) Kim, G.; Shao, L.; Zhang, K.; Pipe, K. P. Engineered Doping of Organic Semiconductors for Enhanced Thermoelectric Efficiency. *Nat. Mater.* **2013**, *12*, 719–723.

(18) Bubnova, O.; Khan, Z. U.; Wang, H.; Braun, S.; Evans, D. R.; Fabretto, M.; Hojati-Talemi, P.; Dagnelund, D.; Arlin, J. B.; Geerts, Y. H.; Desbief, S.; Breiby, D. W.; Andreasen, J. W.; Lazzaroni, R.; Chen, W. M.; Zozoulenko, I.; Fahlman, M.; Murphy, P. J.; Berggren, M.; Crispin, X. Semi-Metallic Polymers. *Nat. Mater.* **2014**, *13* (2), 190–194.

(19) Mochizuki, Y.; Horii, T.; Okuzaki, H. Effect of PH on Structure and Conductivity of PEDOT / PSS. *Trans. Mater. Res. Soc. Japan* **2012**, *37*, 307–310.

(20) Tsai, T.; Chang, H.; Chen, C.; Huang, Y.; Whang, W. A Facile Dedoping Approach for Effectively Tuning Thermoelectricity and Acidity of PEDOT : PSS Films. *Org. Electron.* **2014**, *15* (3), 641–645.

(21) Nicolaides, C.; Nicolaidou, E.; Papagiorgis, P.; Itskos, G.; Hayes, S. C.; Trypiniotis, T. Effect of Structural Conformation of Conjugated Polymers on Spin Transport. *Phys. Rev. Mater.* **2022**, *6* (9), 095601.

(22) Rebetez, G.; Bardagot, O.; Affolter, J.; Réhault, J.; Banerji, N. What Drives the Kinetics and Doping Level in the Electrochemical Reactions of PEDOT:PSS? *Adv. Funct. Mater.* **2022**, *32*, 2105821.

(23) Paulsen, B. D.; Wu, R.; Takacs, C. J.; Steinrück, H.; Strzalka, J.; Zhang, Q.; Toney, M. F.; Rivnay, J. Time-Resolved Structural Kinetics of an Organic Mixed Ionic – Electronic Conductor. *Adv. Mater.* **2020**, *32*, 2003404.

(24) Zozoulenko, I.; Singh, A.; Singh, S. K.; Gueskine, V.; Crispin, X.; Berggren, M.

Polarons, Bipolarons, And Absorption Spectroscopy of PEDOT. *ACS Appl. Polym. Mater.* **2019**, *1*, 83–94.

(25) Łapkowski, M.; Pron, A. Electrochemical Oxidation of Poly(3,4-Ethylenedioxythiophene) — '" in Situ "' Conductivity and Spectroscopic Investigations. *Synth. Met.* **2000**, *110*, 79–83.

(26) Neusser, D.; Malacrida, C.; Kern, M.; Gross, Y. M.; Slageren, J. Van; Ludwigs, S. High Conductivities of Disordered P3HT Films by an Electrochemical Doping Strategy. *Chem. Mater.* **2020**, *32*, 6003–6013.

(27) Volkov, A. V; Singh, S. K.; Stavrinidou, E.; Gabrielsson, R.; Franco-Gonzalez, J. F.; Cruce, A.; Chen, W. M.; Simon, D. T.; Berggren, M.; Zozoulenko, I. V. Spectroelectrochemistry and Nature of Charge Carriers in Self-Doped Conducting Polymer. *Adv. Electron. Mater.* **2017**, *3*, 1700096.

(28) Li, X.; Zou, R.; Liu, Z.; Mata, J.; Storer, B.; Chen, Y.; Weiheng, Q.; Zekun, Z.; Zhang, P. Deciphering the Superior Thermoelectric Property of Post- Treatment-Free PEDOT : PSS/IL Hybrid by X-Ray and Neutron Scattering Characterization. *Npj. Flex. Electron.* **2022**, *6*, 6.

(29) Gao, J.; Stein, B. W.; Thomas, A. K.; Garcia, J. A.; Yang, J.; Kirk, M. L.; Grey, J. K. Enhanced Charge Transfer Doping Efficiency in J-Aggregate Poly(3-Hexylthiophene) Nanofibers. *J. Phys. Chem. C* **2015**, *119*, 16396–16402.

(30) Mansour, A. E.; Valencia, A. M.; Lungwitz, D.; Wegner, B.; Tanaka, N.; Shoji, Y.; Fukushima, T.; Opitz, A.; Cocchi, C.; Koch, N. Understanding the Evolution of the Raman Spectra of Molecularly P-Doped Poly(3-Hexylthiophene-2,5-Diyl): Signatures of Polarons and Bipolarons. *Phys. Chem. Chem. Phys.* **2022**, *24*, 3109–3118.

(31) Yu, Z. G. Spin Hall Effect in Disordered Organic Solids. *Phys. Rev. Lett.* **2015**, *115*, 026601.

(32) Funda, S.; Ohki, T.; Liu, Q.; Hossain, J.; Ishimaru, Y.; Ueno, K.; Shirai, H. Correlation between the Fine Structure of Spin-Coated PEDOT:PSS and the Photovoltaic Performance of Organic/Crystalline-Silicon Heterojunction Solar Cells. *J. Appl. Phys.* **2016**, *120*, 033103.

(33) Garreau, S.; Duvail, J. L.; Louarn, G. Spectroelectrochemical Studies of Poly (3,4-Ethylenedioxythiophene) in Aqueous Medium. *Synth. Met.* **2002**, *125*, 325–329.

(34) Yu, L.; Chen, T.; Feng, N.; Wang, R.; Sun, T.; Zhou, Y.; Wang, H.; Yang, Y.; Lu, Z. Highly Conductive and Wettable PEDOT:PSS for Simple and Ef Fi Cient Organic/c-Si Planar Heterojunction Solar Cells. *Sol. RRL* **2020**, *4*, 1900513.

(35) Kim, B. J.; Ho, P. K. H.; Murphy, C. E.; Baynes, N.; Friend, R. H. Nature of Non-Emissive Black Spots in Polymer Light-Emitting Diodes by In-Situ Micro-Raman Spectroscopy. *Adv. Mater.* **2002**, *14*, 206–209.

(36) Soltzberg, L. J.; Slinker, J. D.; Flores-torres, S.; Bernards, D. A.; Malliaras, G. G.; Abrun, H. D.; Kim, J.; Friend, R. H.; Kaplan, M. D.; Goldberg, V. Identification of a Quenching Species in Ruthenium Tris-Bipyridine Electroluminescent Devices. *J. Am. Chem. Soc.* **2006**, *128*, 7761–7764.

(37) Limbu, S.; Pont, S.; Doust, A. B.; Kwon, S.; Fuller, P.; Tan, E.; Durrant, J. R.; Kim, J. Impact of Initial Bulk-Heterojunction Morphology on Operational Stability of Polymer : Fullerene Photovoltaic Cells. *Adv. Mater. Interfaces* **2019**, *6*, 1801763.

(38) Sakamoto, S.; Okumura, M.; Zhao, Z.; Furukawa, Y. Raman Spectral Changes of PEDOT – PSS in Polymer Light-Emitting Diodes upon Operation. *Chem. Phys. Lett.* **2005**, *412*, 395–398.

(39) Tan, E.; Pappa, A. M.; Nightingale, J.; Wood, S.; Castro, F. A.; Kim, J. S. A Highly Sensitive Molecular Structural Probe Applied to in Situ Biosensing of Metabolites Using PEDOT : PSS. *Biotechnol. Bioeng.* **2019**, *117*, 291–299.

(40) Tsoi, W. C.; James, D. T.; Kim, J. S.; Nicholson, P. G.; Murphy, C. E.; Bradley, D. D. C.; Nelson, J.; Kim, J. S. The Nature of In-Plane Skeleton Raman Modes of P3HT and Their Correlation to the Degree of Molecular Order in P3HT:PCBM Blend Thin Films. *J. Am. Chem. Soc.* **2011**, *133*, 9834–9843.

(41) Yim, K.-H.; Whiting, G. L.; Murphy, C. E.; Halls, J. J. M.; Burroughes, J. H.; Friend, R. H.; Kim, J. Controlling Electrical Properties of Conjugated Polymers via a Solution-Based p-Type Doping. *Adv. Mater.* **2008**, *20*, 3319–3324.

(42) Bruevich, V. V; Makhmutov, T. S.; Elizarov, S. G.; Nechvolodova, E. M.; Paraschuk, D. Y. Raman Spectroscopy of Intermolecular Charge Transfer Complex

between a Conjugated Polymer and an Organic Acceptor Molecule. *J. Chem. Phys.* **2007**, *127*, 104905.

(43) Bailey, J.; Wright, E. N.; Wang, X.; Walker, A. B.; Bradley, D. D. C. Understanding the Role of Ultra-Thin Polymeric Interlayers in Improving Efficiency of Polymer Light Emitting Diodes. *J. Appl. Phys.* **2014**, *115*, 204508.

(44) Yamamoto, J.; Furukawa, Y. Raman Characterization and Electrical Properties of Poly (3-Hexylthiophene) Doped Electrochemically in an Ionic Liquid-Gated Transistor Geometry. *Org. Electron.* **2016**, *28*, 82–87.

(45) Magnanelli, T. J.; Bragg, A. E. Time-Resolved Raman Spectroscopy of Polaron Pair Formation in Poly(3-Hexylthiophene) Aggregates. *J. Phys. Chem. Lett.* **2015**, *6*, 438–445.

(46) Wade, J.; Wood, S.; Beatrup, D.; Wade, J.; Wood, S.; Beatrup, D.; Hurhangee, M.; Bronstein, H.; Mcculloch, I.; Durrant, J. R.; Kim, J. Operational Electrochemical Stability of Thiophene-Thiazole Copolymers Probed by Resonant Raman Spectroscopy Probed by Resonant Raman Spectroscopy. *J. Chem. Phys.* **2015**, *142*, 244904.

CHAPTER 7

IMPACT OF MOLECULAR STRUCTURE ON VIBRONIC SPIN ORBIT COUPLING OF THIOPHENE BASED HETEROACENES

On the aim to explore further the structure - spin-based property relationship of thiophene-based organic materials, we continue to exploit spectroscopic techniques to address questions that concern the excited state processes, focusing now on small organic conjugated molecules. Along with polymers, small molecules have also proven to yield promising semiconducting layered systems. In particular, in the field of spintronics and optoelectronics small heteroacenes were found to unexpectedly exhibit fast intersystem crossing (ISC) due to enhanced spin-orbit coupling induced by vibronic terms, through coupling to out-of-plane vibrational modes. Among them, it was reported that [1]benzothieno[3,2- b]-[1]benzothiophene (BTBT) family of materials which are solution-processable materials with the ability for high charge-carrier mobilities, exhibit strong SOC. In this study we tested differently alkylated BTBT derivatives and a benzothiophene (BT) derivative with flexible core and examine how the degree of planarity and alkylation in the planar molecules affect the effective vibronic spin-orbit coupling (SOC), towards fast ISC. Ultrafast transient absorption (TA) measurements and the extracted kinetics show that 2,7-dialkylated BTBT exhibits the fastest ISC rate. Resonance Raman (RR) revealed that upon alkylation of the BTBT core the conjugation is distorted. We also find through modeling of absorption, fluorescence and Raman cross sections using Resonance Raman Intensity Analysis (RRIA), that the planarity of the core and the extent of alkylation have a strong impact on the extent of change of the molecular geometry in the excited state, extracting the total reorganization energy, which is a key element that affects the efficiency of ISC. Furthermore, RRIA determines the tuning modes and therefore the parts of the structure, which contribute mostly to the reorganization energy. DFT calculations and MD simulations revealed that the rapid ISC cannot be explained by pure electronic SOC, highlighting the necessity of the involvement of vibrational modes through coupling with related excited states. These modes are expected to involve ring deformations in accordance with RRIA. The investigation of the effect of molecular structure on ISC rate (modifying the effective spin-vibronic coupling) of small, planar organic molecules was conducted in collaboration with Prof. Jenny Clark's group from the University of Sheffield, who performed the fluorescence and TA measurements presented in this chapter. DFT calculations were performed by Dr. Theo Keane fin the group of Prof. Antony Meijer from the University of Sheffield, and the MD simulations by Dr. Daniel Cole (School of Natural and Environmental Sciences, University of Newcastle).

7.1 Introduction

Spin-orbit coupling (SOC) is a relativistic effect, which couples the charge's angular momentum to its spin causing shift of electronic energy levels and thus allows electronic states of different multiplicities, such as singlet and triplet states to couple.[1] Strong SOC and small energy gap between the lowest singlet excited state and the adjacent triplet excited state ($\Delta E_{S\text{-}T}$) respectively can turn spin-forbidden processes, such as ISC, into allowed transitions enhancing the ISC rate.[2]

In the vast majority of organic compounds composed by light-weight-element (such as C, H, O, N), SOC effects are expected to be less significant, resulting in slow spin relaxation time and slow intersystem crossing (ISC) from singlet to triplet states, as the SOC strength is proportional to the fourth power of the atomic number.[3] However, the SOC strength is not only related to the atomic number, but can be strongly affected by other factors related to the molecular structure, demonstrating rapid ISC. This property deviates strongly from the common behaviour of most organic molecules where the ratio of ISC to internal conversion (IC) and fluorescence is rather small.[4]

The unexpected ultrafast ISC in organic materials is due to enhanced SOC activated through coupling to out-of-plane low-energy vibrational modes. Out-of-plane vibrations may act as promoting modes, increasing their mutual SOC substantially by mixing some σ-π* character into the electronic wave functions that results in accelerating the El-Sayed forbidden nonradiative transition substantially.[5] When the molecular geometry is distorted along out-of-plane vibrational normal modes, states are able to interact and become mixed and vibronically-induce coupling strength for ISC. We therefore expect efficient ISC, driven by vibronic spin–orbit coupling to be a rather common triplet state population mechanism.[6]

Thiophene derivatives and their oligomers are known to undergo rapid intersystem crossing (ISC) leading to extremely high triplet quantum yields, that takes place shortly after moving out of the Franck–Condon region. According to the literature, the efficiency of ISC path is enhanced by non-planarity, resulting in increased σ-π mixing, which as mentioned above enhances SOC through torsional out-of-plane motion that induces coupling between S_1-T_n states.[7] Therefore, in these cases the correlation of vibronic SOC with the torsion angles of adjacent planar units in oligo (poly)thiophene, is the key property which increases ISC rate.

Particularly, it was shown, through theoretical calculations and experiments,[7–9] that the large thiophene-thiophene dihedral angle corresponded to a larger spin admixture parameter which reflects the SOC strength, and thus a shorter spin diffusion length.[3] Therefore, we would expect that these processes should not manifest for planar molecules, as in this case σ and π orbitals are orthogonal and the energy gap between $\sigma\pi^*(T_n)$ and $\pi\pi^*(S_1)$ states is large. However, recent studies showed that planar molecules such as perylene bisimide (PBI),[10] psoralen[6] and BTBT[11] derivatives exhibited rapid ISC, attributed to vibronic spin-orbit coupling. In particular, planar molecules undergo vibrations that destroy their planar symmetry and mix the σ and π orbitals, such as out-of-plane C–H vibrations.[12]

In the course of this study, a series of heteroacenes were studied (see Figure 7.1), having a planar core, or a more torsionally flexible core. The main focus is on [1]benzothieno[3,2-b][1]-benzothiophene (BTBT), which is a promising core structure for air-stable organic semiconductors that are applicable in photonics, optoelectronics and spintronics.[13–18] We studied monoalkyl and 2,7-dialkyl derivatives, in which solubilizing long alkyl groups are introduced in the molecular long-axis direction of the core. The low intrinsic solubility of the BTBT unit has always necessitated molecular modification. In general, symmetrical substitution using medium-sized alkyl chains in Cn-BTBT-Cn compounds are regarded as a benchmark compound class, promoting highly consistent performance data, thus are more commonly utilized.[19–21]

In the present work, we exploit steady-state and time-resolved spectroscopy, as well as DFT calculations and MD simulations to probe the excited state behaviour of BTBT derivatives and dibenzothiophene molecule (diBT) in solution. The present set of experimental and theoretical results does not allow yet to assign which mode is responsible for the coupling that promotes enhanced SOC and subsequently increase the ISC rate. In order to achieve that, time-resolved resonance Raman can be exploited, which could allow us to monitor the triplet formation, and calculate the reorganization energy from S_1 to T_n, which according to literature[21] should be non-zero, leading to an increase in the ISC rate. However, we could investigate the effect of alkylation on the molecular structure in the excited state through RR measurements and by extracting the mode-specific reorganization energies, that enables us to pinpoint the tuning modes that contribute mostly to the total reorganization of each BT derivative. Our findings suggest that the involvement of low-energy out-of-plane modes in the excited state molecular geometry change is considerable, but the in-plane modes are the ones that contribute most. The deactivation begins by an ultrafast internal conversion (IC) from S_2 to S_1, which acts as a doorway towards T_n state according to DFT calculations and

MD simulation. The fastest ISC rate corresponds to C8-BTBT-C8. Also, according to RR, upon alkylation of the BTBT core the conjugation is distorted. These reveal that alkylation of the fused benzothiophene core (similarly with the decrease in planarity in the case of diBT) modifies the molecular geometry in a way that enhances SOC, and this is what we will try to uncover in our work.

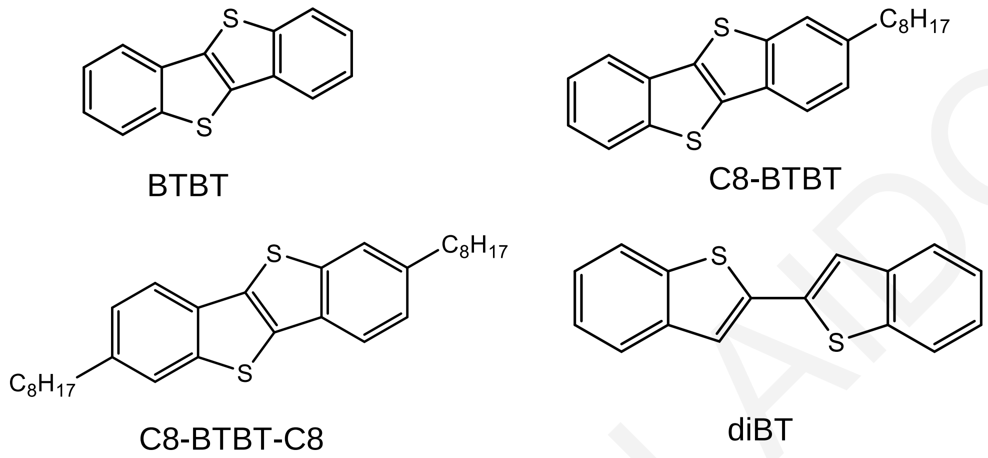

Figure 7.1. Molecular structures of C8-BTBT-C8, C8-BTBT, BTBT and diBT.

7.2 Results and discussion

7.2.1 Optical and structural implications of alkyl substitution

Figure 7.2a presents the absorption spectra of BTBT and its alkylated derivatives, as well as diBT, dissolved in cyclohexane. All spectra are characterized by a nontypical vibronic structure, in accordance with the literature.[15,19] The complexity of spectra can only be produced by the summation of discrete spectra attributed to transitions to different singlet electronic states (i.e. S_1 and S_2). As it is generally known, following photon absorption, rapid relaxation occurs through internal conversion to the lowest vibrational energy level of the excited state, where all subsequent relaxation pathways (fluorescence, non-radiative relaxation, intersystem crossing, etc.) proceed.[6] Therefore, a slight blue shift of 0-0 absorption band of S_1 excited state (~0.023 eV) for C8-BTBT-C8 compared to the other BTBT derivatives may place the lowest vibrational energy level of the S_1 closer to the triplet state favoring the rapid intersystem crossing.[22] The number of attached alkyl chains affects marginally the solution spectroscopic properties, in agreement with the literature, but not as apparently as in solid phase, a bathochromic shift is observed with the increasing number and length of the alkyl chain attached.[19] The absorption spectrum of the diBT displays less pronounced vibronic structure due to increased broadening, that signifies the contribution of multiple energy states, stemming from the deviation from planarity of the core and the proximity of singlet states absorption that construct the absorption spectrum. It is also clearly red shifted (~0.21 eV) compared to the molecules with fused core, due to the longer conjugation length afforded by the extra bond between the two units.

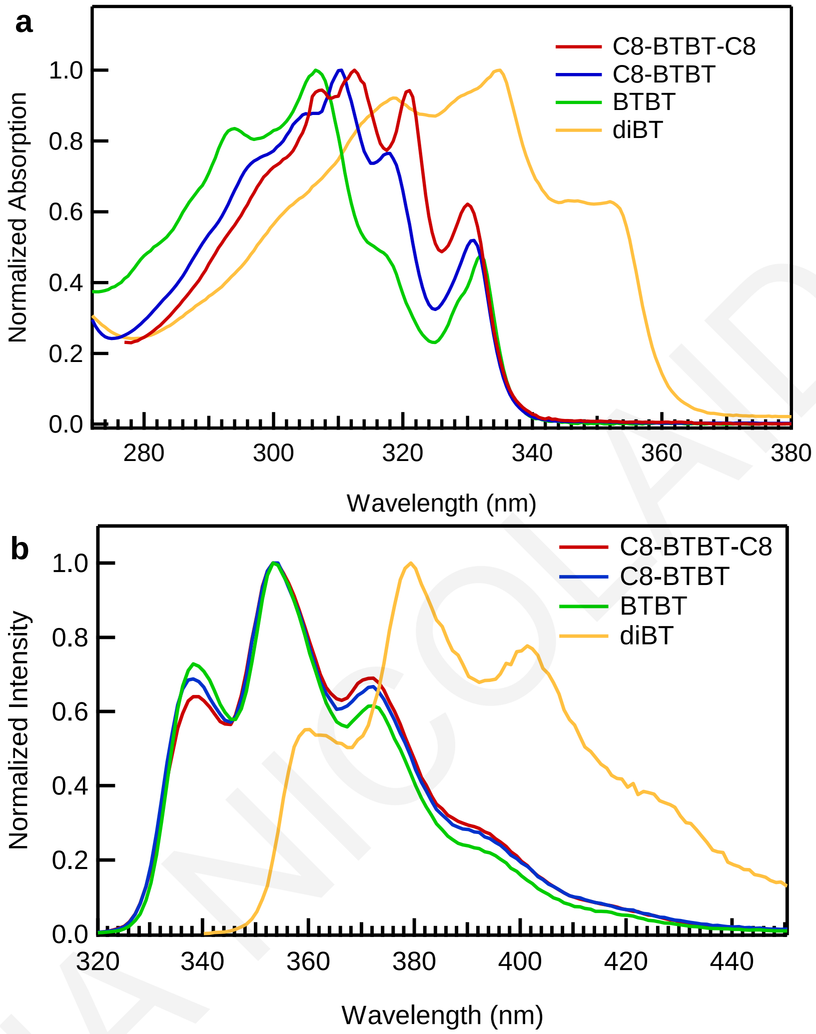

Figure 7.2. (a) Absorption and (b) Fluorescence spectra of C8-BTBT-C8, C8-BTBT, BTBT and diBT in cyclohexane at 20 °C.

The fluorescence spectra on the other hand seem to be less affected by the number of side chains as the emission spectra are similar in all three BTBT derivatives. The small Stokes shift (~0.08 eV) and clear vibronic structure suggests emission comes only from S_1. In agreement with the literature,[19] at Figure 7.2b we observe only differences in I_{0-0}/I_{1-0} ratio, showing the highest ratio for BTBT and the lowest for C8-BTBT-C8 and marginal increase of the broadening as the degree of alkylation increases. On the other hand, the spectrum of diBT differs prominently from the spectra of BTBT derivatives, displaying the lowest I_{0-0}/I_{1-0} ratio, a definite red-shift of ~0.24 eV and increased broadening. In addition, at a first glance, the fluorescence spectrum of diBT is the only spectrum that strongly resembles the mirror image of the corresponding absorption spectrum.

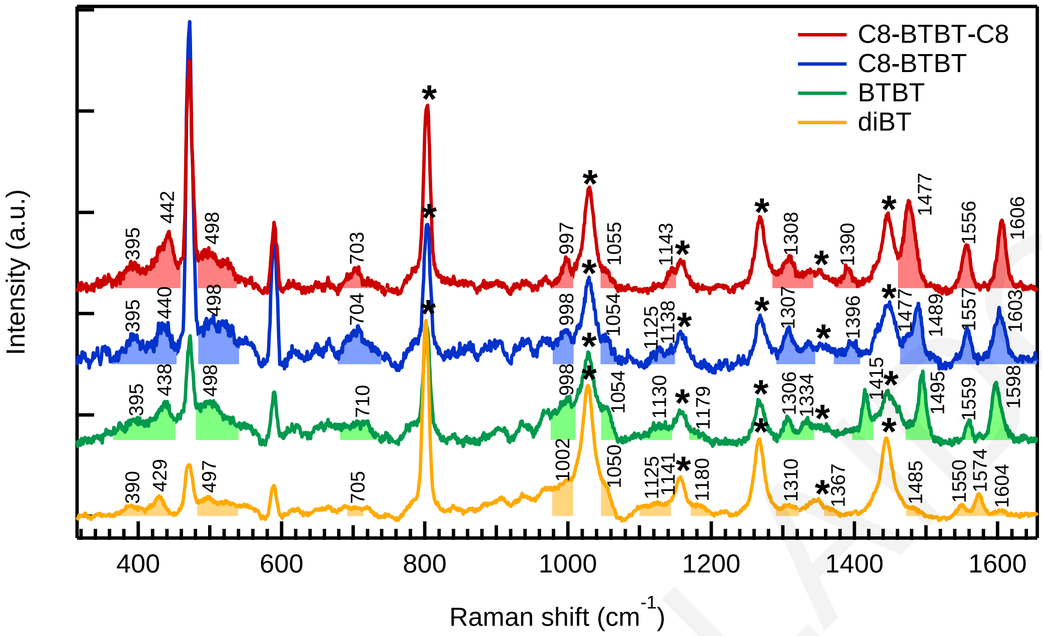

Figure 7.3. Resonance Raman (RR) spectra with excitation at 282 nm for C8-BTBT-C8, C8-BTBT, BTBT and diBT in cyclohexane at 20 °C. Solvent modes are marked with an asterix and molecular modes are shaded. The 480 and 600 cm^{-1} peaks are experimentally-induced artifact features (probably stemming from H_2 rotational lines).

To analyze the absorption and emission spectra in more depth, we first present the resonance Raman spectra, which should relate to the vibronic structure of the optical spectra. Figure 7.3 shows the RR spectra collected with excitation at 282 nm, on resonance with a π-π* transition, from the solutions of BTBT, C8-BTBT, C8-BTBT-C8 and diBT in cyclohexane. The excitation wavelength has been chosen to be close to the absorption maxima but far enough from the onset of fluorescence to avoid its unwanted involvement, as background, to the RR spectra. The assignment of modes is performed by comparing with DFT calculations. For all cases, the vibrational modes that are enhanced are totally-symmetric and can be divided in two regions: 1) the range from ~1000 to 1600 cm^{-1}, in which the vibrational bands are attributed to in-plane modes, namely ring stretches and C-H in plane bends and 2) the range from ~350 to 990 cm^{-1}, including bands mostly attributed to ring deformations both in-plane and out-of-plane. Asymmetric modes that could appear through B-term enhancement are not expected as, according to DFT calculations, the symmetry of BTBT derivatives is C_1 for which there are only totally symmetric modes. A more detailed assignment of the peaks can be found in Table 7.1.

Table 7.1. Frequencies (cm^{-1}) and assignments of dominant RR bands.

C8-BTBT-C8	C8-BTBT	BTBT	diBT	Assignment
Raman shift (cm^{-1})				
395	395	395	390	Ring deformation (thiophene-benzene) (out of plane)
442	440	438	429	C-S-C bend (in plane), ring deformation (benzene) (out of plane)
498	498	498	497	C-S-C bend (in plane)
703	704	710	705	Ring deformation (benzene)
997	998	998	1002	Ring deformation (in plane) (thiophene-benzene)
1055	1054	1054	1050	C-S stretching, C-H in plane bends (benzene)
1143	1125, 1138	1130, 1179	1125, 1141, 1180	C-S stretching, C-H in plane bends (benzene)
1308	1307	1306, 1396	1310	Ring deformation (in plane), C-H in plane bends, (benzene)
1390	1396	1415	1367	C-H in plane bends, C=C stretching (thiophene) (symmetric)
1477	1477, 1489	1495	1485	C=C stretching (thiophene) (symmetric), C-H in plane bends, C=C stretching (benzene) (symmetric)
1556	1557	1559	1550, 1574	C=C stretching (thiophene) (asymmetric), C-H in plane bends, C=C stretching (benzene) (symmetric)
1606	1603	1598	1604	C-H in plane bends, C=C stretching (benzene) (symmetric)

While BTBT, its alkyl substituted derivatives and diBT display similar spectra, some differences are exhibited, mostly at higher energy modes (1390-1600 cm^{-1}) that correspond to C=C stretches of thiophene and benzene fused rings and C-H in plane bends. We observe a downshift of the bands at ~1415 and 1495 cm^{-1} to 1390 and 1477 cm^{-1}, and an upshift of the band at ~438 and 1598 cm^{-1} to 442 and 1606 cm^{-1} with alkyl chain substitution. According to Table 7.1, the bands at ~1415 and ~1495 cm^{-1} are ascribed to C=C stretching of the central bond between the two fused thiophene rings (see Figure S7.1-S7.2). The band at ~1598 cm^{-1} is assigned to C=C stretching of the benzene rings along the BTBT core (Figure S7.4). Considering that the C=C stretching for 1598 cm^{-1} occurs along the core, the upshift of this band indicates that the conjugation is distorted for the alkylated derivatives. That could explain the small blue shift of the 0-0 band of the S_1 (Figure 7.2a). Simultaneously, the downshift of the thiophene C=C stretch, shows that the bond between the fused thiophenes is larger upon alkylation. The lengthening of the thiophene C=C bond explains the upshift of the 438 cm^{-1} band attributed to the C-S-C bend, by making the C-S-C bonds stronger. Considering the above we argue that alkylation distorts the conjugation of the core by enhancing the aromaticity of the benzene rings increasing thus the length of the thiophene C=C bond. The decreased conjugation resembles the case of the less planar diBT.

7.2.2 Resonance Raman Intensity Analysis (RRIA)

The RRIA study performed here by simultaneously modeling the absorption and absolute RR cross sections, extracted the excited state potential surface parameters, which are presented in Tables 7.2 and S7.1-7.3 for C8-BTBT-C8, C8-BTBT, BTBT and diBT respectively. These concern only the excited-state early time dynamics within Frank-Condon (FC) region.

According to the complicated shape of the absorption spectra, a model based on a single transition could not be considered. Therefore, a two-state model (a model based on transition to two electronic excited states, namely S_0 to S_1 and S_0 to S_2,) was employed, obtaining a good fit of the absorption spectra of the complexes (Figure 7.4) and of the corresponding REPs of all the prominent bands in the RR spectra of the BTBT derivatives and diBT (Figures 7.5 (for C8-BTBT-C8) and S7.5-S7.7 (for C8-BTBT, BTBT and diBT respectively)).

In Table 7.3 we compare the homogeneous (Γ) and inhomogeneous (Θ) broadening for all cases, as well as the transition dipole moment M, the E_{00} and reorganization energy λ, which is calculated as already discussed in Chapter 4 (section 4.2.2) using the equation $\lambda_{tot} = \sum \lambda_i = \sum_i \left(\frac{\omega_e^2}{\omega_g}\right)\frac{\Delta_i^2}{2}$. In all cases, Γ and Θ values are low as most of the broadening is introduced through the increase of Δ values of low-energy modes (395-442 cm^{-1}), showing the degree that the electronic transition couples to these modes. The increased broadening of diBT spectrum, discussed above, is attributed, according to the Δ values from the fits, to increased coupling of electronic transitions to low-energy out-of-plane modes. The substitution with alkyl side chains seems to decrease the inhomogeneous broadening, indicating smaller number of available energetic states. Therefore, the density of states of the electronic excited states is smaller for C8-BTBT-C8. Nonetheless, this does not seem to suppress the conversion possibility from singlet to triplet manifold and instead the ISC rate is enhanced, as will be demonstrated further down. The transition dipole moment of S_1 (Table 7.3) is increased with alkylation of BTBT core, in agreement with the experimentally measured extinction coefficients (33100, 22100 and 12400 $cm^{-1}mol^{-1}$), reaching a value of 28500 $cm^{-1}mol^{-1}$ for diBT.

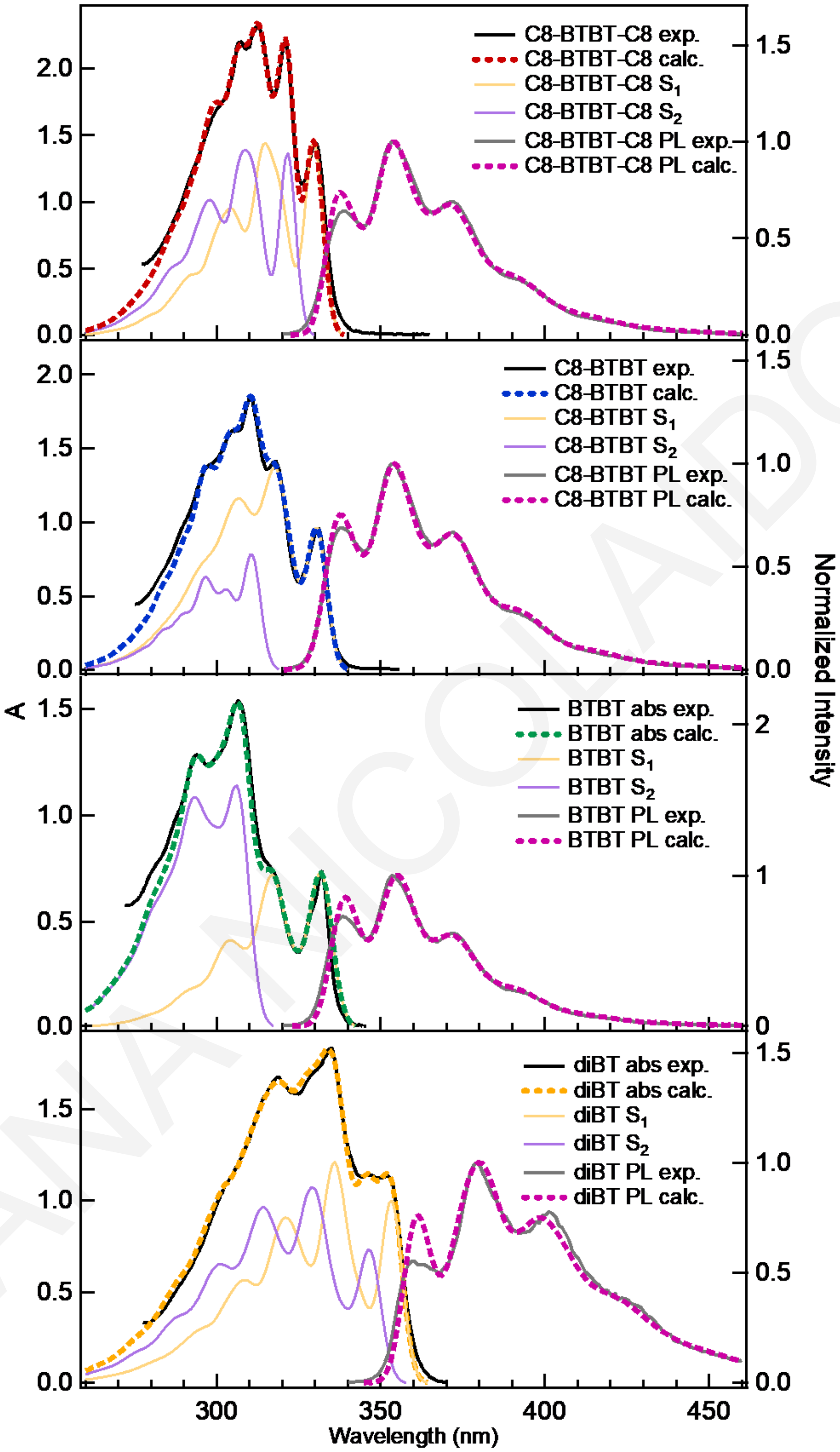

Figure 7.4. Experimental and calculated absorption spectra for C8-BTBT-C8, C8-BTBT, BTBT and diBT.

Table 7.2. Parameters used in the RRIA for C8-BTBT-C8.

Transition	**$\omega_g(\mathrm{cm}^{-1})$**	**$\omega_e(\mathrm{cm}^{-1})$**	**Δ_k**
C8-BTBT-C8 1st state			
ν_1	395	695	0.30
ν_2	442	742	0.30
ν_3	498	708	0.40
ν_4	703	853	0.46
ν_5	997	997	0.64
ν_6	1055	1055	0.60
ν_7	1143	1143	0.39
ν_8	1308	1308	0.47
ν_9	1390	1390	0.35
ν_{10}	1477	1527	0.72
ν_{11}	1556	1556	0.41
ν_{12}	1606	1606	0.55
Γ (cm^{-1})	120		
Θ (cm^{-1})	190		
E_{00} (cm^{-1})	29850		
M (Å)	1.45		
C8-BTBT-C8 2nd state			
ν_1	395	645	0.35
ν_2	442	692	0.35
ν_3	498	748	0.45
ν_4	703	903	0.46
ν_5	997	997	0.70
ν_6	1055	1055	0.58
ν_7	1143	1143	0.46
ν_8	1308	1308	0.64
ν_9	1390	1390	0.42
ν_{10}	1477	1527	0.50
ν_{11}	1556	1556	0.49
ν_{12}	1606	1606	0.52
Γ (cm^{-1})	100		
Θ (cm^{-1})	190		
E_{00} (cm^{-1})	30610		
M (Å)	1.43		

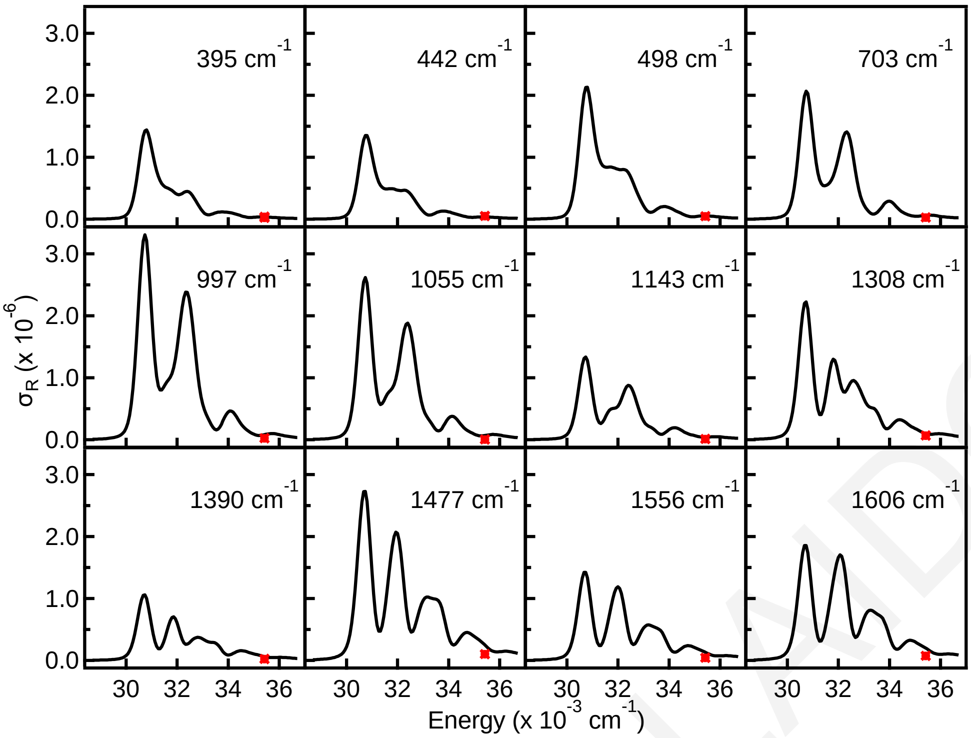

Figure 7.5. Calculated Raman excitation profiles (REPs) for the most prominent vibrational modes of C8-BTBT-C8 complex. The red points denote the experimentally calculated absolute RR cross sections at 282 nm.

Table 7.3. Comparison of parameters used in the RRIA.

Parameter	**C8-BTBT-C8**		**C8-BTBT**		**BTBT**		**diBT**	
Absorption	**S_1**	**S_2**	**S_1**	**S_2**	**S_1**	**S_2**	**S_1**	**S_2**
Γ (cm^{-1})	120	100	150	150	90	145	60	100
Θ (cm^{-1})	190	190	170	170	280	280	240	240
E_{00} (cm^{-1})	29850	30610	29870	31750	29350	31650	27260	28270
M	1.45	1.43	1.51	0.96	1.035	1.325	1.48	1.52
λ (cm^{-1})	1795	1902	1913	1427	1704	1631	2533	3038
Fluorescence								
Γ (cm^{-1})	120		140		95		80	
Θ (cm^{-1})	250		300		305		280	
E_{00} (cm^{-1})	31450		31400		31330		29400	
M	1.45		1.51		1.035		1.48	
Stokes' shift (cm^{-1})	740		668		569		628	

The similar values of transition dipole moment (M) of S_1 and S_2 in C8-BTBT-C8 and diBT indicate that the excitation towards S_1 and S_2 are almost equally possible pathways, whereas for C8-BTBT $S_0 \rightarrow S_1$ and for BTBT $S_0 \rightarrow S_2$ are more possible transitions. In the case that the molecule is excited to S_2, the population is then transferred nearly quantitatively to the lower-lying S_1 state through IC. This state acts as a doorway state from which the T_n state is formed.

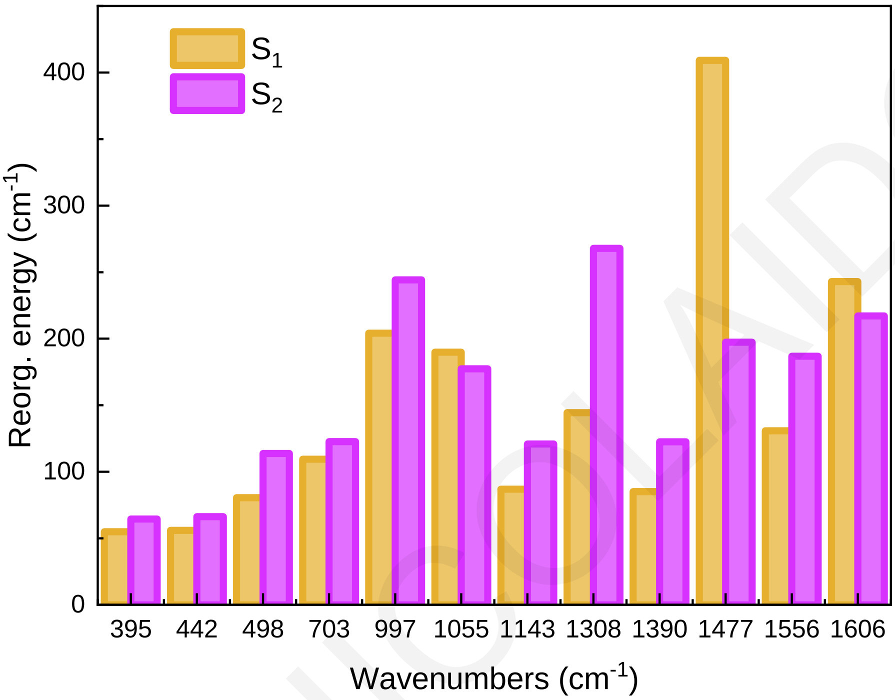

Figure 7.6. Mode-specific reorganization energy for the most prominent vibrational modes of C8-BTBT-C8.

The similarity of the shape of S_1 and S_2 spectra especially for C8-BTBT-C8 (Figure 7.4), that is confirmed by the similarity of the extracted parameters (see Table 7.2) and of the mode-specific reorganization energies of the two states (Figure 7.6), stems from their proximity in energy ($\Delta(E_{0\text{-}0})$=760 cm^{-1}, whereas 1880, 2300, 1010 cm^{-1} for C8-BTBT, BTBT and diBT, respectively), which means that they are similar in nature. The total reorganization energy (Table 7.3 and Figure 7.7) for $S_0 \rightarrow S_2$ transition of C8-BTBT-C8 and diBT is high and remains at a similar level for S_1 with comparable contribution of Δ values of vibrational modes as with S_2, while for C8-BTBT and BTBT reorganization is lower for $S_0 \rightarrow S_2$ transition than $S_0 \rightarrow S_1$ transition. Therefore, the flexible core and bisalkylation induces more considerable changes in molecular structure from the ground state to the S_2 excited state.

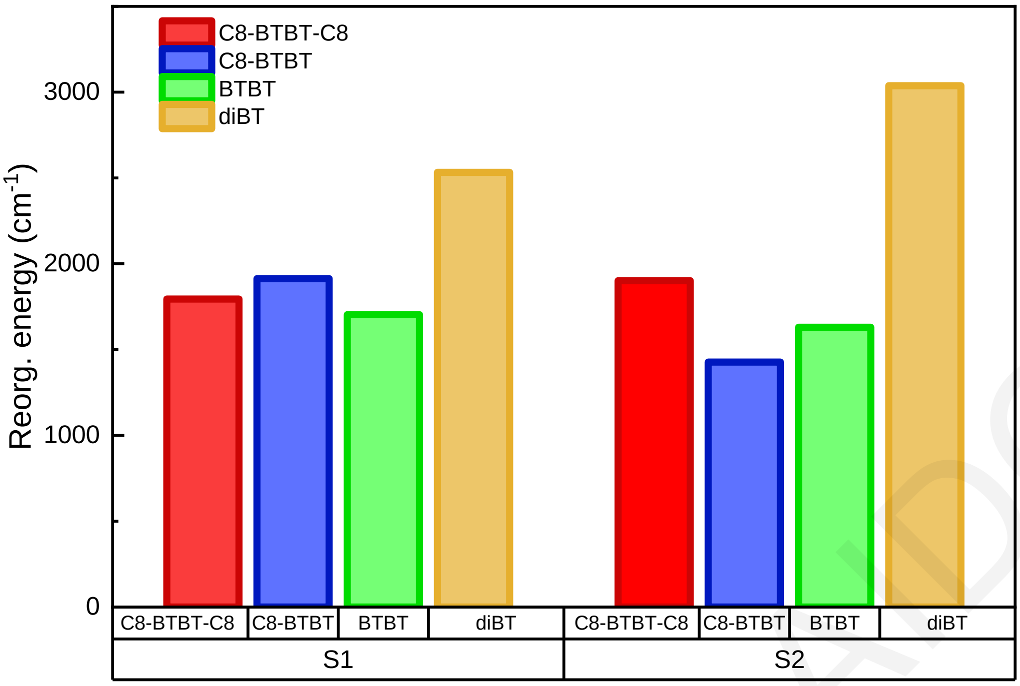

Figure 7.7. Comparison of total reorganization energies of the four benzothiophene derivatives.

To attempt to identify the most important tuning modes that induce changes in the molecular geometry in the excited state, we turn to the distribution profiles of mode-specific reorganization energies of the most prominent vibrational mode relaxations of both S_1 and S_2 (Figure 7.6 for C8-BTBT-C8 and S7.8-S.7.10 for C8-BTBT, BTBT and diBT). These show that in all derivatives the most significant contributions come from a group of modes in the ~1000 cm^{-1} frequency region (which corresponds to a C-S stretching mode and C-H in-plane bends) along with high frequency modes around 1500 cm^{-1}. The contribution from the high frequency region, which mainly arises from the in-plane stretching motion in the conjugated core, is equal to that from the ~1000 cm^{-1} frequency modes. Observing also REPs for C8-BTBT-C8 (Figures 7.5) reveals that again the ~1000 cm^{-1} has the highest displacement while for C8-BTBT, BTBT and diBT (Figures S7.5-S7.7 respectively), the C-S-C bending mode of thiophene (~498 cm^{-1}) exemplifies the highest displacements, meaning that these modes have solely the highest contribution to the change of the molecular geometry in the excited state.

We also find that the vibronic spacing between 0-0 and 0-1 peaks for both electronic transitions varies for differently alkylated BTBT core and for the more flexible benzothiophene core of diBT. In most cases (except C8-BTBT) spacing is considerable (~1370 cm^{-1} for C8-BTBT-C8, ~1100 cm^{-1} for C8-BTBT, ~1400 cm^{-1} for BTBT and ~1470 cm^{-1} for diBT for both electronic transitions) and can only be recreated by increasing the contribution of the low-energy modes (395-442 cm^{-1}) with higher Δ values and by increasing the excited state frequencies mainly of the low-energy modes. The lower contribution of these modes compared to the aforementioned in plane modes is attributed to the fact that, increasing the Δ values of low-energy modes affects not only the ratio of 0-0 to 0-1 peak but increases considerably the broadening of the spectrum. Therefore, in order to reproduce the fine structure of the spectra, these modes could not contribute extensively and high-energy modes are mostly involved to adjust the intensity of the vibronic peaks.

The vibrational fine-structure in emission spectra (Figure 7.4) is characterized by similar peak spacing between 0-0 and 1-0 peaks when comparing the BTBT derivatives and was estimated to be near ~1300 cm^{-1} for BTBT derivatives and 1400 cm^{-1} for diBT. Therefore, the origin of the spacing in absorption and emission spectra differs, indicating that upon excitation and de-excitation, the dominant contribution in each process comes from different modes that are always in-plane vibrations (in agreement with mode-specific reorganization energies), but concerning different parts of the core such as ring deformation, C-H in-plane bends (1100-1300 cm^{-1}) and C=C stretching modes (1370-1500 cm^{-1}). According to the literature[24] the vibrational progression in emission is dominated by ground state vibrations, while the fine-structure of absorption spectra is determined by excited state vibrations. Therefore, we interpret the larger spacing in absorption spectra as being due to a dominating excited state vibration with enhanced bond strength, and the smaller spacing in emission spectra as being due to the corresponding softened vibration in the ground state.

In Figure 7.4 in which the modeling of emission spectra is also displayed (the extracted parameters are presented at Table 7.4 and S7.4-7.6 for C8-BTBT-C8, C8-BTBT, BTBT and diBT respectively) we observe almost mirror image of absorption of S_1 and emission spectrum only for BTBT and diBT. This indicates that excitation does not result in significant relaxation changes (change in charge distribution associated with change in the molecule geometry) in excited state.[15] It is also noteworthy that the calculated emission spectra display an increased 0-0 band intensity compared to the experimental spectra, which corresponded to parameters that were necessary in order to reproduce the higher vibronic intensities; therefore the diminution of the experimental 0-0 intensity is attributed to self-absorption. Even though the deviation from the calculated spectra is observed in all samples, it is more prominent in the spectra of BTBT and diBT. Self-absorption can be exhibited when there is overlap between absorption of S_1 and emission spectra.[25,26] Therefore, the slightly increased overlap of the BTBT and diBT spectra is supported by the lower values of Stokes' shift and the increased broadening (see Table 7.3).

Table 7.4. Parameters used in the emission fitting of C8-BTBT-C8.

Transition	$\omega_g(cm^{-1})$	$\omega_e(cm^{-1})$	Δ_k
C8-BTBT-C8 Fluorescence			
ν_1	395	395	0.40
ν_2	442	442	0.75
ν_3	498	498	0.65
ν_4	703	703	0.50
ν_5	997	997	0.40
ν_6	1055	1055	0.50
ν_7	1143	1143	0.39
ν_8	1308	1308	0.47
ν_9	1390	1390	0.35
ν_{10}	1377	1477	0.95
ν_{11}	1556	1556	0.55
ν_{12}	1506	1606	0.85
Γ (cm^{-1})		120	
Θ (cm^{-1})		250	
E_{00} (cm^{-1})		31450	
M (Å)		1.45	

7.2.3 ISC rate

7.2.3.1 Experimental estimation of ISC rate

To investigate ISC in these molecules, transient absorption (TA) spectroscopy was performed. Figure 7.8 shows the change in transmission as a function of time for the three BTBT derivatives, excited at their S_1 0-0 energy (3.75 eV). As the changes are plotted as transmission rather than absorbance, excited state absorption is negative, with stimulated emission showing up as a positive signal. At 5 ps, the spectra of all four

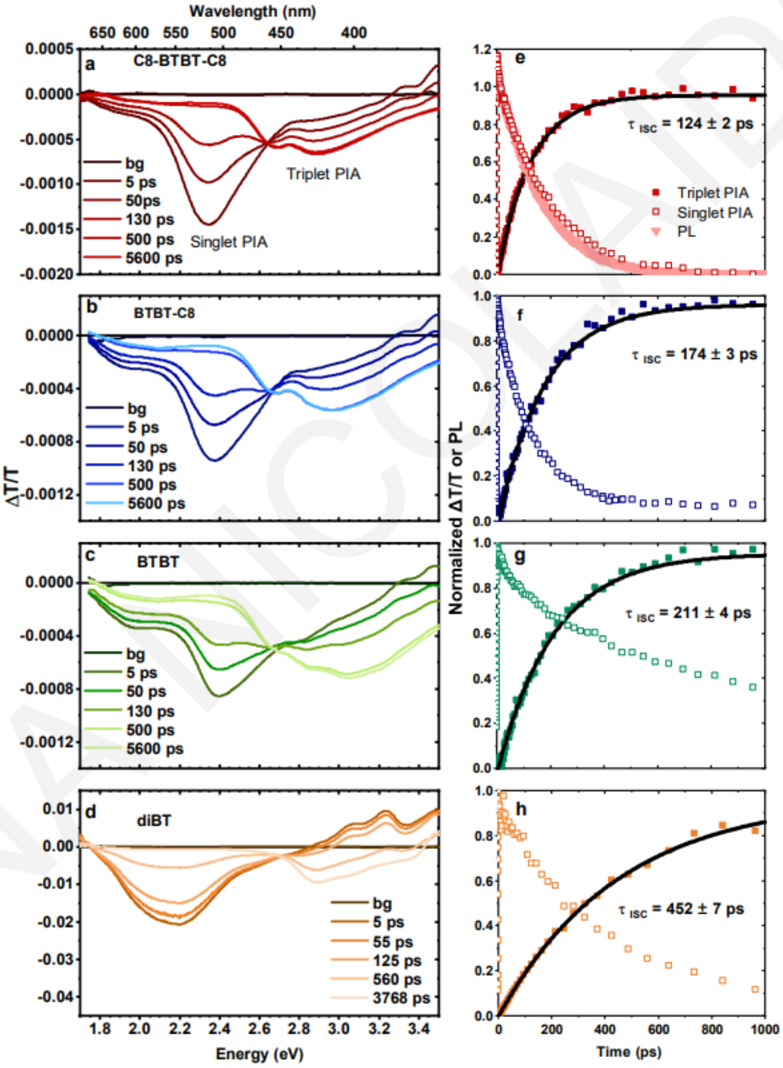

Figure 7.8. Transient absorption spectroscopy of BTBT derivatives. (a)-(d) show transient absorption spectra of C8-BTBT-C8, C8-BTBT, BTBT and diBT respectively. (e)-(h) show transient absorption (squares) and photoluminescence (triangles) dynamics of the same materials. Measurements were performed in dilute toluene solution with excitation at 320 nm. Solid black lines show monoexponential fits to the triplet rise-time with the extracted intersystem crossing time-constant as an inset.

BTBT derivatives are dominated by stimulated emission (above 3.2 eV) and excited state absorption (peaked at 2.2-2.4 eV). We assign these features to the photoexcited S_1 state as both features decay together leaving an excited-state absorption peaked at 3 eV.

Excitation into the S_2 band at 3.86 eV (not shown here) shows similar transient absorption spectra and dynamics within the time resolution of ~200 fs, suggesting fast internal conversion between S_2 and S_1, as expected given the proximity of the states. We assign the excited-state absorption band at 3 eV to triplet T_1-T_n absorption as it does not decay during the timescale of the measurement (7 ns). In addition, the spectral shape is similar to reported T_1-T_n absorption spectra of benzothiophene and dibenzothiophene.[27,28] The presence of an isosbestic point in the transient absorption spectra demonstrates negligible population of any intermediate states or spectral relaxation. Intersystem crossing must therefore proceed either via higher-lying triplet states (T_n) followed by rapid internal conversion in the triplet manifold (100 ps), or directly from S_1 to T_1. The time-scale of intersystem crossing in these molecules (~150 ps) also means that intersystem crossing occurs from the relaxed S_1 state, as relaxation within the singlet manifold is expected to be complete within at most a few 10s of picoseconds. Interestingly, the rate of intersystem crossing increases with the number of alkyl chains by roughly a factor of 2, from 1/213 ps^{-1} in BTBT to 1/124 ps^{-1} in C8-BTBT-C8 (also 1/153 ps^{-1} for C8-BTBT and 1/590 ps^{-1} for diBT).

7.2.3.2 Theoretical estimation of ISC rate

Calculation of the spin orbit coupling matrix element (SOCME) between S_1 and T_n given by $< T_n|H_{SOC}|S_1 >$, gave an ISC rate (k_{isc}), using the equation $k_{isc} = \frac{2\pi}{\hbar}|SOCME|^2\rho$ (where ρ is the density of final states), three orders of magnitude smaller than observed and with the opposite trend compared with experiment (~1/(100 ns) for diBT and ~1/(300 ns) for BTBT). These calculations demonstrate that direct (i.e. pure electronic) intersystem crossing cannot explain the experimentally observed rates. Therefore, we cannot neglect the role of nuclear motion on the intersystem crossing process. To attempt to qualify the nature of these inducing modes, we turn to molecular dynamics calculations. Here, we calculate the molecular dynamics of molecules in the ground- and the first-excited singlet states. We calculate the distribution of SOCMEs between S_1 and T_n and determine a mean value. The mean values of distributions for the different triplet levels are shown in Figure 7.9. This approach uses Marcus-Levich-Jortner (MLJ) formalism for the Franck-Condon Weighted Density of States, which is given by $\rho_{FCWD}^{MLJ}(\Delta E) = \sqrt{\frac{1}{4\pi\lambda k_B T}}\sum_m \frac{S^m e^{-S}}{n!} \times exp\left(-\frac{\Delta E+\lambda+\hbar\omega}{4\lambda k_B T}\right)$, where S is the Huang-Rhys parameter and λ is a classical Marcus-type reorganization energy. By varying λ, k_{isc} was estimated, suggesting the sensitivity of the ISC rate calculation to the reorganization energy. The derived calculated k_{isc} approaches the experimental value when vibronic spin-orbit coupling is taken into account. To determine the effective tuning modes responsible for increasing the SOCME, principal component analysis of molecular motions was performed that are correlated with increased SOCME. The most important of these comprise ring-breathing and ring flexing motions, in C8-BTBT-C8, BTBT and diBT. These motions may relate to the ring deformation mode at ~1000 cm^{-1} which was found to significantly contribute to the structural evolution of these molecules.

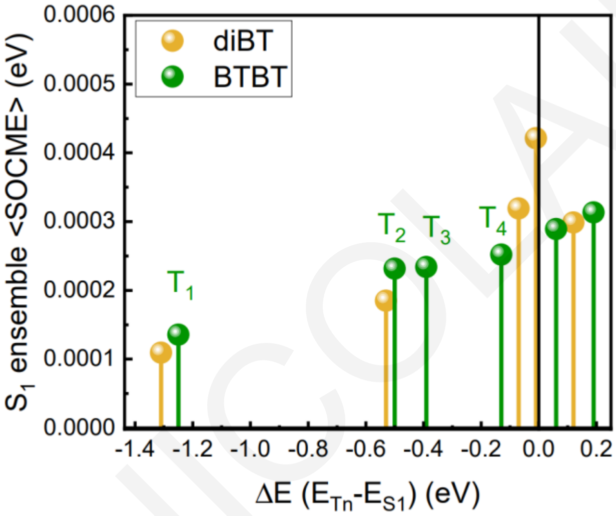

Figure 7.9. Ensemble-averaged Spin-Orbit Coupling Matrix Elements $< T_n|H_{SOC}|S_1 >$ at S_1 geometry for BTBT (green) and diBT (orange) plotted against the energy difference between T_n and S_1.

7.3 Conclusions

Differently alkylated BTBT derivatives and a benzothiophene (BT) derivative with flexible core were investigated in solution. This family of highly planar conjugated molecules exhibited unexpectedly fast ISC, according to TA measurements with the alkylated BTBT derivatives and especially, C8-BTBT-C8 exhibiting the fastest ones. When photon absorption is provided to the molecule for excitation towards S_2, subsequent ultrafast IC steps leads the system to the lower-lying S_1 state, from which transition to T_n state can occur. RR revealed that alkylation of the fused benzothiophene core (similarly with the decrease in planarity in the case of diBT) modifies the conjugation in a way that enhances SOC. The evolution of the molecular structure at the different excited states (S_1 and S_2) of these molecules was investigated by RRIA, through the detail analysis of absorption, emission and

Raman cross sections. This method enabled the examination of the effect of planarity (comparison with diBT) and alkylation in the planar molecules on the extent of change on molecular geometry after photoexcitation. The similarity in the shape of the absorption spectra and the extracted parameters (M, Δ, ω_e, total and mode specific λ) of S_1 and S_2 was observed more prominently for C8-BTBT-C8 and in lesser extent for diBT. This implies that alkylation and flexibility of the core can induce proximity in energy for these two states, causing the similarity in their nature. The vibrational mode that significantly contributes to the change in the molecular geometry in the excited state, is the in-plane ring deformation (~1000 cm^{-1}) for all molecules, as well as the C-S-C in-plane bend only for C8-BTBT, BTBT and diBT. According to theoretical calculations, vibronic-spin orbit coupling should be considered in order to explain the unexpected high ISC rate of BT derivatives and therefore it is strongly related to reorganization energy. MD simulation predicted, in accordance to the literature,[1,5,6] that SOC in these molecules is highly sensitive to coupling to low-energy vibrational modes, such as ring-breathing and ring flexing motions. The fact that RRIA concerns only the early-time dynamics within the FC region (timescale of few fs) does not allow collection of information about processes that occur on longer timescales, such as ISC. Therefore, it was not possible to assign which mode is responsible for the coupling that promotes enhanced SOC and subsequently increases the ISC rate. Nevertheless, it would be interesting to explore further the change of molecular structure between S_1 and T_n by exploiting time-resolved Raman, which could allow to monitor the triplet formation, in order to address the questions mentioned above. The findings here have important implications for the field of spintronics and optoelectronics. This opens the possibility to use vibronic tuning to alter spin behaviour, or spin coherence through molecular design.

7.4 Experimental section

7.4.1 Materials and Sample Preparation

2,7-dioctyl-[1]benzothieno[3,2-b]-[1]benzothiophene (C8-BTBT-C8) (MW: 464,77 g/mol), mono-octyl[1]benzothieno[3,2-b]-[1]benzothiophene (C8-BTBT) (MW: 352,55 g/mol), [1]benzothieno[3,2-b]-[1]benzothiophene (BTBT) (MW: 240,34 g/mol) and dibenzothiophene (diBT) (MW: 266,02 g/mol) were dissolved in cyclohexane, producing stock solution of 1 mM for each sample. These solutions were then diluted to obtain a final concentration of 0.2 mM for absorption and RR measurements.

7.4.2 Experimental details

Absorption spectroscopy. The absorption spectra were acquired on a Shimadzu UV-Vis spectrophotometer (Shimadzu UV-1900). EPR suprasil tubes with diameter of 4 mm placed inside a custom-made EPR tube holder, were used for the absorption measurements and the same tubes were then attached to Raman setup for the RR measurements.

Resonance Raman Studies. Resonance Raman (RR) spectra of BTBT derivatives and diBT were obtained with excitation at 282.35 nm. The 282.35 nm excitation wavelength employed in the RR experiments was produced via Raman shifting at 532 nm in a 1 m tube containing H_2 gas, which was provided by the second harmonic of a Q-switched Nd:YAG laser (PRO-230, 30 Hz, Spectra Physics). The excitation light was focused into a spinning cell consisting of an EPR suprasil tube (diameter: 4 mm) attached to a rheostat-controlled motor for choice of rotation speed. Use of the spinning cell prolonged the lifetime of the samples. Modest excitation energies (0.25 mW at 282.35 nm (8.3 μJ per pulse)) were employed to avoid decomposition of the sample, which was monitored by obtaining the absorption spectrum of the sample before and after exposure. The Raman scattered light was collected in a backscattering geometry and delivered to a 0.75m focal-length Czerny−Turner spectrograph, equipped with a 1200-grooves/mm holographic grating for the visible wavelengths and a 2400 grooves/mm holographic grating for UV excitation. The slit width was set to 100 μm providing for 6 cm^{-1} spectral resolution at the UV wavelength used in this work. The scattered light was detected by a LN_2-cooled 2048 x 512 pixel, back-illuminated UV-enhanced CCD detector (Spec10:2KBUV/LN, Princeton Instruments). Each spectrum with excitation in the visible is the accumulation of 6 × 10 min spectra. Frequency calibration of the spectra was accomplished with the use of cyclohexane. MATLAB and ORIGIN software were used for spectral treatment and analysis.

References

(1) Penfold, T. J.; Gindensperger, E.; Daniel, C.; Marian, C. M. Spin-Vibronic Mechanism for Intersystem Crossing. *Chem. Rev.* **2018**, *118*, 6975–7025.

(2) Zhang, J.; Mukamel, S.; Jiang, J. Aggregation-Induced Intersystem Crossing : Rational Design for Phosphorescence Manipulation. *J. Phys. Chem. B* **2020**, *124*, 2238–2244.

(3) Guo, L.; Qin, Y.; Gu, X.; Zhu, X.; Zhou, Q.; Sun, X. Spin Transport in Organic Molecules. *Front. Chem.* **2019**, *7*, 1–11.

(4) Schnappinger, T.; Marazzi, M.; Mai, S.; Monari, A.; González, L.; De Vivie-Riedle, R. Intersystem Crossing as a Key Component of the Nonadiabatic Relaxation Dynamics of Bithiophene and Terthiophene. *J. Chem. Theory Comput.* **2018**, *14* (9), 4530–4540.

(5) Rodriguez-serrano, A.; Rai-constapel, V.; Daza, M. C.; Doerr, M.; Marian, C. M. Internal Heavy Atom Effects in Phenothiazinium Dyes : Enhancement of Intersystem Crossing via Vibronic Spin – Orbit Coupling. *Phys. Chem. Chem. Phys.* **2015**, *17*, 11350–11358.

(6) Tatchen, J.; Gilka, N.; Marian, C. M. Intersystem Crossing Driven by Vibronic Spin – Orbit Coupling : A Case Study on Psoralen W. *Phys. Chem. Chem. Phys.* **2007**, *9*, 5209–5221.

(7) Kolle, P.; Schnappinger, T.; De Vivie-Riedle, R. Deactivation Pathways of Thiophene and Oligothiophenes : Internal Conversion versus Intersystem Crossing †. *Phys. Chem. Chem. Phys.* **2016**, *18*, 7903–7915.

(8) Skov, A. B.; Larsena, M. A. B.; Liisberga, M. B.; Hansen, T.; Sølling, T. I. Conformationally Controlled Ultrafast Intersystem Crossing in Bithiophene Systems. *Phys. Chem. Chem. Phys.* **2018**, *20*, 13412–13418.

(9) R. S., L.; Vennapusa, S. R. Formation and Decay of Intersystem Crossing Receiver Triplet State in Terthiophene and Quaterthiophene. *Int. J. Quantum Chem.* **2021**, 1–10.

(10) Yang, W.; Zhao, J.; Sonn, C.; Escudero, D.; Karatay, A.; Yaglioglu, H. G.; Küçüköz, B.; Hayvali, M.; Li, C.; Jacquemin, D. Efficient Intersystem Crossing in Heavy-Atom-Free Perylenebisimide Derivatives. *J. Phys. Chem. C* **2016**, *120*, 10162−10175.

(11) Schott, S.; Mcnellis, E. R.; Nielsen, C. B.; Chen, H.; Watanabe, S.; Tanaka, H.; Mcculloch, I.; Takimiya, K.; Sinova, J.; Sirringhaus, H. Tuning the Effective Spin-Orbit Coupling in Molecular Semiconductors. *Nat. Commun.* **2017**, *8*, 1–10.

(12) Köhler, A.; Bassler, H. Triplet States in Organic Semiconductors. *Mater. Sci. Eng. R* **2009**, *66*, 71–109.

(13) Hawly, T.; Johnson, M.; Zhao, B.; Wu, M.; Spath, A.; Streller, F.; Jakel, H. N.; Halik, M.; Spiecker, E.; Watts, B.; Nefedov, A.; Fink, R. H. Asymmetry Matters :

Structure Elucidation and Application Potential of Solution-Processed Monoalkylated BTBT Thin Films. *ACS Appl. Electron. Mater.* **2022**, *4*, 5914−5921.

(14) Inoue, S.; Minemawari, H.; Chikamatsu, M.; Yamada, T.; Horiuchi, S.; Tanaka, M.; Kumai, R.; Yoneya, M.; Hasegawa, T. Effects of Substituted Alkyl Chain Length on Solution-Processable Layered Organic Semiconductor Crystals. *Chem. Mater.* **2015**, *27*, 3809−3812.

(15) Tisovský, P.; Gáplovský, A.; Gmucová, K.; Novota, M.; Pavúk, M.; Weis, M. Synthesis and Characterization of New [1]Benzothieno[3,2-b] Benzothiophene Derivatives with Alkyl-Thiophene Core for Application in Organic Field-Effect Transistors. *Org. Electron.* **2019**, *68*, 121–128.

(16) Shioya, N.; Yoshida, M.; Fujii, M.; Shimoaka, T.; Miura, R.; Maruyama, S.; Hasegawa, T. Conformational Change of Alkyl Chains at Phase Transitions in Thin Films of an Asymmetric Benzothienothiophene Derivative. *J. Phys. Chem. Lett.* **2022**, *13*, 11918−11924.

(17) Yao, C.; Chen, X.; He, Y.; Guo, Y.; Murtaza, I.; Meng, H. Design and Characterization of Methoxy Modified Organic Semiconductors Based on Phenyl[1] Benzothieno[3,2-b][1]Benzothiophene. *RCS Adv.* **2017**, *7*, 5514–5518.

(18) Usta, H.; Kim, D.; Ozdemir, R.; Zorlu, Y.; Kim, S.; Delgado, M. C. R.; Harbuzaru, A.; Kim, S.; Demirel, G.; Hong, J.; Ha, Y.-G.; Cho, K.; Facchetti, A.; Kim, M.-G. High Electron Mobility in [1]Benzothieno[3,2-b][1]Benzothiophene- Based Field-Effect Transistors: Toward N-Type BTBTs. *Chem. Mater.* **2019**, *31*, 5254−5263.

(19) Wawrzinek, R.; Sobus, J.; Chaudhry, M. U.; Ahmad, V.; Grosjean, A.; Clegg, J. K.; Namdas, E. B.; Lo, S. C. Mobility Evaluation of [1]Benzothieno[3,2-b][1]Benzothiophene Derivatives: Limitation and Impact on Charge Transport. *ACS Appl. Mater. Interfaces* **2019**, *11* (3), 3271–3279.

(20) Hawly, T.; Johnson, M.; Sp, A.; Nickles, H.; Wu, M.; Spiecker, E.; Watts, B.; Nefedov, A.; Fink, R. H. Exploring the Preparation Dependence of Crystalline 2D-Extended Ultrathin C8-BTBT-C8 Films. *ACS Appl. Mater. Interfaces* **2022**, *14*, 16830–16838.

(21) Ebata, H.; Izawa, T.; Miyazaki, E.; Takimiya, K.; Ikeda, M.; Kuwabara, H.; Yui, T. Highly Soluble [1] Benzothieno [3,2-b] Benzothiophene (BTBT) Derivatives for High-Performance, Solution-Processed Organic Field-Effect Transistors. *J. Am.*

Chem. Soc. **2007**, *129* (51), 15732–15733.

(22) Etinski, M.; Marian, C. M. Overruling the Energy Gap Law : Fast Triplet Formation in 6-Azauracil. *Phys. Chem. Chem. Phys.* **2010**, *12*, 15665–15671.

(23) Schrode, B.; Jones, A. O. F.; Resel, R.; Bedoya, N.; Schennach, R.; Geerts, Y. H.; Ruzié, C.; Sferrazza, M.; Brillante, A.; Salzillo, T.; Venuti, E. Substrate-Induced Phase of a Benzothiophene Derivative Detected by Mid-Infrared and Lattice Phonon Raman Spectroscopy. *ChemPhysChem* **2018**, *19* (8), 993–1000.

(24) Banerjee, S.; Saalfrank, P. Vibrationally Resolved Absorption, Emission and Resonance Raman Spectra of Diamondoids: A Study Based on Time-Dependent Correlation Functions. *Phys. Chem. Chem. Physicsy* **2014**, *16*, 144–158.

(25) Ye, Y.; Bai, Y.; Qi, L.; Li, T.; Yan, L.; Yin, Q.; Zhang, Y.; Xie, C. Flexible Optical Waveguides in Heterocyclic Schiff Base Self- Assembled Hydrogen-Bonded Solvates. *Chrystal Growth Des.* **2023**, *23*, 1403–1411.

(26) Garcia-Fernandez, R.; Alt, W.; Bruse, F.; Dan, C.; Karapetyan, K.; Rehband, O.; Stiebeiner, A.; Wiedemann, U.; Meschede, D.; Rauschenbeutel, A. Optical Nanofibers and Spectroscopy. *Appl. Phys. B* **2011**, *105*, 3–15.

(27) Seixas de Melo, J.; Pina, J.; Rodrigues, L. M.; Becker, R. S. A Comprehensive Study of the Spectral and Photophysical Properties of Arylthiophenes. *J. Photochem. Photobiol. A Chem.* **2008**, *194*, 67–75.

(28) Wex, B.; Kaafarani, B. R.; Danilov, E. O.; Neckers, D. C. Altering the Emission Behavior with the Turn of a Thiophene Ring : The Photophysics of Condensed Ring Systems of Alternating Benzenes and Thiophenes. *J. Phys. Chem. A* **2006**, *110*, 13754–13758.

CHAPTER 8

CONCLUSIONS

In conclusion, this dissertation discussed various ways that molecular conformation of conjugated systems is affected by external factors exploiting numerous spectroscopic methods mostly vibrational to monitor the structural changes and their impact on the photophysics of thiophene-based materials. The interesting properties for optoeletronic applications that this class of materials possesses were found to comply with the structure-property relation. The results of this work highlight that the importance of monitoring the structural aspects during a chemical (or electrochemical) manipulation or a process after photoexcitation stems from the ability to change the electron distribution along the conjugated backbone. The length over which charge carriers can be delocalized due to the alignment of the adjacent π-system can regulate the ability of the studied system (either conjugated polymers or small molecules) to render effectively their properties. Also, the mechanisms that lead to the alteration of the conjugation length were investigated in order to detect the key parameters to functionally manipulate the structure. For each project, a profitable combination of techniques (mostly spectroscopic) was employed to address the questions arising for each system studied. In this chapter we gather the conclusions that derive from each project of this thesis.

Chapter 4: Structural and photophysical templating of conjugated polyelectrolytes with single-stranded DNA

In this chapter, we have investigated the templating effect of ssDNAs oligomers with different sequence on the ground state conformation of a cationic polythiophene (CPT). To evaluate the ability of an oligonucleotide to induce an extended conformation of CPT with desirable properties, we extracted the structural aspects that contribute for this purpose. We gained crucial insights on the influence of the sequence of the template to the planarity of the ground state backbone conformation of CPT. We determined that an oligonucleotide with consecutive cytosines corresponds to the most effective template inducing increased backbone planarity, while the corresponding ssDNA chain with consecutive adenines displays the least impact on CPT conformation allowing the polymer chain to be flexible. Electrostatic interactions are found to develop to a similar extent in both CPT/ssDNA complexes and therefore do not contribute to the mechanism of the effective templating. In contrast, numerous π-stacking interactions are only present between cytosine and thiophenes. The advantage of cytosines over adenines stems from the ability of an oligonucleotide to overcome the intra-DNA interactions in order to be strongly assembled to CPT. Therefore, cytosines are more available to π-stack with thiophenes, while π-π stacking between adenines hinder additional interaction with CPT other than electrostatic. Moreover, the bases must be consecutive to benefit the maximum planarization, as only every second thiophene stacks with a cytosine. Therefore, the length of the oligocytosine was also addressed exhibiting the maximum templating effect for a length of 10-20 cytosines. The CPT polymer also owns structural aspects that affect the strength of the assembly, placed on the side chains. The imidazole group placed at the end of alkoxy side chain enhances the planarity of the polymer backbone as it is involved in stacking interactions with both thiophenes and cytosines. Therefore, the alkoxy chains must be short enough to allow these interactions to develop. Lastly, the existence of methyl group at the C_β position of thiophene restricts the adoption of torsionally disordered cisoid (syn-syn) conformations. Finally, we suggest that the various electronic and vibrational spectroscopies, combined with MD simulations, exploited in this work, is a suitable methodology for this research area, as optical studies evaluate the templating effect and vibrational spectroscopy along with MD simulation reveal the mechanism that leads to the effect.

Chapter 5: Unravelling excited state dynamics of a ssDNA-assembled conjugated polyelectrolyte

The investigation of the aforementioned CPT/ssDNA complexes proceeded to elucidate the excited state processes and dynamics, focusing the attention primarily on CPT/dC_{20}, which is the most intriguing complex for optoelectronic applications, demonstrating the most successful templating effect of the tested sequences. We used different spectroscopic techniques to monitor the processes that the complex undergoes, exploiting the signal enhancement that selective excitation provides, when on resonance with a specific transition that involves a specific population of a component of the complex. We firstly detected the existence of intrachain excitons with fast dynamics, that absorb in the near-IR for both CPT/dA_{20} and CPT/dC_{20} through TA measurements, denoting that the assembly of CPT with both oligonucleotides results in the hindrance of interchain interactions between polymer chains. TRIR measurements with visible excitation for CPT alone and both CPT/dA_{20} and CPT/dC_{20} complexes revealed polaron formation in all cases but to a larger extent when polymer backbone is characterized by torsional order. The spectroscopic evidence of polarons in TRIR were the background absorption in the mid-IR and the Fano antiresonances, while in transient Raman we observed red shifts of the bands C-C and C=C bands, which are dependent on the conjugated length (quinoid structure) of the excited moieties. The temporal evolution of the vibrational spectroscopic signatures in both TRIR and FSRS spectroscopies exhibited slower dynamics than TA measurements further supporting that the signals correspond to the generation of polarons. Also, we detected the formation of an intermolecular charge transfer complex through TRIR measurements via UV excitation, derived by the observation of a new band associated with the cytosine anion. Therefore, the effective templating of CPT with ssDNA chains can modify the photophysical behaviour of both partners suggesting the ssDNA is not a mere spectator scaffold and one needs to consider how this affects the photophysics that ultimately guide the application of these complexes in molecular electronics.

Chapter 6: Effect of structural conformation of conjugated polymers on spin transport

In this chapter, we investigated the variations of the backbone conformation in the thiophene-based conjugated polymer PEDOT, in which charge carriers exist in the ground state. This polymer is studied as a model for organic semiconductors that can be exploited in spintronics, in order to elucidate the relation of SOC with the structural conformation of the conjugated backbone. Specifically, quinoid structure is adopted to a different extent in the polymer backbone, depending on the type and the concentration of charged species (polarons and bipolarons) affecting the spin parameters. According to the spin admixture parameter γ^2 estimated for different doping/dedoping levels, dedoping suggests weaker SOC strength (increased spin diffusion length). The structural evolution during doping/dedoping processing accessible by chemical and electrochemical manipulation, revealed that for lower doping (decrease of bipolarons and subsequent increased polaron concentration) the PEDOT conformation adopts to a larger extent a quinoid structure, exhibiting increased planarity, which is linked to weaker SOC. Consequently, chemical doping becomes a control factor of SOC strength, while Raman spectroscopy can be a sensitive detection tool to trace it indirectly.

Chapter 7: Impact of molecular structure on vibronic spin orbit coupling of thiophene based heteroacenes

In this chapter, we explored further the relation of SOC strength with the structural changes of organic molecules. This study uses small thiophene-based conjugated molecules instead of polymers to inspect how structural manipulation through alkylation of a planar backbone or decrease of conjugation length by the existence of a freely rotating single bond in the core, affect the excited state processes. With this aim, differently alkylated BTBT derivatives and a benzothiophene (BT) derivative with flexible core were investigated in solution. While the current structural data set does not allow the assignment of the vibrational mode that is responsible for the coupling that promotes enhanced SOC and subsequently increases the ISC rate, we were able to evaluate the effect of alkylation on the conjugation length and to examine the evolution of molecular structure in the different excited states (S_1 and S_2). We found that alkylation of the fused benzothiophene core (similarly with the decrease in planarity in the case of diBT) distorts its conjugation. These reveal that alkylation of the fused benzothiophene core (similarly with the decrease in planarity in the case of diBT) modifies the molecular geometry in a way that enhances SOC. Also, the similarity in the shape of the absorption spectra and the extracted parameters (M, Δ, ω_e, total and mode specific λ) of S_1 and S_2 when alkylation or flexibility of the core are introduced in the conjugated system of benzothiophenes stems from a proximity in energy for these two states, causing the similarity in their nature. The vibrational modes that significantly contribute to the change in the molecular geometry in the excited state is the in-plane ring deformation (~1000 cm^{-1}) for all molecules, as well as the C-S-C in-plane bend only for C8-BTBT, BTBT and diBT.

CHAPTER 9

FUTURE PERSPECTIVES

Considering the above conclusions, some recommendations to be addressed in the future are provided below.

Chapter 4: Structural and photophysical templating of conjugated polyelectrolytes with single-stranded DNA

The spectroscopic techniques reported in Chapter 4 combined with MD simulations can be also exploited for new set of conjugated polymers and cationic polythiophene/ssDNA complexes.

The work presented in Chapter 4 determined key structural aspects of both ssDNA and the cationic polythiophene that are drastically involved in the assembly, resulting in design rules for the optimum cationic conjugated polymer/anionic template complex. Adenine and guanine bases would be excellent aromatic rings to develop strong (and even stronger than cytosine due to the larger conjugated system) π-stacking interactions, if intra-DNA interactions (π-π stacking between neighboring adenines[1,2] and Hoogsteen H-bonds between guanines[3,4]) could be overcome. Nevertheless, according to the present studies only oligocytosine consist consecutive bases that are easily available for effective stacking interactions is cytosine. On the other hand, a systematic study of CPT side chains is required in order to explore in detail the structural characteristics of the side chains necessary to form well-ordered polymer chains. Specifically, (i) a cationic polythiophene with only an alkoxy chain and no methyl group at position 3, and (ii) a cationic polythiophene with a methyl group at position 2 and an alkyl side chain at position 3 can be tested. This study can reveal the interacting sites of the polymer.

In order to solve the problem of agglomeration of the duplexes in solution that usually occurs after ~20 min, it would be interesting to examine the ability to form rotaxanes with macrocycles like cyclodextrins to isolate each CPT/ssDNA complex.[5] In the case of thin film applications, where the same complex aggregation occurs, one can try to employ a solid matrix such as PMMA[6] to avoid inter-complex interactions.

As an alternative for the homopolymers tested in this thesis, a thiophene-based copolymer that includes diketopyrrolopyrrole (DPP) and thiophene rings (named as ES-2-165) that was provided by Mario Leclerc’s group can be also examined to address the structure-property relation. This DPP-based rigid rod polymer can be also studied with Resonance Raman spectroscopy in solution and in film in conjunction with temperature dependent experiments and AFM measurements to monitor any conformational and morphological changes. It would be also interesting to exploit a fluorescence microscope in order to examine single molecule behaviour and visualize any possible energy transfer processes along the chain. These experiments will be useful for comparing the ability for directional charge transport along the chain of this rigid-rod polymer with the ordered CPT conformation in CPT/dC$_{20}$ complex. To achieve this comparison in films, both DPP-based polymer and CPT/dC$_{20}$ complex will be dispersed in a solid matrix such as poly(methyl methacrylate) (PMMA) to avoid interchain coupling and access single molecule properties.

Chapter 5: Unravelling excited state dynamics of a ssDNA-assembled conjugated polyelectrolyte

In order to better distinguish the spectral signals of a charged polymer backbone, we realized that it would have been useful to have acquired the ATR-FTIR and Raman spectra of the oxidized cationic polythiophene and compare it with the TRIR and transient Raman spectra obtained in this thesis. It is a common practise reported in the literature[7–11] that would assist in the detection of the spectral signatures of hole polarons through the variation of the conformation between neutral and oxidized polymer chains.

In addition, we believe that it is important to perform FSRS measurements for CPT alone and CPT/dA$_{20}$ as well, as the FSRS spectra are characterized by enhanced spectral resolution and less complication (background coming from the existence of polaron absorption in the TRIR spectra), for comparison with CPT/dC$_{20}$ to investigate how the excited state structural evolution of the polymer is affected by the different torsional order induced by the interchain interactions (in the case of CPT alone) or the weak templating effect. Then the structural variations and dynamics of the various excited state species and their lifetimes can be correlated in the same manner as for CPT/dC$_{20}$. The FSRS experiments must be improved in terms of selective detection and monitoring of polarons, in order to differentiate more effectively their spectral signatures and dynamics, to obtain a clearer picture of the excited state processes that occur for different conformations of CPT. This could be achieved by using 800-900 nm as Raman pump which is preresonant with the P$_2$ polaron band[12,13] and if possible at 1100 nm in resonance with exciton absorption. In order to detect polarons with Raman pump at 800-900 nm, these measurements should be performed for films of CPT/ssDNA as the P$_2$ polaron band is enhanced only when interchain interactions (between polymer chains) exist.[14,15] Even though the optical properties of CPT/dC$_{20}$ film differ from solution (Figure 9.1), the usage of films will help to reduce the contribution of excitons and allow the selective probing of the polarons. The comparison of the data between these systems will provide a more complete picture of the templating effect on the photophysics of a conjugated polymer.

Furthermore, TA as well as FSRS measurements with excitation at 266 nm especially for CPT/dC$_{20}$ can possibly verify the existence of the cytosine anion and establish the involvement of dC$_{20}$ in the excited state processes of the complex. The possible Raman pump wavelengths that can be tested are at 400nm on resonance with $^1n\pi^*$ state of cytosine[16] or at 266 nm on resonance with cytosine anion absorption,[17] as well as at 900-1100 nm on resonance with the polymer's ESA (or according to what the TA spectra would reveal with 266 nm excitation for CPT).

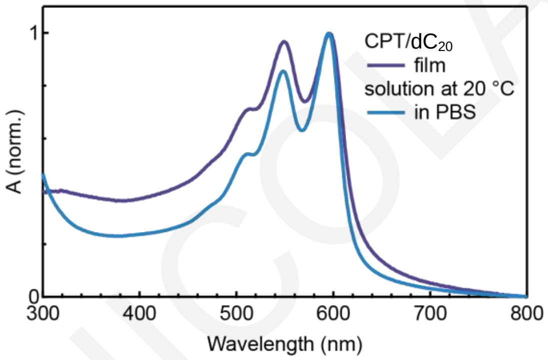

Figure 9.1 Normalized absorption spectra of both film and solution (at 20 °C) of CPT/dC$_{20}$. The spectra were collected by our collaborators (Banerji's group).

The spectroscopic techniques reported in Chapter 5 can be also exploited for a new set of conjugated polymers and cationic polythiophene/ssDNA complexes as mentioned above.

Chapter 6: Effect of structural conformation of conjugated polymers on spin transport

The knowledge obtained by the chemical and electrochemical doping of PEDOT can be further expanded to other conjugated polymers, whose backbone conformation can be easily tuned either via processing or templating (e.g. CPT/ssDNA), by applying the same methodology for structural characterization. The resonance Raman spectroscopy can be combined with spin transport measurements to systematically study the influence of torsional order/disorder on the spin orbit strength in the materials, in a similar manner as reported in our paper,[18] with the added effect of chirality of the polymers in the complexes. The two complexes studied in this thesis induce opposite chirality to the polymer, that could be exploited for spin filtering effects.[19]

Excitation at additional different wavelengths within the absorption band of the BTBT derivatives will allow a more constrained fit of the REPs for the most prominent vibrational modes to the experimentally calculated absolute RR cross sections, as the experimental points obtained with excitation at 282 nm in this thesis are located on the high wavenumber edge of the absorption and REPs, exhibiting lower intensities (see Figure 7.5 and S7.1-S7.3). As seen in the calculated REPs, their shape varies across their wavenumber range, which would possibly lead to other modes becoming dominant in the RR spectrum at different excitation energies,[20] possibly altering the resulting conclusions regarding the contribution of each band to the displacement of excited state potential well and consequently to the structural change in the excited state. We had observed that when excitation wavelengths close to the absorption maxima were used (e.g. 320 nm) strong fluorescent backgrounds were generated drowning the Raman signal. However, the tunability of our laser system should enable us to use additional close wavelengths to 282 nm (e.g. 299 and 309 nm) that can better constrain our fits and avoid as much as possible fluorescence backgrounds.

Moreover, in order to assign which mode is responsible for the coupling that promotes enhanced SOC and subsequently increases the ISC rate, it would be interesting to explore further the change of the molecular structure between S_1 and T_n. To achieve that, time-resolved Resonance Raman can be exploited, which could allow us to monitor the triplet formation, and calculate the reorganization energy from S_1 to T_n, which according to literature[21] should be non-zero, leading to an increase in the ISC rate. Two laser sources with nanosecond pulses need to be used for these experiments with digitally-induced time delay between them. These are usually available in our laboratory but problems with one of the lasers at the time of these experiments that last till today hindered these experiments. These experiments should be possible, however, in the near future with the repair of the laser.

Finally, similar analysis to the modelling of the fluorescence spectra can be performed for the phosphorescence spectra to determine the reorganization energy of the T_1-S_0 transition, as a preliminary step before the estimation of the S_1-T_1 reorganization energy.

References

(1) Mills, J. B.; Vacano, E.; Hagerman, P. J. Flexibility of Single-Stranded DNA: Use of Gapped Duplex Helices to Determine the Persistence Lengths of Poly(DT) and Poly(DA). *J. Mol. Biol.* **1999**, *285* (1), 245–257.

(2) Konorov, S. O.; Schulze, H. G.; Addison, C. J.; Haynes, C. A.; Blades, M. W.; Turner, R. F. B. Ultraviolet Resonance Raman Spectroscopy of Locked Single-Stranded Oligo(DA) Reveals Conformational Implications of the Locked Ribose in LNA. *J. Raman Spectrosc.* **2009**, *40* (9), 1162–1171.

(3) Nikolova, E. N.; Gottardo, F. L.; Al-Hashimi, H. M. Probing Transient Hoogsteen Hydrogen Bonds in Canonical Duplex DNA Using NMR Relaxation Dispersion and Single-Atom Substitution. *J. Am. Chem. Soc.* **2012**, *134* (8), 3667–3670.

(4) Miura, T.; Thomas, G. J. Structure and Dynamics of Interstrand Guanine Association in Quadruplex Telomeric DNA. *Biochemistry* **1995**, *34* (29), 9645–9654.

(5) Cacialli, F.; Wilson, J. S.; Michels, J. J.; Daniel, C.; Silva, C.; Friend, R. H.; Severin, N.; Samori, P.; Rabe, J. P.; O’connell, M. J.; Taylor, P. N.; Anderson, H. L. Cyclodextrin-Threaded Conjugated Polyrotaxanes as Insulated Molecular Wires with Reduced Interstrand Interactions. *Nat. Mater.* **2002**, *1* (3), 160–164.

(6) Bjork, P.; Herland, A.; Scheblykin, I. G.; Inganas, O. Single Molecular Imaging and Spectroscopy of Conjugated Polyelectrolytes Decorated on Stretched Aligned DNA. *Nano Lett.* **2005**, *5* (10), 1948–1953.

(7) Provencher, F.; Berube, N.; Parker, A. W.; Greetham, G. M.; Towrie, M.; Hellmann, C.; Cote, M.; Stingelin, N.; Silva, C.; Hayes, S. C. Direct Observation of Ultrafast Long-Range Charge Separation at Polymer–Fullerene Heterojunctions. *Nat. Commun.* **2014**, *5*, 4288.

(8) Bragg, A. E.; Yu, W.; Zhou, J.; Magnanelli, T. Ultrafast Raman Spectroscopy as a Probe of Local Structure and Dynamics in Photoexcited Conjugated Materials. *J. Phys. Chem. Lett.* **2016**, *7*, 3990–4000.

(9) Yu, W.; Zhou, J.; Bragg, A. E. Exciton Conformational Dynamics of Poly(3-Hexylthiophene) (P3HT) in Solution from Time-Resolved Resonant-Raman Spectroscopy. *J. Phys. Chem. Lett.* **2012**, *3*, 1321–1328.

(10) Roy, P.; Anandan, G. T.; Nayak, N.; Kumar, A.; Dasgupta, J. Raman Snapshots of Side-Chain Dependent Polaron Dynamics in PolyThiophene Films. *J. Phys. Chem. B* **2023**, *127*, 567–576.

(11) Yu, W.; Donohoo-Vallett, P. J.; Zhou, J.; Bragg, A. E. Ultrafast Photo-Induced

Nuclear Relaxation of a Conformationally Disordered Conjugated Polymer Probed with Transient Absorption and Femtosecond Stimulated Raman Spectroscopies. *J. Chem. Phys.* **2020**, *141*, 044201.

(12) Österbacka, R.; An, C. P.; Jiang, X. M.; Vardeny, Z. V. Two-Dimensional Electronic Excitations in Self-Assembled Conjugated Polymer Nanocrystals. *Science (80-.).* **2000**, *287* (5454), 839–842.

(13) Kahmann, S.; Loi, M. A.; Brabec, C. J. Delocalisation Softens Polaron Electronic Transitions and Vibrational Modes in Conjugated Polymers. *J. Mater. Chem. C* **2018**, *6* (22), 6008–6013.

(14) Mansour, A. E.; Lungwitz, D.; Schultz, T.; Arvind, M.; Valencia, A. M.; Cocchi, C.; Opitz, A.; Neher, D.; Koch, N. The Optical Signatures of Molecular-Doping Induced Polarons in Poly(3-Hexylthiophene-2,5-Diyl): Individual Polymer Chains: Versus Aggregates. *J. Mater. Chem. C* **2020**, *8* (8), 2870–2879.

(15) Arvind, M.; Tait, C. E.; Guerrini, M.; Krumland, J.; Valencia, A. M.; Cocchi, C.; Mansour, A. E.; Koch, N.; Barlow, S.; Marder, S. R.; Behrends, J.; Neher, D. Quantitative Analysis of Doping-Induced Polarons and Charge-Transfer Complexes of Poly(3-Hexylthiophene) in Solution. *J. Phys. Chem. B* **2020**, *124* (35), 7694–7708.

(16) Kohl, F. R.; Zhang, Y.; Charnay, A. P.; Martínez-Fernández, L.; Kohler, B. Ultrafast Excited State Dynamics of Silver Ion-Mediated Cytosine-Cytosine Base Pairs in Metallo-DNA. *J. Chem. Phys.* **2020**, *153* (10).

(17) Morita, H.; Nagakura, S. The Electronic Absorption Spectra and the Electronic Structures of Cytosine, Isocytosine, and Their Anions and Cations. *Theor. Chim. Acta* **1968**, *11* (4), 279–295.

(18) Nicolaides, C.; Nicolaidou, E.; Papagiorgis, P.; Itskos, G.; Hayes, S. C.; Trypiniotis, T. Effect of Structural Conformation of Conjugated Polymers on Spin Transport. *Phys. Rev. Mater.* **2022**, *6* (9), 095601.

(19) Aiello, C. D.; Abendroth, J. M.; Abbas, M.; Afanasev, A.; Agarwal, S.; Banerjee, A. S.; Beratan, D. N.; Belling, J. N.; Berche, B.; Botana, A.; Caram, J. R.; Celardo, G. L.; Cuniberti, G.; Garcia-etxarri, A.; Dianat, A.; Diez-perez, I.; Guo, Y.; Gutierrez, R.; Herrmann, C.; Hihath, J.; Kale, S.; Kurian, P.; Lai, Y.; Liu, T.; Lopez, A.; Medina, E.; Mujica, V.; Naaman, R.; Noormandipour, M.; Palma, J. L.; Paltiel, Y.;

Petuskey, W.; Ribeiro-silva, C.; Jos, J.; Santos, E. J. G.; Solyanik-gorgone, M.; Sorger, V. J.; Stemer, D. M.; Ugalde, J. M.; Valdes-curiel, A.; Varela, S.; Waldeck, D. H.; Wasielewski, M. R.; Weiss, P. S.; Zacharias, H.; Wang, Q. H. A Chirality-Based Quantum Leap. *ACS Nano* **2022**, *16*, 4989–5035.

(20) Banerjee, S.; Saalfrank, P. Vibrationally Resolved Absorption, Emission and Resonance Raman Spectra of Diamondoids: A Study Based on Time-Dependent Correlation Functions. *Phys. Chem. Chem. Physicsy* **2014**, *16*, 144–158.

(21) Penfold, T. J.; Gindensperger, E.; Daniel, C.; Marian, C. M. Spin-Vibronic Mechanism for Intersystem Crossing. *Chem. Rev.* **2018**, *118*, 6975–7025.

APPENDIX

SUPPLEMENTARY DATA FOR CHAPTER 4

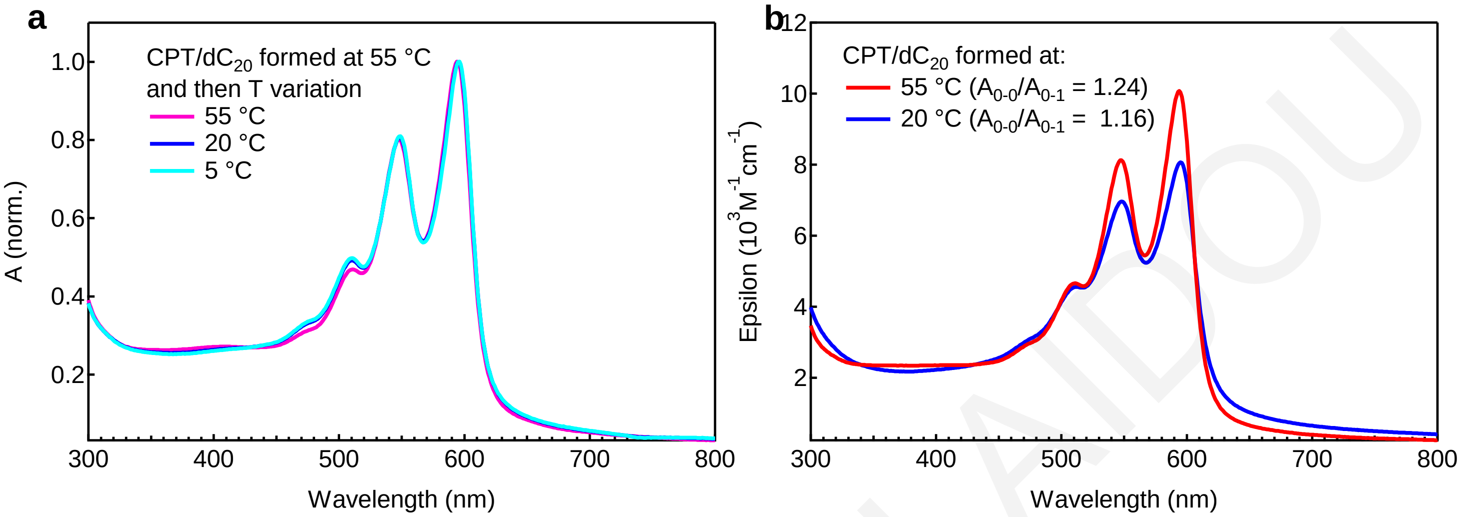

Figure S4.1. (a) Normalised absorption spectra of CPT/dC$_{20}$ in PBS formed at 55°C and then the temperature was varied to 20 and 5 °C. (b) Absorption spectra (y-axis expressed in extinction coefficient) of CPT/dC$_{20}$ formed at 55 °C and at 20 °C. Concentration of $7.3 \cdot 10^{-5}$ M (monomeric basis).

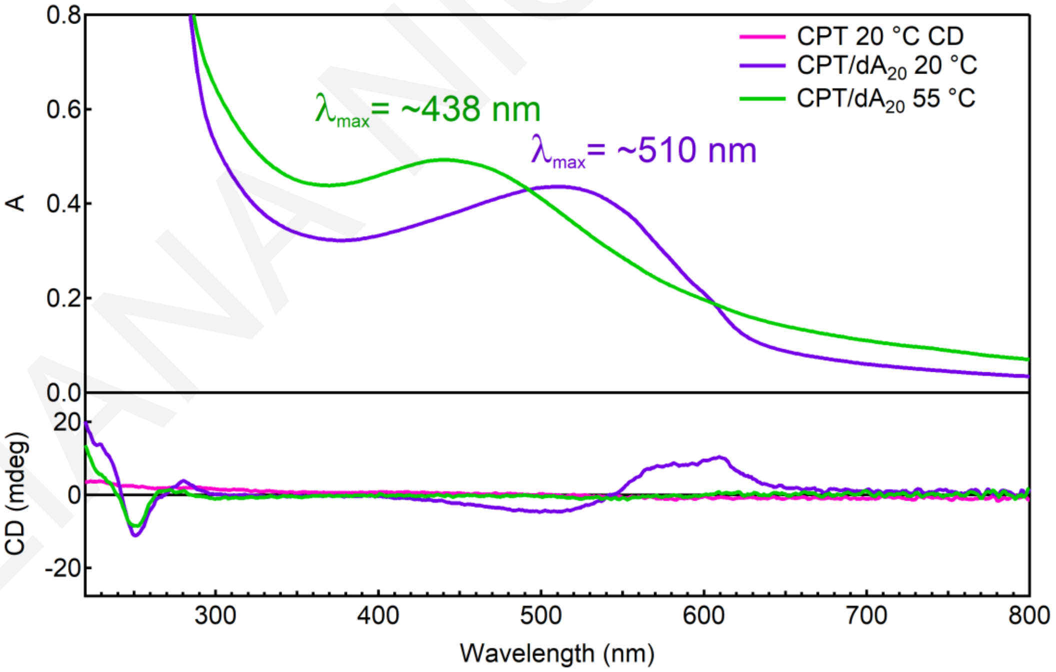

Figure S4.2. Absorption and CD spectra of CPT/dA$_{20}$ in PBS at 20 and 55 °C and CD spectrum of CPT at 20 °C. Concentration of each component is $7.3 \cdot 10^{-5}$ M (monomeric basis)

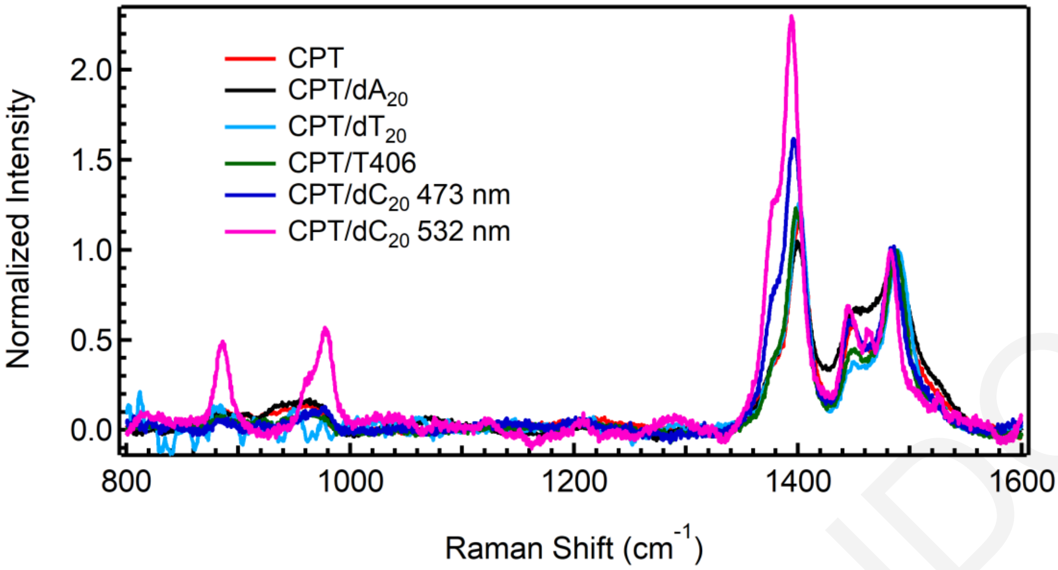

Figure S4.3. Resonance Raman (RR) spectra normalized with respect to the intensity of the band at ~1487 cm^{-1} with excitation at 435.69 nm for CPT/dT$_{20}$, 473 nm for CPT/dA$_{20}$, CPT/T406 and CPT/dC$_{20}$ and 532 nm for CPT/dC$_{20}$, all in PBS buffer with a concentration of 1.5·10^{-4} M (monomeric basis) at room temperature. The spectra are shown over an extended range compared to the main text, in order to show the low frequency modes between 800-1000 cm^{-1}. These modes are greatly enhanced in the case of CPT/dC$_{20}$.

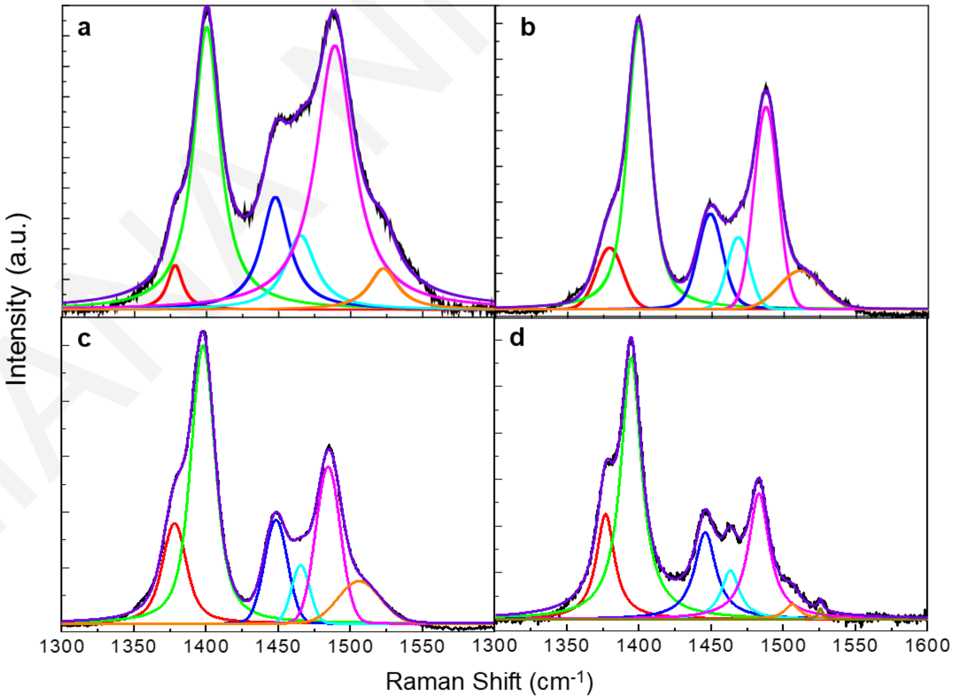

Figure S4.4. Deconvolution of RR spectra for (a) CPT/dA$_{20}$ (b) CPT/T406 (c) CPT/dC$_{20}$ with excitation at 473 nm and (d) CPT/dC$_{20}$ with excitation at 532 nm.

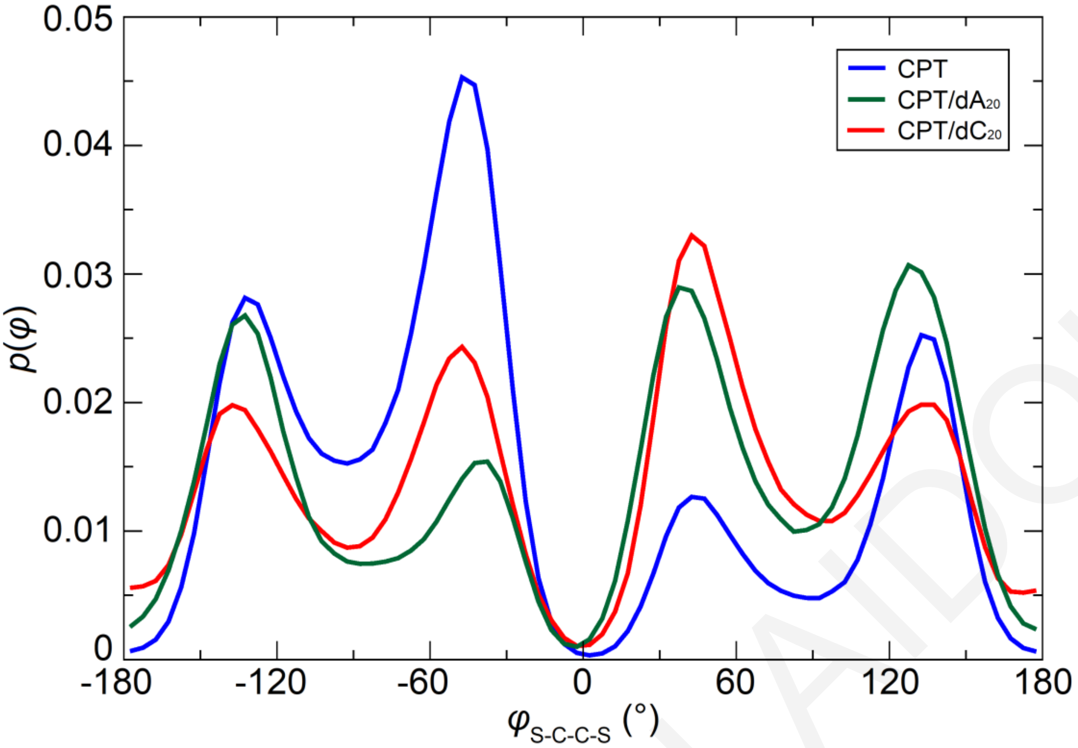

Figure S4.5. Distributions of the S-C-C-S dihedral angle between the adjacent thiophene rings in CPT alone and assembled with dA_{20} and dC_{20}.

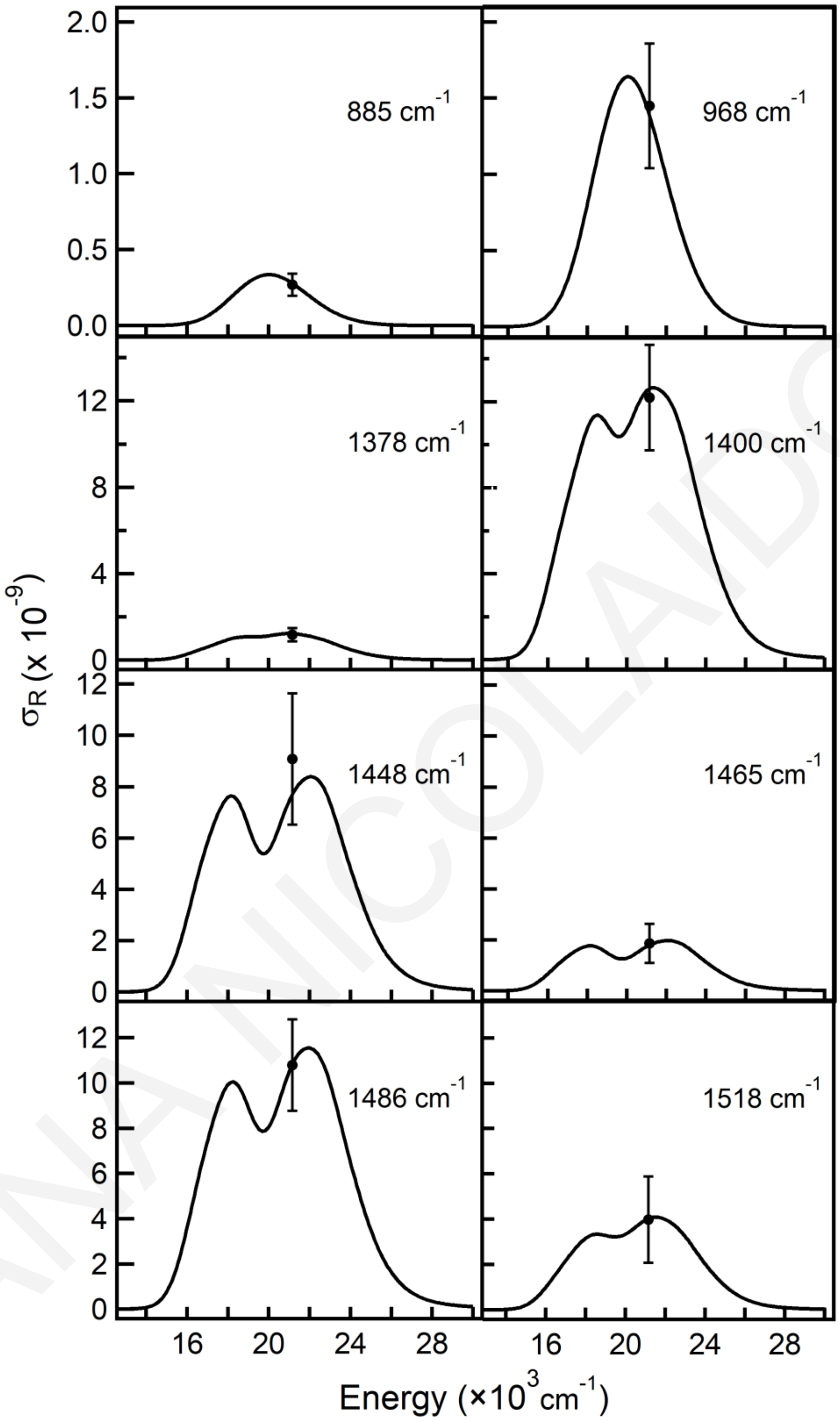

Figure S4.6. Calculated Raman excitation profiles (REPs) for the most prominent vibrational modes of CPT/dA$_{20}$ complex. The points with error bars denote the experimentally calculated absolute RR cross sections at 473 nm.

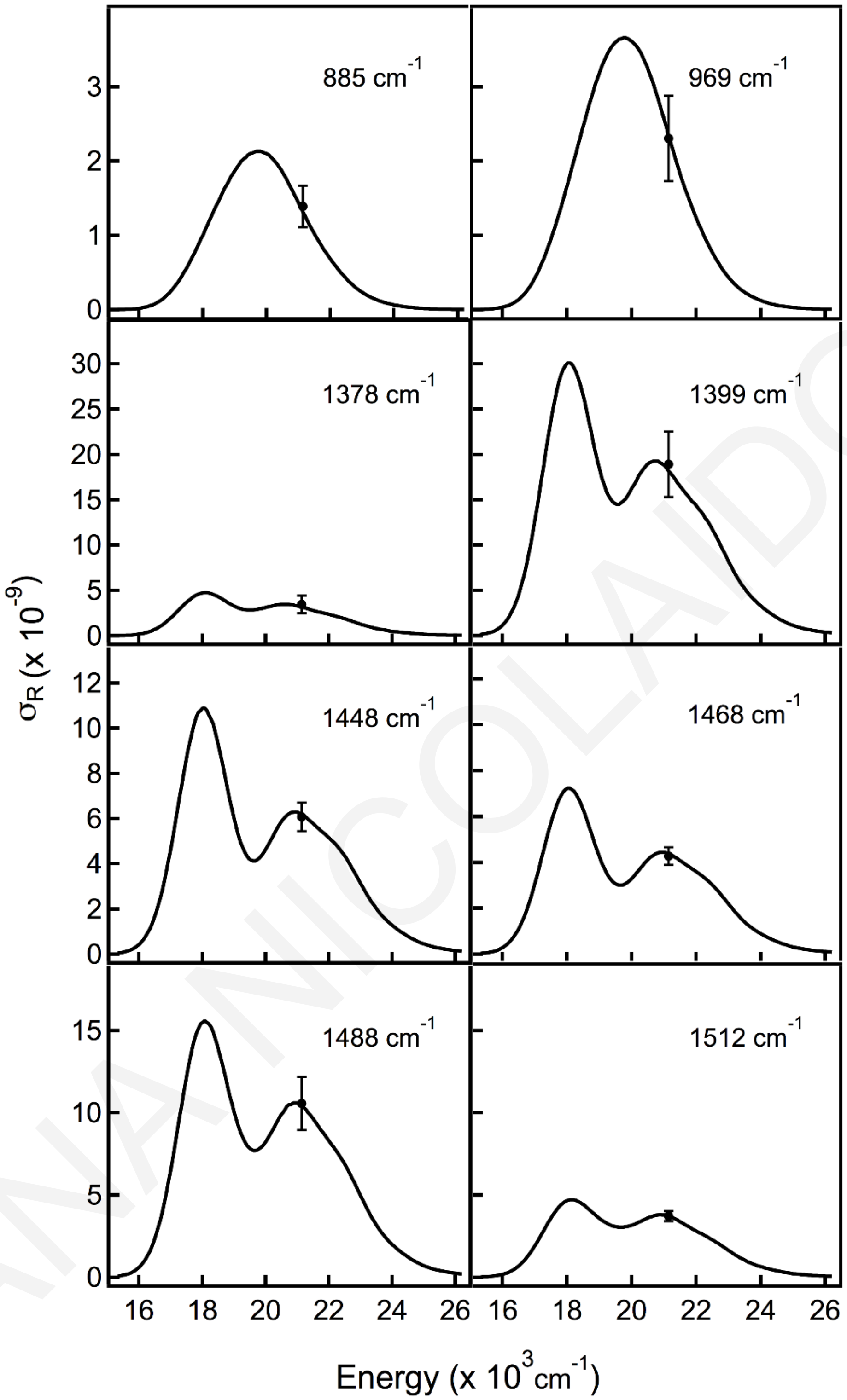

Figure S4.7. Calculated Raman excitation profiles (REPs) for the most prominent vibrational modes of CPT/T406 complex. The points with error bars denote the experimentally calculated absolute RR cross sections at 473 nm.

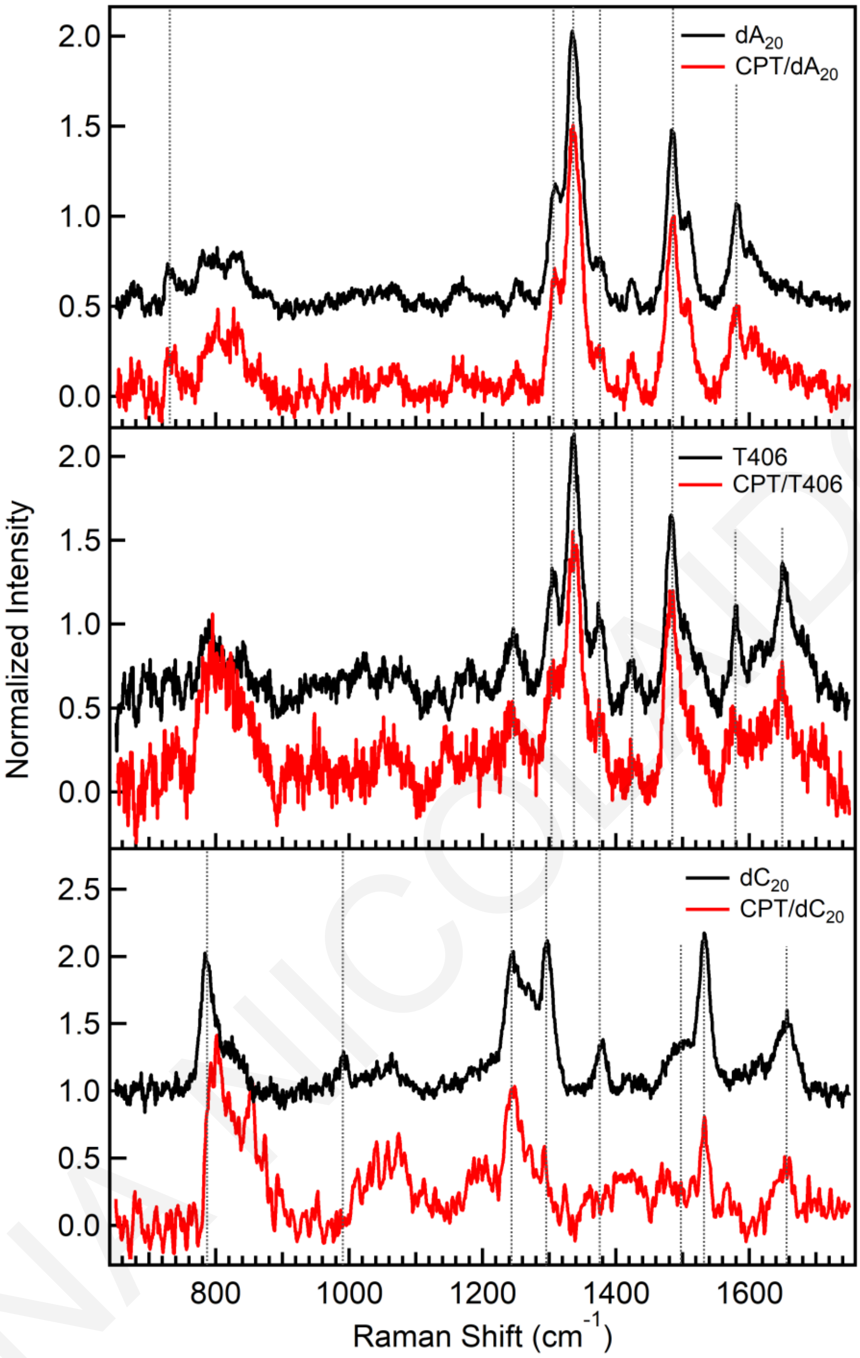

Figure S4.8. UVRR spectra of (a) dA_{20} and CPT/dA_{20} (b) T406 and CPT/T406 in PBS buffer with a concentration of $1.5 \cdot 10^{-4}$ M and (c) dC_{20} and CPT/dC_{20} in PBS buffer with a concentration of $3 \cdot 10^{-4}$ M (monomeric basis) at room temperature with excitation at 266 nm.

Table S4.1. Frequencies (cm^{-1}) and assignments of dominant RR bands in UVRR spectra of ssDNA

dA$_{20}$		**dC$_{20}$**		**T406**	
Frequency (cm^{-1})	**Assignment[1]**	**Frequency (cm^{-1})**	**Assignment**	**Frequency (cm^{-1})**	**Assignment**
1258	N1C6, C6N6	1246	δC6H, C4N4	1246	**A:** N1C6, C6N6 **C:** δC6H, C4N4
1309	N9C8, N3C2, δC8H, δC2H	1297	N1C6, C5C6	1304	**A:** N9C8, N3C2, δC8H, δC2H
1338	N7C5, C8N7	1381	C4N4, N1C2	1334	**A:** N7C5, C8N7
1377	C1N9, C6N6	1532	N3C4, N1C2	1373	**C:** C4N4, N1C2 **A:** C1N9, C6N6
1425	C4N9, δC8H	1618	δNH$_2$, C4N4	1423	**A:** C4N9, δC8H
1484	δC2H, N9C8, δC8H	1656	C2O, C2N3	1483	**A:** δC2H, N9C8, δC8H
1506	N7C8			1506	**A:** N7C8
1581	C5C4, C4N3			1527	**C:** N3C4, N1C2
1603	δNH$_2$, C5C6, C6N6			1579	**A:** C5C4, C4N3 **G:** C4N3, C5C4, N7C5
				1609	**A:** δNH$_2$, C5C6, C6N6
				1650	**C:** C2O, C2N3

[1] Stretching vibrations, unless denoted δ (bending vibrations)

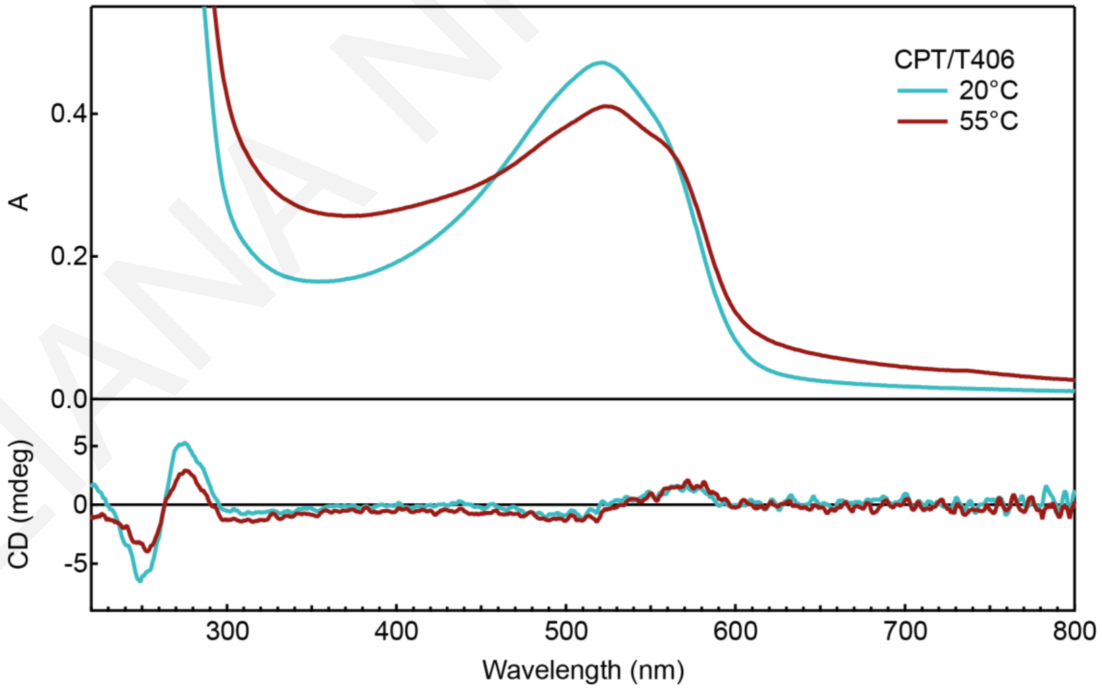

Figure S4.9. Absorption and CD spectra of CPT/T406 in PBS at 20 and 55 °C. Concentration of 7.3·10^{-5} M (monomeric basis).

SUPPLEMENTARY DATA FOR CHAPTER 5

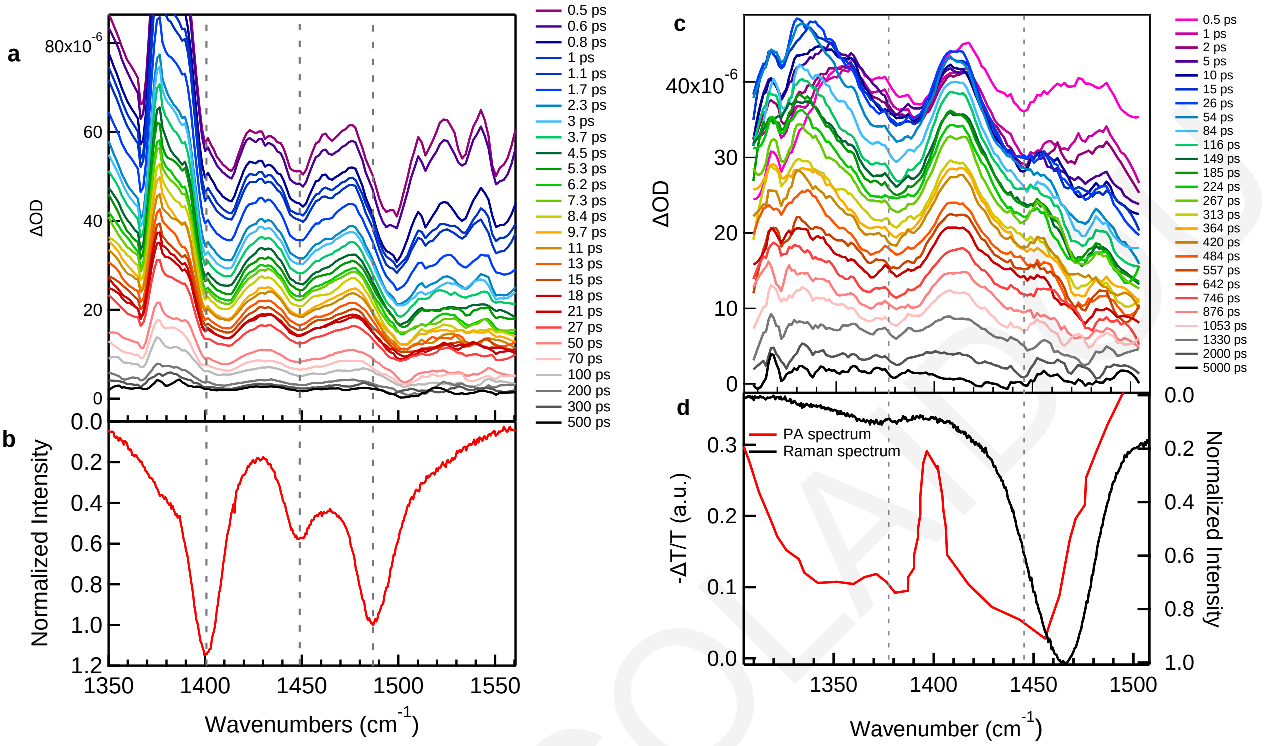

Figure S5.1. (a) TRIR spectra of CPT with excitation at 532 nm. An artifact feature at ~ 1380 cm^{-1} is observed, which is generated by the detector and has been omitted from the data in the main text. (b) Ground state Raman spectrum of CPT with excitation at 532 nm with inverted y axis. (c) TRIR spectra of P3HT without background subtraction with excitation at 532 nm. (d) Photoinduced absorption (PA) in the mid-IR (red, left axis) reproduced from the literature[21] and ground state resonance Raman spectrum of P3HT (black) with excitation at 532 nm with reversed y axis (black, right axis).

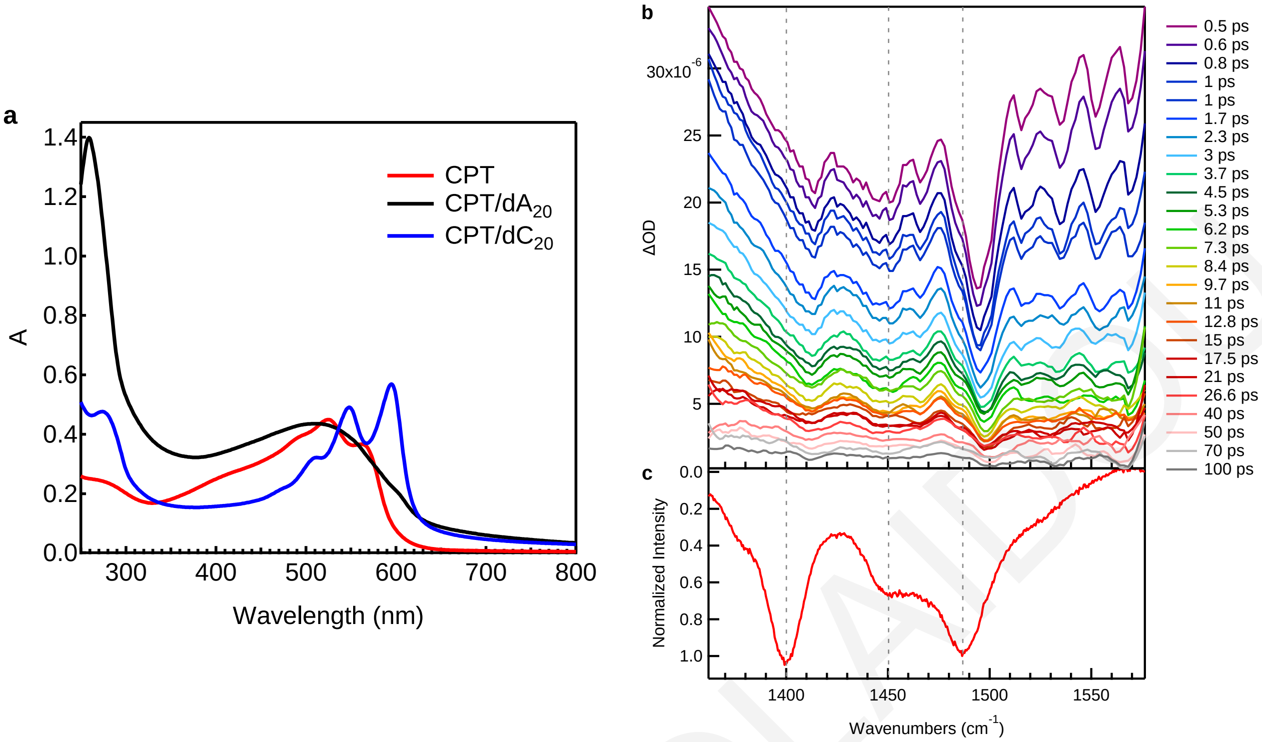

Figure S5.2. (a) Absorption of CPT and its complexes with dA$_{20}$ (black) and dC$_{20}$ (blue). (b) TRIR spectra of CPT/dA$_{20}$ without background subtraction with excitation at 532 nm. (c) Ground state Raman spectrum of CPT/dA$_{20}$ with excitation at 473 nm with reversed y axis.

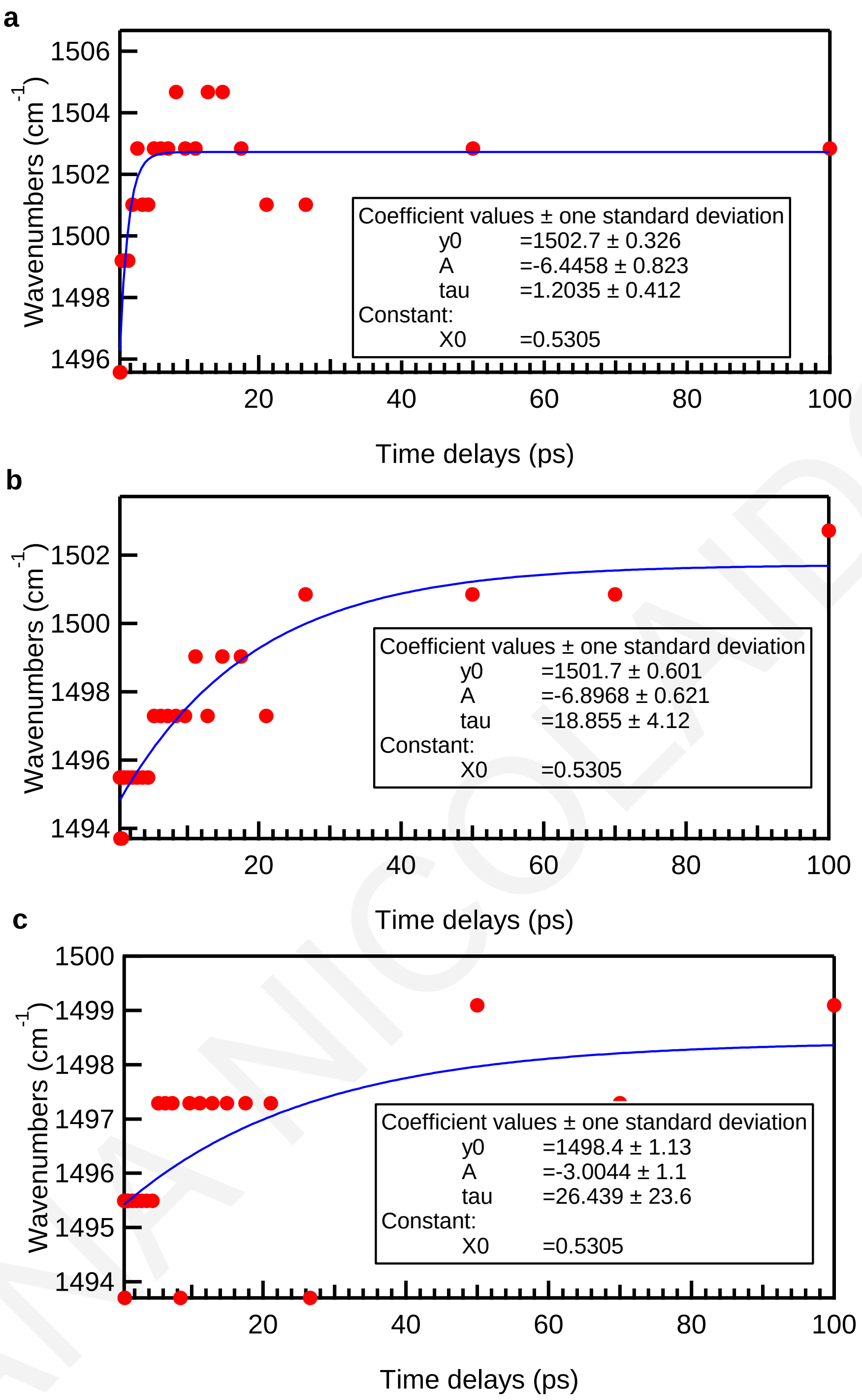

Figure S5.3. Kinetics of the shift of 1501 cm^{-1} band of (a) CPT alone, (b) CPT/dA$_{20}$ and (c) CPT/dC$_{20}$.

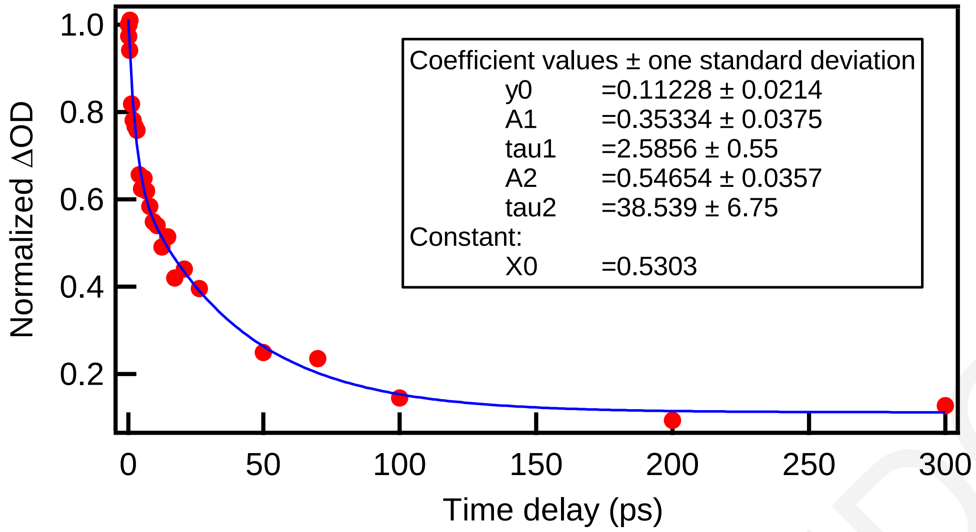

Figure S5.4. Kinetics of the 1501 cm^{-1} band of CPT alone after excitation at 532 nm fitted by a biexponential function. Background contribution was eliminated by subtracting the intensity of the 1501 cm^{-1} band by the intensity of a point considered as representative for the background (1476 cm^{-1}).

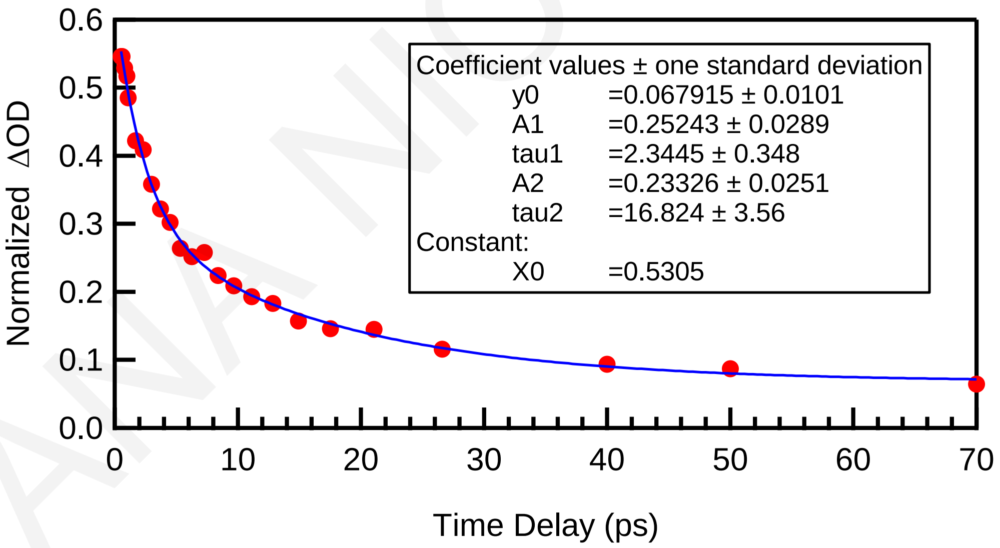

Figure S5.5. Kinetics of the 1497 cm^{-1} band of CPT/dA$_{20}$ after excitation at 532 nm fitted by a biexponential function. Background contribution was eliminated by subtracting the intensity of the 1497 cm^{-1} band by the intensity of a point considered as representative for the background (1476 cm^{-1}).

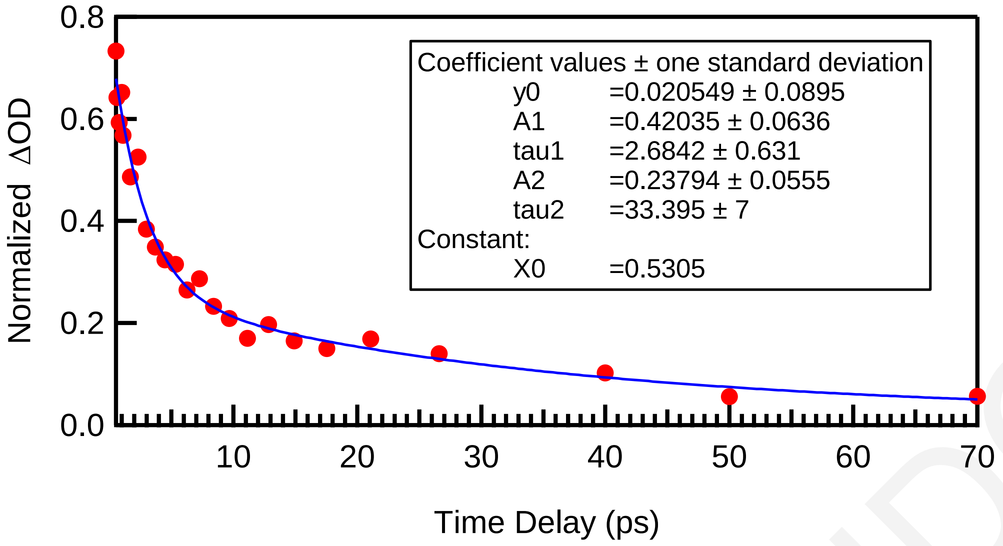

Figure S5.6. Kinetics of the 1497 cm^{-1} band of CPT/dC$_{20}$ after excitation at 532 nm fitted by a biexponential function. Background contribution was eliminated by subtracting the intensity of the 1497 cm^{-1} band by the intensity of a point considered as representative for the background (1476 cm^{-1}).

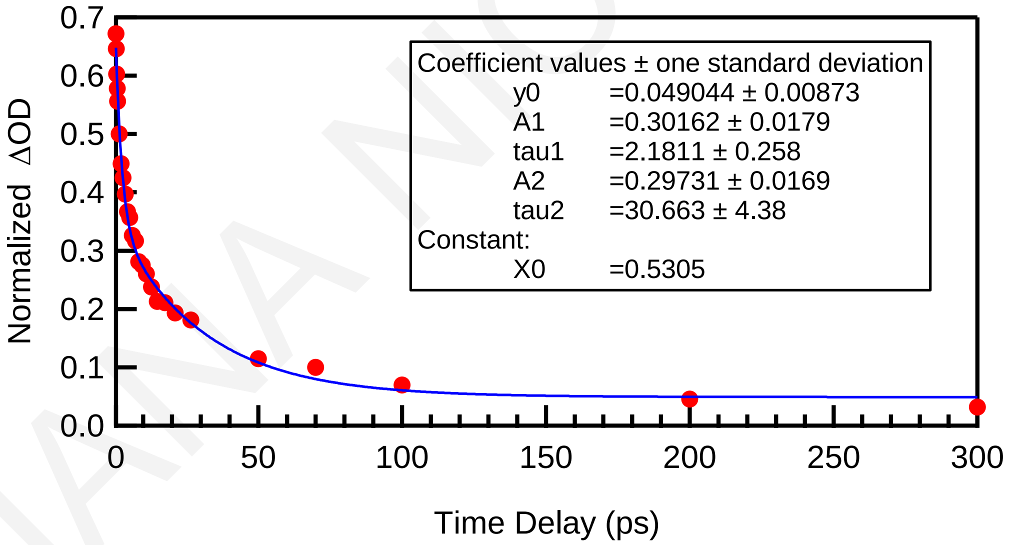

Figure S5.7. Kinetics of the background absorption (considering 1350 cm^{-1} as representative point of background) of CPT alone after excitation at 532 nm fitted by a biexponential function.

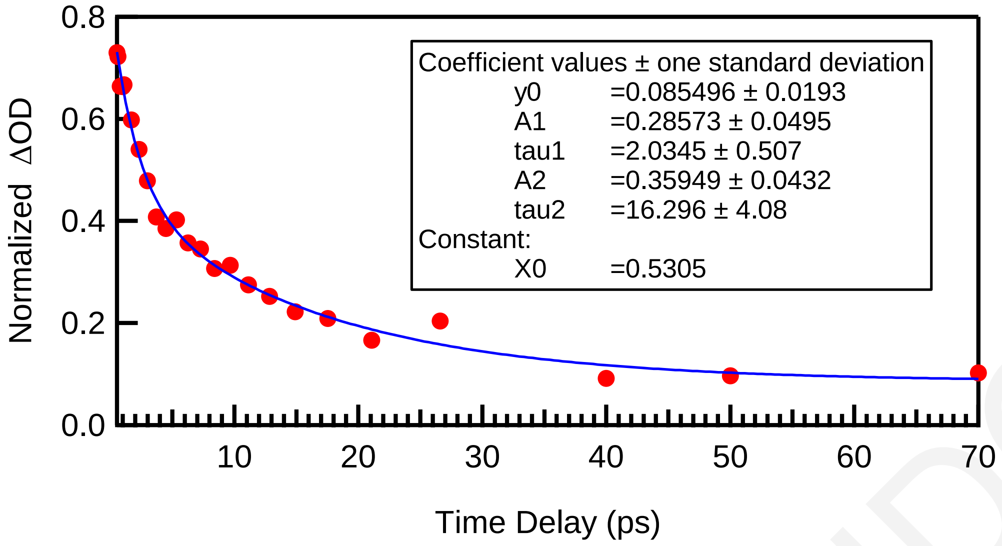

```
Coefficient values ± one standard deviation
        y0      =0.085496 ± 0.0193
        A1      =0.28573 ± 0.0495
        tau1    =2.0345 ± 0.507
        A2      =0.35949 ± 0.0432
        tau2    =16.296 ± 4.08
Constant:
        X0      =0.5305
```

Figure S5.8. Kinetics of the background absorption (considering 1308 cm^{-1} as representative point of background) of CPT/dA_{20} after excitation at 532 nm fitted by a biexponential function.

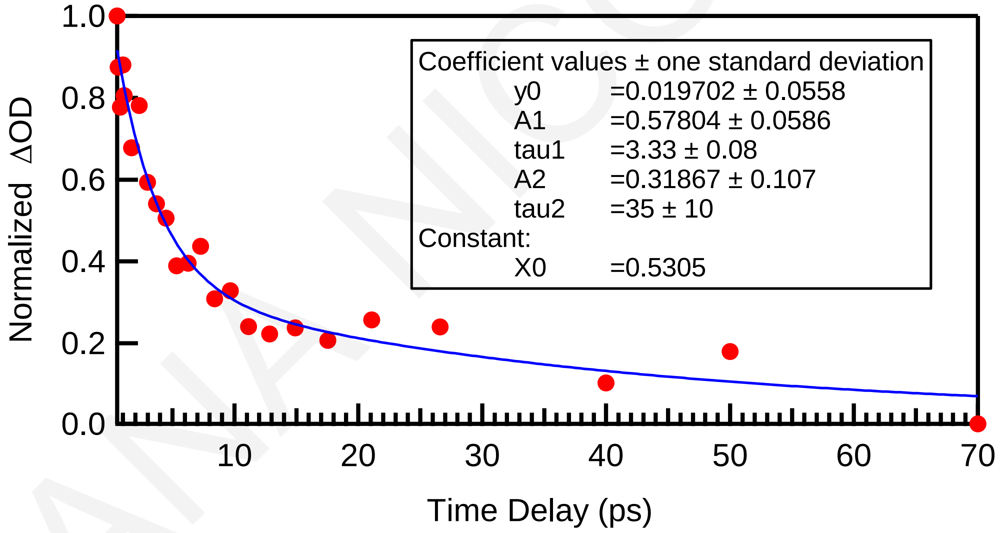

```
Coefficient values ± one standard deviation
        y0      =0.019702 ± 0.0558
        A1      =0.57804 ± 0.0586
        tau1    =3.33 ± 0.08
        A2      =0.31867 ± 0.107
        tau2    =35 ± 10
Constant:
        X0      =0.5305
```

Figure S5.9. Kinetics of the background absorption (considering 1308 cm^{-1} as representative point of background) of CPT/dC_{20} after excitation at 532 nm fitted by a biexponential function.

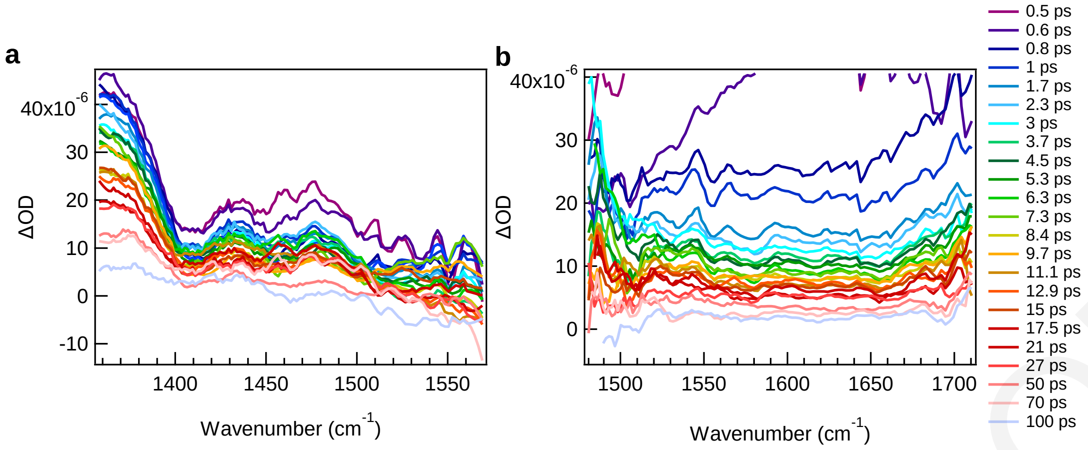

Figure S5.10. TRIR spectra of CPT alone without background subtraction with excitation at 266 nm at (a) lower and (b) higher wavenumbers.

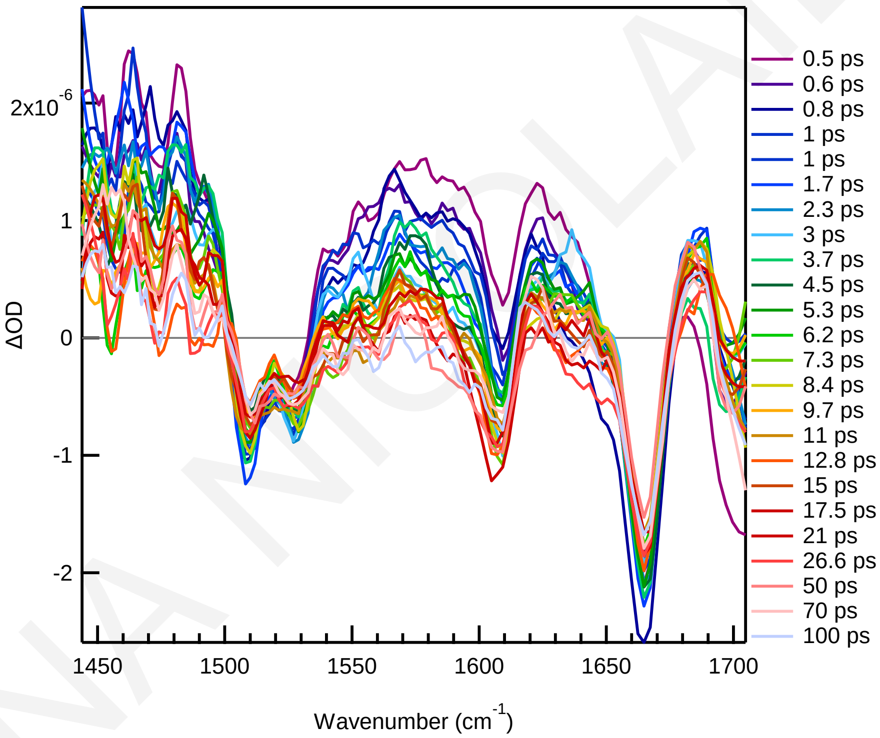

Figure S5.11. TRIR spectra of dC_{20} without background subtraction with excitation at 266 nm.

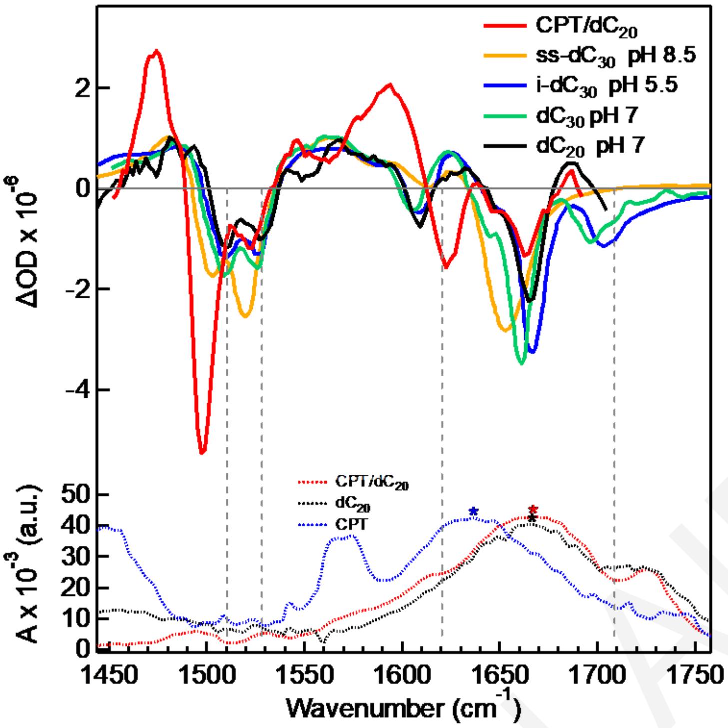

Figure S5.12. TRIR spectra with excitation at 266 nm after the subtraction of the background of CPT/dC20 (red) and dC20 at pH 7 (black) and dC30 at pH 8.5 (yellow), 5.5 (blue) and 7 (green) (TRIR spectra of dC30 were reproduced from the literature) at 2 ps. FTIR spectra of CPT/dC20 (red), dC20 (black) and CPT (blue) are shown in dashed lines below the TRIR. Water bend mode is marked with an asterix.

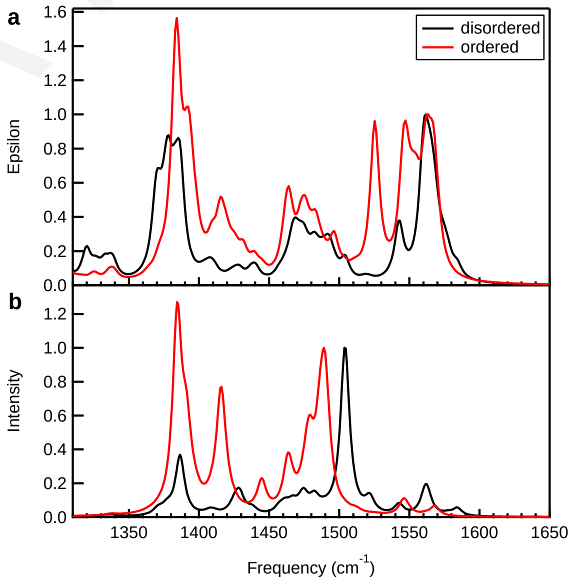

Figure S5.13. DFT calculated (a) IR (b) Raman spectra of disordered (black) and ordered (red) CPT chain (monomer units: n=4).

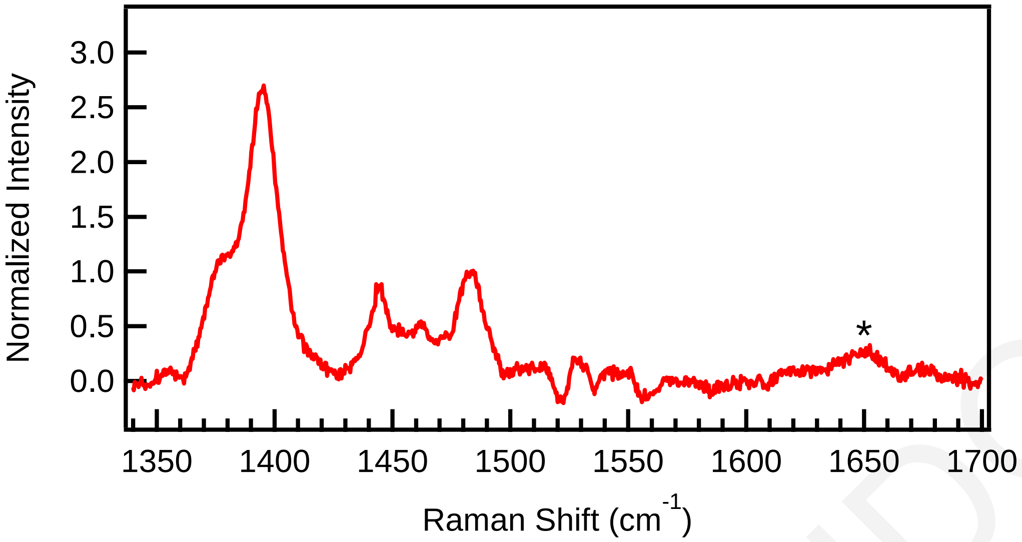

Figure S5.14. Raman spectrum of CPT/dC$_{20}$ with excitation at 532 nm at higher wavenumbers. Water bend mode is marked with an asterix.

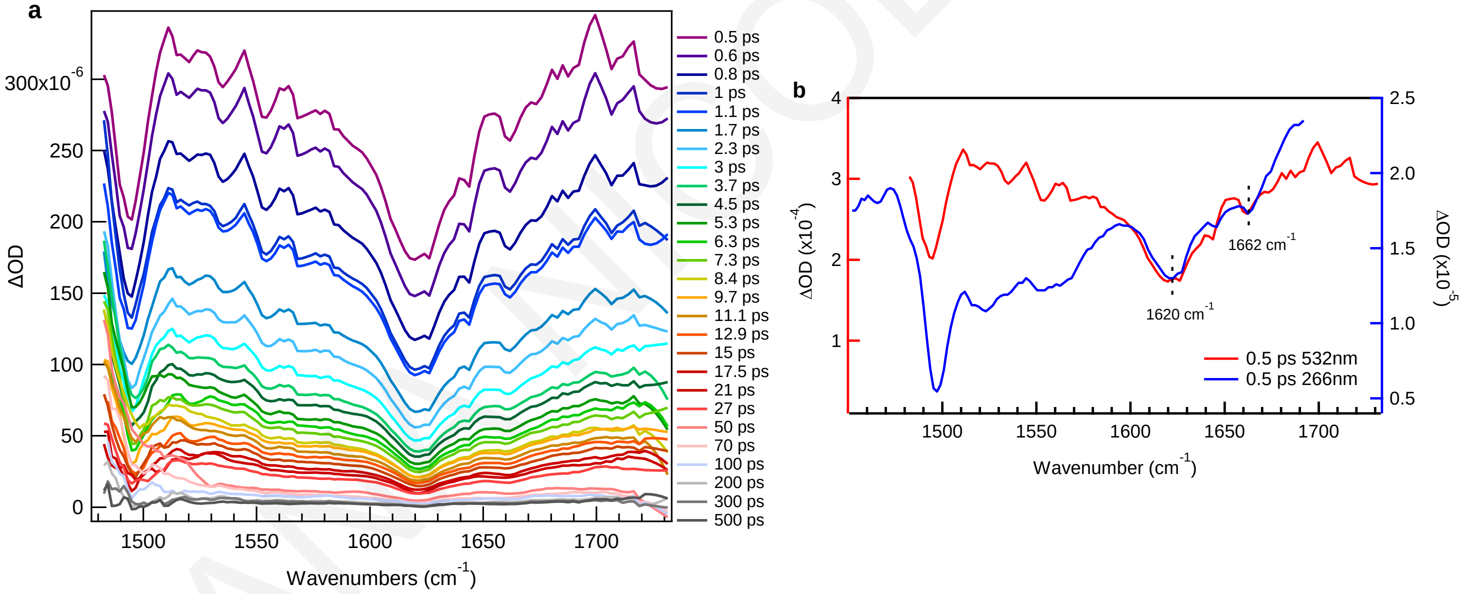

Figure S5.15. (a) TRIR spectra of CPT/dC$_{20}$ without background subtraction with excitation at 532 nm at higher wavenumbers. (b) Comparison of TRIR spectra of CPT/dC$_{20}$ at 0.5 ps with excitation at 266 nm (black) and 532 nm (red).

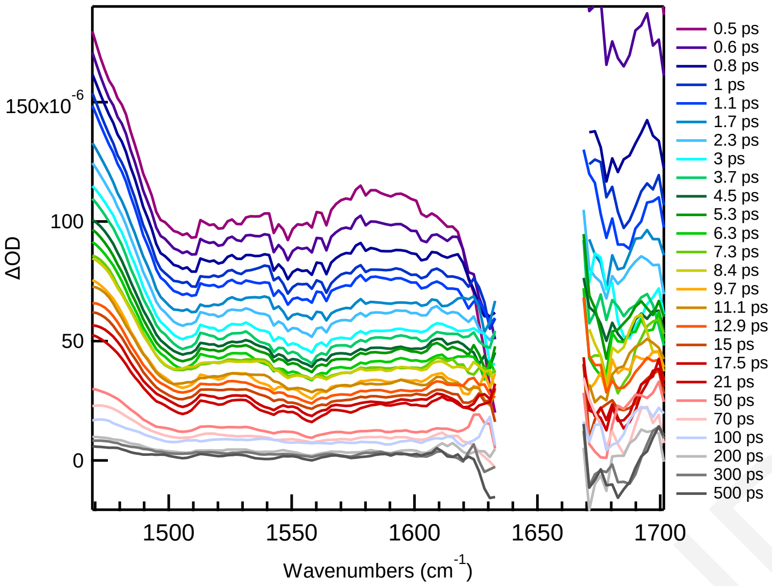

Figure S5.16. TRIR spectra of CPT alone without background subtraction with excitation at 532 nm at higher wavenumbers. There are no data between ~1633 and 1667 cm^{-1} due to complications with the detector. (artifact)

Table S5.1. Assignment of DFT calculated IR and Raman and experimental RR vibrational bands. Computed frequencies refer to individual vibrational modes, and are corrected using the empirical scaling factor for B3LYP (0.97).

Label	**Frequency (cm^{-1})**					**Assignment**
	Computed				**Experimental**	
	IR planar	**IR twisted**	**Raman planar**	**Raman twisted**	**CPT/dC$_{20}$ λ_{exc} = 532 nm**	
ν_1	1384	1378	1384	1386	1376	Mixed C$_\beta$–C$_{\beta'}$ and C$_\alpha$–C$_{\alpha'}$ stretching
ν_2	1415	1408	1416	1409	1394	Mixed C$_\beta$–C$_{\beta'}$ and C$_\alpha$–C$_{\alpha'}$ stretching
ν_3	1464	1469	1445,1464	1428, 1466	1448, 1463	C$_\alpha$=C$_\beta$(O) ring stretching
ν_4	1475, 1483	1483	1478, 1489	1474, 1504	1484	C$_\alpha$=C$_\beta$(Me) ring stretching
ν_5	1525	-	1510	1522	1510	C$_\alpha$=C$_\beta$ ring stretching (anti)
ν_6	1547, 1562	1542, 1562	1546, 1567	1543, 1562, 1584	1625, 1650	C$_\alpha$=C$_\beta$ ring stretching (anti), C=C, C=N ring stretching (anti) (imidazole)

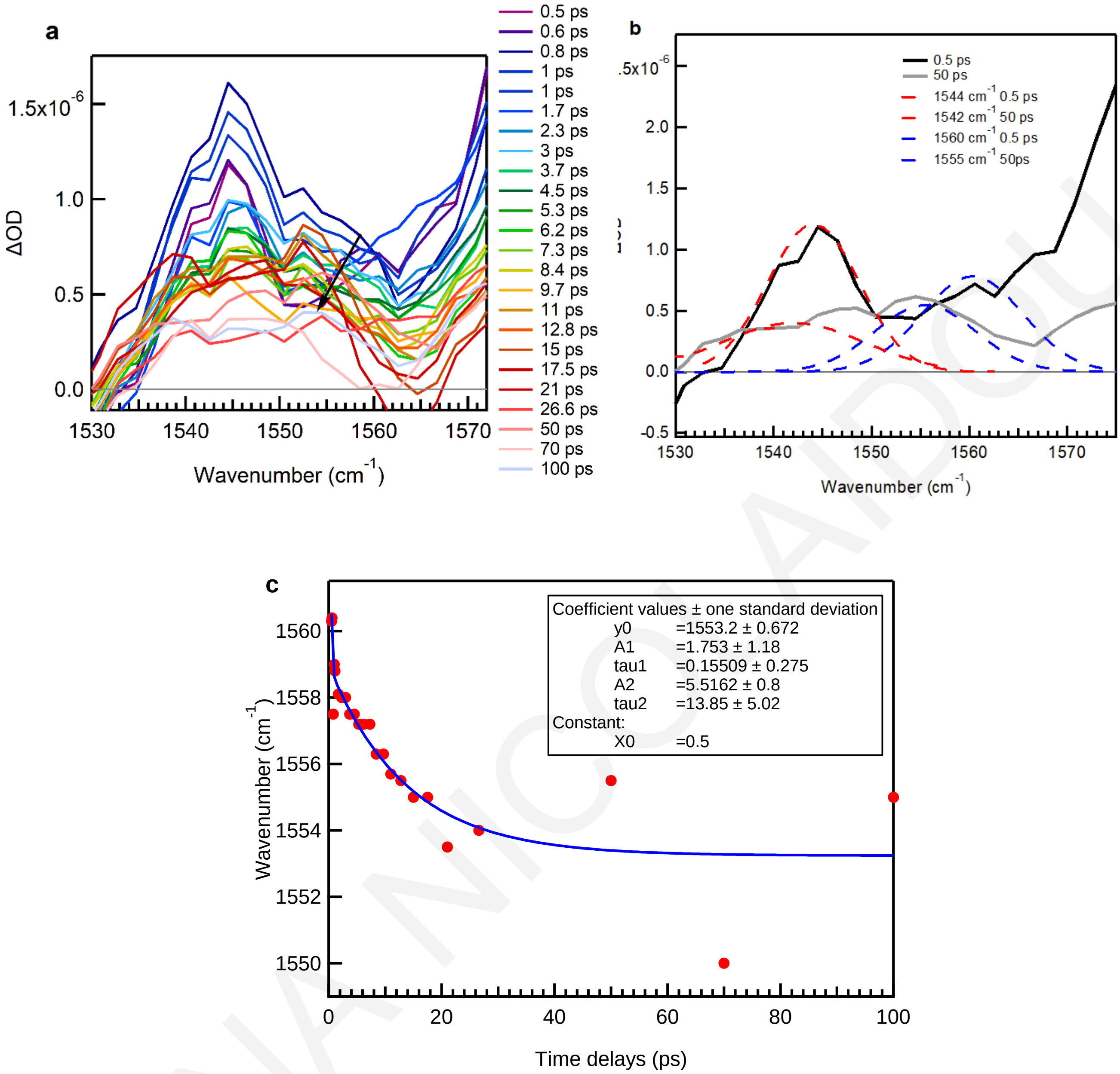

Figure S5.17. (a) Spectral shift of 1558 cm^{-1} band with time indicated with a black arrow. (b) Deconvolution of the 1550 cm^{-1} spectral region for TRIR spectra at 0.5 ps (early) and 50 ps (later) delay times. (c) Kinetics of the shift of 1558 cm^{-1} band of CPT/dC$_{20}$.

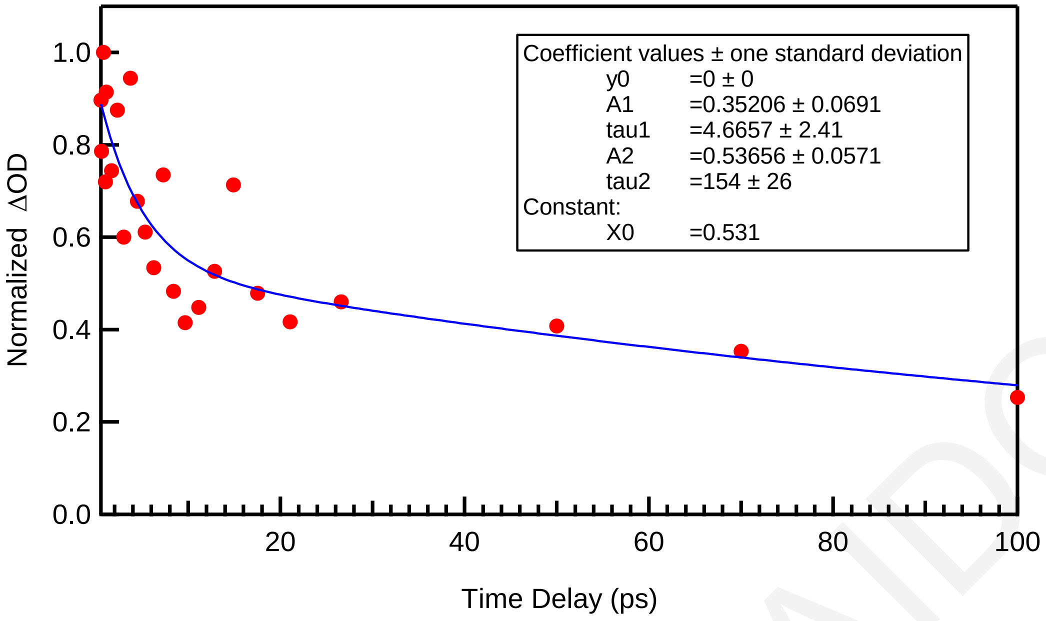

Figure S5.18. Kinetics of the 1569 cm^{-1} band of dC$_{20}$ after excitation at 266 nm fitted by a biexponential function.

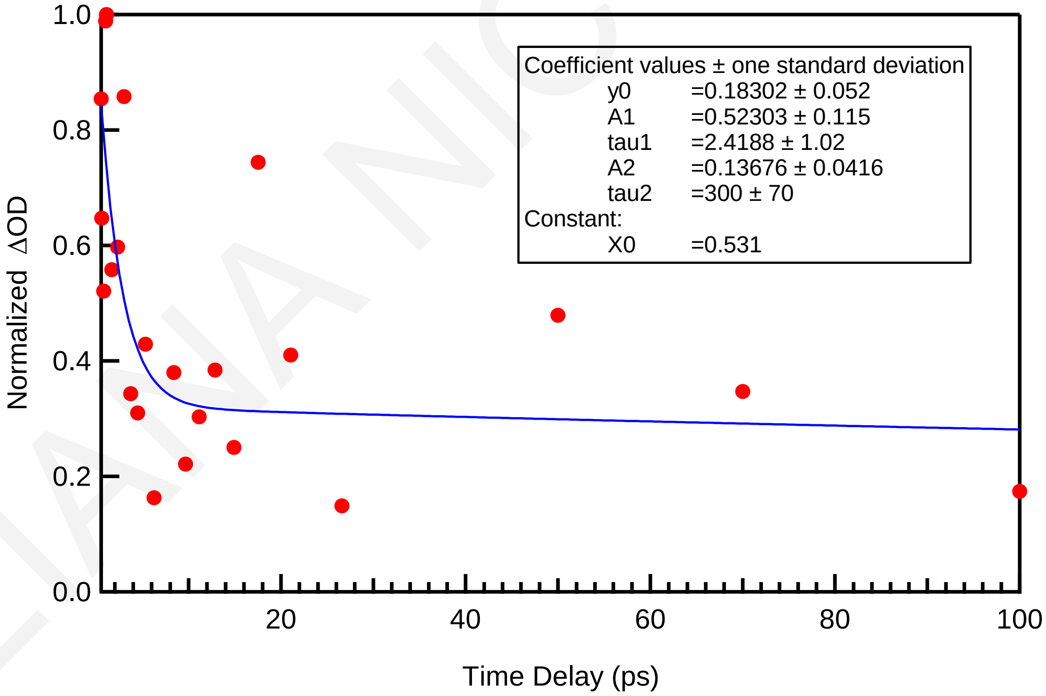

Figure S5.19. Kinetics of the 1542 cm^{-1} band of dC$_{20}$ after excitation at 266 nm fitted by a biexponential function.

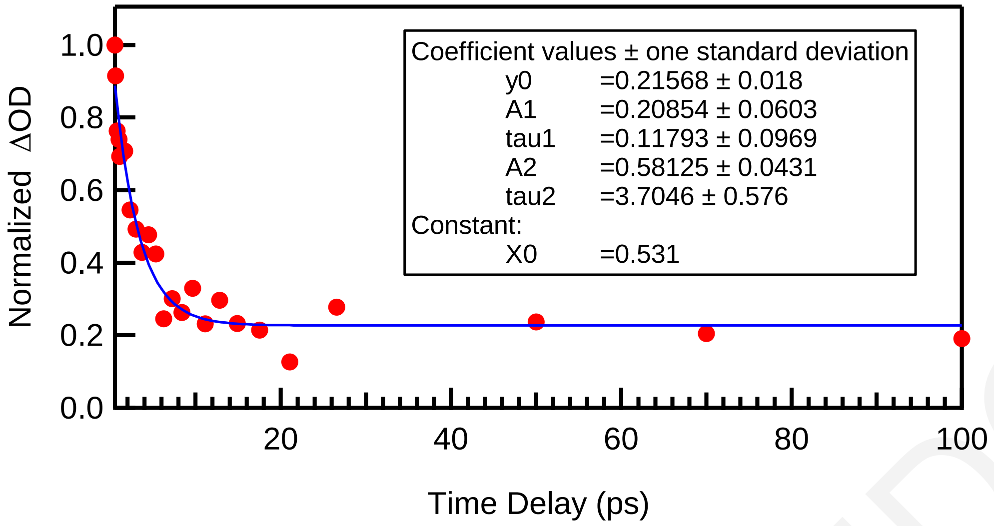

Figure S5.20. Kinetics of the 1577 cm^{-1} band of CPT/dC$_{20}$ after excitation at 266 nm fitted by a biexponential function.

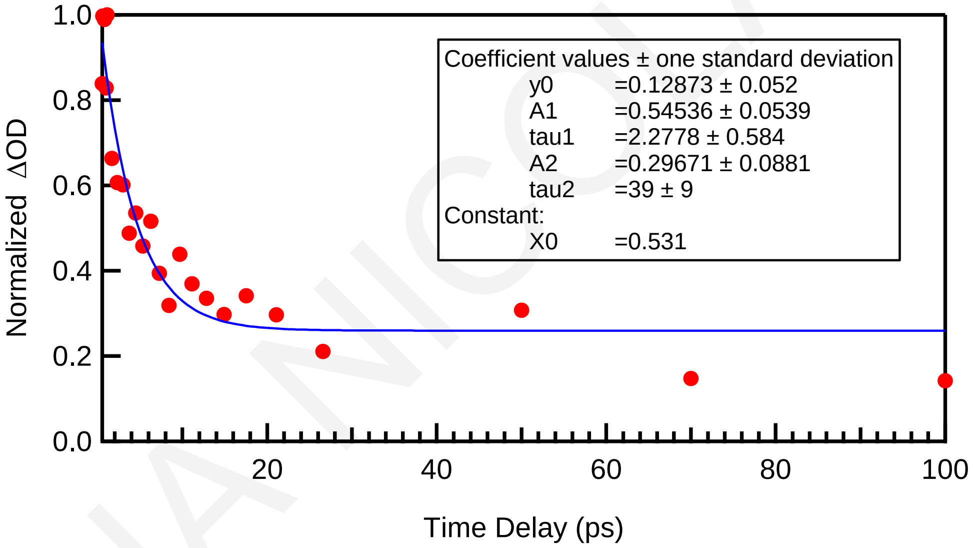

Figure S5.21. Kinetics of the 1544 cm^{-1} band of CPT/dC$_{20}$ after excitation at 266 nm fitted by a biexponential function.

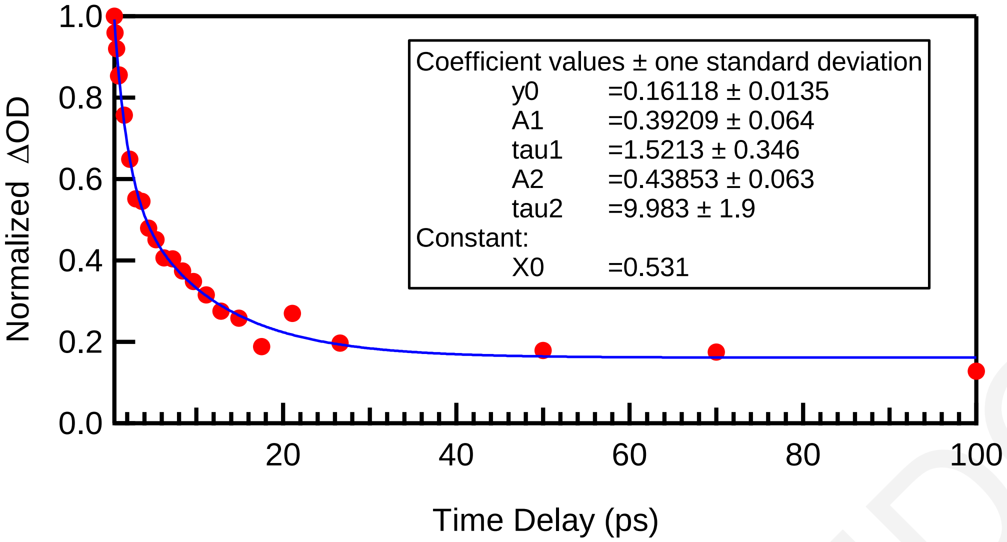

Figure S5.22. Kinetics of the 1498 cm^{-1} band of CPT/dC$_{20}$ after excitation at 266 nm fitted by a biexponential function.

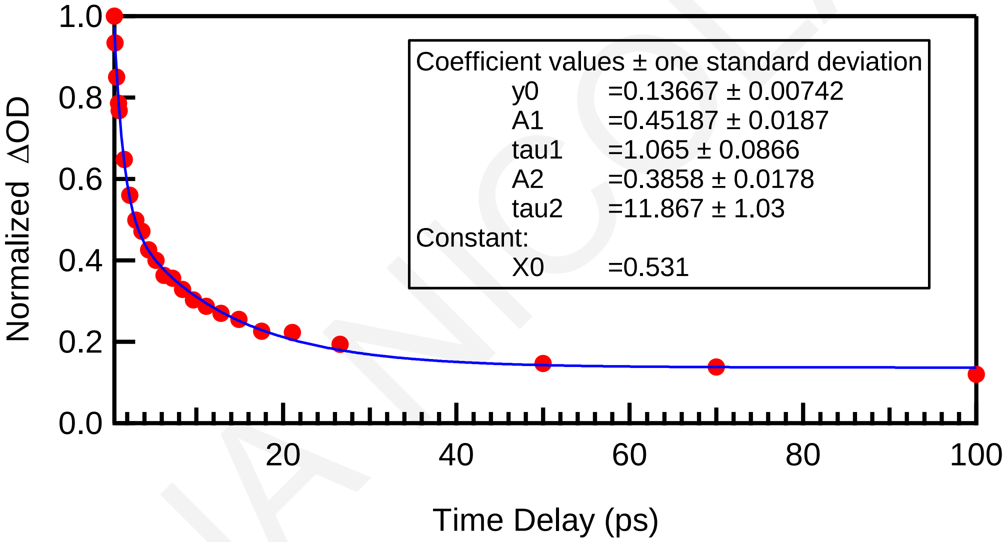

Figure S5.23. Kinetics of the background absorption of CPT/dC$_{20}$ after excitation at 266 nm fitted by a biexponential function.

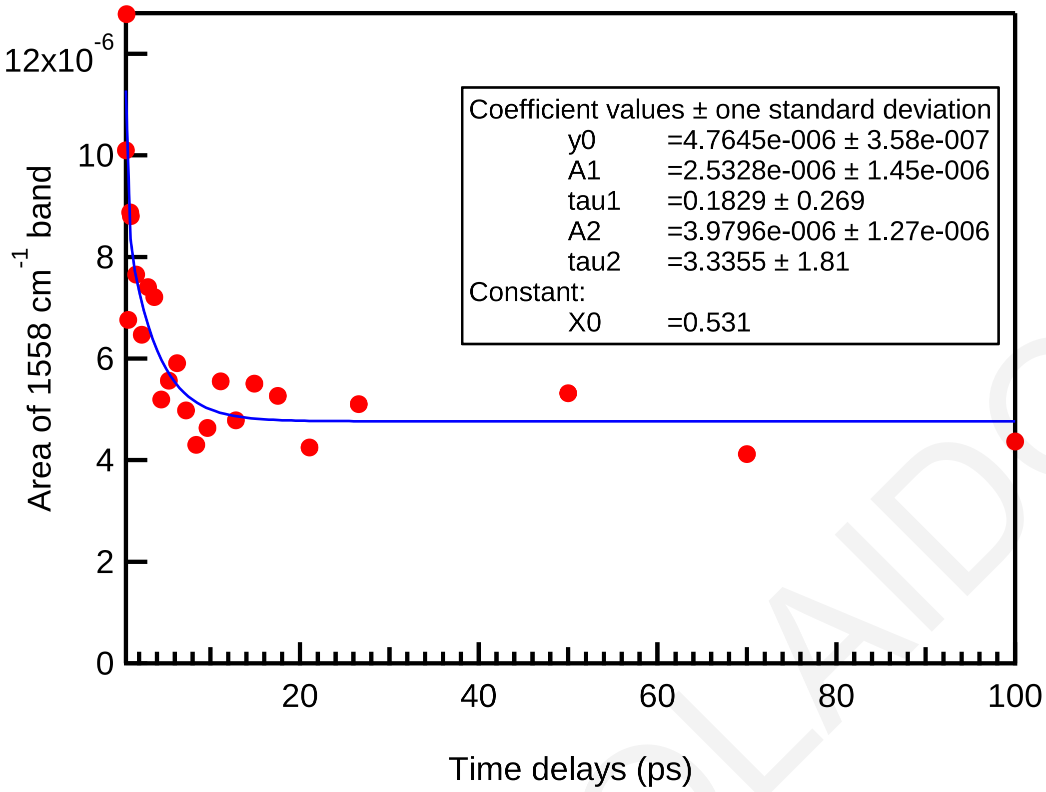

Figure S5.24. Kinetics of the 1558 cm^{-1} band area of CPT/dC$_{20}$ after excitation at 266 nm fitted by a biexponential function.

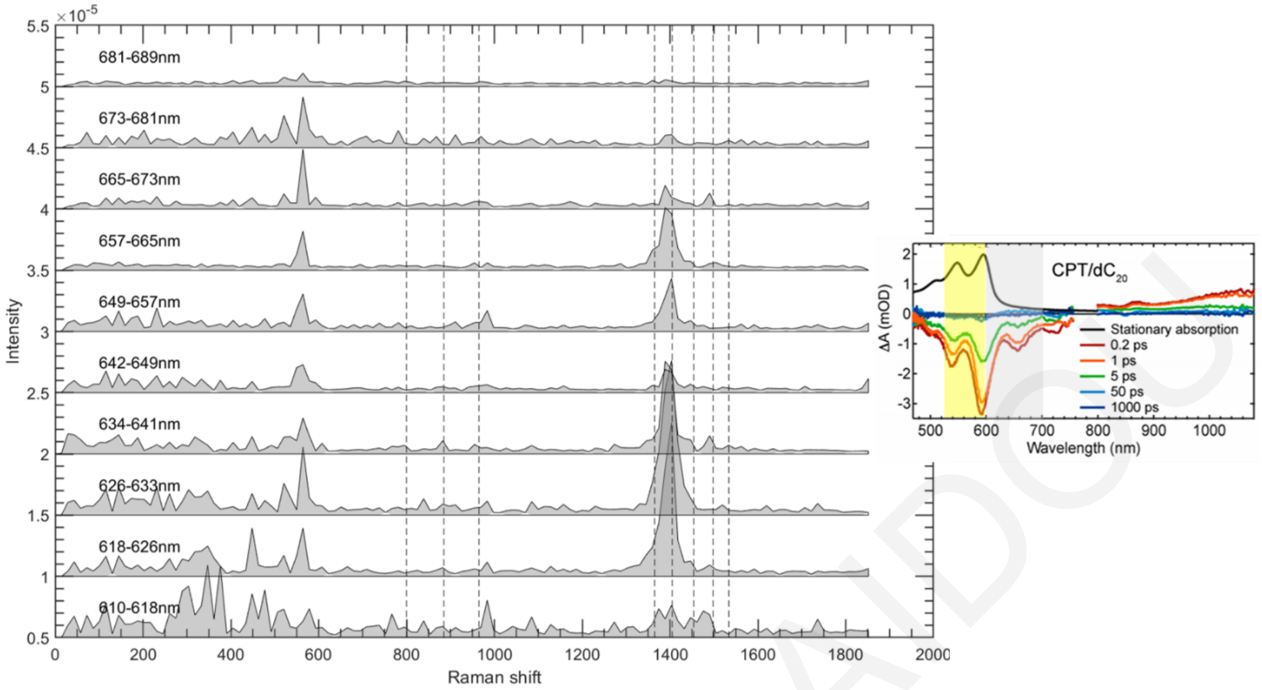

Figure S5.25. Comparison of ISRS spectra of CPT /dC$_{20}$ integrated over different probe wavelength regions (specified on the left of each spectrum) from 610 to 689 nm (stimulated emission), and coherent oscillations were Fourier transformed. The inset at the right side corresponds to TA spectra, recorded following excitation at 400 nm at selected time delays (adopted by Figure 5.1), where the yellow box marks the region of pump excitation wavelengths (on resonance with absorption: 500-600 nm) and the grey box marks the region of probe wavelengths (on resonance with SE: 600-700 nm).

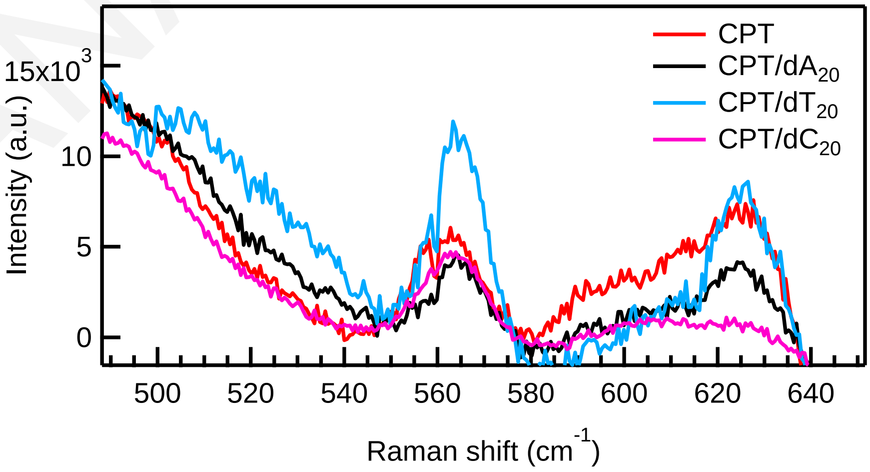

Figure S5.26. Ground state Resonance Raman (RR) spectra with visible excitation at 473 nm for CPT, CPT/dA$_{20}$, CPT/dT$_{20}$ and CPT/dC$_{20}$ in PBS buffer with a concentration of 1.5x10^{-4} M (monomeric basis) at 20 °C.

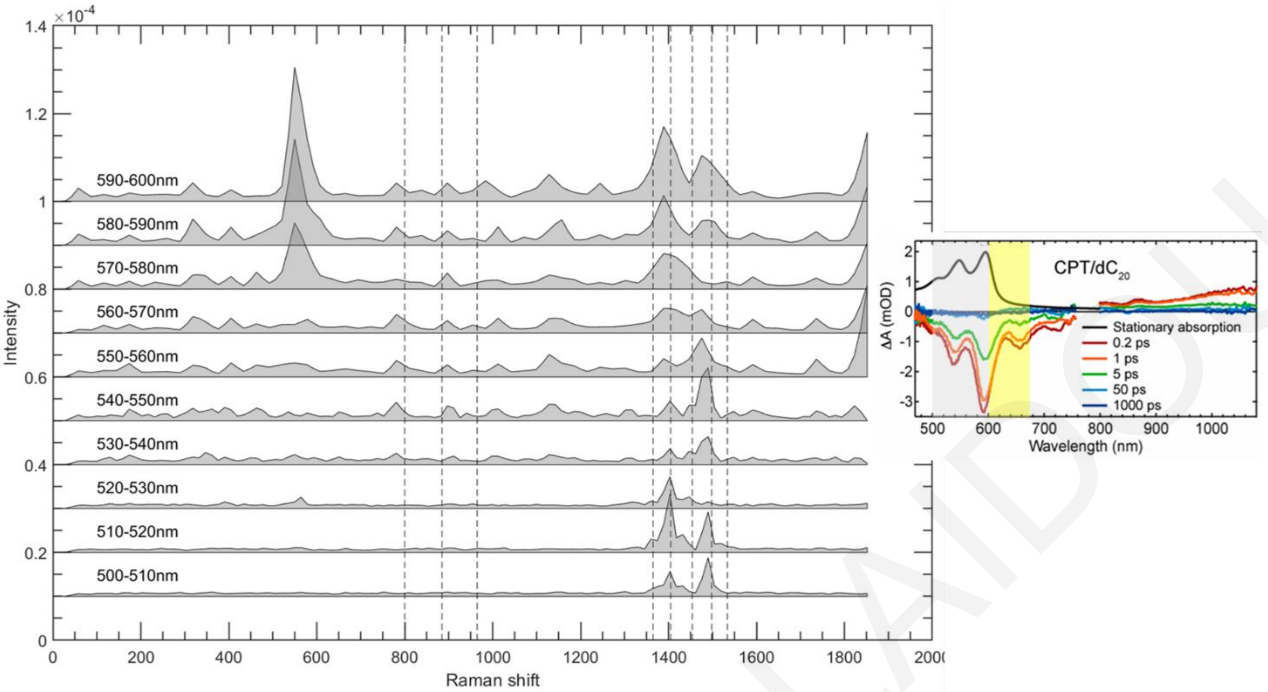

Figure S5.27. Comparison of ISRS spectra of CPT /dC$_{20}$ integrated over different probe wavelength regions (specified on the left of each spectrum) from 500 to 599 nm (absorption), and coherent oscillations were Fourier transformed. The inset at the right side corresponds to TA spectra, recorded following excitation at 400 nm at selected time delays (adopted by Figure 5.1), where the yellow box marks the region of pump excitation wavelengths (on resonance with SE: 600-700 nm) and the grey box marks the region of probe wavelengths (on resonance with absorption: 500-600 nm).

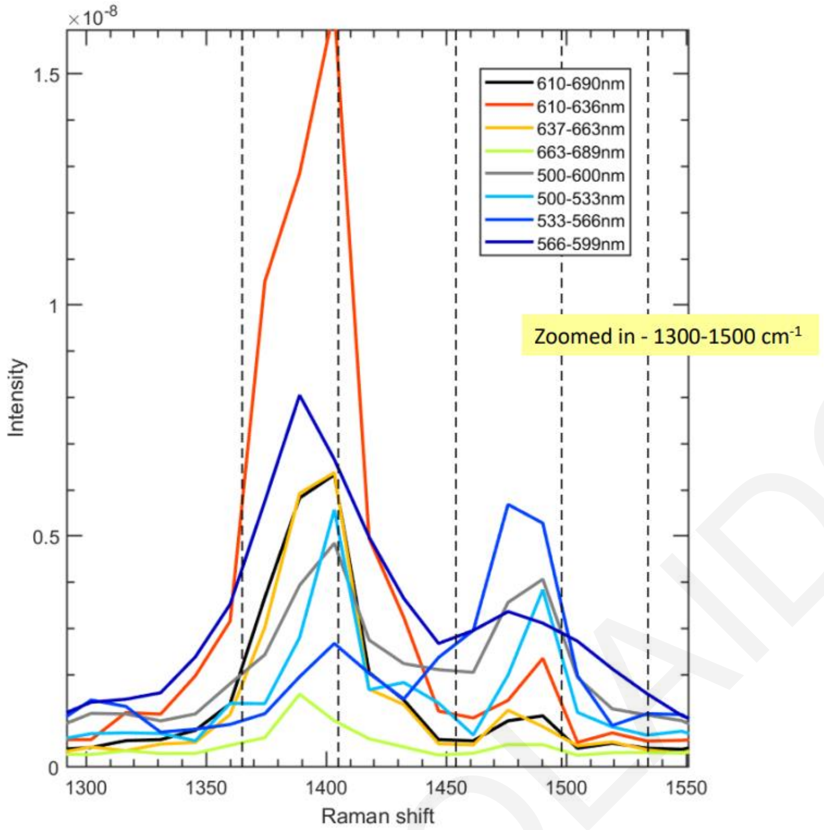

Figure S5.28. Comparison of ISRS spectra of CPT /dC_{20}, presented at Figure 5.x1 and 5.x3, which are the result of integration over different probe wavelength regions (specified on the legend) from 500 to 690 nm and coherent oscillations were Fourier transformed. The region of pump excitation wavelengths covers the range of 500-600 nm (on resonance with absorption), when probing at 600-700 nm and the range of 600-700 nm (on resonance with SE), when probing at 500-600 nm.

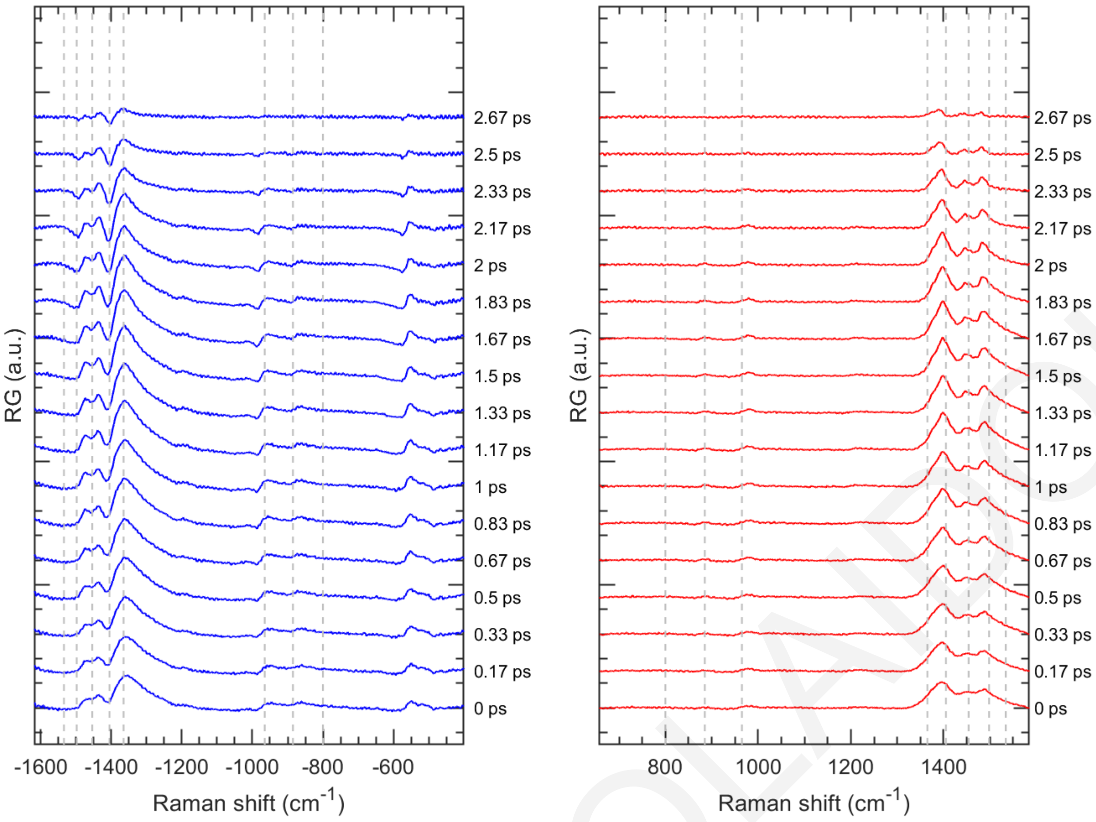

Figure S5.29. Time evolution of SRS spectrum of CPT /dC$_{20}$ using 599 nm as Raman pump wavelength, when probing at blue (center of spectral region: 566 nm, spectra at right) and red (center of spectral region: 643 nm, spectra at left) side of Raman pump wavelength.

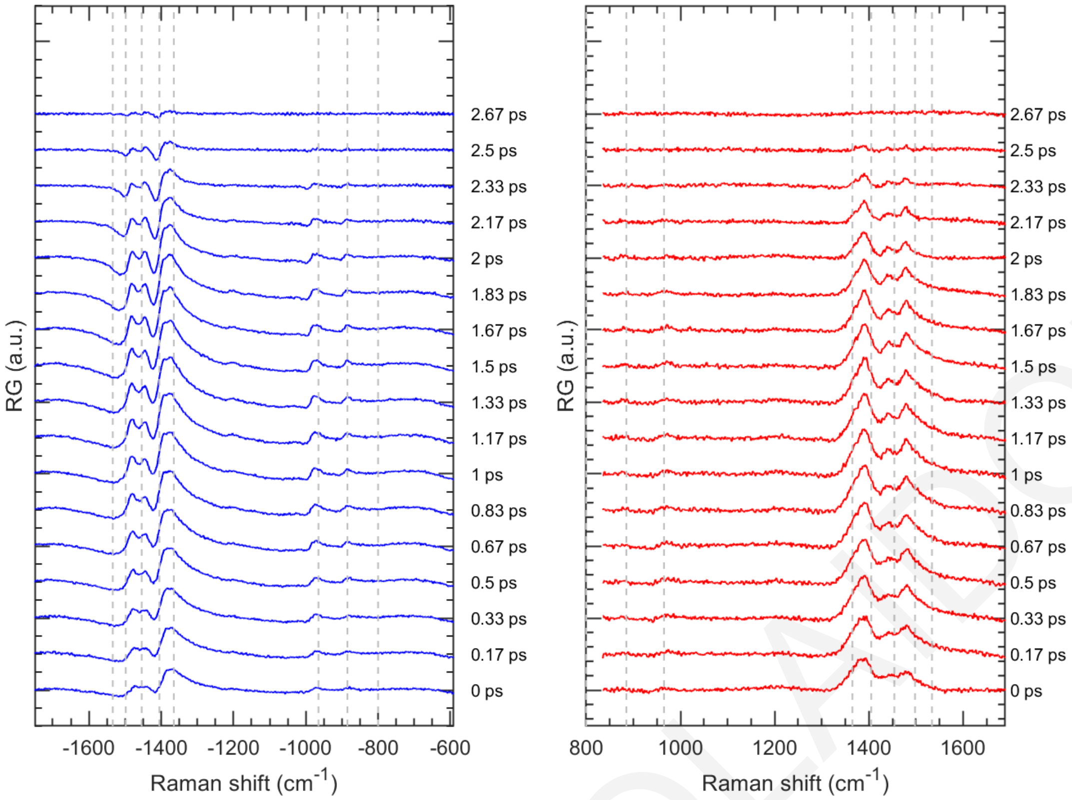

Figure S5.30. Time evolution of SRS spectrum of CPT /dC_{20} using 614 nm as Raman pump wavelength, when probing at blue (center of spectral region: 574 nm, spectra at right) and red (center of spectral region: 666 nm, spectra at left) side of Raman pump wavelength.

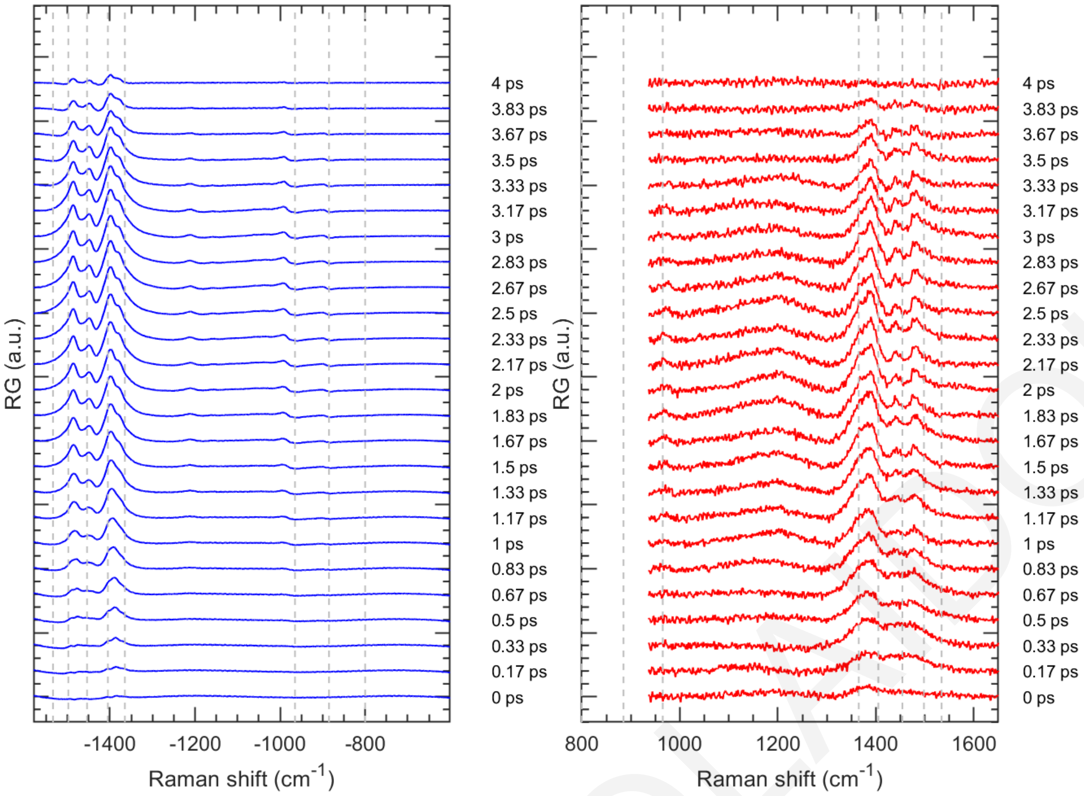

Figure S5.31. Time evolution of SRS spectrum of CPT /dC$_{20}$ using 644 nm as Raman pump wavelength, when probing at blue (center of spectral region: 604 nm, spectra at right) and red (center of spectral region: 704 nm, spectra at left) side of Raman pump wavelength.

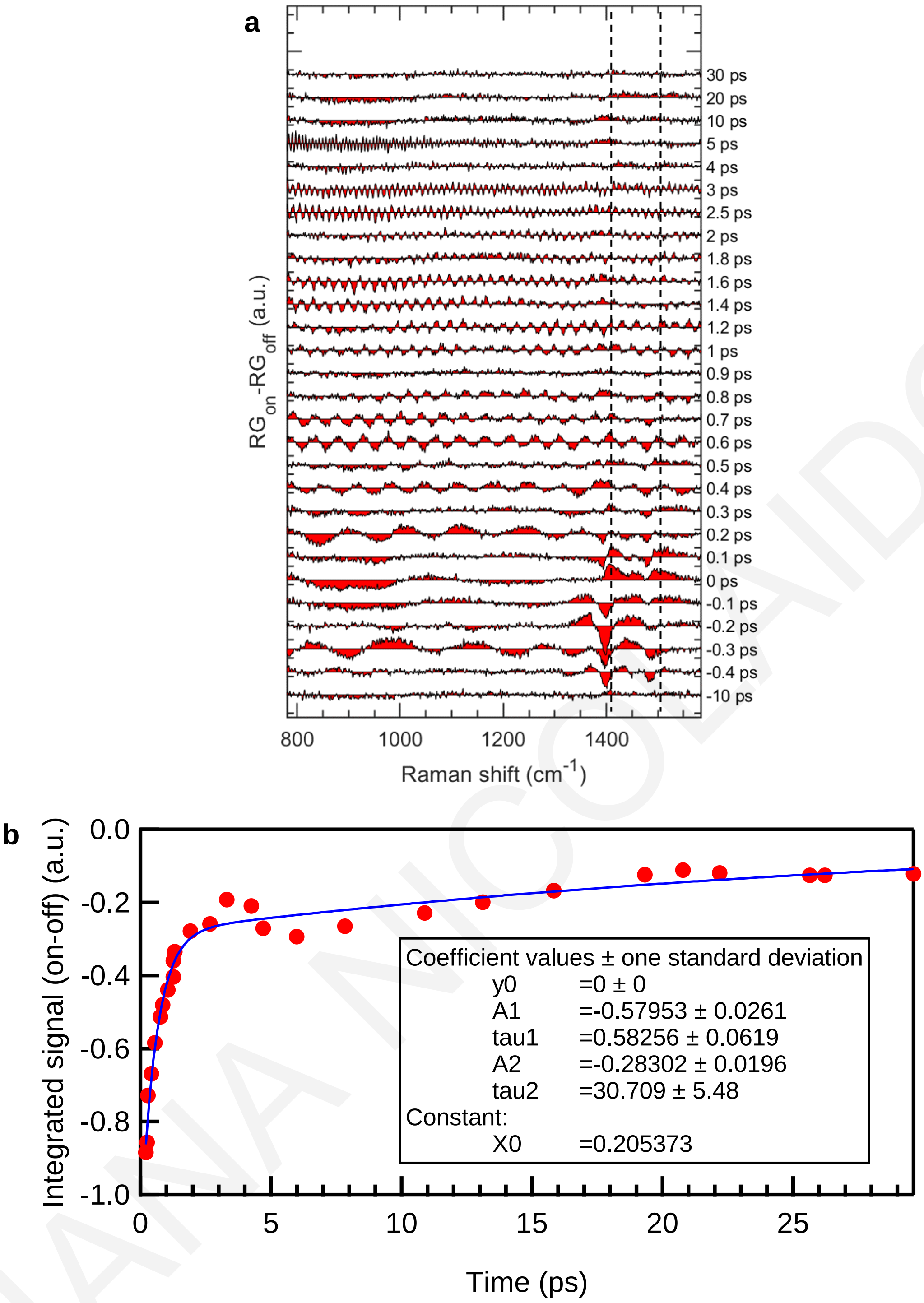

Figure S5.32. (a) Temporal evolution of difference of actinic pump on – pump off spectra of CPT /dC_{20} normalized by the actinic pump off intensity and (b) fitted kinetics by a biexponential function of integrated difference signal of the actinic pump on – pump off spectra of CPT /dC_{20} using 599 nm as Raman pump wavelength, when probing at red side of Raman pump wavelength (center of spectral region: 643 nm).

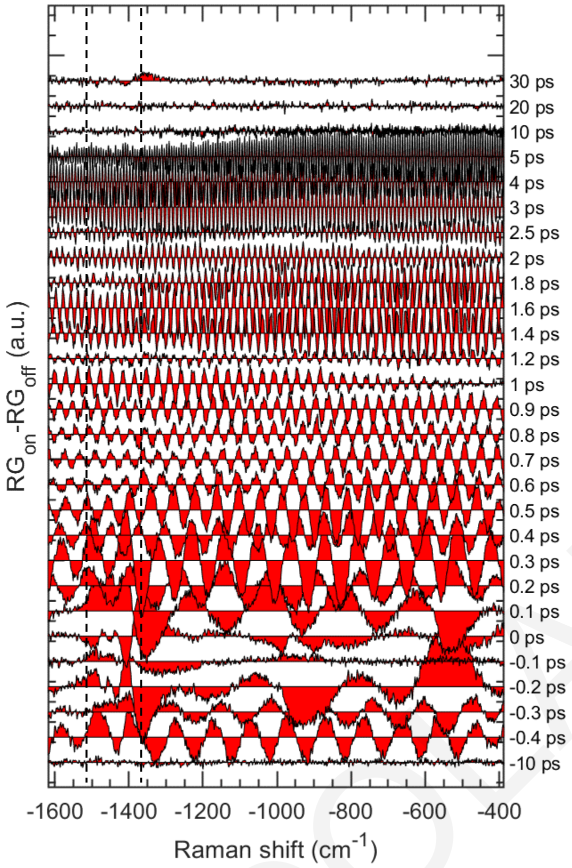

Figure S5.33. Temporal evolution of difference of actinic pump on – pump off spectra of CPT /dC$_{20}$ normalized by the actinic pump off intensity using 599 nm as Raman pump wavelength, when probing at blue side of Raman pump wavelength (center of spectral region: 566 nm).

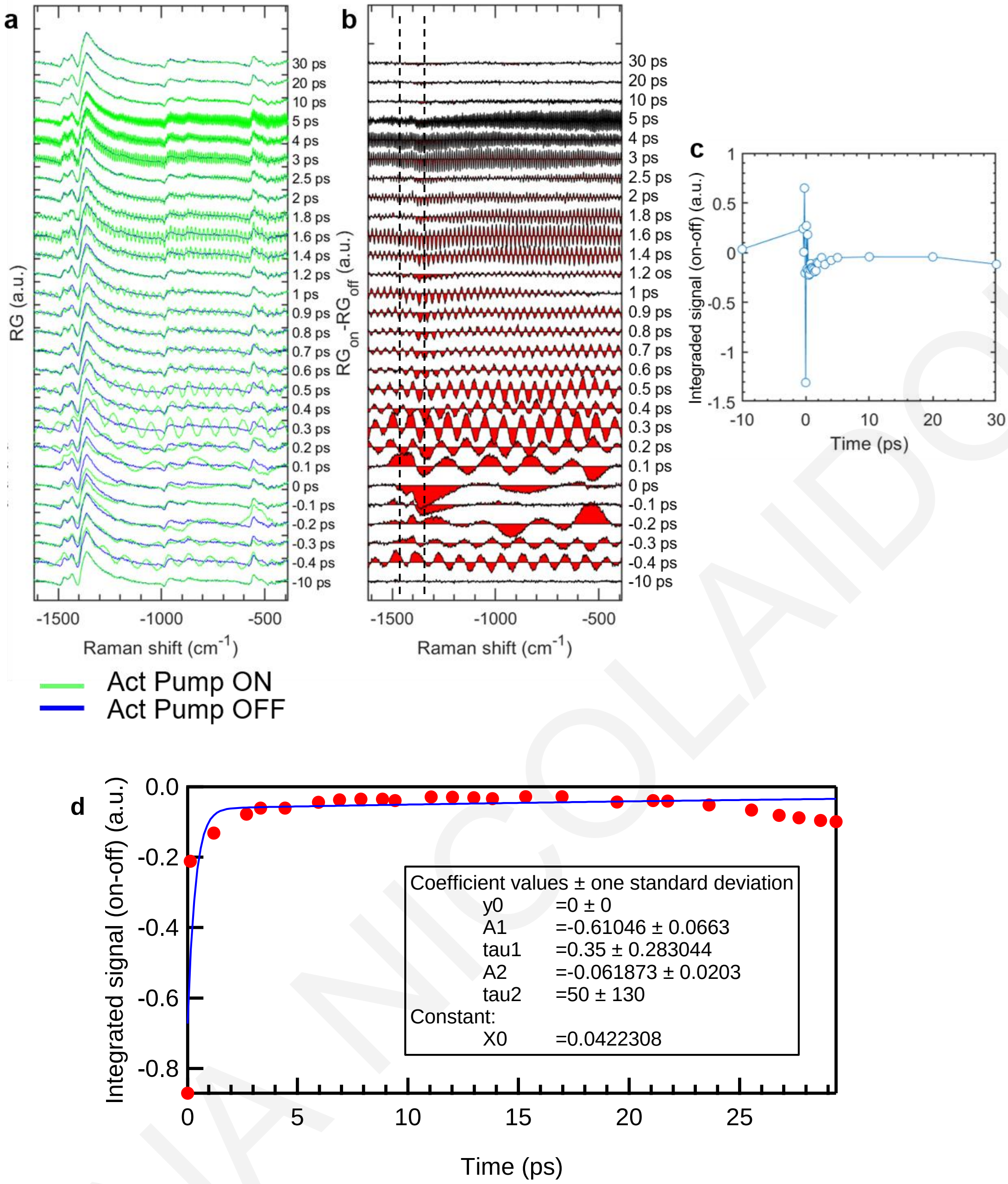

Figure S5.34. a) Temporal evolution of actinic pump on and pump off spectra (green and blue spectra respectively) of CPT /dC$_{20}$ using 599 nm as Raman pump wavelength, when probing at blue side of Raman pump wavelength (center of spectral region: 566 nm). b) Difference of actinic pump on – pump off spectra in panel a at different time delays. c) Kinetics of integrated difference signal of the actinic pump on – pump off spectra obtained by panel b fitted by a biexponential function at panel (d).

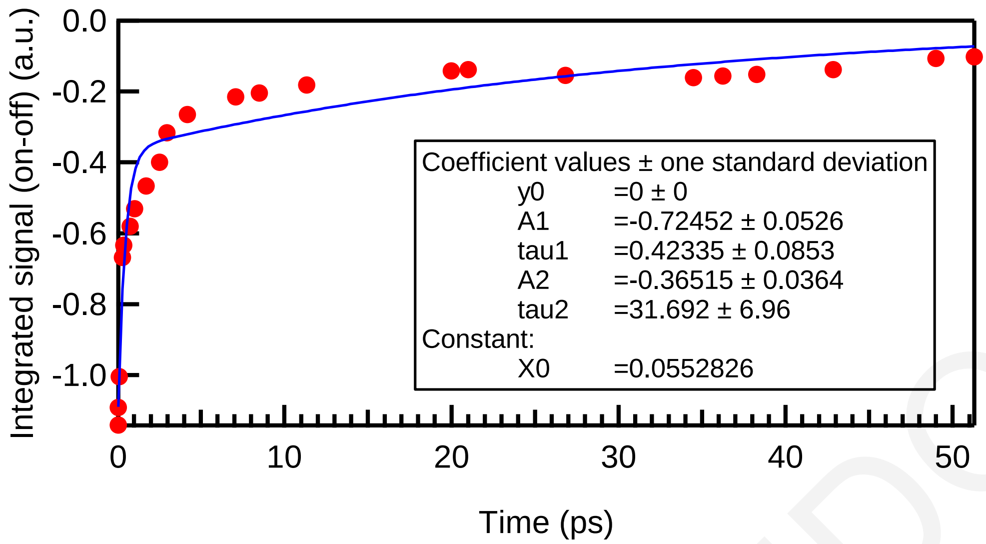

Figure S5.35. Fitted kinetics by a biexponential function of integrated difference signal of the actinic pump on – pump off spectra of CPT /dC$_{20}$ using 614 nm as Raman pump wavelength, when probing at red side of Raman pump wavelength (center of spectral region: 666 nm).

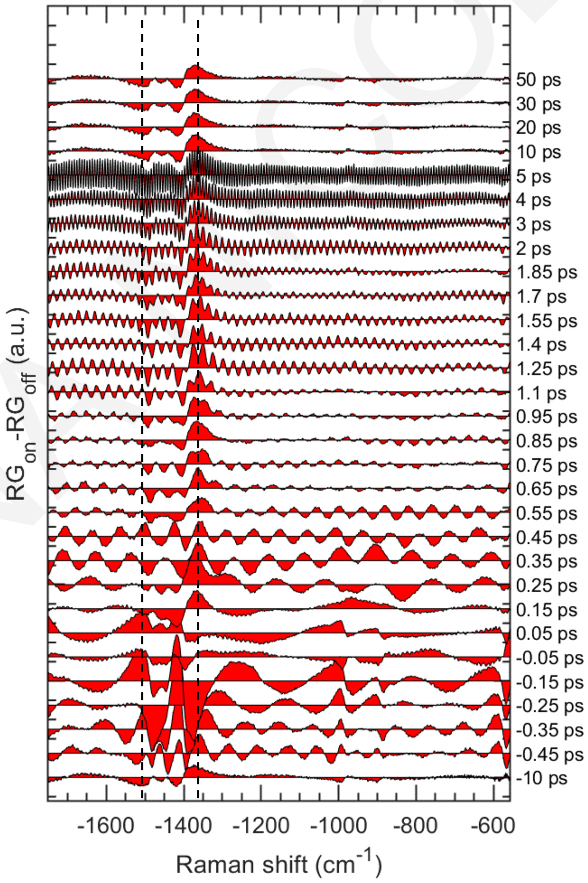

Figure S5.36. Temporal evolution of difference of actinic pump on – pump off spectra of CPT /dC$_{20}$ normalized by the actinic pump off intensity using 614 nm as Raman pump wavelength, when probing at blue side of Raman pump wavelength (center of spectral region: 574 nm).

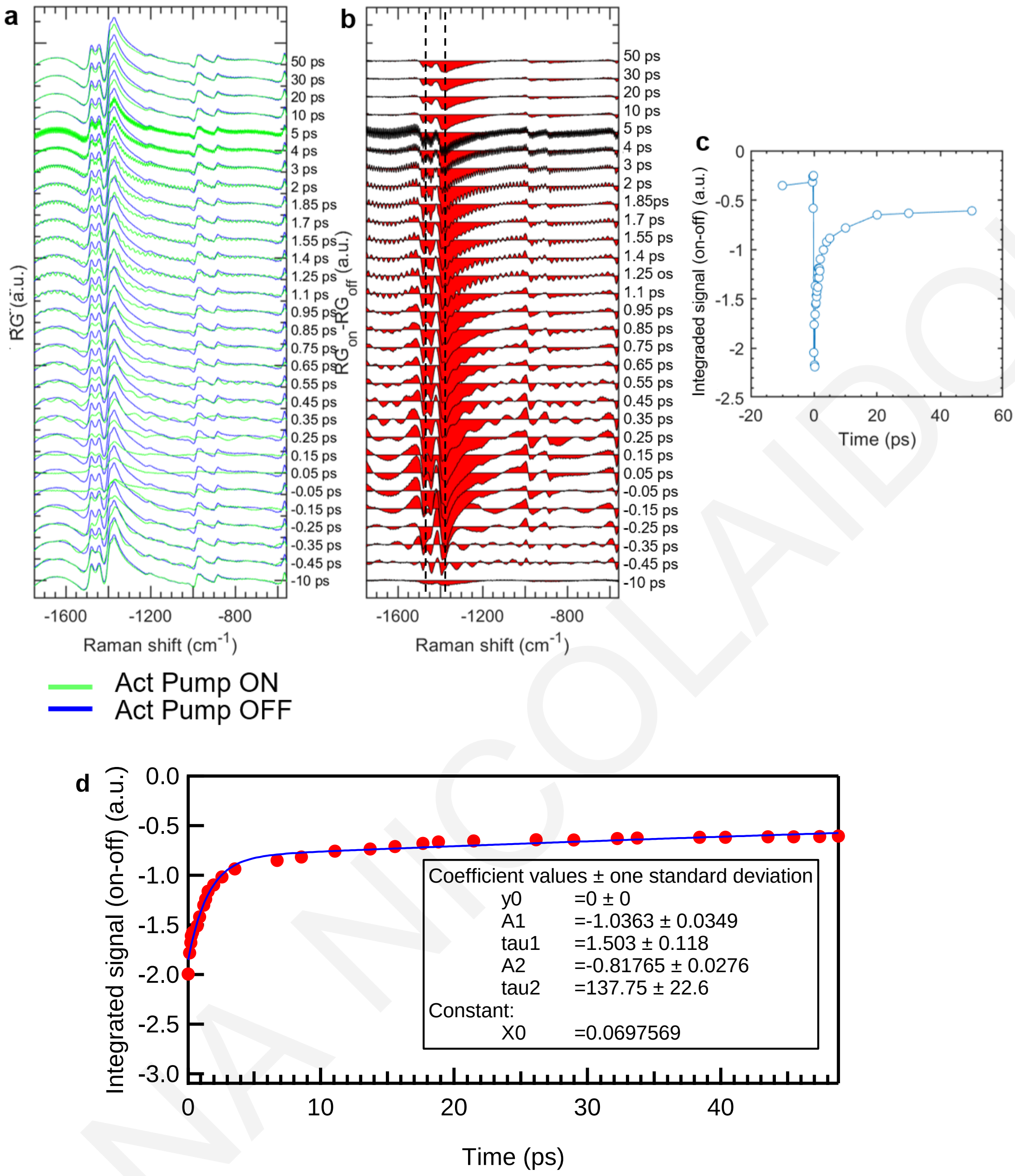

Figure S5.37. (a) Temporal evolution of actinic pump on and pump off spectra (green and blue spectra respectively) of CPT /dC$_{20}$ using 614 nm as Raman pump wavelength, when probing at blue side of Raman pump wavelength (center of spectral region: 574 nm). (b) Difference of actinic pump on – pump off spectra in panel a at different time delays. (c) Kinetics of integrated difference signal of the actinic pump on – pump off spectra obtained by panel b fitted by a biexponential function at panel (d).

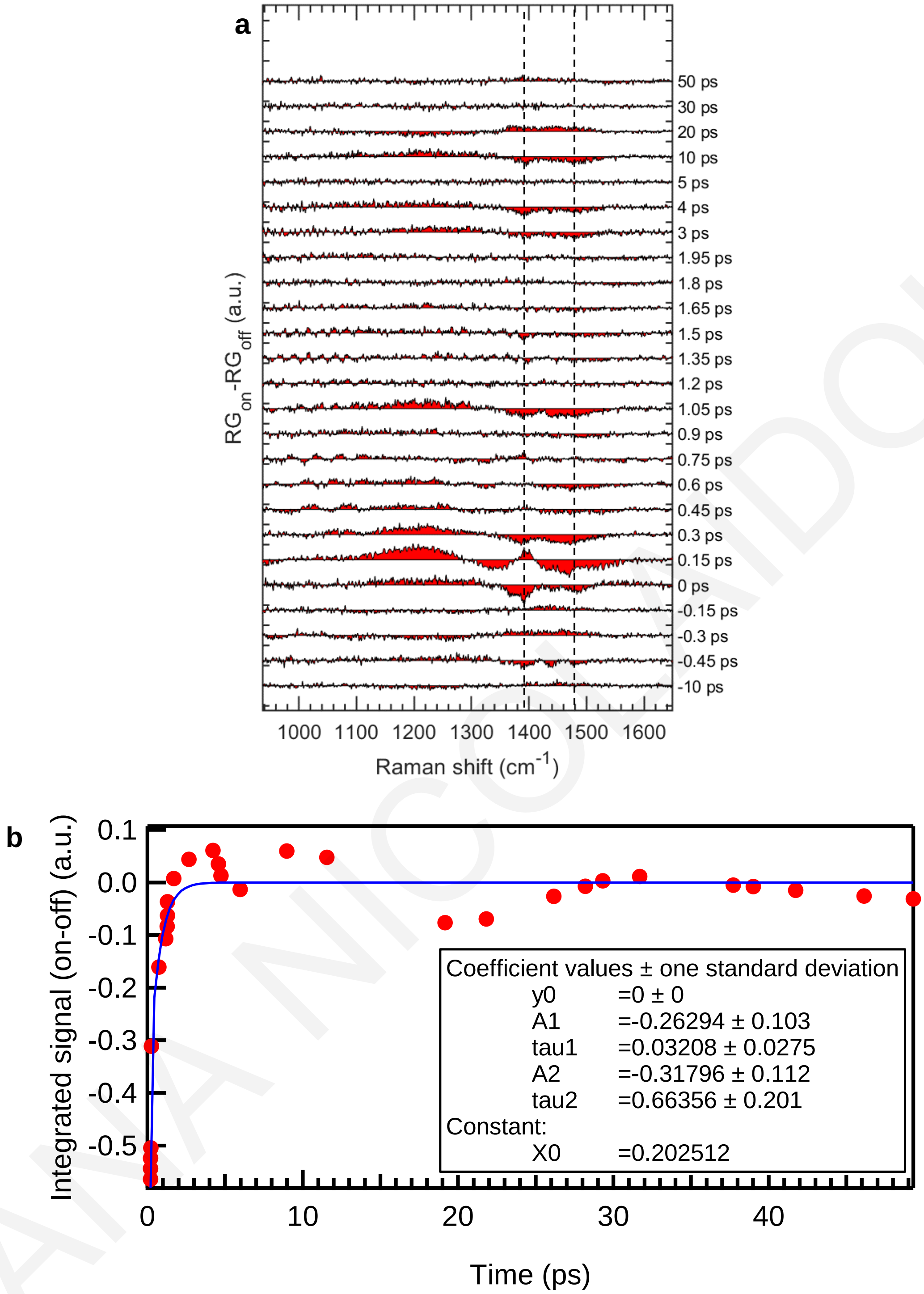

Figure S5.38. (a) Temporal evolution of difference of actinic pump on – pump off spectra of CPT /dC$_{20}$ normalized by the actinic pump off intensity and (b) fitted kinetics by a biexponential function of integrated difference signal of the actinic pump on – pump off spectra of CPT /dC$_{20}$ using 644 nm as Raman pump wavelength, when probing at red side of Raman pump wavelength (center of spectral region: 704 nm).

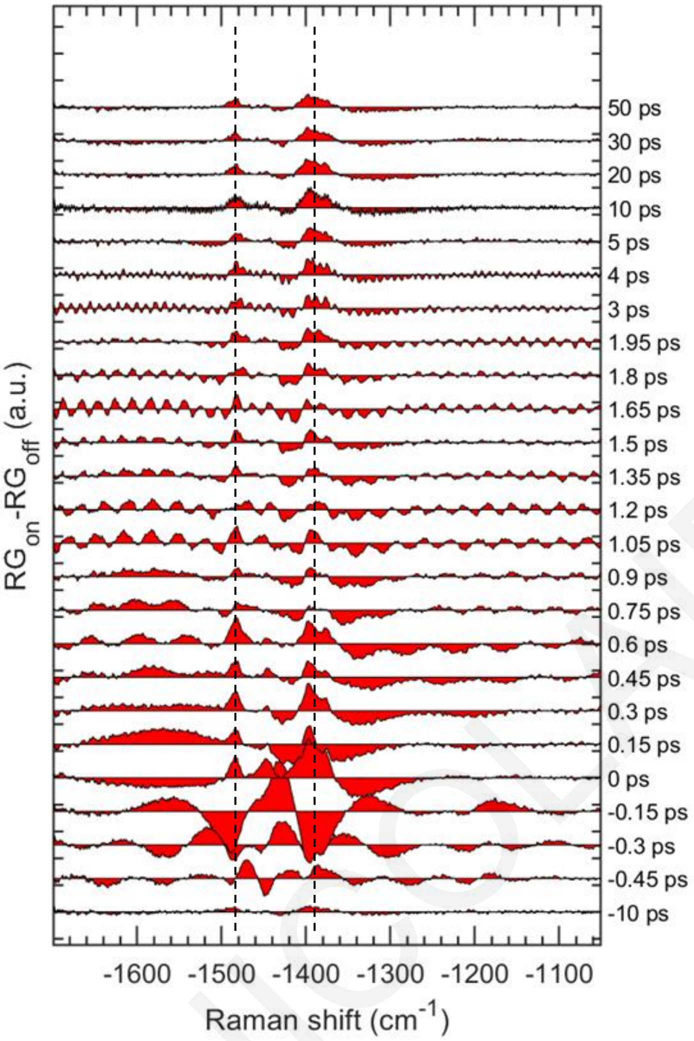

Figure S5.39. Temporal evolution of difference of actinic pump on – pump off spectra of CPT /dC_{20} normalized by the actinic pump off intensity using 644 nm as Raman pump wavelength, when probing at blue side of Raman pump wavelength (center of spectral region: 604 nm).

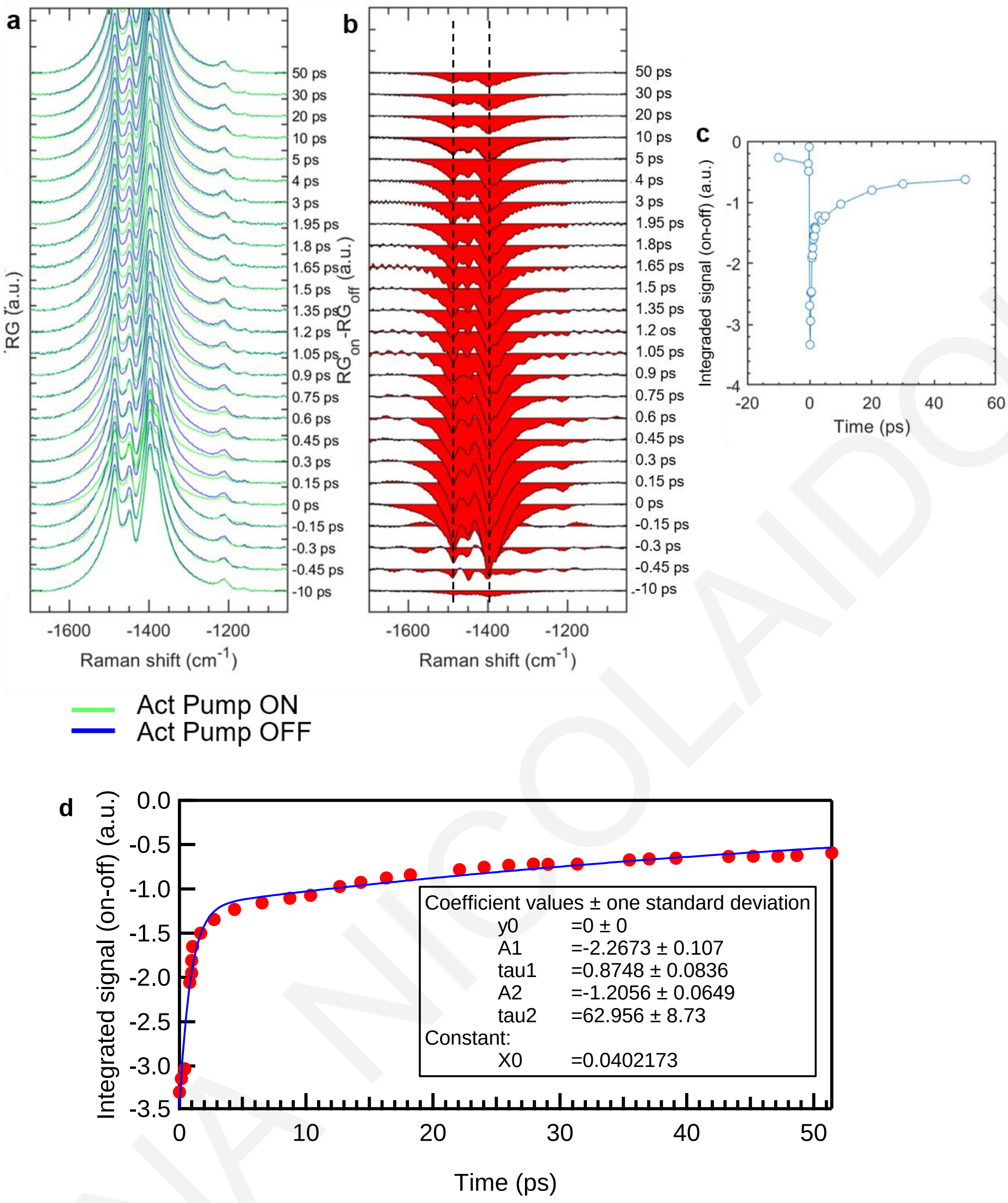

Figure S5.40. (a) Temporal evolution of actinic pump on and pump off spectra (green and blue spectra respectively) of CPT /dC$_{20}$ using 644 nm as Raman pump wavelength, when probing at blue side of Raman pump wavelength (center of spectral region: 604 nm). (b) Difference of actinic pump on – pump off spectra in panel a at different time delays. (c) Kinetics of integrated difference signal of the actinic pump on – pump off spectra obtained by panel b fitted by a biexponential function at panel (d).

SUPPLEMENTARY DATA FOR CHAPTER 6

Table S6.1. Parameters used for the deconvolution of the Raman spectrum with excitation at 532 nm of P1.

Frequency (cm^{-1})	**Width Gaussian**	**Width Lorentzian**	**Area**
1235	4	42	7499
1258	3×10^{-5}	22	24837
1321	1×10^{-6}	47	8793
1366	4×10^{-2}	37	43532
1403	34	3×10^{-2}	33852
1436	36	8×10^{-2}	111758
1456	16	11	19802
1495	51	3×10^{-20}	40586
1535	27	1×10^{-44}	6740
1565	50	2×10^{-19}	27164

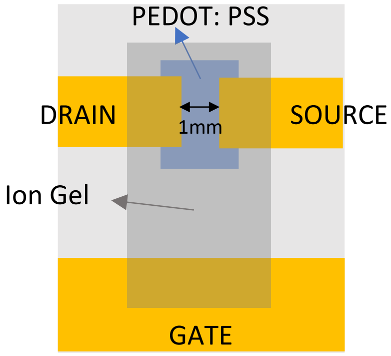

Figure S6.1. Schematic illustration of a top contact side-gate geometry for electrolyte-gating with an ion gel on a spin-coated film of PEDOT:PSS (top view).

SUPPLEMENTARY DATA FOR CHAPTER 7

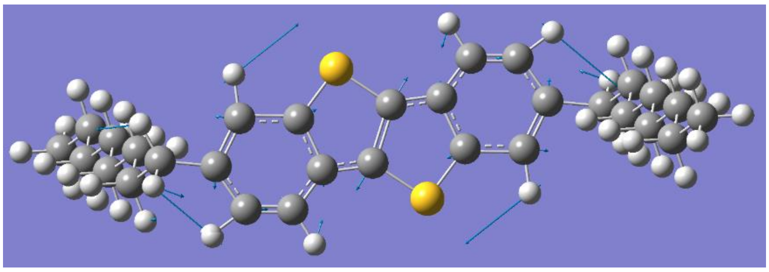

Figure S7.1. Depiction of vibrational mode at 1390 cm^{-1} (The blue arrows represent the direction of the molecular vibration).

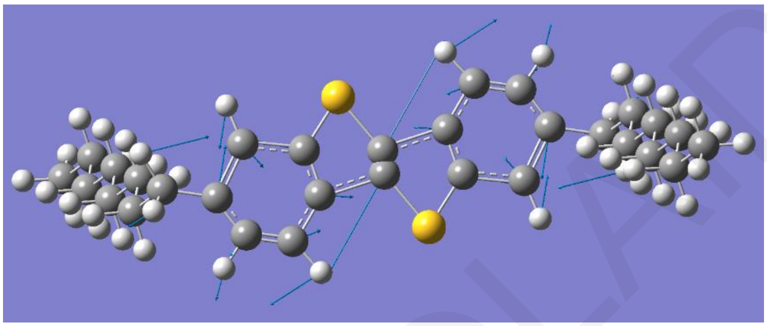

Figure S7.2. Depiction of vibrational mode at 1477 cm^{-1} (The blue arrows represent the direction of the molecular vibration).

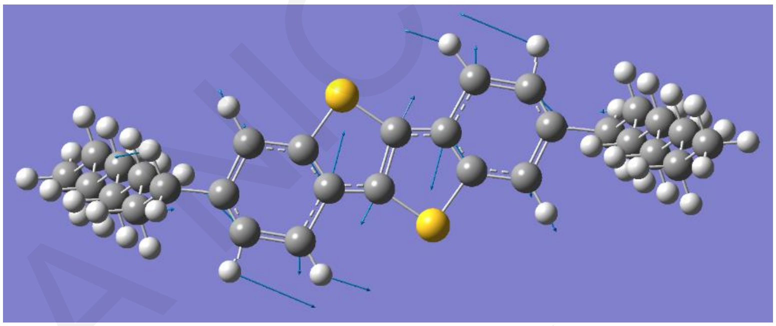

Figure S7.3. Depiction of vibrational mode at 1556 cm^{-1} (The blue arrows represent the direction of the molecular vibration).

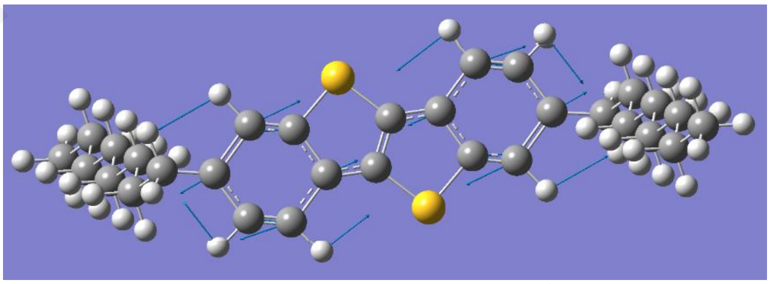

Figure S7.4. Depiction of vibrational mode at 1606 cm^{-1} (The blue arrows represent the direction of the molecular vibration).

Table S7.1. Parameters used in the RRIA for C8-BTBT.

Transition	**ω_g(cm^{-1})**	**ω_e(cm^{-1})**	**Δ_k**
C8-BTBT 1st state			
ν_1	395	645	0.52
ν_2	440	600	0.47
ν_3	498	698	0.54
ν_4	704	954	0.50
ν_5	998	998	0.67
ν_6	1054	1054	0.62
ν_7	1125	1125	0.32
ν_8	1138	1138	0.22
ν_9	1307	1307	0.66
ν_{10}	1396	1396	0.34
ν_{11}	1477	1477	0.26
ν_{12}	1489	1489	0.49
ν_{13}	1557	1557	0.30
ν_{14}	1603	1603	0.50
Γ (cm^{-1})	150		
Θ (cm^{-1})	170		
E_{00} (cm^{-1})	29870		
M (Å)	1.51		
C8-BTBT 2nd state			
ν_1	395	645	0.57
ν_2	440	600	0.45
ν_3	498	798	0.76
ν_4	704	954	0.45
ν_5	998	998	0.38
ν_6	1054	1054	0.10
ν_7	1125	1125	0.11
ν_8	1138	1138	0.10
ν_9	1307	1307	0.10
ν_{10}	1396	1396	0.15
ν_{11}	1477	1477	0.15
ν_{12}	1489	1489	0.47
ν_{13}	1557	1557	0.42
ν_{14}	1603	1603	0.55
Γ (cm^{-1})	150		
Θ (cm^{-1})	170		
E_{00} (cm^{-1})	31750		
	0.96		

M (Å)	

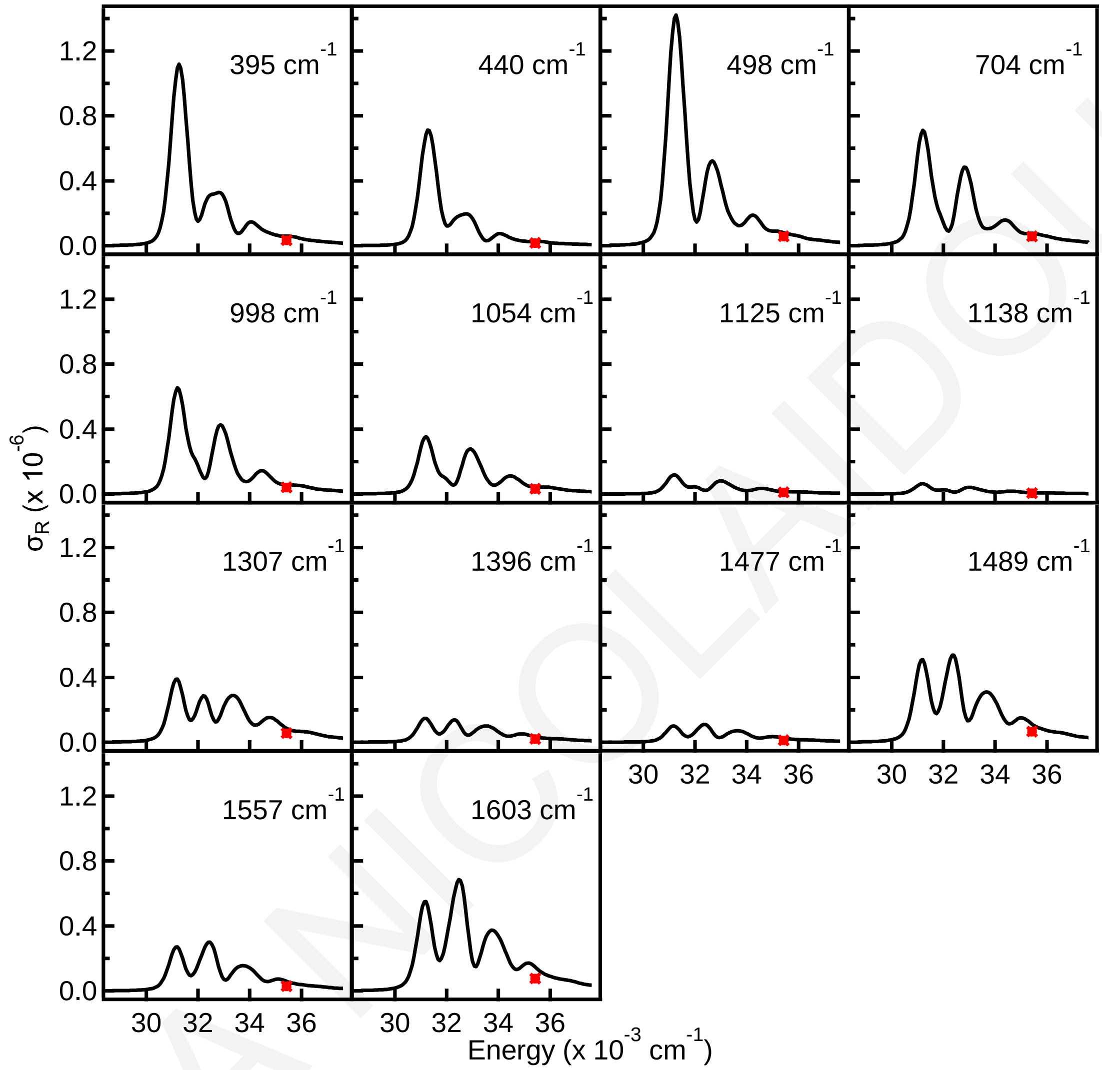

Figure S7.5. Calculated Raman excitation profiles (REPs) for the most prominent vibrational modes of C8-BTBT complex. The red points denote the experimentally calculated absolute RR cross sections at 282 nm.

Table S7.2. Parameters used in the RRIA for BTBT.

Transition	$\omega_g(cm^{-1})$	$\omega_e(cm^{-1})$	Δ_k
BTBT 1st state			
ν_1	395	595	0.37
ν_2	438	638	0.40
ν_3	498	698	0.47
ν_4	710	810	0.36
ν_5	998	1198	0.50
ν_6	1054	1254	0.38
ν_7	1130	1330	0.32
ν_8	1179	1179	0.35
ν_9	1306	1306	0.42
ν_{10}	1334	1534	0.32
ν_{11}	1415	1415	0.48
ν_{12}	1495	1695	0.50
ν_{13}	1559	1559	0.36
ν_{14}	1598	1598	0.56
Γ (cm^{-1})	90		
Θ (cm^{-1})	280		
E_{00} (cm^{-1})	29350		
M (Å)	1.035		
BTBT 2nd state			
ν_1	395	595	0.47
ν_2	438	638	0.51
ν_3	498	698	0.64
ν_4	710	810	0.57
ν_5	998	998	0.47
ν_6	1054	1254	0.30
ν_7	1130	1330	0.28
ν_8	1179	1179	0.20
ν_9	1306	1306	0.27
ν_{10}	1334	1534	0.38
ν_{11}	1415	1515	0.43
ν_{12}	1495	1695	0.47
ν_{13}	1559	1659	0.20
ν_{14}	1598	1698	0.50
Γ (cm^{-1})	145		
Θ (cm^{-1})	280		
E_{00} (cm^{-1})	31650		
	1.325		

M (Å)	

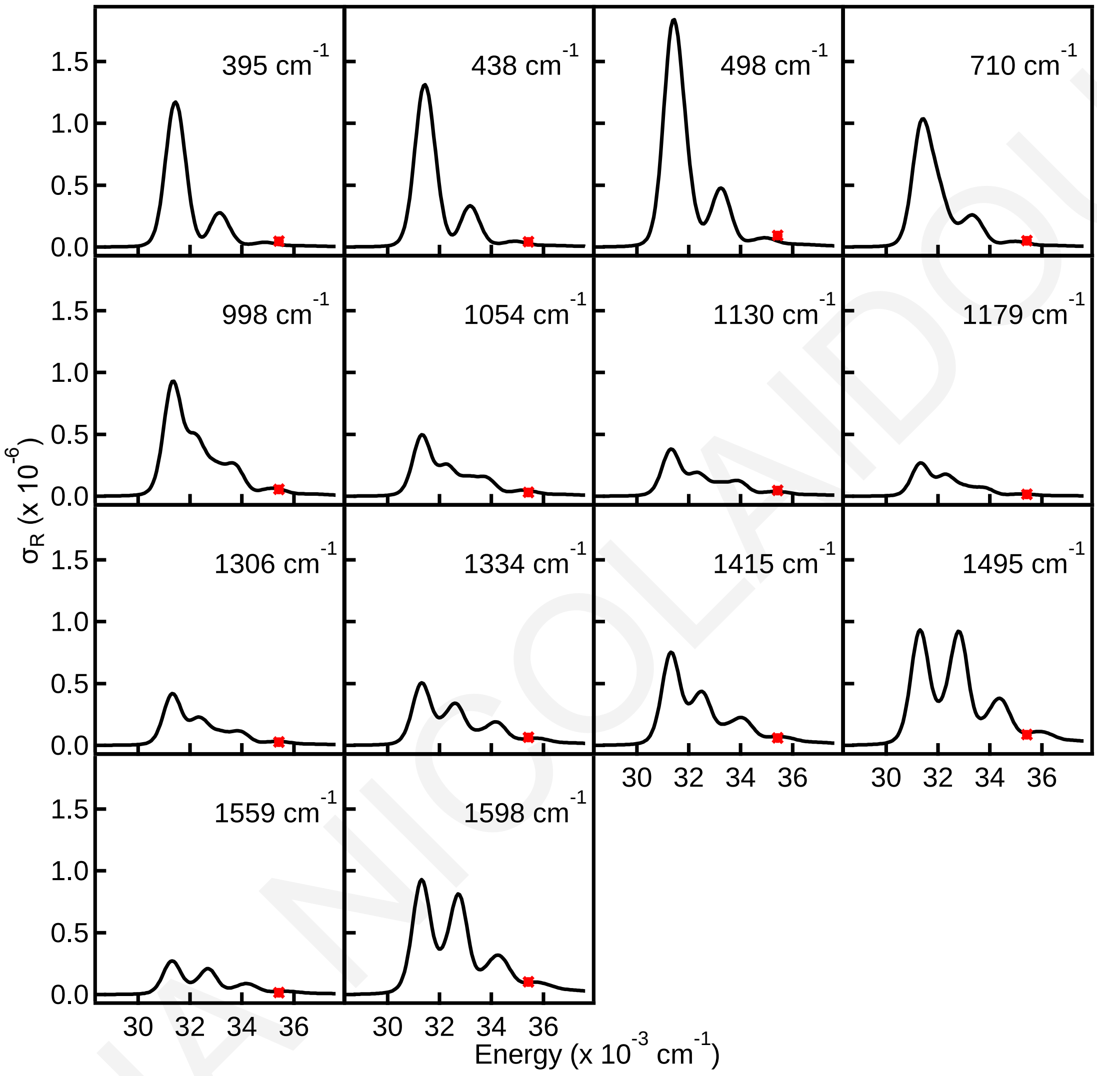

Figure S7.6. Calculated Raman excitation profiles (REPs) for the most prominent vibrational modes of BTBT complex. The red points denote the experimentally calculated absolute RR cross sections at 282 nm.

Table S7.3. Parameters used in the RRIA for diBT.

Transition	**ω_g(cm^{-1})**	**ω_e(cm^{-1})**	**Δ_k**
diBT 1st state			
ν_1	399	399	0.50
ν_2	497	797	0.68
ν_3	705	905	0.60
ν_4	1002	1302	0.68
ν_5	1050	1350	0.50
ν_6	1125	1625	0.60
ν_7	1141	1341	0.45
ν_8	1180	1380	0.35
ν_9	1310	1310	0.45
ν_{10}	1367	1367	0.23
ν_{11}	1485	1485	0.35
ν_{12}	1550	1750	0.43
ν_{13}	1574	1574	0.45
ν_{14}	1604	1604	0.33
Γ (cm^{-1})	60		
Θ (cm^{-1})	240		
E_{00} (cm^{-1})	27260		
M (Å)	1.48		
diBT 2nd state			
ν_1	399	399	0.35
ν_2	497	697	0.73
ν_3	705	705	0.48
ν_4	1002	1502	0.73
ν_5	1050	1250	0.57
ν_6	1125	1125	0.40
ν_7	1141	1141	0.30
ν_8	1180	1180	0.57
ν_9	1310	1310	0.57
ν_{10}	1367	1367	0.38
ν_{11}	1485	1485	0.20
ν_{12}	1550	1750	0.53
ν_{13}	1574	1754	0.75
ν_{14}	1604	1604	0.64
Γ (cm^{-1})	100		
Θ (cm^{-1})	240		
E_{00} (cm^{-1})	28270		
	1.52		

M (Å)	

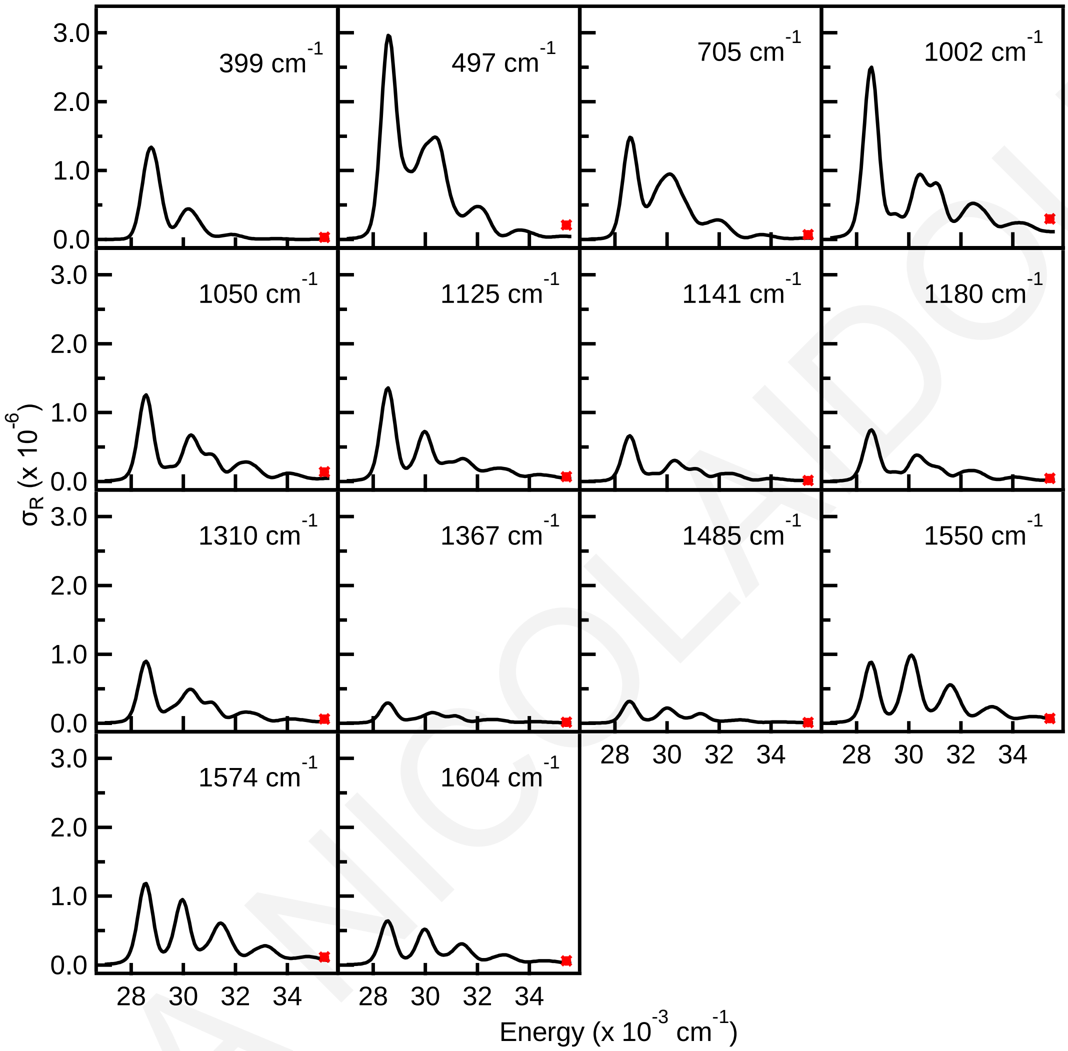

Figure S7.7. Calculated Raman excitation profiles (REPs) for the most prominent vibrational modes of diBT complex. The red points denote the experimentally calculated absolute RR cross sections at 282 nm.

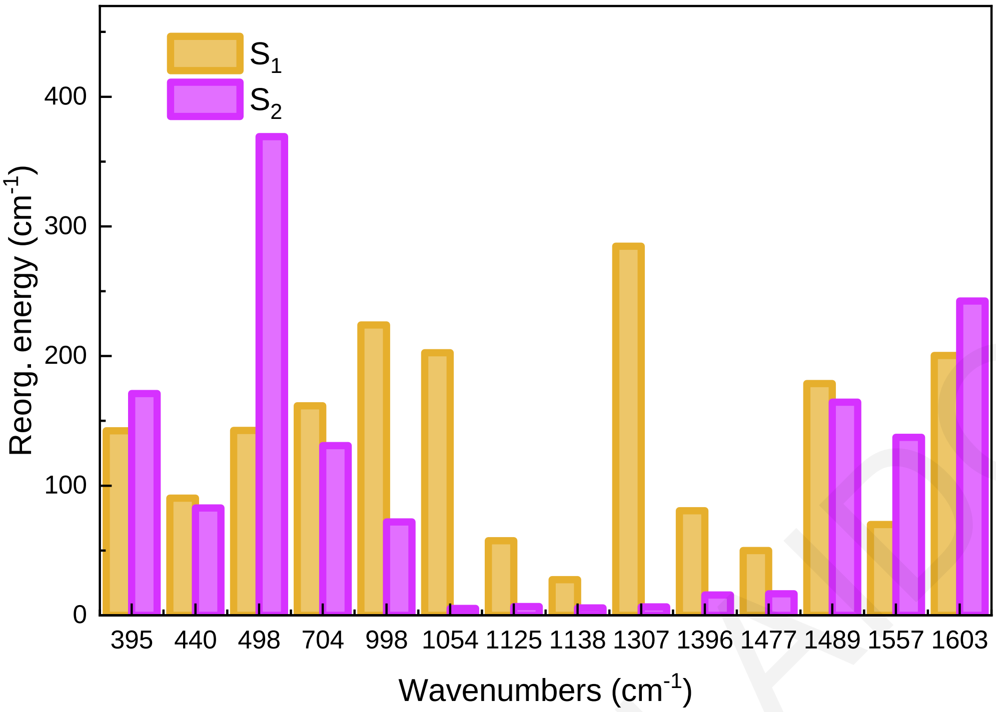

Figure S7.8. Mode-specific reorganization energy for the most prominent vibrational modes of C8-BTBT.

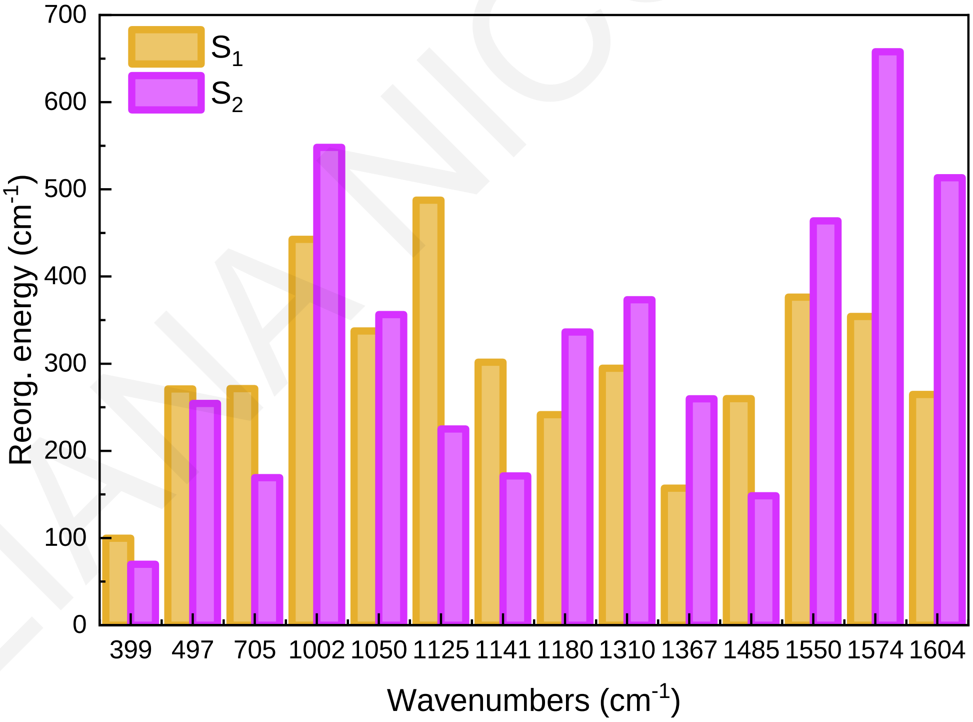

Figure S7.9. Mode-specific reorganization energy for the most prominent vibrational modes of BTBT.

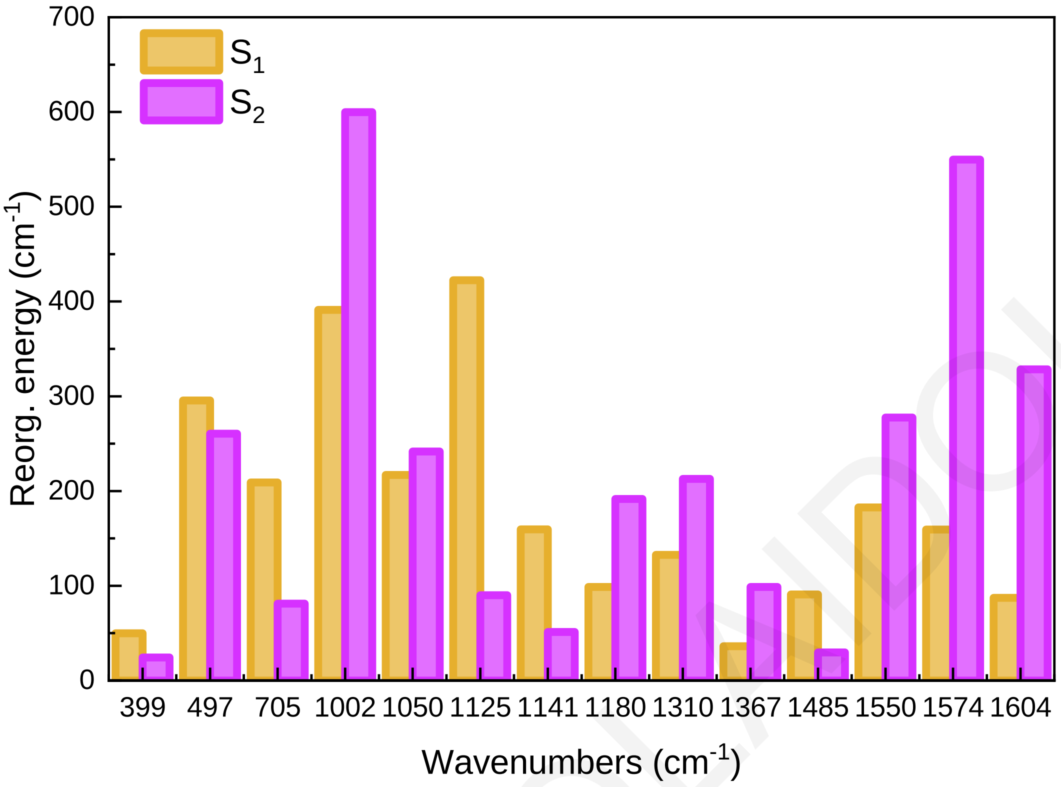

Figure S7.10. Mode-specific reorganization energy for the most prominent vibrational modes of diBT.

Table S7.4. Parameters used in the emission fitting of C8-BTBT.

Transition	ω_g**(cm^{-1})**	ω_e**(cm^{-1})**	Δ_k
C8-BTBT Fluorescence			
ν_1	395	395	0.45
ν_2	440	440	0.52
ν_3	498	498	0.52
ν_4	704	704	0.48
ν_5	998	998	0.40
ν_6	1054	1054	0.40
ν_7	1125	1125	0.27
ν_8	1138	1138	0.22
ν_9	1307	1307	0.50
ν_{10}	1396	1396	0.34
ν_{11}	1477	1477	0.45
ν_{12}	1489	1489	0.90
ν_{13}	1557	1557	0.45
ν_{14}	1603	1603	0.90
Γ (cm^{-1})	140		
Θ (cm^{-1})	300		
E_{00} (cm^{-1})	31400		
M (Å)	1.51		

Table S7.5. Parameters used in the emission fitting of BTBT.

Transition	**ω_g(cm^{-1})**	**ω_e(cm^{-1})**	**Δ_k**
BTBT Fluorescence			
ν_1	395	395	0.35
ν_2	438	438	0.50
ν_3	498	498	0.50
ν_4	710	710	0.40
ν_5	998	998	0.50
ν_6	1054	1054	0.51
ν_7	1130	1130	0.37
ν_8	1179	1179	0.40
ν_9	1306	1306	0.50
ν_{10}	1334	1334	0.35
ν_{11}	1415	1415	0.66
ν_{12}	1375	1495	0.66
ν_{13}	1439	1559	0.40
ν_{14}	1598	1598	0.63
Γ (cm^{-1})	95		
Θ (cm^{-1})	305		
E_{00} (cm^{-1})	31330		
M (Å)	1.035		

Table S7.6. Parameters used in the emission fitting of diBT.

Transition	**ω_g(cm^{-1})**	**ω_e(cm^{-1})**	**Δ_k**
diBT Fluorescence			
ν_1	399	399	0.40
ν_2	497	497	0.65
ν_3	705	705	0.30
ν_4	1002	1002	0.70
ν_5	1050	1050	0.65
ν_6	1125	1125	0.60
ν_7	1141	1141	0.45
ν_8	1180	1180	0.35
ν_9	1310	1310	0.45
ν_{10}	1367	1367	0.23
ν_{11}	1485	1485	0.35
ν_{12}	1550	1550	0.67
ν_{13}	1574	1574	0.90
ν_{14}	1604	1604	0.33
Γ (cm^{-1})	80		
Θ (cm^{-1})	280		
E_{00} (cm^{-1})	29400		
M (Å)	1.48		